Visuotopy and optic flow processing in monkey's visual cortex : an fMRI investigation

Samy Rima

Université de Toulouse

THÈSE

En vue de l'obtention du

DOCTORAT DE L'UNIVERSITÉ DE TOULOUSE

Délivré par :

Université Toulouse 3 Paul Sabatier (UT3 Paul Sabatier)

Présentée et soutenue par :
Samy RIMA

Le mardi 28 novembre 2017

Titre :

Visuotopie et traitement du flux optique chez le singe: une investigation par IRMf

---

ED CLESCO : Neurosciences

Unité de recherche :

UMR 5549 CerCo

Directeur(s) de Thèse :

Dr. Jean-Baptiste Durand

Rapporteurs :

Dr. Suliann Ben Hamed
Dr. Koen Nelissen

Autre(s) membre(s) du jury :

Pr. Patrizia Fattori
Dr. Michael Schmid
Pr. Pier-Giorgio Zanone

VISUOTOPY & OPTIC FLOW PROCESSING IN MONKEY'S VISUAL CORTEX: AN FMRI INVESTIGATION

Visuotopie et traitement du flux optique dans le cortex visuel du singe : une investigation par IRMf

Acknowledgements

Starting acknowledgements is never an easy task, for the rules of language impose that you start somewhere, implicitly prioritizing what you are thankful for. I wish that all people being thanked here, know that you were pillars in the elaboration of this work, for each of you have brought exactly what was needed, at the right time and the right place. Here goes nothing.

Jean-Baptiste, you have been the older brother I have never had. You are a true role model and I know that all PhD students in this lab, wished to have you as a supervisor. You taught me patience and perseverance, you taught me how to love what I am doing despite the hard times, you taught me the true meaning of being a mentor. You trusted me when you sent me to Leuven, you trusted me when I came back. I think you knew I would come back. I shouldn't make this longer than it needs to be. You gave me a lot, and I know my job is to transmit that to as many students as I can.

Asma et Chaoukat, mes parents, sans vous tous cela n'aurait pas été possible. Non pas parce que vous m'avez donné la vie, mais parce que vous m'avez donné l'envie, et le plaisir de la vivre.

Ingrid, je te remercie parce que tu as persisté. Je t'aime parce que tu fais sortir le mieux en moi. Je te remercie parce que tu m'as aidé et soutenu comme personne ne sait le faire.

Youn, Benoît & Marcello. You have also been great teachers and friends, the interactions we had were of utmost significance, both scientifically and humanly. I wish we could continue working together. I love you guys.

Je remercie le Croissant Fertile et tous mes camarades, avec qui je partage ce projet de vie, de renaissance !

Je remercie l'équipe de l'animalerie, passée et présente. Camille et Emilie, je vous remercie aussi de votre aide, mais surtout de votre ténacité, qui m'a appris à être carré (pas autant que vous l'auriez souhaité peut-être, mais ça viendra, promis) dans mes interactions avec les animaux.

Je remercie aussi Nathalie, Jean-Pierre, Yohann, Fred et Hélène. Vous avez été extrêmement aimables et surtout indispensables. C'était un plaisir de travailler avec vous, et surtout de prendre l'apéro à l'IRM lorsqu'on un animal a bien travaillé !

I thank also all of the people I met at the CerCo, past and present members. This network of exceptional people has been the birthplace of original ideas, solid friendships and unforgettable memories.

“The seeker after truth is not one who studies the writings of the ancients and, following his natural disposition, puts his trust in them," the first scientist wrote, "but rather the one who suspects his faith in them and questions what he gathers from them, the one who submits to argument and demonstration and not the sayings of human beings whose nature is fraught with all kinds of imperfection and deficiency. Thus, the duty of the man who investigates the writings of scientists, if learning the truth is his goal, is to make himself an enemy of all that he reads, and, applying his mind to the core and margins of its content, attack it from every side. he should also suspect himself as he performs his critical examination of it, so that he may avoid falling into either prejudice or leniency.”

— Ibn al-Haytham

إن الباحث عن الحقيقة ليس هو من يدرس كتابات القدماء، على حالتها ويضع ثقته فيها، بل هو من يُعلّق إيمانه بهم ويتساءل ما الذي جاء منهم. هو الذي يبحث عن الحجة، ولا يعتمد على أقوال إنسان طبيعته يملأها كل أنواع النقص والقصور. وبالتالي فإن من الواجب على من يحقق في كتابات العلماء، إذا كان البحث عن الحقيقة هدفه، هو أن يستنكر جميع ما يقرأه، ويستخدم عقله حتى الذاع لبحث تلك الأفكار من كل جانب وعليه أن يتشكك في نتائج دراسته أيضًا، حتى يتجنب الوقوع في أي تحيز أو تساهل.- ابن الهيثم

Preamble

My path towards academic research started when I conducted my first internship in the field of Neuroscience with Dr. Jean-Baptiste Durand during the first year of my Master's degree. I had met J-B's brother during one of my courses and we had become close acquaintances. During a conversation about our career goals, I had mentioned to him my will to work in Neuroscience. Promptly he told me that his brother was a researcher in the domain at the CNRS and that I should contact him. In addition to getting frisky with a male macaque's teeth, my first in-depth research experience under the supervision of J-B was extremely motivating and enriching. He had all the right mentorship skills to convey his passion towards his area of expertise. It was during the time the CerCo had first moved to a new location and the MR platform had just entered service. J-B, along with some of his colleagues had the daunting task of putting together the awake monkey fMRI technique from scratch, with very limited monetary, technical, and human resources. At the end of my internship, and after having accumulated all the positive energy from that inspiring team, I asked J-B to help me find a lab in which I could familiarize myself better with monkey fMRI. Happy with my request, he enthusiastically recommended me to the Leuven lab in which he performed one of his postdocs, to conduct my master's thesis under the supervision of Pr. Wim Vanduffel and Dr. John Arsenault.

The object of my master's thesis was the study of the role of the primate ventral tegmental area in reinforcement and motivation. This internship was a true challenge, as it opposed me to my deepest fears and weaknesses. Extensive work and sleepless nights, during which I had to learn new complex skills, have profoundly changed me. Nevertheless, I am grateful to have endured them. During this internship, I have gained a lot knowledge about the neuroscience of reward. I also learned to manipulate macaques, I have assisted in many surgeries and learned to operate an MRI scanner and acquire and analyze fMRI data. I also learned a great deal about chronic implanted electrodes and electric microstimulation. Amid that tsunami of information and struggle to adapt

to a new society, I realized that I had surmounted a lot of obstacles and broken many barriers within my own psyche. I had learned to seek new experiences instead of avoiding them, to boldly defend my ideas and even to go meet my idols. Antonio Damasio was invited to Leuven to be awarded an honorary doctorate, and gave a talk in the university, which I attended. I went to meet him, and we had a long hour discussion about everything, from science to politics, and I had finally asked him to be a reviewer for my thesis, which he accepted.

Upon the end of my master's thesis and having co-authored a paper published in Current Biology (Annex 1), which is an annex in the present manuscript, I was resolved to come back to Toulouse and conduct a PhD under the supervision of J-B. I applied to and won a grant from a Lebanese organization, which then allowed me to contact J-B and discuss with him that opportunity. I came back to the CerCo because I wanted to take part in developing the awake monkey fMRI technique to be able to implement elsewhere. But most importantly, I wanted to continue studying the primate visual cortex.

Knowing that the development a technique as heavy and complex as awake monkey fMRI, and publish with that technique within the 3 years of my PhD funding, was a risky bet. Which is why I developed a secondary axis of research which relates to the subject of my Master's thesis. Fortunately, we were not only able to finish developing the technique and publishing the first awake monkey 3T fMRI paper in France, but we also managed to submit a paper describing a new visuotopic cluster in the monkey posterior parietal cortex. Furthermore, we submitted a study about the effects of reward on visual perception, which is included as an annex in this manuscript (Annex 2).

Dear reader, I hope you enjoy reading this manuscript, as much as I enjoyed writing it.

Summary

Functional magnetic resonance imaging (fMRI) allows addressing the functional organization of the human brain with minimal invasiveness and in healthy individuals. The implementation of that technique in non-human primates represents an important achievement in systems neuroscience. On the one hand, monkey fMRI contributes to the reduction and refinement of invasive approaches in non-human primates, by revealing the regions of interest in which focal electrophysiological and/or anatomical investigations should be carried out. On the other hand, the knowledge acquired with such invasive approaches can be more safely transposed to humans, once inter-species homologies and differences have been identified through the use of similar fMRI protocols in human and non-human primates.

The first part of this thesis reviews the most common approaches that have been used to study brain functions, either in humans or in non-human primates. It is shown that despite progresses in the human approaches, invasive studies in monkeys remain necessary for understanding the neuronal mechanisms underlying cognitive functions. Then follows a description of the evolution of the monkey fMRI techniques and some of its achievements in bridging the gap between non-invasive human studies and invasive animal studies, notably for deciphering the neural mechanisms supporting visually-guided grasping. The end of this first part is purely methodological. It undertakes the description of the monkey facilities and the MR platform in Toulouse, and details the necessary milestones for conducting fMRI research in macaque monkeys. The second part of the thesis presents the 4 studies we have conducted with monkey fMRI. The first study is a preparatory experiment for characterizing the monkey hemodynamic response function, which is a prerequisite for proper analysis of subsequent monkey fMRI data. The second study addresses the visuotopic organization of the primate dorsal visual cortex with a novel technique of wide-field (80°) phase-encoded visual stimulation, coupled with a state of the art surface-based analysis of population receptive fields. The results obtained in 2 animals uncover a new cluster of visuotopic areas in the posterior parietal cortex of the macaque monkey, bringing a fresh view to the functional organization of this piece of cortex and opening a promising avenue for inter-species comparisons. The third study unveils the cortical network involved in optic flow processing in non-human primates and it compares this network to that recently described in humans. To that end, we replicated in macaque monkeys an experiment previously conducted in human subjects with optic flow stimuli that are either consistent or inconsistent with egomotion. Besides confirming the involvement of areas previously identified through electrophysiological recordings, our results reveal new cortical areas involved in the processing of optic flow, drawing the picture of a network sharing many similarities, but also striking differences, with that documented in the human brain.

In summary, the ambition of this thesis is two-fold: (1) providing guidelines for setting-up monkey fMRI techniques, drawn from our own experience and (2) exposing a set of studies we have conducted with this approach, dealing with the visuotopic organization of the dorsal visual cortex and its involvement in the processing of visual motion. Besides bringing a fresh view to the functional organization of the dorsal visual pathway in non-human primates, these studies illustrate how monkey fMRI bridges the gap between electrophysiological studies in non-human primates and functional imaging studies in humans.

Keywords: Visuotopic organization, motion processing, visual cortex, non-human primates

Résumé en français

L'imagerie par résonance magnétique fonctionnelle (IRMf) permet d'examiner l'organisation fonctionnelle du cerveau humain de manière non-invasive et chez les sujets sains. L'implémentation de cette technique chez des primates non-humains représente un progrès important dans les neurosciences des systèmes. D'une part, l'IRMf singe permet la réduction et le raffinement des protocoles invasifs impliquant des primates non humains, en révélant les régions d'intérêts dans lesquelles les approches focales invasives, électrophysiologiques ou anatomiques, devraient être menées. D'un autre côté, les connaissances acquises avec ces approches invasives peuvent être transposées plus aisément à l'homme, une fois que les homologies et différences interspécifiques ont été identifiées au travers de protocoles d'IRMf menées en parallèle chez les primates humains et non-humains.

La 1ère partie de cette thèse présente les approches conventionnelles d'étude des fonctions cérébrales. Nous montrons que des études invasives chez l'animal demeurent nécessaires pour comprendre les mécanismes neuronaux qui sous-tendent nos fonctions cognitives, malgré le progrès des techniques d'investigation chez l'homme. Suit une revue sur l'évolution des techniques d'IRMf singe et certaines de ses réalisations majeures comme pont dressé entre les études non-invasives menées chez l'homme et les études invasives réalisées chez l'animal, notamment en ce qui concerne notre compréhension des mécanismes neuronaux permettant la saisie manuelle d'objets sous contrôle visuel. Purement méthodologique, la fin de cette 1ère partie décrit l'animalerie et la plate-forme d'IRM à Toulouse et expose les jalons de l'implémentation de l'IRMf chez le singe macaque vigile. La 2ème partie de la thèse présente les 4 études que nous avons menées en IRMf singe. La 1ère étude modélise la réponse hémodynamique chez le singe, un outil indispensable à l'analyses de données d'IRMf, acquises dans les études suivantes. La 2ème étude traite de l'organisation visuotopique du cortex visuel dorsal des primates, et y décrit un nouvel assemblage d'aires visuotopiques chez 2 animaux, grâce à l'usage de nouvelles techniques de stimulation visuelle et d'analyse de champ récepteurs. Ces résultats apportent un point de vue neuf sur l'organisation fonctionnelle de la voie visuelle dorsale et ouvrent de nombreuses perspectives pour les comparaisons entre espèces. La 3ème étude cartographie le réseau d'aires corticales impliqué dans le traitement du flux optique chez les primates non humains et le compare à celui décrit récemment chez l'homme. Grâce à la réplication d'une étude réalisée chez l'homme, nous avons confirmé chez 3 macaques l'implication de zones précédemment identifiées par des enregistrements électrophysiologiques. Nos résultats révèlent de nouvelles zones corticales impliquées dans le traitement du flux optique, dessinant l'image d'un réseau cortical partageant de nombreuses similitudes, mais ayant également des différences frappantes, avec celui documenté dans le cerveau humain.

En résumé, l'ambition de cette thèse est double : (1) fournir des recommandations pour la mise en place de techniques IRMf chez le singe, tirées de notre propre expérience et (2) exposer les résultats d'un ensemble d'études que nous avons menées avec cette approche, traitant de l'organisation visuotopique du cortex visuel dorsal et de son implication dans le traitement du mouvement visuel. En plus d'apporter une perspective nouvelle sur l'organisation fonctionnelle du cortex visuel chez les primates non humains, ces études illustrent la contribution de l'IRMf singe comme pont entre études électrophysiologiques chez les primates non humains et études d'imagerie fonctionnelle chez l'homme.

Mots clés : Organisation visutopique, traitement du mouvement visuel, cortex visuel, primates non-humains

Résumé long en français

Le développement de l'IRMf (Imagerie par Résonance Magnétique fonctionnelle) chez des primates non-humains (PNH) a instauré la possibilité d'établir le lien tant attendu entre les données issues d'études invasives chez le PNH et celles d'imagerie fonctionnelle obtenues chez l'humain. Cette technique représente un progrès important car elle permet la réduction et le raffinement des protocoles invasifs impliquant des primates non humains, en révélant les régions d'intérêts dans lesquelles les approches focales invasives, électrophysiologiques ou anatomiques, devraient être menées. Par ailleurs, les connaissances acquises avec ces approches invasives peuvent être transposées plus aisément à l'homme, une fois que les homologies et différences interspécifiques ont été identifiées au travers de protocoles d'IRMf menées en parallèle chez les primates humains et non-humains. Conscient des avantages que fourni le modèle PNH, l'objectif primordial de cette thèse était le développement de la technique IRMf chez le singe éveillé au CerCo (Centre de recherche sur le cerveau et la cognition) à Toulouse, afin d'étudier l'organisation fonctionnelle de la voie dorsale chez cette espèce et de la comparer avec celle de l'Homme.

En guise d'introduction, cette thèse présente les approches conventionnelles d'étude des fonctions cérébrales et montre que des études invasives chez l'animal demeurent nécessaires pour comprendre les mécanismes neuronaux qui sous-tendent nos fonctions cognitives, malgré le progrès des techniques d'investigation chez l'homme. Suit une revue sur l'évolution des techniques d'IRMf singe et certaines de ses réalisations majeures comme pont dressé entre les études non-invasives menées chez l'homme et les études invasives réalisées chez l'animal, notamment en ce qui concerne notre compréhension des mécanismes neuronaux permettant la saisie manuelle d'objets sous contrôle visuel. Cette revue bibliographique est suivie par un chapitre purement méthodologique, qui décrit l'animalerie et la plateforme IRM du pavillon Baudot qui accueille le CerCo. Cette partie expose les étapes qui ont permis l'implantation des techniques d'IRMf singe sur la plateforme. Elle détaille la mise en place des 2 postes de conditionnement qui, en mimant

l'environnement de l'IRM, permettent la familiarisation des animaux aux différentes contraintes de ce milieu et leur entrainement aux différentes tâches qu'ils doivent pratiquer pendant les sessions d'acquisition d'images fonctionnelles. Sont discutés aussi le développement d'une antenne 8 canaux dédiés à l'imagerie chez les macaques et la création d'outils d'analyses des données fonctionnelles et oculométriques.

Dans la continuité de la description de la mise en place de l'IRMf chez le singe éveillé à Toulouse, la partie suivante décrit la modélisation de la réponse hémodynamique du cortex visuel du singe macaque. L'IRM n'offre qu'une mesure indirecte de l'activité neuronale, qui repose sur la détection des perturbations du champ magnétique dans un volume de cerveau défini (voxel) induit par une modification du rapport d'hémoglobine oxygénée/hémoglobine désoxygénée et dont la dynamique est nommée réponse hémodynamique (HRF). L'analyse des données d'IRMf dépend d'une bonne estimation de la HRF, qui est non seulement propre à chaque espèce, mais peut aussi varier entre les différentes aires du cerveau. Dans cette étude préliminaire, nous avons estimé la HRF du cortex visuel sur 3 macaques, à partir des activations IRM induites par une impulsion visuelle (l'affichage très bref d'un damier scintillant couvrant une grande partie du champ visuel) et d'une fonction modèle de type double-gamma. Les paramètres de ce modèle sont discutés en termes de variabilités interindividuelles et interspécifiques.

Ce modèle de HRF est ensuite utilisé dans 2 études. Dans la première, qui constitue le cœur de ma thèse, je me suis intéressé à l'organisation visuotopique de la voie dorsale chez le singe macaque. Le cortex visuel du macaque a été extensivement étudié et de multiples modèles de son organisation fonctionnelle ont été proposés. Cependant, l'organisation visuotopique de certaines aires et notamment celles de la voie dorsale demeurent débattues. Plusieurs difficultés surgissent lors de l'investigation de cette région de cortex. D'abord, les aires visuelles de la voie dorsale présentent de grands champs récepteurs couvrant les zones les plus périphériques du champ visuel. De plus, beaucoup de ces zones ne présentent pas une organisation rétinotopique conventionnelle du fait

qu'elles traitent aussi d'autres modalités sensorielles que la vision. Enfin, l'attention semble jouer un rôle important dans l'activation de ces zones. Ainsi, l'activation de cette région requiert des stimuli capables de couvrir la quasi-totalité du champ visuel et qui présentent des attributs d'importance comportementale, pouvant attirer l'attention des sujets.

Grâce à l'emploi d'une technique de stimulation large-champ (80° d'excentricité) et l'utilisation d'un stimulus visuel représentant un panier de fruits en mouvement comme stimulus, nous avons été capable d'activer de façon robuste une grande partie de la voie visuelle dorsale chez 2 macaques. Suite à la projection des données volumétriques sur la surface corticale, nous avons utilisé un filtre fréquentiel avant d'effectuer une analyse des champs récepteurs de population. L'analyse des résultats issus de ces traitements nous a permis de détecter des inversions de gradients d'angle polaire et d'excentricité des champs récepteurs de population le long de la surface corticale, qui confirment et synthétisent les connaissances acquises au moyen d'approches invasives sur ce modèle. Ces inversions de gradients révèlent de plus les frontières d'un nouvel assemblage d'aires visuotopiques. Cet assemblage d'aires (« cluster »), nommé PIP (posterior intraparietal) est situé dans la partie postérieure du sillon intra pariétal et est constitué de 2 aires récemment décrites (CIP 1/2) et de 2 nouvelles aires (PIP 1/2). Ainsi, grâce à la combinaison de l'IRMf et de la cartographie rétinotopique large-champ, nous avons décrit des structures organisationnelles non caractérisée jusque-là, que ça soit par des méthodes invasives ou des méthodes de cartographie rétinotopique traditionnelles.

La seconde étude avait pour but de caractériser le réseau d'aires corticales impliquées dans le traitement du flux optique compatible avec le mouvement de soi. Une étude récente publiée par Andrew Smith du Royal Holloway à l'université de Londres, décrit l'implication d'un large réseau d'aires corticales dans cette fonction, bien plus étendu que ne pouvait suggérer les données invasives chez l'animal. Cette étude confirme certaines aires qui correspondent à des aires homologues trouvées chez le singe par électrophysiologie mais décrit surtout une aire qui semble

être particulièrement sélective au mouvement de soi. Cette aire dénommé CsV (Cingulate sulcus Visual) ne possède aucun homologue connu chez le singe. En collaboration avec Andrew Smith, nous avons répliqué l'étude menée chez l'homme afin de caractériser le réseau cortical impliqué dans le traitement de mouvement et d'évaluer un homologue de l'aire CsV chez le singe. En contrastant l'activité corticale résultante d'un stimulus de flux optique compatible avec le mouvement et celle du même stimulus répliqué 9 fois (3x3) sur l'écran (incompatible avec le mouvement de soi), nous avons révélé un réseau cortical qui soutient les données électrophysiologiques et anatomiques précédemment décrites chez le PNH. La comparaison de ces données avec les données humaines révèlent que malgré le fait que les réseaux corticaux chez les 2 espèces partagent des similitudes (MST/hMST, VIP/hVIP,VPS/PIC et pmCsV/CsV), ils demeurent différents. D'une part, certaines aires sont propres au singe et ne sont pas retrouvées chez l'humain, tel que les aires 7a, STPm, FEFsem et FEFsac. D'autre part, des activations robustes des aires V6, P2V et Pc ne sont pas retrouvées chez le singe.

Cette thèse poursuivait un double objectif :1) fournir des recommandations pour la mise en place de techniques IRMf chez le singe, tirées de notre propre expérience et (2) exposer les résultats d'un ensemble d'études que nous avons menées avec cette approche, traitant de l'organisation visuotopique du cortex visuel dorsal et de son implication dans le traitement du mouvement visuel. En plus d'apporter une perspective nouvelle sur l'organisation fonctionnelle du cortex visuel chez les primates non humains, ces études illustrent la contribution de l'IRMf singe comme pont entre études électrophysiologiques chez les primates non humains et études d'imagerie fonctionnelle chez l'homme.

Mots clés : Organisation visuotopique, traitement du mouvement visuel, cortex visuel, voie dorsale, primates non-humains

Table of content

A. General Introduction

A.1 Human approach to cognitive neuroscience

With its billions of interconnected neurons, the human brain is the most complex system in the known universe and as such, a paramount challenge for scientific research. Our brain supports recognition, attention, memory, decision making and many other higher cognitive functions by which we can challenge daily basic struggles, navigate, use tools, cooperate and build societies. Although the anatomy and physiology of many other organs can be reasonably apprehended through studies in rodents, taking advantage of their high similarities with human organs, studying the human brain is another level of dilemma. Many of the higher cognitive functions it operates are specific to humans or shared only with its closest relatives, i.e. the non-human primates. Understanding those functions requires in-depth knowledge of the underlying neural mechanisms, knowledge that spans across the functional organization of the brain to the dynamics of single neurons. Accessing this knowledge constitutes an ethical quandary, since it requires invasive procedures that are difficult to conduct in humans. However, much progress has been made through approaches involving notably human brain lesions studies and more recently, non-invasive functional imaging studies. Those approaches are briefly described in the following sections.

A.1.1 Human lesions

In 1861, Paul Broca boldly suggested that the third convolution of the inferior frontal gyrus is involved in speech production. Support for this claim came from the brain of a patient (Figure 1) who had been able to produce only one syllable (tan), in the form of stereotyped recurrent utterances: tan-tan-tantan… Although Broca was not the first to relate language to the left hemisphere, his finding launched a new age of discovery. Specifically, Broca's approach to localizing human brain function by studying the correlation between the location of a brain lesion

and a behavioral affliction founded a long tradition of neuropsychological research, which has greatly advanced our understanding of brain function.

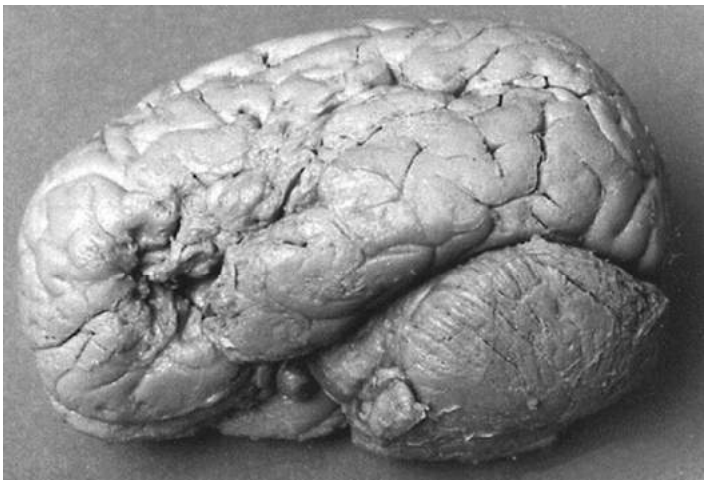

Figure 1. ***Leborgne's brain*** (source: Dronkers NF, et al., Paul Broca's historic cases: high resolution MR imaging of the brains of Leborgne and Lelong. Brain 2007;130:1432-1441)

Although in historical terms, lesions caused by accidents, war injuries, strokes or even neurosurgical excisions were the pillar of neurophysiology for a long time (Cowan et al., 2000), there are several fundamental problems with the lesion method that have caused neuroscientists to become critical about the technique.

Firstly, in the case a lesion could be detected and localized, highly sophisticated psychological and physiological assessments are needed to be able to pinpoint the nature of the impairment caused by the lesion. Furthermore, many brain functions might be carried out in a distributed manner, with large portions of the brain working in a flexible fashion rather than each region having a fixed function. Consequently, it is very difficult to exclusively link a lesion to a cognitive function. Indeed, accidental lesions or lesions caused by trauma, almost always span across many cytoarchitectonic areas. Additionally, almost constantly concomitant white matter insults disengage the connection between different areas, which implies that it cannot be excluded that the diagnosed impairment is not due to an interruption of functional connectivity instead of a focalized lesion per se. Moreover, since a certain amount of time would have passed between the lesion and the beginning of its investigation, functional reorganization of the cortex would have most probably occurred, thus misleading our interpretation about the function of the area in the normal brain.

The human 'lesion method' was seminal for our understanding of functions as diverse as language, memory, hemispheric specialization, emotion, vision and motor control, but to relate behavioral functions to anatomy using the lesion approach, it is necessary to identify the location and extent of a brain injury. At the time when Broca conducted his work (in the 1860s), researchers had to wait for a patient to die before they could examine the brain, a new method was thus needed.

A.1.2 Brain imaging

Fortunately, William H. Olendorf got unsatisfied with the traumatic, tedious, invasive studies on his patients at the University of Minnesota Hospital. Indeed, these studies provided only limited and indirect information about the brain. So, he strived for something better. William Henry Oldendorf (1925–1992) was an American neurologist, physician, researcher, medical pioneer and founding member of the American Society for Neuroimaging (ASN). From his basement, he modeled a new instrument incorporating principles and hardware used in modern computed tomography (CT) scanners. The description of the model was published in 1961. Standard X-Ray manufacturers were not thrilled with Olendorf's idea and dismissed it as impractical. A letter from one company ended: "Even if it could be made to work as you suggest, we cannot imagine a significant market for such an expensive apparatus which would do nothing but make a radiographic cross-section of a head". Despite his failure to interest manufacturers with his invention, Oldendorf's description was patented in 1963 and this has been of invaluable importance to researchers in the field of neuroimaging.

Soon after the invention of CAT (Computer Automated Tomography), the development of radioligands started the functional imaging revolution. Thanks to the work of Marcus Raichle and coworkers, functional imaging took a large step forward with the development of oxygen-15 labelled water (H_2O^{15}) imaging (Herscovitch et al., 1983). H_2O^{15} emits positrons and creates images based on regional blood flow within the brain. Since active neurons recruit a robust blood supply,

H_2O^{15} positron emission tomography (PET) allowed investigators to make regional maps of brain activity during various cognitive tasks. Concurrently, magnetic resonance imaging (MRI or MR scanning) was developed. Scientists soon learned that the large blood flow changes measured by H_2O^{15}PET were also imaged by MRI. Functional magnetic resonance imaging (fMRI) was born(Ogawa et al., 1990). Since the 1990s, fMRI has come to dominate the brain mapping field due to its low invasiveness, lack of radiation exposure, and relatively wide availability.

Studying brain functions in healthy subjects using very precise cognitive tasks performed inside the scanner provides access to peak activity that is restricted to cytoarchitectonic areas and that lie in grey and not white matter, without the worry of possible cortical reorganization such as can be found in patients. Whether PET or fMRI is used, the functions of an area can be inferred by contrasting tasks that differ in only one aspect. Nevertheless, showing that an area is active during a task does not necessarily means that it is mandatory for performing the task accurately, nor does it indicate its precise functional role. For example, many studies have reported activity in the anterior cingulate cortex when subjects are engaged in judgement tasks about the thoughts of others (theory of mind) (Gallagher 2003). However, a patient with a large bilateral lesion of this area had no problem in succeeding on similar tasks (Bird et al., 2004), questioning the central role of this area in such tasks. Recent developments in fMRI may also allow measuring the covariance in activity between various areas (Rogers et al., 2007), introducing the possibility to study functional interactivity between distant portions of the cortical surface. Yet these methods still rely on measures of correlation, a limitation which can only be resolved through interference with the activity of one of the areas. There are several other limitations to brain imaging techniques such as PET or fMRI: neither provides a direct measure of neural activity. The signal measured in fMRI is blood oxygen level dependent (BOLD), which is an indirect measure of blood flow. Granting that PET measures direct fluctuations of blood flow, both techniques indirectly measure the activity of a whole population of cells, with no information on specific cellular dynamics. Admitting that these

techniques are suitable for functional studies, the same cannot be said for the study of how functions are implemented at the neuronal level. The cellular machinery has a temporal resolution on the order of milliseconds, while PET has a temporal resolution of around 60 seconds and fMRI has a rough temporal resolution of 1-3 seconds. Consequently, we cannot fathom the order of events in the brain. The temporal caveats of fMRI and PET can be resolved with techniques such as the electroencephalogram (EEG) or the magnetoencephalogram (MEG). EEG measures voltage fluctuations resulting from ionic current within the neurons of the brain at a distance. The first human EEG was recorded in 1924 by German physiologist and psychiatrist Hans Berger (1873–1941) (Swartz, 2017). It is a non-invasive method that detects local variations of the electric field with electrodes placed along the scalp. EEG has a temporal resolution on the order of the millisecond and even the microsecond, which makes it ideal to study signal propagation. EEG is less subject to motion artifacts and it is a portable technique that can even be used on infants and claustrophobic subjects. One serious drawback is its poor spatial resolution. Indeed, because of the bad conductibility of the scalp, the measured electrical field fluctuations tend to disperse, making it difficult to localize their sources. The other technique with a high temporal resolution, is MEG. MEG signals were first measured by University of Illinois physicist David Cohen in 1968 (Cohen, 1968), It measures changes in magnetic fields on the surface of the scalp. The additional advantage over EEG is that it possesses a better spatial resolution, because magnetic field fluctuations are not distorted by the scalp. MEG is an expensive technique though, it is not portable and requires pairing with MRI for proper areal localization.

Until today, no single novel technique could fuse the advantages of fMRI and EEG/MEG. Although combined studies of fMRI and EEG have achieved noteworthy results(Mullinger and Bowtell, 2011; Huster et al., 2012), despite the inherent methodological problems that arise from the combination of these techniques, a tool with the ability to acquire both high temporal and spatial resolution data would be the holy grail of brain imaging.

A.1.3 Causal approaches

The aforementioned imaging techniques, no matter their resolution remain correlational approaches, they inform about the relationship between indirect measures of brain activity and behavioral performances in sensory, motor or cognitive tasks. However, knowing whether the recorded activity in a particular brain location is necessary for executing the task at hand or simply an epiphenomenon requires tampering with its activity. Application of electrical currents to modify/investigate brain functions is a technique that dates back to the 19th century (Selimbeyoglu, 2010). Methods such as trans-cranial magnetic stimulation (TMS) (Sparing and Mottaghy, 2008), that deliver localized magnetic perturbations inducing increased or debilitated activity depending on the adopted mode, can inform us on the causal role of a cortical area. This technique is nevertheless restricted to the first 3 cm of cortical depth, as it cannot reach deep brain structures such as the thalamus or the basal ganglia. Additionally, it is only as precise as the experimenter's localization and positioning abilities, although precision can be increased using online neuro-navigation. In addition, the effects of TMS are quite brief.

Other causal approaches include transcranial direct current stimulation (TDCS). This technique is inexpensive, easy to administer, non-invasive and virtually painless. TDCS has been shown to modulate human brain functions by inducing focal, prolonged, but reversible shifts of cortical excitability. Studies combining TDCS with other brain imaging and neurophysiological mapping promise to provide invaluable insights on the causation between modification of behavior and its underlying neurophysiologic underpinnings (Sparing and Mottaghy, 2008).

A.1.4 Neural recordings in patients

Measuring directly the neural activity of single cells or cell populations during cognitive tasks represents an essential step for gaining a better knowledge of the neural codes underlying those cognitive functions. Electrophysiological recordings in humans, while feasible, are restricted to

patients suffering from epilepsy and that are about to undergo ablation surgery of the epileptic foci (Nobre and Mccarthy, 1995), or patients being outfitted with brain-machine interfaces for the control of prosthetic limbs or for interaction with computers (Andersen et al., 2004). Despite the limitations, this technique is a promising one, as it already brought decisive findings, such as the "Jennifer Anniston" neurons in the hippocampus (Quiroga et al., 2005).

A.2 Non-human primates: a necessary alternative

Non-human primate (NHP) research has helped resolve a great deal of the limitations inherent to the study of human brain functions. The brain of the macaque monkey closely resembles that of humans in both structural and functional terms (Orban et al., 2004; Sereno and Tootell, 2005), furthermore they share with us similar cognitive and perceptive abilities, and they can be taught to perform complex tasks. Thus, the macaque model is fundamental to our understanding of our mental world.

Monkey research has provided the basis for ground-breaking discoveries despite being the focus of very vocal and sometimes violent opposition from well-funded groups waging war against animal-based biomedical research. Opposing groups often argue that the palette of techniques available in humans, combined to modeling approaches, is sufficient for studying brain functions (Bailey and Taylor, 2016). Yet this argument fails to distinguish between methods that record or disrupt large cell populations in cortical regions dictated by clinical considerations, and methods that disrupt small populations or even single cells in chosen regions of interest. As mentioned previously, the spatial resolution of techniques such as fMRI, EEG and MEG is adequate for linking anatomy to behavior, but much finer spatial and temporal resolution is needed to understand the underlying neuronal computations. Invasive studies are necessary, notably because the only way to understand the function of brain areas and to understand the language of the brain,

is to directly and selectively interfere with the activity of these regions and record each set of neuronal types.

A.2.1 Anatomical exploration of NHP cortex

Anatomically speaking, the brain of the rhesus macaque has been explored in detail. The cortical circuitry of the monkey cortex has been thoroughly studied using tractography (Felleman and Van Essen, 1991; Young, 1992, 1993). By injecting tracers in localized areas and following their migrations along axons, one can establish the connectivity pattern between cortical areas. A database that collates information from 391 papers, including data on 7007 sites and around 37000 connection details, is available online (www.cocomac.org). This database also includes information on the specific interconnectivity of cortical layers. Feedforward and feedback connections do not project to the same cortical layers. Thus, knowing how cortical layers connect to each other is crucial for understanding the flow of information in the brain. Diffusion tractography imaging (Soares et al., 2013), a variant of fMRI can provide information about the patterns of wiring, yet the level of detail that we have in macaque monkeys is far from being reached in the human brain. Although there has been criticism about probable differences between macaque and human connectomics (Miranda-Dominguez et al., 2014), no major differences have been observed so far.

A.2.2 Monkey neurophysiology: the backbone of modern neuroscience

The pioneering work on monkeys of Hubel and Wiesel (1968) propelled electrophysiological recordings in monkeys to the stature of a pillar in systems neuroscience. By using metal, glass or silicon electrodes to record electrical signals associated with ion fluxes across neuronal membranes, electrophysiology allows listenning directly to the language of neurons at an extremely high signal-to-noise ratio. This is the main strength of the method, because electrical activity is recorded directly, without the need for a 'translator', that is, a probe that transforms electrical activity into a different signal. However, this is also the main weakness of electrophysiology, because access to

the electrical activity of neurons necessitates physical contact with the tissue under investigation. The advantages this technique presents over its equivalent in humans are unquestionable. Firstly, recordings are done on normal brains in monkeys, whereas recordings in humans are normally done on patients. Second, the time limit to record single cells in monkeys is enough to test each under a variety of conditions (Rainer et al., 1999), which is not the case for patients given the requirements of surgery. Furthermore, electrode arrays can be used to acquire data from multiple cells concomitantly, and from several cortical areas (Takeda and Funahashi, 2004). Furthermore, computers models of signal integration can then be constructed through the combination of information from the different sources (Carmena et al., 2003).

The advancement of neurophysiology in NHPs has been and will always be the necessary precursor to human neurophysiological recording and stimulation. It is not imaginable to conduct such procedures in humans without validating them in NHPs beforehand. The development of direct brain computer interfaces in NHP will undoubtedly introduce new major technologies not only for the palliation of motor deficits in patients, but also for the enhancement of normal subjects (Nicolas-alonso and Gomez-gil, 2012).

A.2.3 Monkey lesion and interference

Electrophysiological recordings can also be combined with causal techniques. Lesion studies in NHPs are more precise than their human counterparts, considering that the lesions are experimentally controlled and can be restricted to the grey matter of a single cytoarchitectonic area. Furthermore, one does not depend on meta-studies encompassing dozens of patients, since the same lesion can be replicated across multiple animals. To avoid induced cortical reorganization, one can replace physical insults with temporary pharmacological perturbations (Tanji and Shima, 1994; Shima and Tanji, 2011) or use cooling for focal and transient cortical inactivation (Lomber, 1999). Perturbation experiments include also electrical stimulation of both cortical matter and deep

nuclei. A recently developed tool, optogenetic stimulation (OS) (Gerits et al., 2012) allows controlling of cell-type-specific neuronal activity on a millisecond timescale, which has been shown to induce changes in behavior. Furthermore, the combination of OS and electrophysiological recording established a selective koniocellular LGN influence on V1 supra-granular layers (Klein et al., 2016). Interference techniques can be used in combination with cell recordings to elucidate the link between 2 cortical areas (Mushiake et al., 1991; Chafee and Goldman-Rakic, 2000; Wallis and Miller, 2003).

In the wake of my master's thesis, I have been involved in a study that exemplifies many of the advantages offered by the NHP model for understanding the link between behavior and its neuronal underpinnings (Arsenault et al., 2014). This work had a twofold purpose: 1) investigating the role the ventral tegmental area (VTA) on reinforcement learning, and 2) characterizing the network of areas activated by VTA electrical stimulation. This required us to implant 2 monkeys with chronic electrodes. To make sure we properly targeted this deep structure, we used anatomical scans to monitor the position of the electrode during surgery, which itself required precisely controlled anesthesia and state of the art imaging for trajectory correction. Electrical stimulation of VTA was subsequently used to demonstrate its causal involvement in establishing instrumental associations. Furthermore, combining such stimulation with fMRI allowed us to reveal the areas functionally connected to VTA. Of course, such a study has little chance of being conducted in humans. Although some patients are fitted with electrodes for deep brain stimulation, the big majority are not compatible with fMRI. Furthermore, it would be ethically unfathomable to use such technique to manipulate instrumental preferences for stimuli.

A.2.4 Complications in relating human and monkey studies

Since modern macaque monkeys and humans have been separated for 30 million years (Kay 1997), one would expect to find significant differences between the brains of monkeys and humans.

Anatomical differences are not the only thing differentiating these 2 species (Kaas, 2006). There are marked behavioral differences, and these must depend partly on differences in the brain and its selective adaptation to distinct environments. Humans can speak and use grammar, reflect on their own mental states as well as those of others and can mold the environment through explicit understanding of causes in the physical and mental world.

A hypothetical monkey of the same body weight as human would have a brain that is 4.8 times smaller. Furthermore, the proportions of the human brain are not those that would be predicted by a plot of the changes in proportions in other primates as brain size increases. For example, the human neocortex is 35% larger than predicted for a primate with a similarly sized brain (Passingham, 2009). An increase in brain size could mean an increase in the number of specialized regions. In addition, the amount of cortical tissue devoted to a body part relates to the sophistication of the analysis or control, rather than the size of that part: the amount of information received by the eye of a monkey and that of a human does not greatly differ, yet the inferior temporal cortex, devoted to the identification of visual objects in both species (Denys, 2004), is 12 times larger in the human brain (Kaas, 2006). The absence of one-to-one correspondence indicates that homologies but also differences are likely to exist in the functional organization of the cortex, which prevents direct transposition of NHP research to humans. Then, one might argue that there is a problem interpreting functional imaging data in humans with data obtained from cells in NHPs.

Undoubtedly, how can one know that the area activated in human brains is the homolog area from which recording has been undertaken in the monkey brain? Indeed, establishing a relationship between human and monkey studies is far from straightforward. Signals measured with non-invasive techniques in humans are not direct estimations of neural activity. In contrast, invasive electrophysiology in macaques measures the direct electrical activity of single cells or a small population of neighboring cells. Differences in the nature of measured signals renders it difficult

to disentangle dissimilarities caused by parallel brain evolution from those caused by a difference of recorded signals.

A.3 Conclusion

The brain is a highly complex system of which the workings occur on multiple spatial and temporal scales. Thus, understanding such a machinery requires the combination of multiple techniques, some of which can be implemented in humans (non-invasive) and others not (invasive). For such, the NHP model imposes itself as a necessity for what can only be resolved through invasive techniques. The major challenge then is to integrate the knowledge gathered from the invasive approaches in NHPs with the data acquired from non-invasive approaches in humans.

B. fMRI bridges the gap between single cell and human imaging studies

B.1 Closing the loop

FMRI is an important technique that helps identify the neuronal structures underlying cognitive functions in healthy human volunteers and patients. But direct comparison between monkey electrophysiology and human fMRI is difficult because those approaches differ in species and technique. Indeed, properly establishing a link between human imaging and single cell studies must begin with the comparison between single cells with fMRI in monkeys and addressing the effect of the technique, and then fMRI in humans and monkeys, to investigate species differences.

Monkey fMRI is an important advancement in systems neuroscience. On one hand, it supplies a bird's eye view of the cortical distribution of cognitive functions, which constitutes a precious guide for electrophysiological recordings and reversible perturbations. Consequently, monkey fMRI serves both the reduction and refinement of invasive protocols involving non-human primates. Combining fMRI with invasive techniques can also help us better understand and interpret (BOLD) signal. fMRI has been in use since the early 1990s, and while the BOLD signal is obviously a marker of brain function, it is still not clear what exactly it represents. For example, it is not known whether all neural processes elicit a BOLD response (e.g. synaptic input vs. spiking activity, stimulus-driven and neuromodulatory activity, feedforward and feedback processes, inhibitory and excitatory potentials) or whether these processes are all equally represented in the BOLD signal (Goense and Logothetis, 2008).

On the other hand, knowledge acquired with monkey fMRI can be directly related to that acquired in humans with the same approach, allowing the identification of homologies and differences in brain functions, a necessary step for integrating the wealth of results from invasive research in animals with the ever-expanding human imaging data sets. NHP research helps with the interpretation of findings obtained with neuroimaging techniques in humans, and, vice versa, findings in humans aid in the interpretation of the results obtained in NHPs.

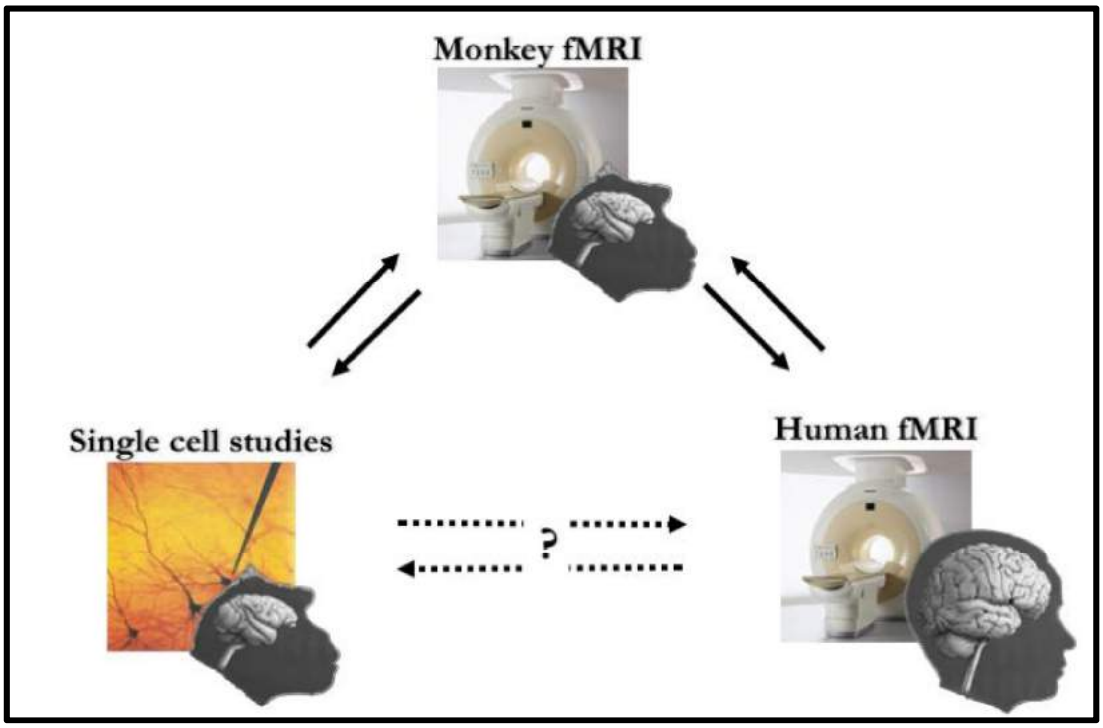

Figure 2. **Monkey fMRI draws a bridge between single-cell studies and human functional imaging studies**

B.2 Monkey fMRI: the journey

B.2.1 First attempts

Functional imaging in monkeys did not await the advent of fMRI. While some have attempted using PET imaging in monkeys (Takechi et al., 1997), this technique never really gained wide use because of multiple methodological problems and inherent technical limitations. Indeed, PET requires the use of radioligands that expose the subject and experimenters to radioactivity, which limits the repeatability of experiments, thus restraining the robustness of data, especially when this data is issued from complex cognitive tasks. Furthermore, PET has very low temporal and spatial resolutions. A transition towards fMRI was thus inevitable and many obstacles were to overcome for the proper transfer of this technology from humans to monkeys.

The first studies (Dubowitz et al., 1998; Stefanacci et al., 1998) to report stimulus-induced neuronal activity-related signals in the visual cortex of an awake monkey using fMRI, employed a low-field (1.5 T) clinical horizontal MR scanner. They trained rhesus macaques in a mock MR environment to remain immobile in a prone position, with body restrained and head fixed to the primate chair via a custom-designed, nonmetallic head-post surgically attached to their skull. With the purpose of activating the visual cortex, the experimenters subjected the monkey to visual stimuli rich in movement, color and texture. In one of the studies (Dubowitz et al., 1998), the images that figured in the study show activation of a small region at the pole of the occipital lobe mixed with some ghosting artifacts. This activation was problematic, as it was located bilaterally about 8 degrees peripheral to the cortical representation of the monkey's fovea. No response was evident in the animal's cortical representation of the macula. In the other study (Stefanacci et al., 1998), stimulus-induced activation was impossible to localize because signal variation was dominated by motion artifacts. These first attempts at monkey fMRI provided rich insight on necessary improvements to make such procedure worthwhile, all while raising important issues.

B.2.2 The battle for SNR

FMRI eliminated the risks related to exposure to radioactivity, while providing better spatial and temporal resolutions compared to PET. Yet, many obstacles are still to overcome for the proper use of monkeys in an MR environment, especially if the purpose is to test humans and monkeys in similar conditions with relatable cognitive tasks. Generally speaking, scanning strategies and methodologies cannot be simply transferred from human fMRI to awake monkey fMRI. There are several significant technical challenges involved in carrying out fMRI experiments in monkeys, arising from the need to use alert animals.

Monkeys have relatively small brains and smaller functional structures compared to humans. The average area of the cerebral cortex in macaque monkeys is 100 cm^2 (Felleman and Van Essen, 1991), compared to 2500 cm^2 in humans. Functional structures are also smaller, for example the ocular dominance columns in macaque monkeys (Ts'o et al., 1990) are half the size of those in humans (Cheng et al., 2001; Yacoub et al., 2007). The higher spatial resolution that is necessary for the smaller monkey brain causes a loss of signal-to-noise ratio (SNR). For human fMRI, resolution is typically about $3 \times 3 \times 3$ mm^3, which leads to a voxel size of almost 30 μl before any spatial smoothing is applied. For awake monkeys, a typical spatial resolution is on the order of $1.5 \times 1.5 \times 2$ mm^3 (4.5 μl voxels), while for anesthetized monkeys the resolution is even higher. Depending on acquisition and pre-processing parameters, the SNR of monkey fMRI can easily be 5–30 times lower than that of human fMRI. This is a large SNR loss that needs to be taken into account when the experiment is designed, for instance by offsetting the SNR loss with smaller RF-coils (Logothetis et al., 2002; Janssens et al., 2012), using iron-based contrast agents to enhance the functional signal (Vanduffel et al., 2001; Leite et al., 2002; Fize et al., 2003), or using high-field scanners.

Another significant problem is animal motion. While human subjects can be selected based on their ability not to move, the task is harder for animals that are naturally uncooperative. Any

movement of the animal that causes the brain to change position inside the magnetic field during scanning produces inconsistencies in phase and amplitude, which can generate blurring and ghosting motion artifacts larger even than the activation signals (Pfeuffer et al., 2007).

B.2.3 Pedal to the metal: High-field vertical fMRI

Another adopted course for monkey fMRI was through the use of custom built high-field (4.7 T) vertical bores. The pioneers of this technique (Logothetis et al., 1999) showed that BOLD imaging at very high spatiotemporal resolution is possible in both the anesthetized and the alert monkey. In the initial study, fifteen animals in total were scanned, distributed between behaving and anesthetized configurations. In the latter configuration, the level of anesthesia, the precise control of respiration and the correct positioning of the visual stimulus, virtually eliminated motion artifacts whether they were voluntary or simply related to physiological function. In contrast, experiments on anesthetized monkeys were hampered by the upright position of the animal, as it became substantially more difficult to maintain normovolemia and constant blood pressure. On the other hand, the behaving animal configuration, benefitted greatly from the upright position. Being more natural, this position permitted easier training of the animals and reduced unwanted body movements. In both configurations, stimulus-specific activation was observed in the LGN, striate and early extrastriate cortices, and in the temporal and mediotemporal structures that are involved in the processing of facial identity and expression. In the anesthetized monkey, activation was highly dependent on the depth of anesthesia.

This high complexity and cost of setting up this technique and maintaining it proved to be to prohibitive to allow its widespread adoption.

B.2.4 On the home stretch: democratizing monkey fMRI

The beginning of the 21st century witnessed a steep increase of interest in awake monkey fMRI. Thus, striving to render this technique more accessible, without the need to build expensive custom scanners, one lab greatly contributed to the simplification and refinement of this technique.

Amongst the flagship studies that set the tone for subsequent monkey fMRI, was one published in 2001 by Vanduffel and colleagues. They demonstrated that robust visually driven activations could be detected using the more available horizontal, low field, clinical scanners. To accomplish this feat, they used iron oxide contrast agents to significantly enhance the functional brain imaging in awake behaving macaques, compared to the BOLD signal. They showed that the use of such contrast agents yielded approximately a 10-fold increase in the percent signal change relative to comparable BOLD measurements at 1.5T, thus becoming an excellent alternative to BOLD imaging with high field scanners. This enhancement allowed them to link between the motion sensitive areas found in fMRI with and those that have been described in single cell studies. The advancements provided by this team over the years made their approach to monkey fMRI a reference for those who wanted to try their hand at scanning monkey brains. Significant advancements in monkey fMRI techniques were introduced in the following years, with the development of implanted focal single loop coils (Logothetis et al., 2002), combined EEG/fMRI at 4.7T (Schmid et al., 2006) external phased array coils (Ekstrom et al., 2008), spin-echo imaging (Ku et al., 2011), and implanted phased array coils (Janssens et al., 2012).

B.3 Feather in the cap: some achievements of monkey fMRI

B.3.1 Monkey fMRI sheds light on the nature of the BOLD signal

Since the introduction of fMRI in humans as a method for measuring behavior-related neural activity in the human brain, the relation between the BOLD signal and underlying neural activity has been an open and actively researched question. BOLD measures a combination of cerebral blood flow and oxygen metabolism. Theoretical predictions (Attwell and Laughlin, 2001; Attwell and Iadecola, 2002) suggest glucose utilization primarily reflects in the work involved in synaptic signalling and that metabolic measures of brain activity correlate most strongly with measures that reflect synaptic processing rather than spike rate alone.

Local field potential (LFP) are thought to represent post-synaptic and pre-synatpic activity at multiple neurons, and thus is most accurately described as "peri" synaptic activity. A landmark study (Logothetis et al., 2001) that attempted to empirically determine whether spike rate or LFPs correlated with the BOLD signal, constructed a recording device that allowed simultaneous acquisition of fMRI, LFPs, and the spiking activity of neurons in monkey visual cortex. Anesthetized monkeys viewed contrast gratings while BOLD and electrophysiological activity was recorded in primary visual cortex. The authors reported a strong correlation between BOLD and LFPs and robust but slightly weaker correlation between BOLD and multi-unit activity (MUA). The fact that the LFP accounted for significantly greater amounts of variance across recording sites suggested that the LFP correlated better with the BOLD signal than spike rate (Logothetis and Wandell, 2004). The subsequent investigation of individual recording site indicated that dissociations between spiking and the LFP always resulted in a strong correlation between the BOLD signal and the LFP and not spike rate. These data suggested that correlations between spike rate and LFPs contributed to the correlation between BOLD and spiking activity. Later studies also suggested that significant (but weaker) correlations between BOLD and LFPs could be obtained in the visual cortex of awake behaving monkeys as well (Goense and Logothetis, 2008).

B.3.2 The grasping network

The brain is remarkably adept at orienting the wrist and shaping the span of the fingers to match an object. The prehensile hand is a major characteristic that distinguishes primates from other mammal species. All primates can grasp an object and hold it in part or entirely using a single hand. Comparative kinematic studies on grasping behavior in humans and macaques have been carried out to investigate the similarities and differences existing across the two species (Fogassi et al., 1991; Roy et al., 2000, 2006; Christel and Billard, 2001; Sacrey et al., 2009; Jindrich et al., 2011; Pouydebat et al., 2014). These studies mostly indicate similarities in hand shaping across species. For example, the fact that the hand aperture seems to be scaled relatively to the size of the object. Although some differences emerge, the similarities still place the macaque monkey as an excellent model for the study of the neuroscience of grasping.

B.3.2.1 From single cells to whole brains

A particular brain region in the non-human primate parietal cortex is strongly associated with this ability. This region, termed AIP, is found in the anterior-lateral intraparietal sulcus (area 7b). The functional properties of area AIP have been extensively investigated at the single unit level (Taira et al., 1990; Jeannerod et al., 1995; Sakata et al., 1995; Murata et al., 2000; Gardner et al., 2007) while macaque monkeys performed visually guided grasps of differently shaped 3D objects. The visual and motor responses of AIP neurons were tested in three experimental conditions: grasping in light, grasping in dark, and object observation. The results showed that while some AIP neurons respond during grasping execution in light and dark, others respond only during grasping in light and finally, some neurons discharge when the monkey fixates an object even when no grasping of the object is required. There is congruence between the visual and motor responses of AIP neurons: a neuron is active when the monkey observes one object selectively and discharges for grasping of the same object. Indeed, grasping related movements require processing of the visual properties of the object and those that control hand movement. It is thus primordial to perform a

rigorous transformation of an object's properties such as size, orientation and shape into a fitting motor scheme, shaping the hand for proper grasping.

The observation that single neurons in AIP display a combination of visual and motor properties suggests that these neurons code the visual features of the observed objects and that together with F5 (premotor cortex) neurons they transform them into the appropriate hand configuration for grasping (for review Rozzi and Coudé, 2015). The visuomotor properties of area AIP also include the processing of the 3D shape of objects. The early studies in area AIP had reported object-selective responses in this area (Murata et al., 2000) but it was unclear whether these neurons encoded differences in 3D structure, 2D contour, orientation or any other feature that differed between the objects used in those experiments. A recent study (Srivastava et al., 2009) recorded single-cell activity in the AIP of awake fixating rhesus monkeys using disparity-defined curved surfaces. They report robust selectivity for disparity-defined slanted and curved surfaces in a high proportion of AIP neurons, thus confirming its involvement in the processing of the 3D shape of objects.

Reversible pharmacological lesions of area AIP, have been reported to affect hand preshaping (i.e., grasping) (Gallese et al., 1994), leaving the reach component unaffected (Murata et al., 2000). The deficit was evident only, or mainly, when a precision grip was required. The fact that this impairment is more pronounced in the preshaping phase of grasping rather than during object manipulation emphasizes the crucial role of AIP in visuomotor transformation. The implication of AIP as part of the network responsible for 3D-shape perception was further stressed in a recent experiment of focal perturbation (Verhoef et al., 2016). Through a task of categorization of disparity-defined 3D shapes during concomitant microstimulation of 3D-shape selective AIP neurons, Verhoef and colleagues (2015) found that microstimulation effects on preferences and latency depended on the 3D-shape preference of the stimulated site. Additionally, they show that

electrical stimulation of the same cells, during either the 3D-shape-categorization task or a saccade task, has different effects on behavior.

Until the advent of fMRI in awake behaving monkeys, electrophysiologists had to rely on assumptions drawn from previous reports to define their functional regions of interest, and they used stereotaxic coordinates or anatomical landmarks reported in those reports to reach these regions. With monkey fMRI, it is now possible to precisely localize the regions of interest through an exhaustive functional screening of the whole visual cortex on the individuals that will be used for single cell recordings.

The study by Srivastava and colleagues (2009) had relied on a previous study by same group for its electrophysiological recordings. Indeed, Durand and colleagues (2007) performed fMRI on behaving macaques to study the regions processing the depth structure of either 3D objects or 3D arrangements of visual elements. This study was the first of its kind to have allowed the localization of regions involved in processing shape information in 3D, while all previous studies had only investigated 2D shape processing (Denys, 2004; Sawamura, 2005) and stereoscopic depth processing (Tsao et al., 2003). Their results suggest the implication of an extensive network of parietal areas (AIP, CIP, LIP) in the processing of objects' 3D shape, as well as their involvement in extracting their depth structure and their position in depth. This study further underscored the importance of stereopsis for extracting the 3D shape and position of objects in parietal areas involved in goal-directed actions.

Another study (Nelissen and Vanduffel, 2011), sought to link human imaging and monkey single cell and lesion studies. They investigated the brain areas involved in reaching and grasping movements by training macaques to perform grasping movements in the scanner using an MR compatible pneumatic rotating grasping device. They recorded activations from AIP and ventral premotor area F5, in addition to area PFG in the rostral inferior parietal lobule, somatosensory areas (SI, SII, area 5), and the hand field of F1. In addition to confirming the roles of AIP and F5

in grasping control, this study brought forward some controversial data. Indeed, Battaglini et al. (2002) showed that lesions of V6A influence both reaching and grasping (abnormal wrist orientation and flexion) in monkeys, while Nelissen and Vanduffel failed to see clear grasping-related activity inV6A. They argued that the lack of V6A activation was related to the fact that the monkeys performed the grasping task in the dark. This issue was recently resolved in single unit activity studies (Breveglieri et al 2016, 2017) which compared neuronal activity in V6A during conditions where a behaving monkey had to reach and grasp an object either in the light or in the dark. They found that the grasping activity of area V6A could be modulated by visual information. Furthermore, the authors compared the grasp-related activities of V6A and AIP, stating that both areas were involved in the on-line control of prehensile hand movements, with V6A being less sensitive than AIP to fine visual details of the objects to be grasped, but more involved in coordinating reaching and grasping (Fattori et al., 2017).

Decoding techniques have recently been employed to further investigate the areas involved in reaching and grasping in both humans and macaques. The earliest of those studies (Di Bono et al., 2015) used multivoxel analysis on fMRI data previously acquired from human subjects who were required to perform either reaching-only movements or two reach-to- grasp types (precision or whole hand grasp) upon spherical objects of different sizes. MVPA has also been used in a recent awake macaque fMRI study (Nelissen et al., 2017), where monkeys performed different reach-an-grasp tasks in the dark. Last but not least, decoding of neural activity has been used on macaque electrophysiological data acquired from area V6A.

B.3.3 Comparing human and monkey neuroimaging

Initial attempts to localize a human homologue of area AIP within the intraparietal sulcus involved PET imaging of cerebral blood flow during tasks that required grasping objects compared to pointing at objects. Although the resolution was insufficient to identify a distinct patch of activity within the IPS, grasping generally induced a relative increase of blood flow in a broad region that

encompassed the post-central sulcus (Grafton et al., 1996). Later on, in humans, fMRI studies have demonstrated the existence of localized cortical reach-to-grasp areas similar to those described in monkeys (Filimon, 2010a). Overall, grasping fMRI studies converge in considering the anterior part of the human intraparietal sulcus (hAIP), a likely homolog of monkey AIP (Filimon, 2010b; Vingerhoets, 2014). Furthermore, results from human neuroimaging studies appear to fit nicely with the neuropsychological findings in optic ataxia. The key role of hAIP in the dynamic control of grasping movements has also been confirmed in a series of TMS studies (Vingerhoets, 2014). TMS applied to the left aIPS disrupts online grasping execution (Rice et al., 2006).

On the other hand, studies on the extraction of 3D shape properties have also revealed the functional homologies between humans and macaques. In 2009, following the same protocol from their previous research, Durand and colleagues (Durand et al., 2009) conducted an fMRI study on humans in which they report the homology between anterior IPS regions in humans and macaque monkeys. They show that two areas, which they called DIPSM (dorsal IPS medial) and DIPSA (dorsal IPS anterior) correspond to macaque anterior LIP and posterior AIP respectively. DIPSM and DIPSA are sensitive to depth structure defined from disparity, both in connected random lines and in textured surfaces (Georgieva et al., 2009a) as are anterior LIP and posterior AIP (Durand et al., 2007). Both human regions are sensitive to 2D shape (Denys, 2004; Durand et al., 2009; Georgieva et al., 2009b) as are the corresponding monkey regions (Denys, 2004; Durand et al., 2007) and this result does not depend on familiarity with the objects (Denys, 2004). Both human regions have a central representation (Orban et al., 2006), which they possibly share (Swisher et al., 2007) as do LIP and AIP (Ben Hamed et al., 2001; Orban et al., 2003). DIPSM but not DIPSA is sensitive to saccades, as is the case for anterior LIP and not AIP (Durand et al., 2007).

Studies on the role of AIP in the visuomotor control of grasping have also revealed functional differences between humans and monkeys. DIPSM shows sensitivity to 3D shape from motion, but not LIP (Vanduffel et al., 2002). Similarly, DIPSA in humans shows sensitivity to motion while

AIP does not. Such differences between the two species have been recently theorized to be linked to tool use in humans (Orban, 2016). The left anterior supramarginal (aSMG) responds specifically to observation of tool actions, but not hand actions with similar goals, unlike the putative human homolog of AIP. Stimuli used to activate aSMG does not yield any specific activation in the inferior parietal lobule (IPL) of the macaque, even after extensive training using tools.

B.4 Conclusion

The use of monkey fMRI to study the cortical areas that process 3D-shape properties (Durand et al., 2007), and then to study the cortical network involved in grasping (Nelissen and Vanduffel, 2011) has undoubtedly resolved a missing link between previous single cell studies in monkeys and human imaging data, revealing that monkeys and humans have homologous networks for the processing of grasping hand movements and for its visual control. Furthermore, they have established a launching pad for subsequent electrophysiological, focal perturbation and fMRI research (Srivastava et al. 2009; Verhoef et al. 2015; Premeureur et al. 2015; Van dromme et al. 2016, Nelissen et al. 2017), and comparative monkey-human neuroimaging studies (Durand et al. 2009; Flave et al. 2016).

C. Methodology for Monkey

fMRI

C.1 Monkey fMRI facilities in Toulouse

The centre for research on brain and cognition (CEntre de Recherche Cerveau et COgnition – CERCO) is a research facility that aims to investigate the neural basis of sensory perception, cognition and consciousness through a multilevel (neurons, neuronal populations, networks and behaviour) and multidisciplinary approach that uses a wide range of converging techniques including anatomy, physiology, integrative neurophysiology, cognitive neurosciences, computational neurosciences and theoretical approaches with a strong interface between biology and engineering. Such investigation relies on a parallel approach in monkeys, humans and patients, bridging fundamental and clinical research.

Within the research facility (Figure 3) there is a state of the art monkey research department that includes the animalium, which houses both rhesus macaques and marmosets, 4 electrophysiology setups and 2 fMRI conditioning and psychophysics setups. The animalium contains a quarantine area for initial reception of new animals, a thoroughly equipped surgical room, and a cleaning facility. Housed in large social enclosures of at least 2 individuals, the macaques have access to enriched environments that allow foraging behaviour and exercise. The facility is governed by a strict protocol of staff flow for maximum isolation from external pathogens. The animals undergo regular health check-ups, including blood tests, weightings and dental care. A team of experts in animal behaviour regularly maintains the facility and provides counselling in animal handling and well-being.

The main attraction of the CerCO is its 3T Philips wide bore MR scanner. Dedicated for neuroscience research, it is fitted with a variety of apparatus, such as eye-trackers, response boxes, physiological monitoring systems, in addition to an LCD back projector, binocular stimulation goggles and an MR compatible LCD monitor. The platform is available for both human and NHP research, and its location at the interface of human and monkey research facilities, makes it a hinge

for comparative human and monkey studies. The platform is available for the entire staff of the research facility, where a team provides expertise in MRI protocol implementation, such as optimization in MRI sequences and data handling and pre-processing.

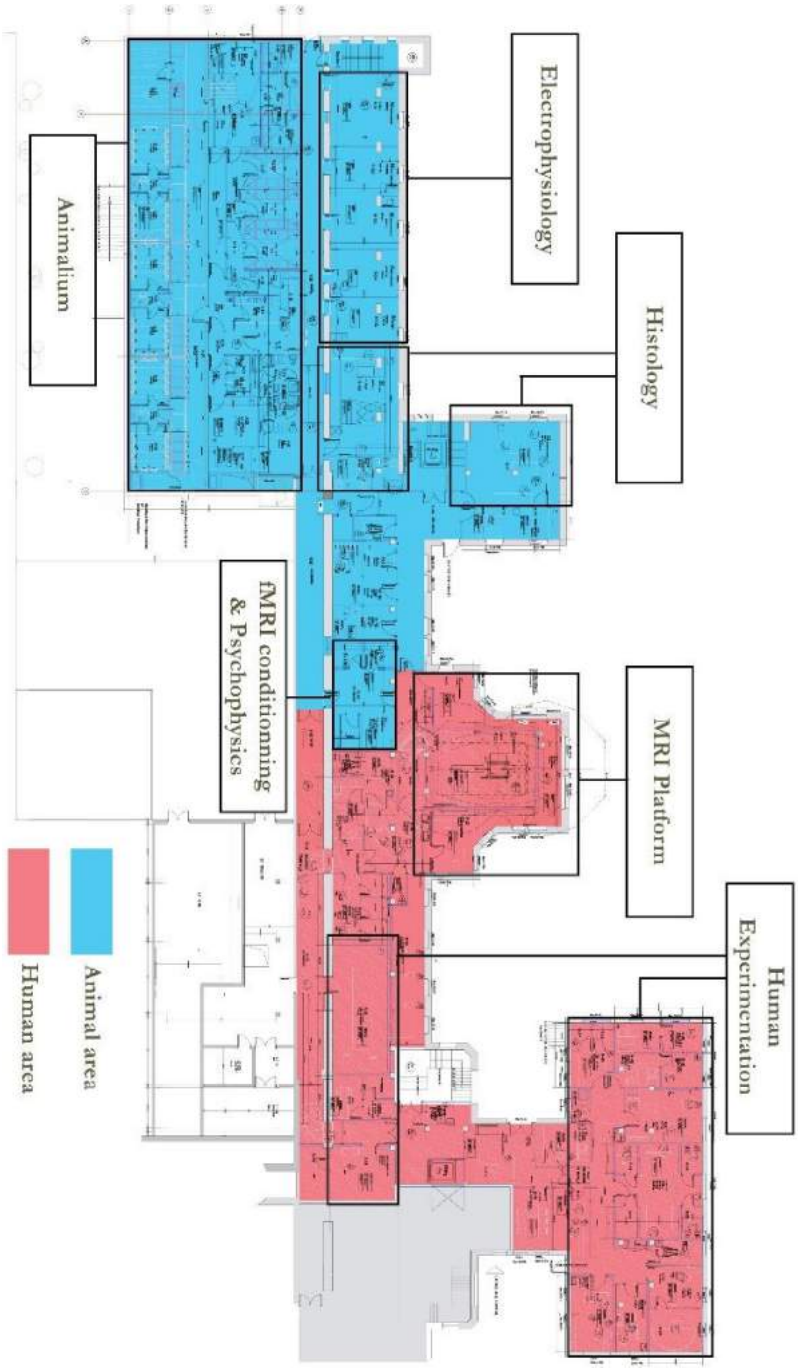

Figure 3. **Architectural layout of the base floor of the CerCo research institute.** It is divided into separate human and animal experimentation areas with the MRI platform serving as an interface.

C.2 Creating the setups: an environment for fMRI conditioning

Despite our nice facilities, the MRI environment remains relatively hostile: dark, noisy and confined. The MR mechanics subject the scanned individual to vibrations and sometime involuntary muscle contractions. Furthermore, changing magnetic field gradients can also cause nausea and disorientation. The uncooperative nature of macaque monkeys makes habituating them to such an environment a necessity prior to any experimentation. In addition to familiarizing the animals with the MR environment, it is essential to provide them with the essential training to perform complex tasks, like that administered to humans, to allow interspecies comparisons, one of the main purposes of this technique. A mock setup of the MRI milieu, that simulates the conditions in which the animal will be scanned is a useful tool to ensure minimal movement and stress during scanning sessions. Since most laboratories use clinical horizontal bore scanners that are often shared with multiple research facilities, mock MRI setups allow extended periods of training to be conducted without the risk of hogging scanning time, that would still have to be paid even though no data is acquired.

During my PhD, I have assembled 2 mock MR setups for both training and psychophysical data acquisition. The setups were in a preparation room on the ground floor of the CerCo lab, at the interface between the animal facility and the scanner (Figure 3). The strategic position of this room allowed easy transfer of the animals between the two areas, and provided constancy for the animals, which was critical for their familiarity with the environment. The 2 setups were virtually identical, with minor differences. The setups (Figure 4) consisted in isolation boxes where the monkeys were trained and a control desk located on the outside wall of the box. Both setups were fitted with flat 24" LED monitors (BenQ XL2411Z, 144Hz refresh rate), standard stereo sound systems, with the option of surround sound stimulation. In addition to audio-visual stimulation, the animal's gaze could be tracked with video-based eye-trackers (IScan®, Eyelink®). A reward system (CRIST instruments®) was modified so that the liquid conducting nozzle could be fitted to the different

primate chairs and their sipping tubes. The mock MRI bore was constructed from rigid polycarbonate and polystyrene. The mock bore was a precise replica of the middle portion of the actual scanner bore. Wireless infrared cameras were also installed to monitor the monkey's general behavior. We could control audio-visual stimulation, monitor the monkey's gaze and its general behavior from the control desks. The control desks consisted of 2 computers, a monitoring tablet receiving direct video feed from the IR camera and an audio amplifier. The first computer controlled the eye-tracking camera, while the second, the master computer controlled and synchronized all the above. To synchronize the ocular signal with reward, the eye-tracking computer and the reward delivery system were connected to the master computer through analog inputs, 2 for the eye-tracking system (X and Y coordinates), and 1 for the reward system, via an acquisition card (National Instruments®). Our team negotiated a partnership with Okazolab.inc, to provide us with a state of the art software (EventIDE®) for generating stimuli, designing experiments, acquiring biophysical and behavioral data and synchronizing stimulus onset and offset with input and output signals.

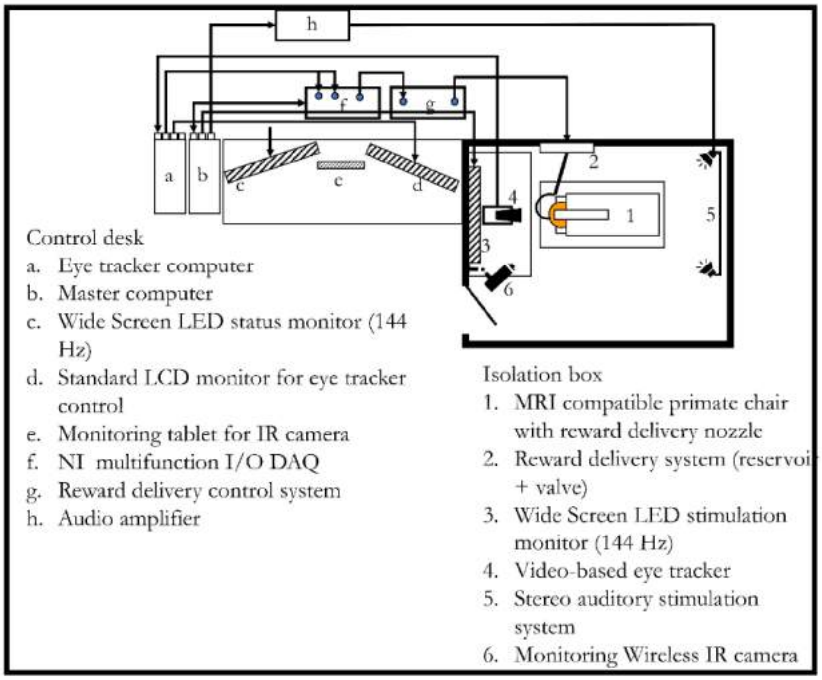

Figure 4. **Monkey fMRI draws a bridge between single-cell studies and human functional imaging studies.**

C.3 Animal preparation

C.3.1 Legal authorizations

Animal housing, handling, and all experimental protocols (surgery, behavioral training, and MRI (magnetic resonance imaging) recordings) followed the guidelines of the European Union legislation (2010/63/UE) and of the French Ministry of Agriculture (décret 2013–118). All projects were approved by a local ethics committee (CNREEA code: C2EA – 14) and received authorization from the French Ministry of Research (MP/03/34/10/09).

C.3.2 Surgical procedures

During this PhD, I have been involved in the surgical preparation and behavioral training of 6 animals. Initially, each monkey was habituated to receiving food and fluid rewards in a monkey chair, first in the animal facilities and then in the training setups and scanner room. Once familiarized with those different environments, animals were surgically implanted with a plastic head-post. Glycopyrrolate (Robinul, Baxter; 0.004 mg/kg) was administered intramuscularly 20 minutes before anesthesia induction, to reduce salivary, tracheobronchial, and pharyngeal secretions and to block cardiac vagal inhibitory reflexes. Anesthesia was induced with intra-muscular injections of Tiletamine/Zolazepam (Zoletil 100, Vibrac; 10 mg/kg) and Medetomidine (Domitor Pfizer; 0.04 mg/kg). An intra-venous catheter was installed for saline perfusion during the surgery. Animals were then intubated for inhalational anesthesia (Isoflurane: 1.5%, N2O: 50%, O2: 50%) and their head was placed within a stereotaxic holder. Under sterile conditions, a sagittal incision was performed on top of the head and tissues were set apart to expose the skull. The plastic head-post was positioned on top of the skull and 8 to 10 ceramic screws (Thomas recording®) were implanted around the head post. The head-post and the screws were then sealed together and to the skull with a bone cement containing an antibiotic (Palacos®, medium viscosity with Gentamicicin®, Heraeus®). The animal's constants were monitored during the whole surgery.

An analgesic (Tolfedine®) and an antibiotic (Terramycine®) were administered after the surgery and on a daily basis during a week post-surgery. The macaques recovered for two months before resuming the behavioral training.

C.3.3 Behavioral training

After the post-surgery resting period, the animals were first familiarized with having their head restrained by the head-holder, while lying in a sphynx position within the monkey chair (Vanduffel et al., 2001). This is a critical phase of training. Animals must learn to remain still and ignore any startling noise. Furthermore, animals will tend to force their way out of the chair or in, either by pushing or pulling on the attached head-post. Depending on the animals, some may have enough strength to rip their implants. A lack of focus on this training phase, not only subjects the animals to the dangers of exposing their skulls resulting in trauma, but can also leave them with the bad habit of moving to contest unsatisfactory reward delivery, which is catastrophic for fMRI data acquisition.

Behavioral conditioning to a passive fixation task started once the animals could remain quiet and still for prolonged periods in the head restrained position. Then, they were water scheduled and involved in daily training sessions. We insured that the animals always received sufficient daily amounts of water regarding their needs (evaluated during periods without restrictions), either fully during the training sessions or through complements after the sessions. The weight of the animals under restriction was checked daily, and restriction was halted if it decreased by >5% from the weight before restriction. During the training sessions, the animals were installed in the dark training setup, facing a screen on which a fixation target was displayed (green square, viewing distance: 50 cm; target size: 0.3° x 0.3°). Eye position was monitored online with an infrared video-based eye tracker. The animals had to maintain their gaze within ±1° from the center of the fixation target to receive fluid reward. Fixation periods (about 3 minutes) alternated with periods of rest,

mimicking the temporal structure of the fMRI sessions. The frequency of reward distribution was progressively augmented if the fixation was not interrupted, to encourage prolonged fixation periods. Once the fixation task had been learnt, the different stimuli were introduced in the background and the animals had to learn to keep their eyes on the fixation target. Training was considered as completed once the animals could spend most of the time of the fixation periods (>90%) on the fixation target. The last elements introduced during the training period were the mock scanner bore and sounds produced by the scanner to mimic the physical and sound environment encountered during the MRI recordings.

C.4 Dedicated monkey coils

To conduct the pilot scanning sessions on Monkey M00, we used 2 multi-purpose, vendor provided transmit/receive Flex coils, that were held in place on the monkey's head post using adhesive tape. This solution was not durable, and with limited replicability, furthermore it was very susceptible to animal motion. Nevertheless, it provided us with rich elementary results concerning image quality, and allowed us to test a myriad of imaging sequences, as well as acquire invaluable experience on monkey behavior within the scanner. Image distortions due to body and jaw motion (from reward consumption) can be mitigated through the application of parallel imaging techniques with phased array coil systems. A major advancement in the monkey fMRI technique in Toulouse was the development of a custom 8-channel phased array coil system (RapidBiomed®) specially designed to fit the skull of macaques for maximum proximity and reproducibility, while preserving their field of view. One coil circled the head post while the 7 others were distributed along the circumference of the monkey's head. The coils and electronics were secured in a durable MR compatible polymer casing, with an opening on the top to allow a tight fit with the head post. As shown in Figure 5, the coil system can be fitted with anaglyphs for 3D viewing.

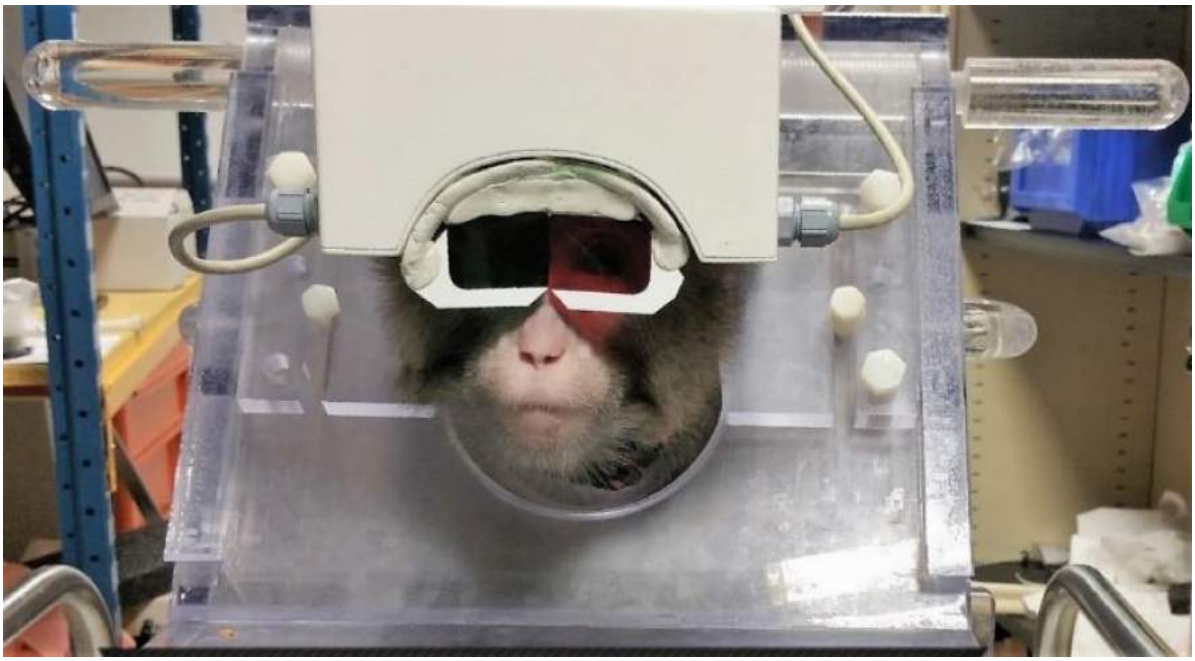

Figure 5. **M02 in primate chair with mounted red and green anaglyphs.**

C.5 Magnetic resonance imaging

C.5.1 Set-up overview

After the animal has completed the training phase in the mock MRI setup, it is introduced to the actual scanning environment. The habituation starts with a couple of trips to the scanner room, while the monkey is in the primate chair, free from any head restraint. The animal remains for about an hour in the scanner room, while being rewarded with fruits for calm behaviour. The next habituation sessions involve the animal being trained to fixate within the scanner, with no running acquisition sequences. Once the animal has confidently fixated for >90% of the time within the scanner, the same procedure is applied while sequences are running. Inside the bore of the scanner, as in the mock MR setup, the animal sits in a sphinx position within the primate chair, head restrained by the head-post, with the 8 channels, phase array coil located on top of the head (Figure 6). The animal is involved in a passive fixation task, i.e., maintaining the gaze on a green fixation target back-projected on a stimulation screen by a video-projector. Eye position is monitored by

an infrared video-based eye-tracker (ASL®). Correct fixation triggers the delivery of fluid rewards during the runs.

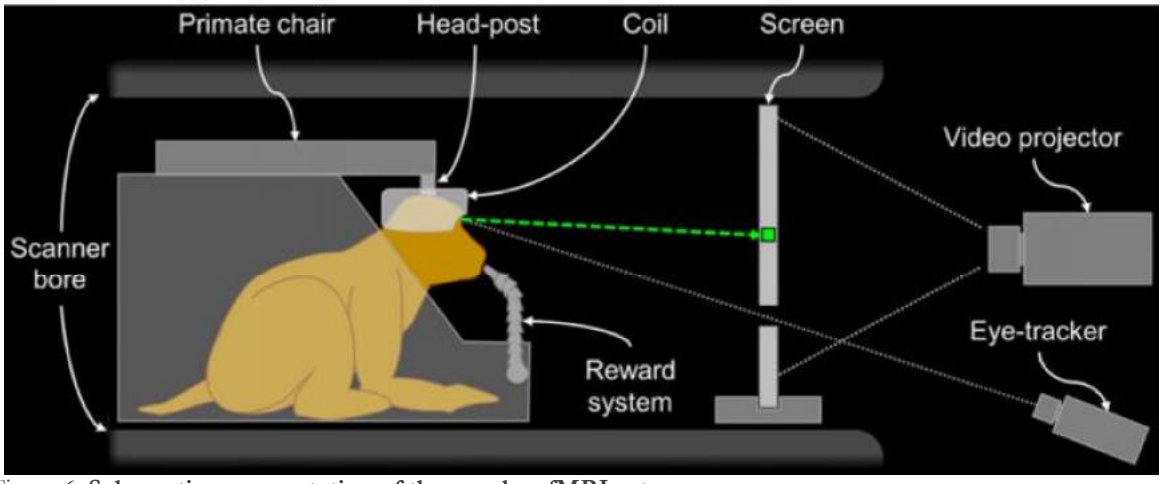

Figure 6. **Schematic representation of the monkey fMRI set-up.**

C.5.2 Acquisition sequences

Functional volumes were acquired with echo-planar parallel imaging sequences (GE-EPI; TR = 2000ms, TE = 30ms, flip angle = 90°, SENSE factor = 1.6; voxel size = 1.25 × 1.25 × 1.5mm, 32 axial slices). For visualization of fMRI results, statistical maps are often displayed on a high-resolution "anatomical" volume image or a surface reconstruction based on the segmentation of grey and white matter. MRI can be used to segment the different tissues types in the brain. Since the microscopic environment around the hydrogen nuclei differs for different tissue types, this results in different MR signals for each tissue type, which can be exploited to visualize the location of these tissue types. Commonly, a high- resolution T1-weighted image with a uniform signal intensity acquired with a sequence optimized for grey-white matter contrast is used as anatomical image. The sequences used to acquire the anatomical volumes were T1-weighted magnetization prepared rapid gradient echo (MPRAGE; repetition time [TR] = 10.3ms; echo time [TE] = 4.6ms, flip angle = 8°; voxel size = 0.5 × 0.5 × 0.5mm; 192 slices).

C.5.3 Anatomical and functional templates

After the surgical implantation of the head post for each of our monkeys, we built anatomical, and functional brain templates from acquisitions made in a single session while the animals were slightly anaesthetized (Zoletil 100:10mg/kg and Domitor: 0.04mg/kg). During the session, the animals were in the exact position they would be during functional scanning sessions, with head fixed to the primate chair. Cushions were installed beneath the monkey's chest to provide support in the absence of muscular tonus. The animals' constants were monitored during the whole session (about 1 h) with an MR compatible oximeter. During that session, we acquired 4 anatomical volumes and 300 functional volumes using the sequence parameters mention in the previous section. To build the templates we first realigned the images to the first acquired volume to account for any movements between the acquisitions. Next, we reoriented the realigned images to the 112-RM space to allow for proper co-registration with this template. We then segmented the mean image obtained from the previous step, to generate files containing only grey matter, white matter or cerebro-spinal fluid. This segmentation step is essential for proper surface reconstruction. The image is then resampled to 1x1x1mm voxels and cropped. The segmented, resampled and cropped image is then verified using MRIcron. This step has the purpose of manually modifying any errors the automatic segmentation might have made. Finally, we normalize the manually modified image, resample to 0.5x0.5x0.5 mm voxels and create the T1 image mask. The same procedure was applied to create an EPI template.

C.5.4 Cortical surface reconstruction

One purpose of fMRI is to decipher visual-cortical organization, yet many hurdles need to be overcome to acquire a detailed view of visual area distribution. Such a purpose requires a high-fidelity model of the cortical surface which will allow us to visualize the anatomical distribution of functional data with adequate precision. Indeed, incremental difficulty arises when we are

confronted to the mosaic of small areas that lie beyond the primary visual area and the first extrastriate area (V1-V2). Furthermore, the gyrencephalic nature of the cortex in higher order primates such as humans and macaques, implies that most of the sensory cortices, and most notably the visual cortex, lie buried deep within complex and irregular sulci, which makes it a hindrance to the visualization of spatial relationships among the neighbouring visual areas. Another problem arises when trying to compare the visual cortical organization from several individuals. The pattern of folding significantly varies from one individual to the next (geographic variability), which adds to the variability in the size and shape of visual areas and their location relative to geographic landmarks (functional variability). Taken together, geographic and functional variability exacerbate the visualization problems arising from the irregularity of cortical convolutions and make it harder to assess the consistency of subtle areal boundaries.

Cortical surface reconstruction resolves many of the above-mentioned issues. Indeed, this technique allows the creation of a variety of cortical reconstructions ranging from fiducial surfaces to flat maps, which means that any projected data onto that surface can be viewed in multiple configurations. Cortical surface reconstruction also allow surface based coordinates which are inherently advantageous over conventional stereotaxic coordinates because they respect the topology of the cortical sheet (Drury et al., 1996; Sereno et al., 1996). Functional and geographical variability among individuals can be assessed through surface warping. Indeed, surface-based warping allows individual hemispheres to be deformed to an atlas map while preserving neighborhood relationships on the cortical sheet (Dale et al., 1999). Such warping also opens the way for interspecies comparisons, as it provides a practical strategy for addressing these impediments and for evaluating the degree to which there is a common organizational plan in terms of the identities of visual areas and their topological relationships with one another across the cortical sheet.

To reconstruct the cortical surfaces of our monkeys, we employed the SureFit (Surface Reconstruction by Filtering and Intensity Transformations) algorithm provided in the CARET software. SureFit is a method for rapidly generating accurate surface reconstructions of the cerebral cortex from structural MRI data (Drury et al., 2000). A distinctive feature of SureFit is that it generates segmentation and surfaces running along the cortical mid thickness. This gives a representation of cortical surface area that is roughly proportional to the associated volume of cortical gray matter. An example of cortical reconstruction is given in Figure 7. The cortical surface reconstructions were generated from the T1 templates (see previous section).

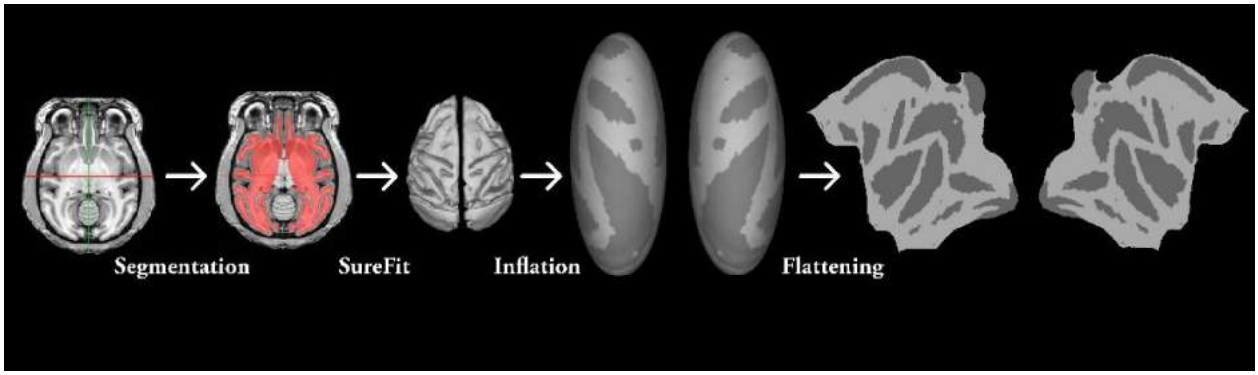

Figure 7. **Cortical surface reconstruction.** The SureFit reconstruction follows the segmentation of the T1 weighted anatomical image. The reconstruction produces a fiducial surface which should be inflated before it can be cut and flattened.

C.6 Functional data processing

C.6.1 Functional signal: BOLD vs. IRON

When a certain region in the brain is activated, small temporal signal changes related to changes in the concentration of the paramagnetic deoxyhaemoglobin (dHb) can be measured. BOLD contrast. This BOLD response is relatively small (up to a few percents) and corrupted by many sources of noise from the subject (motion, breathing, heart rate, etc.) or external to him (temperature, vibrations, fluctuations in magnetic field homogeneity, etc.). In some cases, the low signal-to-noise (SNR) of the BOLD signal can represent a strong limitation for conducting robust functional explorations. An alternative technique was developed in rodents (Kennan et al., 1998; Mandeville

et al., 1998; van Bruggen et al., 1998) and later applied in monkeys (Vanduffel et al., 2001; Leite et al., 2002) to increase the SNR. The technique is referred to as Increased Relaxation for Optimized Neuroimaging (IRON) fMRI or cerebral blood volume (CBV) fMRI and makes use of an exogenous contrast called agent Monocrystalline Iron Oxide Nanopartical (MION), usually coated with dextran, a polysaccharide which has the purpose of reducing the cytotoxicity of the MION particles (Yu et al., 2012). This contrast agent is administered to the bloodstream where it remains present for several hours. Due to the strongly paramagnetic properties of MION the temporal signal in an activated brain region strongly decreases proportionally to the increase in CBV. Therefore, the IRON signal is negative compared to the BOLD signal and the SNR of IRON is approximately 3 times larger than the SNR of BOLD at a magnetic field strength of 3T (Mandeville, 2012). In addition, in BOLD contrast the peak response arises from the large blood vessels at the pial surface, whereas the IRON contrast peaks around the middle cortical layers, making it more suited for high-resolution fMRI studies (Zhao et al., 2006; Jin and Kim, 2008). IRON fMRI has also been applied in high-resolution human fMRI, although its use remains highly controversial (Kim et al., 2014). The use MION in monkeys raises a few dilemmas: (1) the development of an immune response to dextran and the gradual accumulation of iron in excess of body requirements which could damage the monkey's health and reduce its life expectancy, (2) the stress and invasiveness related to intra-venous injections of MION prior to each scanning session and (3) the limitation it may introduce for direct comparison with human BOLD responses. Before the development of the custom built 8 channel phased array coil, we observed unsatisfactory SNR during the use of the Flex coils, which prompted us to employ MION. The signal provided by the custom-built coil alleviated the need for it, and satisfactory SNR was reached using the conventional BOLD signal.

C.6.2 Basic pre-processing steps

Arguably the biggest challenge in awake monkey fMRI, is animal motion. Animal motion always degrades image quality to a greater or lesser extent. Although the head of the monkey is fixed to the primate chair, animal motion remains a nuisance. In addition to sudden body movement, motion artefacts can arise from consumption of reward (jaw motion). Problems due to animal motion affect fMRI at all field strengths but are worse at high field.

In human fMRI, motion artefacts arising from slow drift can be corrected using rigid body registration, where a 3D rigid body model with six degrees of freedom (three translational movements $Tran_x$, $Tran_y$, and $Tran_z$ and three on rotational movements Rot_{Pitch}, Rot_{Yaw}, and Rot_{Roll}) are estimated. All images within a run are then realigned to the image in the middle of the times eries of each run. This strategy can correct some displacements, but it remains inadequate in monkeys since motion artefacts are caused by sudden body movement. Non-rigid distortions are even more complicated to correct. Their correction introduces more degrees of freedom and the low resolution and contrast of functional images may not support accurate image registration with many terms.

Another solution to removing signal fluctuations caused by motion can be done by extracting noise regressors using PCA from non-brain voxels (muscles, eyes) and employing these regressors in further analyses, as demonstrated in a later study (Section E). Motion regressors that are derived during the motion correction step of the pre-processing pipeline, can also be introduced in the general linear model (see below). The same can be applied to physiological data such as cardiac rhythm and respiration, unless these have been accounted for through temporal filtering. Behavioural data such as eye-tracking data and reward consumption should also be included as regressors, whenever available. Nonetheless, the exceptional training of the animals remains a

prerequisite for proper acquisition of fMRI, as all the motion correction strategies will fail if too much motion occurs.

C.6.3 Visual field mapping techniques

In human visual field mapping, we estimate the position in visual space eliciting maximal responses at each cortical voxel by calculating the phase-difference between a periodic visual stimulus presentation and fMRI signals recorded from occipital cortex (Engel et al., 1994, 1997; Sereno et al., 1995b; DeYoe et al., 1996). This in turn allows the localization and delineation of different retinotopic visual field maps according to their polar angle and eccentricity representations (Wandell et al., 2007; Bridge, 2011). This technique is easily transposable to monkeys, and has been used extensively (for review Vanduffel et al., 2014).

While these methods are effective in localizing and delineating different retinotopic areas, probing the underlying characteristics of the RFs of individual neurons, such as the tuning curve, size, or shape, is another dilemma. Since the signal captured by fMRI methods combines the activity of hundreds of thousands of neurons in a single voxel, so in visually responsive cortex the signal from specific locations will reflect a complex aggregate of the properties of individual receptive fields (RFs). The aggregate properties of a large number of neighbouring neurons is referred to as the population RF (pRF). In the study developed in Section E, we adopted the pRF estimation method introduced by (Dumoulin and Wandell, 2008). We use the analyzepRF toolbox (Kay et al., 2013b) which can be found on http://kendrickkay.net/analyzePRF/. The purpose of the toolbox is to estimate a model of the pRF by generating voxel time series predictions that best fit with the observed data.

Briefly, the toolbox uses a model-based approach to measure pRFs. The area of visual space that elicits responses in a single voxel is modelled as a Gaussian function (Larsson and Heeger, 2006) as in the equation below:

Equation 1 $$g(x,y) = e^{-\left(\frac{(x-x_0)^2+(y-y_0)^2}{2\sigma^2}\right)}$$

where (x_0, y_0) is the centre and σ is the Gaussian spread (standard deviation). These parameters are stimulus-referred; the units of x_0, y_0 and σ are all in degrees of visual angle. Next, an effective stimulus, s(x, y, t) is defined. The stimulus which could be a contrast pattern, either a checkerboard or a dartboard, or a more complex image or video, is revealed as the stimulus aperture (rotating wedges, expanding/contracting rings, or drifting bars) moves across the pattern. The formula thus describing the effective stimulus is simply a binary indicator function that marks the position of the stimulus aperture at each time. We then calculate the predicted response for a given pRF model and given stimulus. The first step towards predicting the fMRI time series is to calculate the overlap between the effective stimulus and the model pRF at a given voxel.

Equation 2 $$r(t) = \sum_{x,y} g(x,y)s(x,y,t)$$

An important subsequent step is to convolve the overlap r(t) with a model of the subject's HRF.

Equation 3 $$p(t) = r(t) * h(t)$$

The goodness-of-fit (RSS) is calculated between the prediction, p(t), and the data, y(t). An error term that accounts for the unknown units of the fMRI signal is calculating by introducing an unknown scale factor, β.

Equation 4 $$RSS = \sum_t (p(t) - y(t)\beta)^2$$

A very large repertory of theoretical time series is produced for a very large combination of pRF positions and spread. By comparing multiple combinations of receptive field properties (e.g., location, spread) with the observed data, a best-fitting pRF model is obtained for each cortical location.

C.6.4 Basic statistical analyses

As in humans, the purpose of a monkey fMRI experiment is to identify voxels whose time series differ significantly between the experimental and control conditions.

The general linear model (GLM) allows the examination of the temporal synchrony between each voxel's time series and the predicted response of the experiment (Bandettini et al., 1993) – derived by convolving the experimental design matrix with a hemodynamic response function (HRF) (see Section D). A correlation coefficient R is derived to quantify the temporal synchrony. To allow for the variability of temporal delays in HRFs across different brain voxels, cross correlation – which estimates the correlation coefficient as a function of the temporal lag of one signal relative to the other, may be applied (Friston et al., 1995). Briefly, y is a vector of values showing BOLD signal strength at a single voxel in successive scans (a voxel time-series). It is modelled as a linear mixture of several regressors and white Gaussian distributed additive noise term ε as below:

Equation 5 $$\boldsymbol{y = \beta_0 + x_1\beta_1 + x_2\beta_2 + \cdots x_n\beta_n + \varepsilon}$$

where x_i denotes each regressor, and the parameter weight β_i is the scaling term indicating the contribution of a regressor to the dependent variable y. When y refers to many dependent variables, such as different time points across a scan in an fMRI study, Equation 5 represents the GLM. Statistical testing of the GLM estimates how well each voxel's time series is fit by the linear combination of regressors. To assess the significance of regressors' contribution to y, t-statistics or F-statistics are applied (Friston et al., 1995; Worsley and Friston, 1995).

Through versatile modifications of regressors, this approach allows more flexible shapes of the predicted response. It is worthy to mention that noise is an integral part of a voxel's time-course. Such noise, which is assumed to be unrelated to the experimental conditions, may improve estimates of the related components of the BOLD signal if handled properly. Thus, any denoising procedure requires a careful selection of the noise regressors. Inaccurate regressors that fail to capture a significant portion of the noise, may worsen the GLM estimates. to use as noise regressors (Kay et al., 2013a), which are then introduced in the GLM.

In contrast with humans, the small sample size in monkey fMRI experiments prohibits the use of group statistics, as we rarely surpass the scanning of 3 different animals in an experiment. One strategy for gaining statistical power can be averaging the volumetric data across hemispheres, which doubles the sample size. Volumetric data from all hemispheres are deformed to adhere to a common space (e.g F99), before being averaged and analysed. Another fundamental strategy to strengthen statistical power is the use of individual hemodynamic response functions (HRF). The need for individual HRFs will be detailed in the following section. To further strengthen conclusions about the data, one may consider splitting the data into two halves (e.g odd runs vs even runs). In a GLM analysis, the odd runs in the data can be used to find the local maxima, while the even runs can be used to perform a region of interest analysis (ROI). This strategy has been used in the study described in Section F. Dividing the data can also be useful in pRF analysis. Also, the distribution of the RF parameters (polar angle, eccentricity, size) can be correlated between the 2 halves of the data. This strategy has been used in the study described in Section E.

D.Estimating the Monkey hemodynamic response function (HRF)

D.1 The hemodynamic response

The body must respond to physical activities, external temperature, and other internal or external factors through the homeostatic adjustment of its blood flow to deliver oxygen and nutrients such as glucose to stressed tissues to allow them to function. The hemodynamic response (HR) allows the rapid delivery of blood to active neuronal tissues. During information processing, there is an increase of neuronal activity in different parts of the brain. This increase in neuronal activity elicits an increase in oxygen and glucose consumption supplied by the vascular system. The MRI signal measured in functional imaging is usually a signal that measures changes in the microvasculature oxygenation. More precisely, it deals with venous oxygenation (oxygenation in arteries is always 90-100%). The relationship between venous oxygenation and the MR signal strength corresponds to the BOLD signal.

The hyper-perfusion of the local tissue (Mcintyre et al., 2003) is the basis of the BOLD signal. During activation, the oxygen level increases from 60-80 % at rest, to up to 90% in the venous system and the Hb/dHb ratio increases. This increase in oxygenation might be required for waste removal and heat regulation (Yablonskiy et al., 2000), or to supply distal active cells (Devor et al., 2011); increased blood flow might also be needed to provide higher levels of glucose (Fox and Raichle, 1986; Fox et al., 1988; Paulson et al., 2010). The BOLD signal increases about 2 seconds after the neural activity; it then reaches a peak at about 4 seconds in monkeys and about 6 seconds in humans. If the neural activity continues, a plateau can occur. Once the neural activity goes back to its baseline level, the signal also returns to baseline 8 to 11 seconds later. Finally, a transient change referred to as the undershot can be observed. Maximal variance is observed between subjects and minimal variance between scans of the same subject (Aguirre et al., 1998). However, within subject variance increases when comparing several areas – i.e. the shape of the hemodynamic response is influenced by the local vasculature which differs from one area to the other.

Since the BOLD signal is a metabolic signal, it only provides an indirect measure of the underlying neural activity. In order to solve this dilemma of neurovascular coupling, Logothetis and colleagues (Logothetis, 2002) have demonstrated, through an experiment of concomitant electrophysiological recording and fMRI in macaque monkeys, that a strong correlation exists between the amplitude of the BOLD signal and local field potentials which are the electric potentials recorded in the extracellular space in brain tissue, using micro-electrodes. They also report correlation between spike rates and BOLD, although not as robust. Similarly, the amplitude of fast event related potentials (ERP), which are measured by means of electroencephalography (EEG), seems to vary linearly with BOLD (Sabatinelli et al., 2007). Slow ERPs, which are believed to arise from postsynaptic potentials, correlate with BOLD in parietal cortex (Schicke et al., 2006). This implies that BOLD seems to reflect more the input to a neuronal population as well as its intrinsic processing, than direct spiking activity per se.

D.2 Motivation to measure the HRF

The study of brain activity using fMRI is built on the ability of estimating the sensitivity of a large population of neighboring neurons belonging to the same voxel, to a certain stimulus and/or task. Standard analysis of fMRI data relies on a GLM approach to look for correlations between the fluctuations of the BOLD signal and the experimental design. Crucially, this approach relies on a number of assumptions about the data that must be met to reach valid inferences. The aim of a statistical analysis is to determine which voxels have a time-course that correlates most with a known pattern of stimulation. In the GLM approach, the time-course associated with each voxel is modeled as a weighted sum of one or more known regressors (e.g., the onset and offset of an experimental condition) plus an error term. The aim of the analysis is to estimate if, and to what extent, each regressor contributes to the variability observed in the voxel's time-course.

To transform a neural response to on-off stimulation into a predicted vascular signal, the regressors are typically convolved with an HRF (Boynton et al., 1996). The HRF thus characterizes the input–output behavior of the system (Stephan, 2004), imposing an expectation on how the BOLD signal in a voxel should vary in response to a stimulus. Incorrect modeling of the HRF might cause significant discrepancy between the predicted and the observed BOLD signal, increasing the variance of the GLM coefficients, degrading both statistical power and model validity (Aguirre et al., 1998; Loh et al., 2008; Waldorp, 2009). Furthermore, one should note that the HRF is known to be highly variable across species, individuals, and, within individuals, across scanning sessions, experimental designs and brain regions (Aguirre et al., 1998; Handwerker et al., 2004). Classical fMRI data processing softwares, such as SPM, use a human canonical HRF model for the GLM analysis. Certainly, it is not adequate to use such a model for macaque monkeys whose brain size, vasculature, diet and liquid intake greatly differ (Leite et al., 2002). It is thus useful to estimate the HRF for each monkey involved in an fMRI experiment to ensure model validity and better statistical power.

D.3 Estimating the HRF in macaque monkeys

D.3.1 Stimuli

To estimate the BOLD HRF of our animals, we followed the procedure described in (Dumoulin and Wandell, 2008). Stimuli were full-field counter phasing (10Hz) checkerboards (40°, 16 sectors) that were displayed at full contrast, for 4s followed by a 30s blank (Figure 8b). During each scan, this cycle of 34 seconds was repeated 6 times for a total duration of 204s. A fixation point was always displayed in the center of the screen. Surgical preparation and training procedures are detailed in Section C.

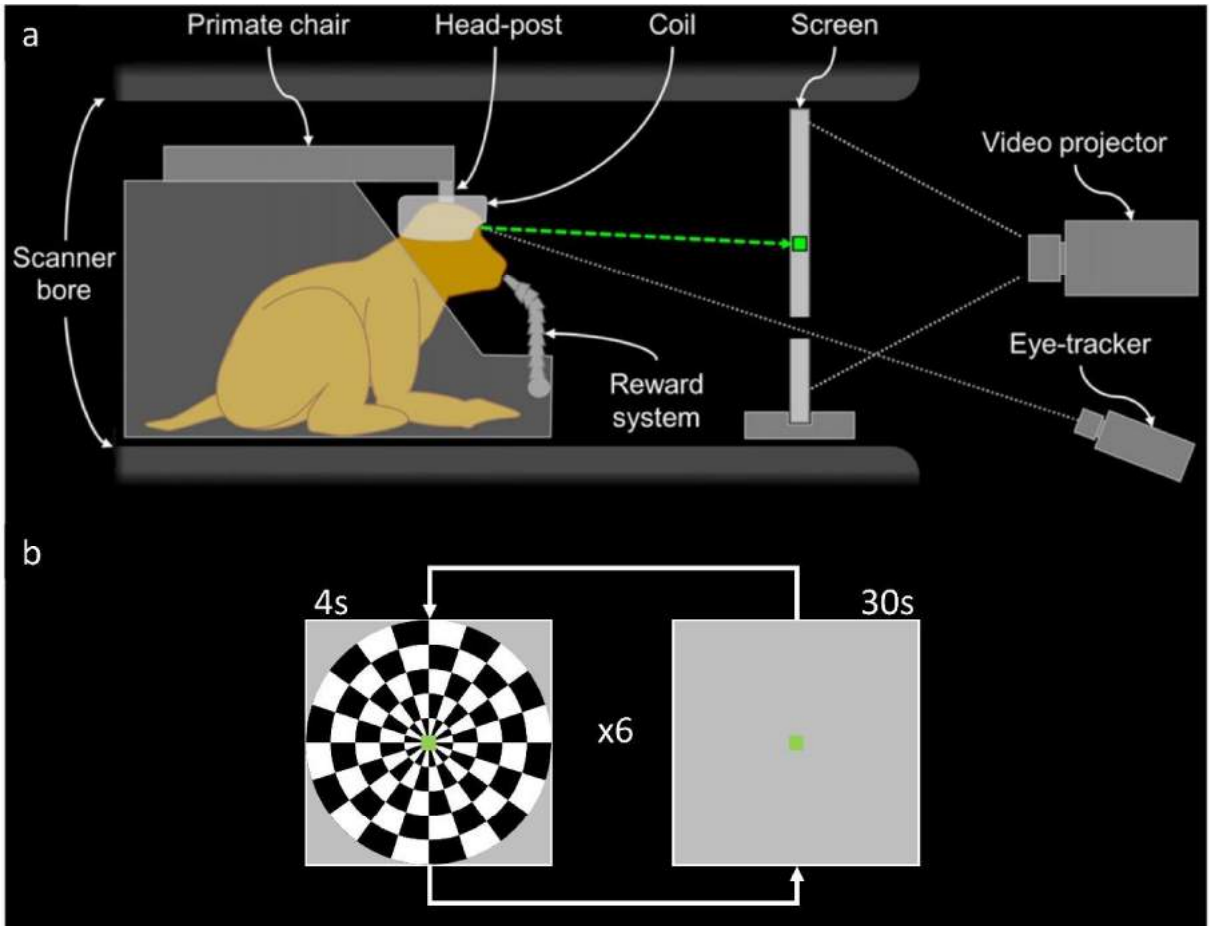

Figure 8. **(a) Schematic representation of the monkey fMRI set-up. (b) Illustration of the stimuli and experimental design.**

D.3.2 Preprocessing

Within each run, volumes were rigidly realigned with each other on a slice-by-slice basis using a subpixel cross-correlation algorithm (Guizar-Sicairos et al., 2008). This was followed by slice-time correction. A mean image of the functional volumes was then computed for each run and used for normalization on the functional template of the same individual. Those run-dependent normalization parameters were combined to the run-independent parameters linking the functional template to the anatomical one in a single deformation step, during which the functional volumes were resampled at 1 × 1 × 1mm and slightly smoothed with a spatial Gaussian kernel (FWHM = 1.5 × 1.5 × 1.5mm).

D.3.3 Data analysis

For each animal, the HRF was estimated from 12 runs for which the percentage of correct fixation was above 85%, to minimize the influence of eye movements in blood-oxygen-level dependent (BOLD) signal fluctuations. If the HRF is usually estimated from voxels in area V1 (Dumoulin and Wandell, 2008), its properties might slightly change from one cortical area to the other (Handwerker et al., 2004). For this reason, we took a more general approach and estimated the HRF from all the brain voxels that significantly responded to the visual stimulation. These voxels were selected from a Fourier analysis of the average time-courses across the runs. For each voxel, we computed a signal-to-noise (SNR) ratio where the signal corresponded to the Fourier coefficient amplitude at the stimulation frequency F (i.e. $F = 1/34$) and the noise was given by the average moduli at the two neighboring frequencies (i.e. $F - \delta f$ and $F + \delta f$, where $\delta f = 1/2$ is the resolution of our frequency analysis). Only the voxels with SNRs greater than 3 were kept for further analysis. We computed the average time-course of these voxels during one cycle and used this average time-course for estimating the HRF. The HRF was derived as the response to a 2s stimulus (our fMRI sampling rate). Note however that our stimulus duration was 4s rather than 2s because linearity deteriorates at short durations (Boynton et al., 1996; Logothetis and Wandell, 2004) and because this duration was used in a previous monkey fMRI study that characterized the BOLD HRF in macaque (Leite et al., 2002).

D.4 Results

Functional imaging was conducted at 3T on awake behaving animals, performing a simple fixation task. The stimulus consisted of full-field counter phasing (10Hz) checkerboards that were displayed for 4s followed by a 30s blank. Figure 9 shows the time-courses in voxels with significant SNRs, in responses to a 4s pulse (highlighted in pale blue). In order to fit these time courses, we adopted he dominant analysis strategy which assumes that BOLD responses to events add linearly (Boynton et al. 1996) and use a set of smooth functions to model the underlying HRF. We parameterized the HRF as difference of two gamma functions (equation 6) (Lindquist et al., 2009) since this form describes the late undershoot of the response more precisely than a single gamma function (Boynton et al., 1996). In equation 6, A = amplitude, α_1 = delay of response relative to onset, α_2 = delay of undershoot, β_1= dispersion of response, β_2 = dispersion of undershoot, c = ratio of response to undershoot. The resulting fits are shown in pale red and green, respectively. The average time course fitting explained 98% of variance for all 3 animals. The parameter values for each monkey are shown in Table 1.

Equation 6 $$\boldsymbol{h(t) = A(\frac{t^{\alpha_1 - 1}\beta_1^{\alpha_1} e^{-\beta_1 t}}{\Gamma(\alpha_1)} - c\frac{t^{\alpha_2 - 1}\beta_2^{\alpha_2} e^{-\beta_2 t}}{\Gamma(\alpha_2)})}$$

Monkey	α_1	α_2	β_1	β_2	c
M01	4.2728	26.9917	1.6767	3.8906	0.7878
M02	3.8958	27.7752	1.0556	3.5909	1.1467
M03	3.8571	26.0207	1.7344	2.9018	0.8672

Table 1. **Parameter values of fitted double gamma function.**

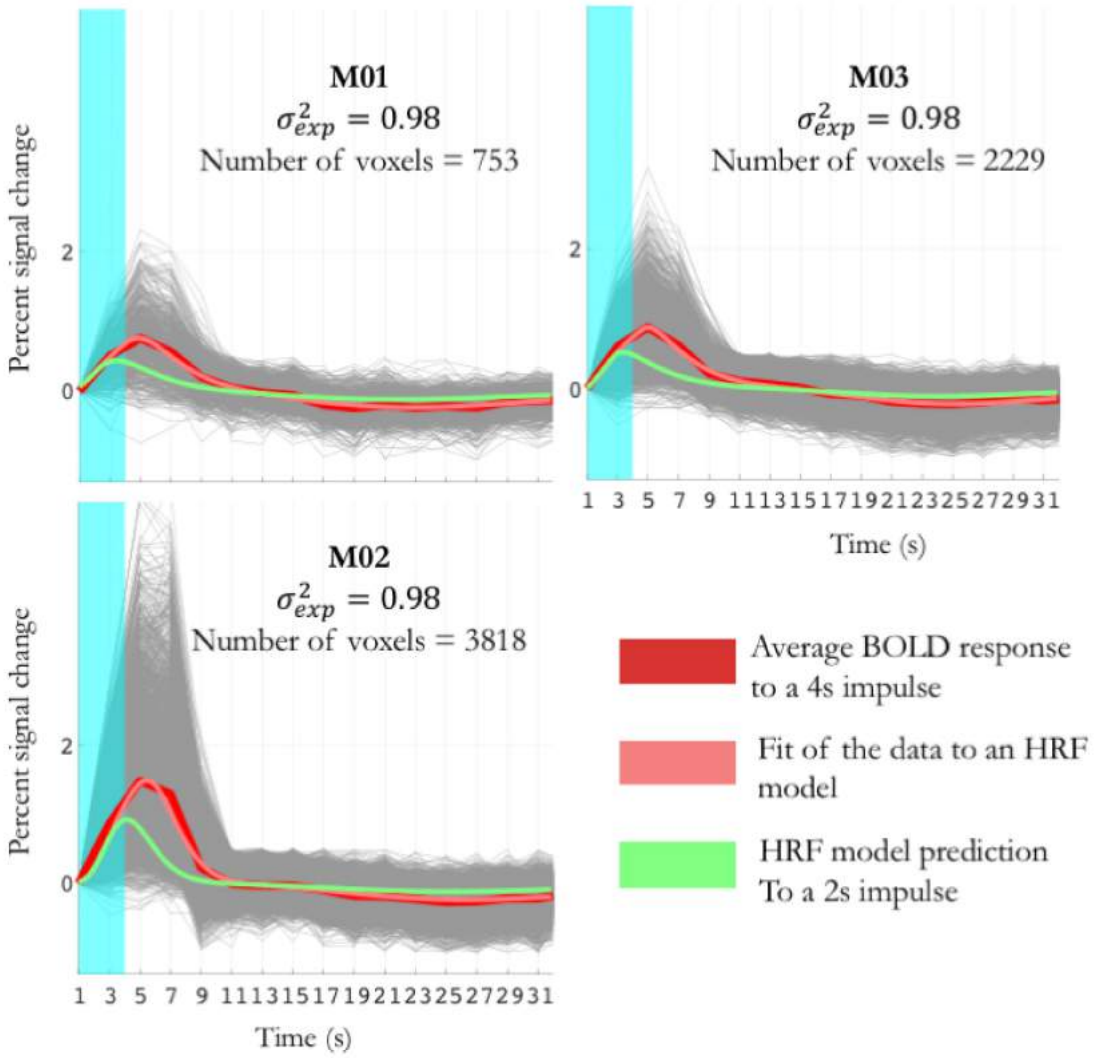

Figure 9. **Characterization of the hemodynamic response function (HRF).** A) For each monkey, the grey time-courses give the responses to a 4s pulse (highlighted in pale blue) in voxels with significant SNRs. The average of these time-courses is shown in dark red. The fit to this average response using a difference of gamma functions and the corresponding HRF (i.e. the corresponding response to a 2s stimulus) are shown in pale red and green. The percentage of variance explained is provided in the upper-right of each panel.

D.5 Discussion

In a typical fMRI experiment, a series of stimuli are presented to an observer and evoked brain activity, in the form of BOLD signals, are measured from voxels with a certain dimension. The task is then to infer the tuning of the voxels to features in the presented stimuli based on the evoked BOLD signals. To make this inference quantitatively, it is necessary to have a model of how BOLD signals are evoked in the presence of stimuli. Thus, having an accurate model of the HRF of the voxel is one of the basic assumptions that we must make to use the GLM. A common practice is to use a canonical HRF model established from previous empirical studies of fMRI time series. However, voxels throughout the brain and across subjects exhibit a variety of shapes, so the canonical model is often imprecise. To palliate to this problem, we estimated the HRF in each of our monkeys. While we followed the procedures of Dumoulin and Wandell (2008), our HRF estimation relied on all voxels that significantly responded to the visual flash, encompassing voxels for higher tier visual areas. We chose this strategy to account for variability across cortical areas that are sensitive to visual stimuli. Furthermore, to limit linearity deterioration caused by short visual pulses, we derived our HRF from a 4s visual pulse, which corresponds de twice the sampling resolution (2s) used in the following studies.

Although the HRF has been thoroughly characterized temporally, human and animal studies have demonstrated that there many factors that can influence the shape of the HRF. Hirano et al. 2011 note that the discrepancy between the BOLD signal and the CBF (cerebral blood flow) becomes significant when stimuli extend in time, a discrepancy which could be related to the different contributions of venous and arterial hemodynamic contributions to the neuroimaging signals at different time points. Another confound, is the distinct neuronal and vascular architecture that characterizes the different areas and layers of the cortex, which are undeniably a source of variability in the hemodynamic response. Improving our estimation of the HRF must combine a better temporal sampling, and finer spatial sampling of the vascular dynamics, preferably on the scale of

the whole brain. One could explain the scarcity of research in neurovascular coupling because of the lack of techniques that can combine both high temporal and spatial sampling, a combination needed to understand the vascular dynamics of each cortical region, and the interplay between neighboring regions.

E. Wide-field retinotopy of macaque visual cortex

E.1 Retinotopy is a solution to costly wiring

Metabolically speaking, it is costly for neurons to make long connections. Longer connections make for higher energy expenditure and increased transmission time, which is not suitable for a system whose prerogative is quick and efficient information processing. A solution to such problem is the spatial grouping of neurons that are highly connected. Ordered topography, is a characteristic shared by all sensory systems of most vertebrates. An illustrate example of such topographic ordering is retinotopy.

A visual cortical area is called retinotopic if nearby cortical neurons receive inputs from nearby retinal neurons. Our visual apprehension of the external world relies on the spatial correlations between objects, thus, in its early stages, the visual system combines information coming from the adjacent points in the visual field in order to build a global percept from local information. The purpose of a retinotopic map is then to group together, in an orderly fashion, neurons with adjacent receptive fields to reduce the length of intracortical connections that are required for processing local features of the visual space. The obvious evolutionary advantage is the reduction of the overall volume and weight of the brain and an increase in the speed of processing. Such connections are most likely to be made between groups of neurons with similar functional properties, and in proportion to the degree of similarity.

The processing of the neural signal happens on multiple scales. Whether it is sub-micron range of the molecular computations happening in synapses, the sensory computations between synapses separated by a few hundred microns, or cortical structures integrating information over a distance of centimetres, signal processing on multiple scales require a great amount of organization. The visual system is organized as a hierarchic succession of multiple topographic maps, beginning from the ganglion cells in the retina that project to the lateral geniculate nucleus (LGN) of the thalamus and from there to the primary visual cortex (V1); adjacent locations on the retina are represented

by adjacent neurons in the LGN and V1. This topographic organization is preserved along most if not all visually responsive cortical areas, with varying degrees of precision depending on the quantity and density of visually responsive cells within a given area. In addition to their hierarchic organization, some visual maps are organized as clusters (Wandell and Winawer, 2011). Such visual maps share a common representation of the fovea, and each of them represents a consequent portion of the visual field. Maps within a cluster are distinguished based on reversions of the polar angle. It is believed that such cluster organization has the purpose of sharing computational resources while minimizing long range axonal connections. It has also been theorized that functional specializations for perception are organized around the activities within these clusters rather than single visual field maps (Bartels and Zeki, 2000).

E.2 Retinotopic mapping using fMRI

E.2.1 The standard paradigm: Travelling wave

The most common method for mapping out the retinotopic organization with fMRI makes use of phase-encoded stimuli and Fourier analysis or the GLM (Engel et al., 1994, 1997; Sereno et al., 1995b). Phase-encoded stimuli possess a certain periodic frequency f, that elicits a periodic fluctuation in the MR signal in the responsive cortical areas. This method maps out the preferred polar angle coordinates (eccentricity and polar angle) at each voxel. The preferred eccentricity is probed in an experiment where the subjects keep central fixation while presented with centered rings that are slowly and periodically expanding or contracting. The polar angle is mapped out in a similar manner using clockwise or counter-clockwise rotating wedges. The preferred eccentricity and polar angle can be determined by correlating the periodic response signal to a sinusoidal regressor at the stimulation frequency f (Bandettini et al., 1993) or by examining the Fourier transform of the response signal (Sereno et al., 1995b). The phase of the sinusoid (or equivalently the phase angle at the frequency f in Fourier space) indicates the preferred eccentricity or polar angle. The amplitude of the sinusoid (or, equivalently, the magnitude at the frequency f in Fourier

space) is related to the statistical significance of the signal. The measurement of these two, orthogonal dimensions is vital for the correct definition of visuotopic maps, as these two measurements allow for the unique mapping of the responses of the neurons within a single voxel in cortex to a unique location in visual space. If only a single dimension is measured, the cortical response can only be localized to a broad swath of visual space, which does not allow for accurate delineation of map boundaries.

These travelling wave stimuli are typically comprised of a set of high contrast flickering checkerboard stimuli that are designed to maximally drive primary visual cortex neurons and elicit maximum modulation of the fMRI signal. Other stimuli (faces, objects) have been used in studies aimed at measuring the retinotopic organization of higher order visual cortex, although the checkerboard stimulus has proven to drive even these regions in many studies, with discussable efficiency. The traveling wave name comes from the fact that these stimuli create a travelling wave of cortical activity from one end of the map to the other along isopolar or isoeccentric lines. Thus, the phase of the signal varies smoothly across the cortical surface, which defines the most preferred eccentricity or polar angle of a voxel, giving the "phase-encoded" characteristic to the travelling wave method. The visuotopic map is then read by assigning each polar angle and eccentricity value a colour on the cortical surface.

E.2.2 Population receptive field modelling

Although the travelling wave method has demonstrated its reliability in mapping many areas of the visual cortex, it has shown limits in dealing with maps that have large RFs. To address this issue, researchers developed a method that relies on the measurement of the population RF of each voxel (Dumoulin and Wandell, 2008). To accomplish this, the pRF model first creates a very large database of possible pRF sizes and centres that cover the field of view of the stimulus. Then, the model convolves each of the pRF possibilities with an HRF. Finally, the model uses a least-squares fitting method to iteratively test each of the pRF possibilities for each voxel independently against

the actual data collected. Whichever pRF best fits the data is then assigned as the pRF for that voxel. Only voxels that contain activity above a chosen threshold of variance explained as determined by the model are included for further analysis. Further details on the pRF method can be found in Section C.

The pRF method has the additional benefit of measuring neuronal population properties other than preferred polar angle and eccentricity, such as receptive field size and laterality. These measurements have the possibility of demonstrating internal receptive field structure differences between, for example, a hemifield map in primary visual cortex (V1) and a hemifield map in lateral cortex (Larsson and Heeger, 2006). The underlying properties of the neuronal populations within these two maps are actually quite different than what has been found using the travelling wave method, with finely tuned neurons in V1 and more broadly tuned neurons in lateral cortex. The models of the underlying neuronal properties from the pRF method can measure these receptive field differences, as well as the amount of input from ipsi- and contralateral visual fields (Amano et al., 2009).

The success of pRF modelling will most likely be the cause of demise for the travelling wave method. PRF modelling has primarily used a two-dimensional Gaussian profile for the pRF estimates, but researchers are working on the use of center-surround Gaussian pRFs, multiple location pRFs, and non-classical pRF shapes, which may allow for better pRF estimation as time continues (Zuiderbaan et al., 2012; Zeidman, 2016; Wandell and Winawer, 2017).

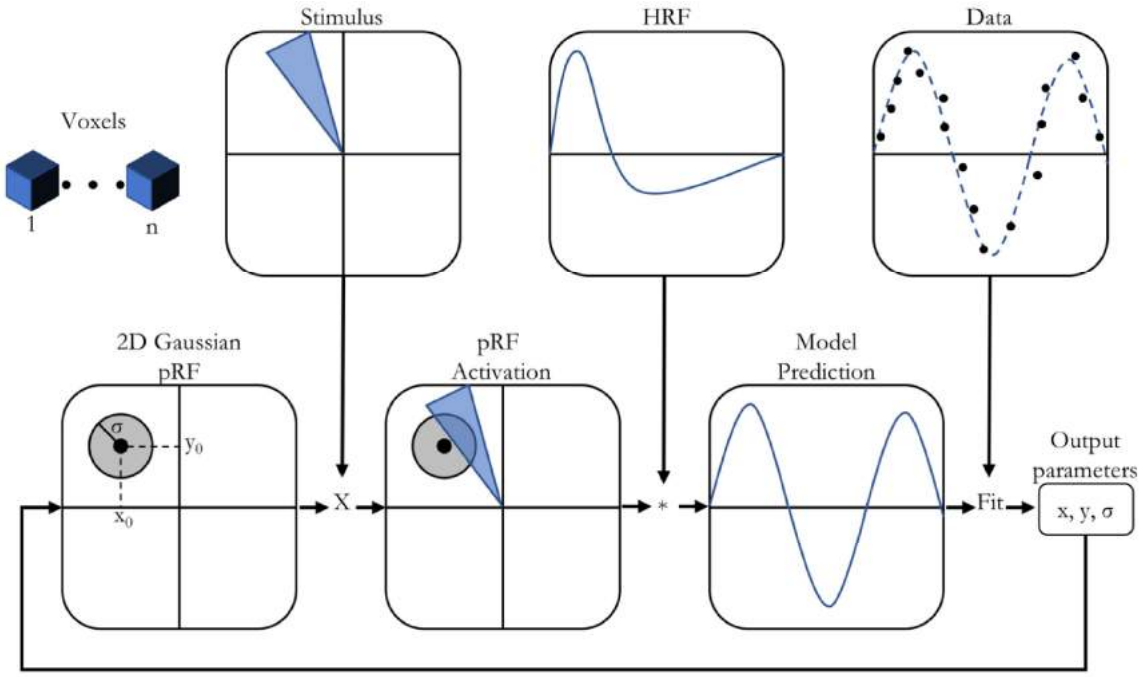

Figure 10. **Population receptive field modelling.** The population receptive field is represented as 2D Gaussian with Cartesian coordinates and spread value. Thousands of time course model predictions are generated for each voxel with different pRF parameters. The models are then fitted to the actual data and those with the highest correlation values are kept for further analysis. The figure is adapted from Brewer et al. 2012.

E.2.3 Homologies of retinotopic maps in humans and monkeys

Phase-encoded retinotopic mapping along the polar angle and eccentricity dimensions using functional magnetic resonance imaging (fMRI) has been widely used to reveal topographic organization within the human (Sereno et al., 1995; Engel et al., 1997; Schneider, 2004; Brewer et al., 2005; Larsson and Heeger, 2006; Swisher et al., 2007; Konen and Kastner, 2008; Arcaro et al., 2009; Kolster et al., 2010) and also the macaque monkey visual system, for review (Vanduffel et al., 2014). The homologies between retinotopic areas in humans and monkeys are straightforward for areas V1 through V3 whereas the topography of V4 significantly differs between the two species. Monkey V4 is a split-field representation that extends on portions of the dorsal and ventral occipital surfaces, while human V4 is confined to the ventral occipital surface, limited by an upper vertical meridian border posteriorly and a lower vertical meridian anteriorly. Beyond V4, homologies of areas MT and PITv/d, show similarities in their topographies, response properties, and population receptive fields. Higher order visual areas, such as the ones found in parietal and frontal cortices

remain a matter of debate. Little consensus has been reached as to the exact boundaries of such areas in any species, which hinders the possibility of finding homologies.

The findings from retinotopic mapping in both humans and monkeys have had a significant impact on the study of the visual system. In addition to revealing visual field maps and their organization as clusters, retinotopic mapping has demonstrated that any visual area that is organized retinotopically is subject to the constraints common to all visual maps in the brain. Because laboratories have been mostly using standard phase encoded retinotopy that rarely extends beyond 20° of eccentricity, although they have been shown to be visually responsive, many areas of the brain have been considered "non-retinotopic", or containing only an eccentricity bias. The fact that has been interpreted as only the early portion of the visual system is retinotopic and that at some point a fundamental change in the way the visual system is constructed changes, is a major theoretical claim. This would require a potentially complex transformation from a retinotopic framework to some other non-spatial organization. The better probability though, is that higher order visual areas are retinotopic, maintaining organized dispersed receptive field centers despite an increase in their size. Thus, the problem is of methodological order, since it makes no evolutionary sense to develop an entirely different way to deal with visual information when the simple solution of using large receptive fields and population codes within visual maps does not require a change in organization or connectivity. Thus, measuring the topography of higher tier visual areas requires a refinement of retinotopic measurement methodology, such that employed stimuli have a better chance of driving areas with larger receptive fields and pronounced sensitivity to behaviorally relevant objects.

The following section evaluates previous studies that have attempted to study the topography of higher order visual areas such as the PPC and presents a study making use of the novel methodology for the measurement of the topography of visual areas in this part of the cortex.

E.3 Investigating the visuotopic organization of the posterior parietal cortex (PPC)

E.3.1 Introduction

In primates, the posterior parietal cortex (PPC) constitutes the end stage of the dorsal visual pathway and as such, it is notably involved in visuospatial and visuomotor functions (Buneo and Andersen, 2006). Most of what we know about how those functions are implemented in the PPC emanates from invasive (anatomical and electrophysiological) studies performed in macaque monkeys. They have notably demonstrated the existence of a myriad of structurally and/or functionally distinct areas (Pandya and Seltzer, 1982; Colby et al., 1988; Andersen et al., 1990; Lewis and Van Essen, 2000), although their precise number and boundaries remain debated (Van Essen, 2004). Such invasive studies have led to the view that monkey PPC is only marginally visuotopic, with coarse topographic representations of visual space restricted to the lateral intra-parietal (LIP) area (Blatt et al., 1990; Ben Hamed et al., 2001), a portion of the dorsal prelunate (DP) area (Heider et al., 2005) and possibly in the parieto-occiptal area V6A (Galletti et al., 1999). Because those areas appear more as isolated patches than as a structured ensemble, visuotopy has not been considered so far as a useful criterion for parsing monkey PPC.

In striking contrast, several visuotopic areas have been progressively unveiled in human PPC (Sereno, 2001; Schluppeck et al., 2005; Silver et al., 2005; Swisher et al., 2007; Konen and Kastner, 2008), thanks to the development of functional magnetic resonance imaging (fMRI) techniques for non-invasive retinotopic mapping (Sereno et al., 1995a; Engel et al., 1997). These studies have drawn the view of a dense arrangement of abutting visuotopic maps in human PPC (Wandell et al., 2007; Silver and Kastner, 2009) . The apparent discrepancy with results obtained from invasive studies in monkey PPC might partly reflect inter-species differences in PPC functional organisation, notably linked to the emergence of specific human skills such as the use of tools

(Kaas and Stepniewska, 2016; Orban, 2016; Kastner et al., 2017). However, it might also betray the advantage of fMRI-based approaches for uncovering the visuotopic organisation of higher-order visual areas, where neurons generally exhibit large and coarsely organised receptive fields (RF) (Patel et al., 2010).

This second hypothesis has received support in a recent study by Arcaro and colleagues (Arcaro et al., 2011). By implementing those non-invasive mapping procedures in macaque monkeys, the authors confirmed the visuotopic organization of LIP and DP but, additionally, they revealed 2 new visuotopic maps, CIP1 and CIP2, in the caudal portion of the intra-parietal sulcus.

Building on this seminal success, and inspired by recent developments in human mapping studies (Pitzalis et al., 2013b), we introduce adaptations to the mapping procedure of Arcaro and colleagues (2011), and notably wide-field visual stimulation with moving and behaviorally-salient objects, in order to boost the recruitment of PPC neurons. Besides confirming the existence of CIP1 and CIP2, our results show that they form a visuotopic cluster with 2 additional previously unknown areas of the posterior intraparietal sulcus, PIP1 and PIP2. This PIP cluster is bordered by other visuotopic areas: V3A/DP laterally, V6/V6A medially and LIP anteriorly. This finding suggests that in macaques, as in humans, the PPC manifests a dense arrangement of visuotopic maps.

E.3.2 Material and Methods

E.3.2.1 Animal model.

Two adult female rhesus macaques, M01 and M02 (age: 8 and 9 years old, weight = 5.2 and 5.5 kg), were involved in the present study. Animal housing, handling, and all the experimental protocols (surgery, behavioural training and MRI recordings) followed the guidelines of the European Union legislation (2010/63/UE) and of the French Ministry of Agriculture (décret 2013-118). The project was approved by a local ethics committee (CNREEA code: C2EA – 14) and received authorization from the French Ministry of Research (MP/03/34/10/09). The animals were housed together in a large, enriched enclosure and could thus develop social and foraging behaviors. Health

inspections were carried out quarterly on these animals. After habituation to the monkey chair and experimental set-ups, animals were surgically implanted with a plastic head-post, sealed to the skull with ceramic screws (Thomas recording) and bone cement (Palacos+Gentamycine, medium viscosity, Heraeus). After a post-surgery period of about 8 weeks, the animals resumed the behavioral training through daily sessions in a passive fixation task. Details of the surgery procedure and behavioral training are provided in Section C.

E.3.2.2 MRI recordings.

Whole-brain images were acquired on a 3 Tesla MR scanner (Phillips Achieva) using a custom 8-channel phased array coil (RapidBiomed) specially designed to fit the skull of macaques while preserving their field of view. High-resolution T1-weighted anatomical images were acquired with an MP-RAGE sequence (repetition time [TR] = 10.3 ms; echo time [TE] = 4.6 ms, flip angle = 8°; voxel size = 0.5 x 0.5 x 0.5 mm; 192 slices). Functional images were acquired with a GE-EPI sequence with interleaved slice acquisition (TR = 2000 ms, TE = 30 ms, flip angle = 90°, SENSE factor = 1.6; voxel size = 1.25 × 1.25 × 1.5 mm, 32 axial slices).

E.3.2.3 Experimental set-up and behavioral task.

During the scanning sessions, the animals were head-fixed, seated in a sphinx position within their primate chair, into the bore of the magnet (Figure 11A). They were facing a translucent screen at a viewing distance of 25 cm. This short viewing distance allowed the presentation of wide-field stimuli (~80° of visual angle), rear-projected on the screen by a video projector (Hitachi, CP_X809). The position of one eye was monitored with an infrared video-based eye-tracker at 60 Hz (ASL). During the acquisition of functional sequences (typically 8 to 12 runs per daily session), the animals were involved in a passive fixation task. They had to maintain their gaze within ±1.5° of a small green square (0.4° x 0.4°) displayed at the center of the screen in order to receive fluid reward. The frequency of reward distribution was progressively increased as long as the fixation was not interrupted, in order to encourage prolonged fixation periods. Only runs in which animals

maintain their gaze on the fixation target for at least 85% of the total run duration were retained for further analyses.

E.3.2.4 Visual stimuli.

The visual stimuli were displayed on the translucent screen, behind the fixation target and centered on that latter. They consisted in home-made videos (resolution = 700 x 700 pixels, refresh rate = 16 Hz) covering a large portion of the visual field (~80° of visual angle) and depicting a fruits basket that seemed to approach or recede in depth (through zooming) while also moving back and forth along both the horizontal and vertical dimensions (Figure 11B). By using stimuli with (1) a large coverage of the peripheral field of view, (2) coherent motion and (3) objects (fruits) the animals might wish to grasp, we intended to maximize the chances to evoke BOLD activations in dorsal visual cortex. The EventIDE software (OkazoLab) was used for real-time control of the behavioral task and stimuli presentation.

E.3.2.5 Experimental paradigms.

Both animals participated in 2 experimental paradigms involving wide-field visual stimulation and performed during distinct scanning sessions: (1) retinotopic mapping and (2) motion localizer. These paradigms are now described in more detail.

E.3.2.5.1 Wide-field retinotopic mapping.

Wedges rotating clockwise or counter-clockwise and rings expanding or contracting were used for retinotopic mapping. However, instead of being filled with luminance-defined checkerboards, as those generally used to map early visual cortex, the wedges and rings served as apertures applied on top of our video (Figure 11C). Conditions with wedges serve to measure the preferred polar angle of the population receptive fields (PRFs), while conditions with rings are used to estimate their preferred eccentricity. During the acquisition of a functional sequence, one of the 4 stimulus conditions was shown for a total duration of 230 s (the conditions were interleaved across runs), with the central fixation target always visible. In all cases, the stimuli started with the last 10 s of a

cycle (in order to reach the steady state of visual responses), and further accomplished 5 full cycles of 44 s. The wedges had a radius of ~40° and an angular extent of 49°, so that every point of the visual field covered by the stimulus was stimulated during 6 s per cycle. The rings had a mean eccentricity varying linearly between 0° and ~40°, with a constant width of 11° between their inner and outer borders (leading again to 6 s of stimulation per cycle for each point covered by the stimuli). For monkey M01 (M02), we have kept for further analyses 24/25 (24/26) runs for clockwise/counter-clockwise wedges and 23/24 (24/26) runs for expanding/contracting rings, collected over 7 (16) distinct sessions.

E.3.2.5.2 Motion localizer.

The motion localizer consisted in 4 visual conditions: central (<3° of retinal eccentricity) and peripheral (>3°) portions of the fruits basket video shown with intact motion or with static images sampled randomly from the video and refreshed at 1 Hz to minimize visual adaptation (Figure 11C, right-hand panel). All 4 conditions (Central–Motion, Central-Static, Peripheral-Motion and Peripheral-Static) lasted for 6 s and were surrounded by 10 s periods of blank screen (Baseline condition). The 4 visual conditions were repeated 3 times during a run, in a presentation order that varied between runs. In total, each run lasted 202 s, during which the central fixation target was always visible. Motion sensitivity in the central and peripheral fields of view was assessed by contrasting the visual conditions (Central-Motion > Central-Static) and (Peripheral-Motion > Peripheral-Static), across voxels with significant visual activations ([Central-Motion + Central-Static + Peripheral-Motion + Peripheral-Static] > 4 x Blank Baseline). In total, 18 (25) runs of motion localizer collected over 3 (5) sessions were kept for further analyses in monkey M01 (M02).

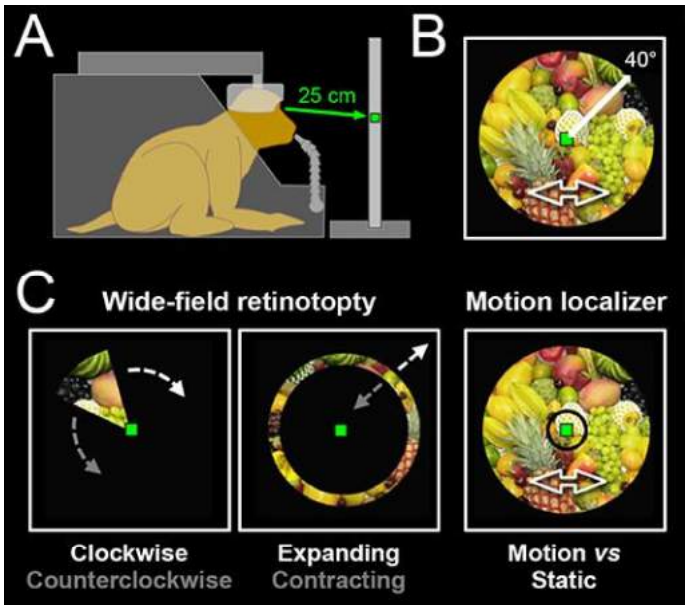

Figure 11. **Experimental set-up and protocol.** (A) Schematic drawing of a head-restrained macaque in an MRI compatible primate chair, fixating a central green dot located on a screen at a viewing distance of 25 cm. (B) Illustration of the shaking fruits basket video used for wide-field visual stimulation (covering 80° of the visual field). (C) Wide-field retinotopy is done with a wedge aperture rotating either clockwise or counterclockwise on top of the video for polar angle mapping (left panel) and with an expanding or contracting ring aperture for eccentricity mapping (middle panel). Motion localizer (right panel) was performed with central (<3°) or peripheral (>3°) circular aperture on top of either the video (motion condition) or static images extracted from the video (static condition). Monkeys were trained to maintain fixation on the central green dot during visual stimulation.

E.3.2.6 Data processing

E.3.2.6.1 Retinotopic mapping: volume-based preprocessing of the functional data.

During a preliminary session, functional (GE-EPI, n=300) and anatomical (T1, n=4) volumes were collected for each animal under slight anesthesia (see Section C). Functional volumes were averaged into an individual functional template and anatomical volumes were averaged into an individual anatomical template. Affine and non-rigid normalization parameters bringing the functional template onto the anatomical template were estimated from the grey matter maps of both templates, using the normalization tools of the SPM12 software. During the following sessions, only functional volumes were acquired for being preprocessed run by run. They were first slice-time corrected to compensate for the delay caused by the sequential (interleaved) acquisition of the slices. A mean image was then generated for each run for co-registration with the individual functional template. Co-registration parameters were then combined with the normalization parameters transforming the individual functional template to the individual anatomical template. Those combined parameters were then applied to all the functional images of the run in a single

interpolation step, which was also used to resample the functional volumes to 1 x 1 x 1 mm voxels. No smoothing was applied to the volumetric data. Rigid realignment between the functional volumes was also omitted since the animal's head was immobilized by the head-post. Non-rigid deformations could arise, principally caused by sudden postural changes of the animal within its chair. To regress out the signal fluctuations caused by such events, time courses of voxels outside the brain (muscles, eyes, etc.) were extracted and the 10% showing the highest temporal variance were submitted to principal component analysis (PCA) after z-score normalization. The 18 first PCA components were used to regress out all signal fluctuations correlating with those noise regressors within the brain voxels. The number of PCA components was determined empirically, as the one leading to the highest number of cortical surface nodes for which the PRF could be mapped across the 2 animals (see below).

E.3.2.6.2 Retinotopic mapping: surface-based processing of the functional data.

Models of the cortical surfaces were generated for each individual with the Caret software (Van Essen et al., 2001a) based on the grey/white matters segmentation of the high-resolution anatomical images (T1). Functional data were then projected from volume space to surface space as follows. For all surface nodes, 7 sampling points were computed along the normal vectors (from -0.75 mm to + 0.75 mm), to account for cortical thickness (1.5 to 2.5 mm in macaques). For each node and each run, time courses for the 7 sampling points were extracted by trilinear interpolation from the functional volumes. They were first converted to percent signal change and then averaged in a single mean time course attributed to the surface's node. Finally, all the time courses belonging to a same node and same type of run were averaged (Figure 12).

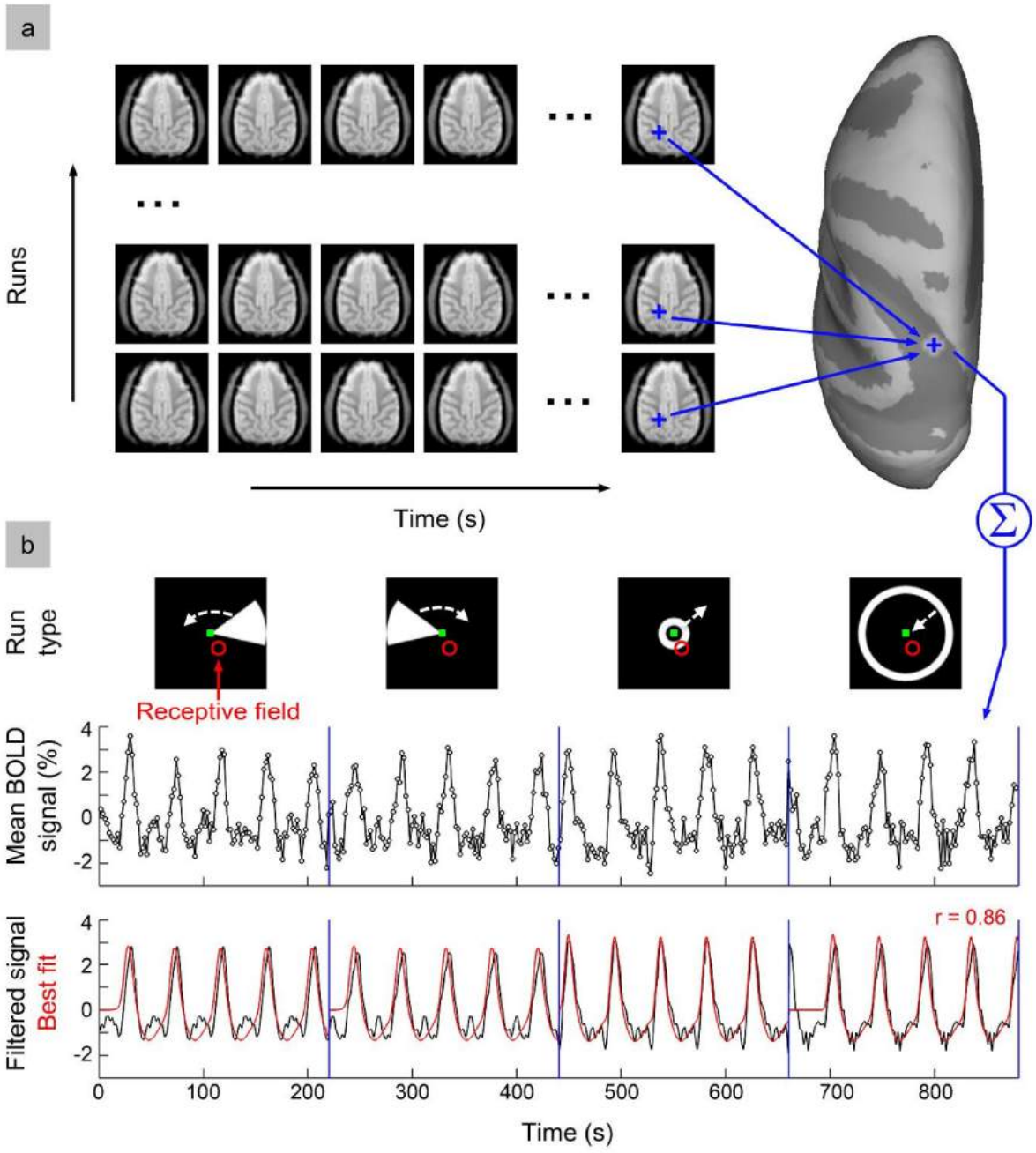

Figure 12. **Illustration of retinotopic data processing.** (A) After pre-processing, functional volumes were projected onto the reconstructed cortical surfaces and averaged to produce mean BOLD time courses, after conversion to percent signal change unit. (B) For the 4 types of run shown in the upper panels (clockwise and counterclockwise wedges, expanding and contracting rings), the mean BOLD time courses (black curve in the middle panel) were Fourier filtered to retain only the signal components corresponding to the fundamental frequency of the periodic stimuli and all its harmonics (black curve in the lower panel). The PRF analysis resulted in selecting the model time course (red curve in the lower panel) exhibiting the highest correlation with this filtered signal. If the correlation coefficient was superior to 0.5 (r=0.86 in the present example), the PRF parameters attached to the theoretical time course (polar angle, eccentricity and size) were retained. In the present example, those parameters define the PRF shown in red in the upper panels.

E.3.2.6.3 Retinotopic mapping: population receptive fields (PRFs) analysis.

The BOLD time courses evoked by periodic ring and wedge stimuli are generally processed with a phase-encoding method that is performed in the frequency domain after a Fourier transform (Sereno et al., 1995a; Engel et al., 1997). However, more and more research groups working on retinotopic properties of visual cortex in human now privilege approaches based on the PRFs analysis (PRFs) (Dumoulin and Wandell, 2008; Kay et al., 2013c) because they provide better estimations of retinotopic properties than conventional approaches (Dumoulin and Wandell, 2008; Kay et al., 2013c; Alvarez et al., 2015). The greater robustness of this approach, combined with the fact that it provides additional information about the size of the PRFs, led us to favor this newer type of analysis. Because our stimuli were frequency encoded, we used the fact that responses to this type of stimuli always have a spectral content constrained to the fundamental frequency (f0 = 1/44 Hz) and its harmonics (nf0 where n is an integer) to filter the data at those frequencies before the PRF analysis. This filtering was performed in the frequency domain. The PRF analysis was then conducted with the publicly available analyzePRF toolbox for Matlab, which is based on (Kay et al., 2013c). Following Dumoulin and Wandell (2008), the PRFs were modelled as simple isotropic Gaussian. Basically, the hemodynamic response functions that have been estimated for both M01 and M02 (See Section D) were convolved with regressors produced by a very large combination of PRFs positions (5352 positions covering the central 90° of the visual field) and PRFs sizes (30 sizes ranging from 0.5° to 60°) to produce a huge repertory of theoretical time courses (n= 160560). For each node, the PRF parameters attached to the theoretical time course showing the highest Pearson correlation coefficient (r) with the actual time course was retained. Threshold was set at $r>0.5$, which corresponds to a t value = 5.35 and an uncorrected one-tailed p value < 10-6 (assuming that for each of the 4 types of run, the filtering collapses the 5 cycles, ending up with a correlation involving 88 samples: 1 cycle = 22 TR x 4 types of run). The signal filtering and modeling procedures are illustrated in Figure 12 and the final r-score maps are shown in Figure 13. Additionally, we assessed the robustness of the model parameters by performing the same analyses

on the odd and even runs separately and by comparing the obtained results. As shown in Figure 14, excellent reproducibility was observed, confirming the robustness of our approach. The percentages of PRFs in contralateral space or very close to it (polar angle < 5° or eccentricity <2°) were 97.8% (96.4%) and 99.0% (97.4%) for the left and right hemispheres of M01 (M02). Only those PRFs were retained to build our polar angle and eccentricity maps.

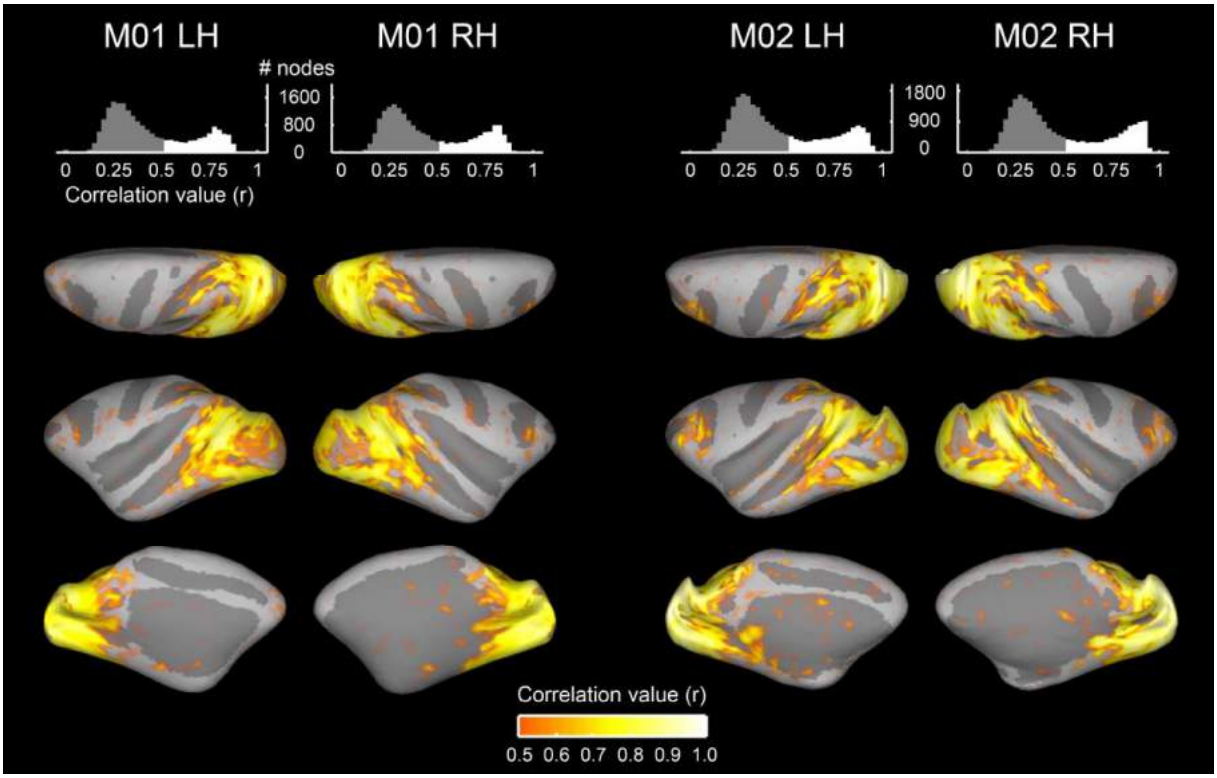

Figure 13. **Maps of PRFs goodness of fits**. The top row shows the distribution of correlation coefficients (r) across nodes for each of the 4 reconstructed cortical surfaces. Only nodes for which r>0.5 (corresponding to an uncorrected p value < 10^{-6}) were retained for further analysis. The distribution of those nodes is shown on dorsal, lateral and medial views of the 4 reconstructed cortical surfaces, color coded as a function of their r value.

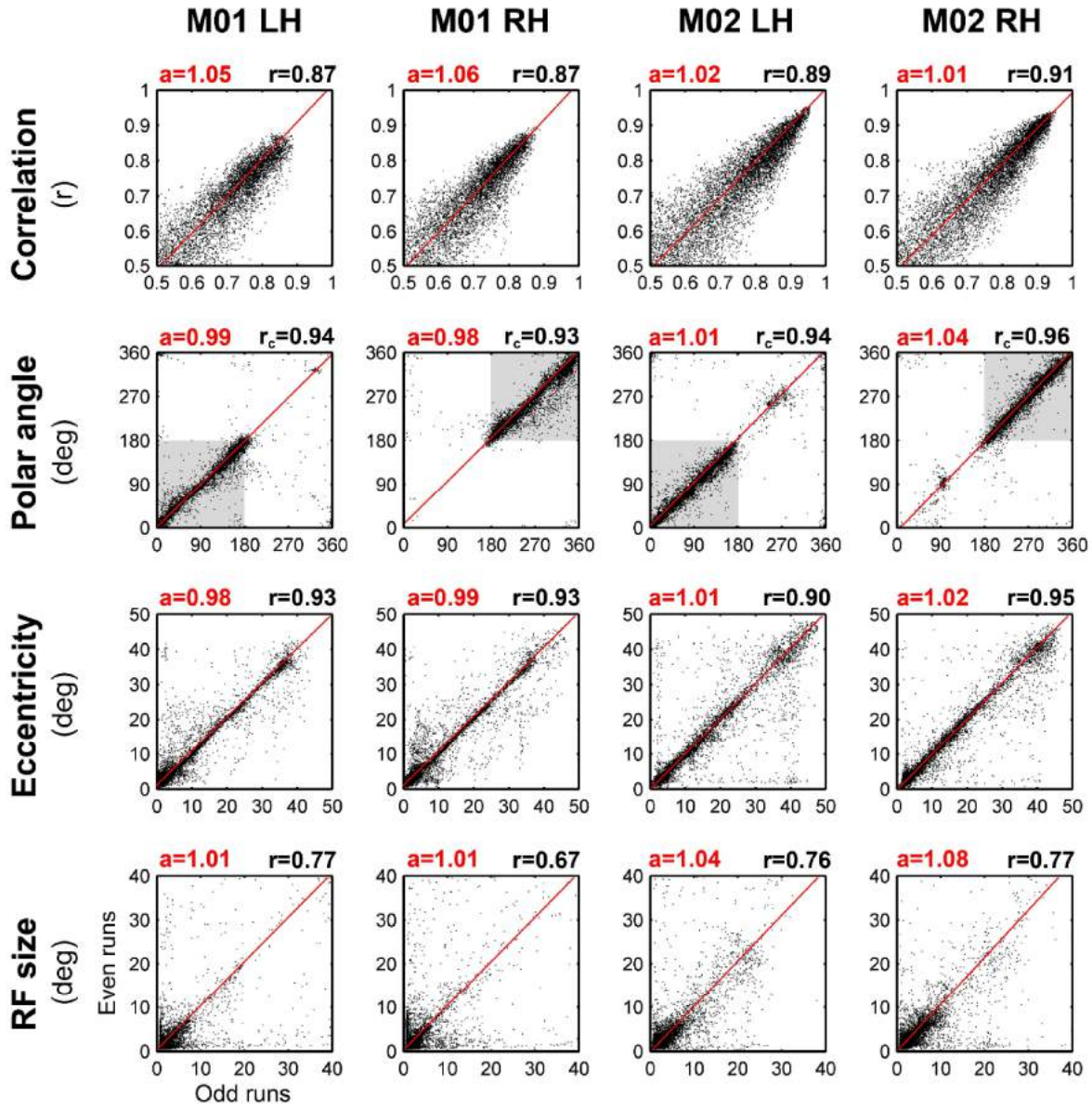

Figure 14. **Test-retest analysis of the PRF model parameters.** The PRF analysis was performed separately on the odd and even runs and the model parameters obtained with these two independent data set were compared. Comparison of the correlation coefficient (r), polar angles, eccentricities and receptive field sizes show a great level of reproducibility in all 4 cortical hemispheres, as indicated by correlation values and slopes of the regression line slopes which are all close to unity. For the polar angle values, circular correlation (r_c) was used and the grey zones indicate contro-lateral space (i.e., left visual hemi-field for the right cortical hemispheres and right hemi-field for left hemispheres). The percentages of nodes in contralateral space or very close to it (delta polar angle < 5° or eccentricity <2°) were 97.8% and 99.0% for the left and right hemispheres of M01 (LH M01 and RH M01), and 96,4% and 97.4% for the left and right hemispheres of M02 (LH M02 and RH M02).

E.3.2.7 Motion localizer.

Functional images were preprocessed run by run in a way similar to that described for retinotopic mapping. Additionally, functional images were slightly smoothed spatially with a Gaussian kernel (full width at half maximum of 2 mm). Statistical analyses were performed within the framework of the GLM as implemented in SPM12, with the 4 visual conditions and baseline conditions as principal regressors and 18 noise regressors derived from a PCA analysis similar to that described for retinotopic mapping.

E.3.3 Results

We have investigated the visuotopic organization of primate PPC with fMRI in 2 behaving macaque monkeys. Visuotopic mapping is classically performed with checkerboard patterns seen through wedge or ring apertures of moderate size (10-20° of retinal eccentricity). Since the PPC is known to process moving and salient objects, with emphasis on the periphery of the visual field, we have replaced those classical stimuli with a wide-field "shaking fruit basket" video, seen through much wider ring or wedge apertures (up to 40° of retinal eccentricity; see Figure 1). Population receptive fields (PRFs) analysis (Dumoulin and Wandell, 2008; Kay et al., 2013c) was applied to data filtered in the frequency domain (see Material and Methods) in order to increase signal-to-noise ratio (see Material and Methods). Those analyses were performed on spatially unsmoothed data after projection on cortical surface reconstructions.

E.3.3.1 Early dorsal visual areas.

Figure 15 presents the polar angle (left panels) and eccentricity (right panels) maps of the PRFs on inflated reconstructions of the dorsal visual cortex in monkey M01. Maps obtained in M02 area are provided in Figure 16 and the description below applies to both animals. Maps of PRFs sizes for both animals are provided in Figure 17. A representation of the lower vertical meridian (LVM) of the visual field defines the frontier between the dorsal aspects of the primary and secondary visual

areas (V1d/V2d; green color code and solid black line in left panels of Figures 2 and 3), while the V2d/V3d frontier is identified by a representation of the horizontal meridian (HM, blue color code and solid white line). Laterally, V3d and V4 are separated by a LVM. Anterior to V4 in the superior temporal sulcus, the MT cluster recently described by Kolster and colleagues (2009, 2014) is clearly observable. It encompasses 4 visuotopic areas (MT, V4t, MSTv and FST) with a foveal confluence (red color code in right panels of Figure 15 and Figure 16) but with nonetheless distinct representations of both lower (green to blue) and upper (blue to red) quadrants of the contralateral visual hemi-field.

E.3.3.2 Parieto-occipital complex V3A/DP.

Anterior to V3d, V3A and the Dorsal Prelunate (DP) area appear to form a cluster with a lateral foveal confluence and 2 mirror representations of the contralateral hemi-field. This organization entails a postero-anterior gradient of polar angle from lower to upper quadrant (green to blue to red) in V3A, and from upper to lower quadrant (red to blue to green) in DP, although the DP gradient is mostly observable in both hemispheres of M01. The exact lateral demarcation of the V3A/DP complex is difficult to operate in both monkeys, partly because DP lacks a clear eccentricity gradient. Altogether, these observations fit remarkably well with those of Arcaro and colleagues (2011).

E.3.3.3 Parieto-occipital complex V6/V6A.

Medial to V3d, the anatomical and electrophysiological investigations of Galletti and colleagues (Gamberini et al., 2015 for review) have evidenced 2 areas, V6 and V6A, occupying medial locations along the floor and anterior wall of the parieto-occipital sulcus. Some characteristics of the V6/V6A complex are clearly observable in our data. For instance, on the anterior wall of the parieto-occipital sulcus, there are in all 4 hemispheres an inversion of eccentricity gradient together with a representation of the vertical meridian (principally its lower component), which have been described as marking the frontier between V6 and V6A. In addition, the dorso-anterior aspect of

V6A has been shown to house a representation of the central-to-intermediate visual field, which is also consistently found in our data. Finally, the V6/V6A complex has been implied in the processing of visual motion, and our motion localizer clearly indicates the strong motion sensitivity of this cortical sector (Figure 17B). Medially, the demarcation between V3d and V6 cannot be safely delineated. According to the electrophysiological description of this boundary (Galletti et al. 1999), no reversal in polar angle or eccentricity gradients is to be expected, compromising the ability to robustly identify this boundary based on polar angle or eccentricity maps. Unfortunately, neither the maps of PRFs sizes nor our motion localizer could provide clear-cut evidences regarding the exact location of this boundary. Thus, this point will deserve further investigation. In the present study, we therefore indicate the location of this complex but with no attempt to clearly define its borders. Only the V6A component could be more safely delineated in all 4 hemispheres. Its MNI coordinates and surface coverage are provided in Table 2.

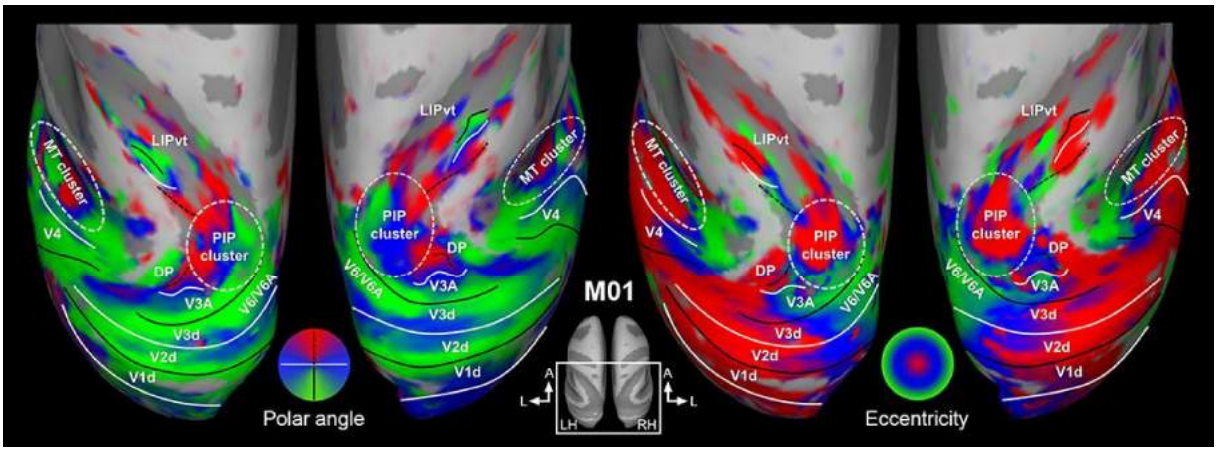

Figure 15. **Polar angle and eccentricity maps in monkey M01.** Thresholded PRF results (r>0.5; see Material and Methods) are shown on inflated surface reconstructions of the dorsal visual cortex in the left and right hemispheres (LH and RH) of M01. Polar angle maps are on the left. The color code reflects the proximity of the PRFs with the upper-vertical (red), horizontal (blue) and lower-vertical (green) meridians of the visual field. Dotted black lines, solid white lines and solid black lines, further signal those meridians respectively, for delineating the various visual areas. Eccentricity maps are on the right. The color code indicates the foveal (red), intermediate (blue) and eccentric (green) location of the PRFs with respect to the visual field center. Together with the configuration of meridians, reversal in eccentricity gradients have been used to delineate the MT cluster, anterior to area V4 and the newly defined PIP cluster (yellow dotted ellipses).

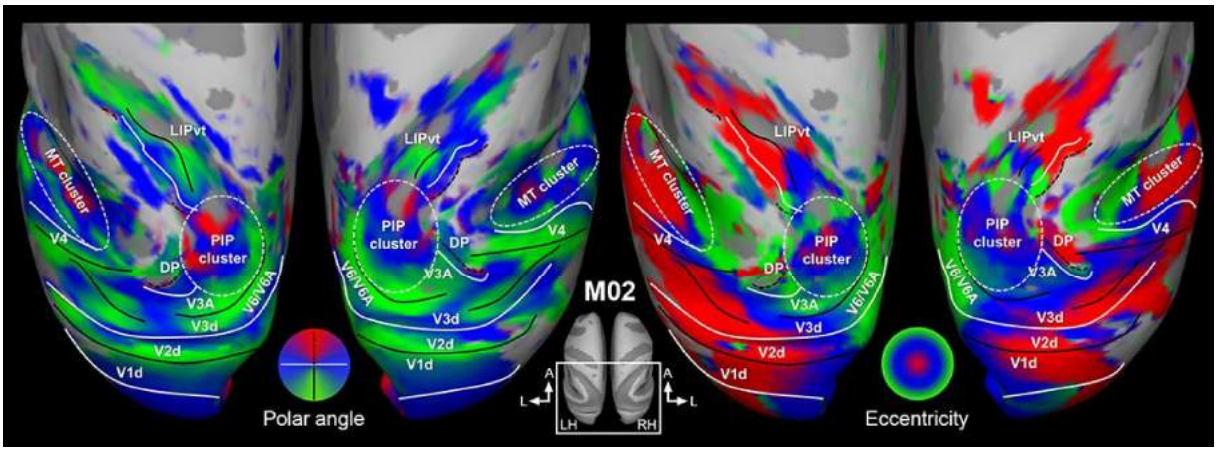

Figure 16. **Polar angle and eccentricity maps in monkey M02.** Same conventions as Figure 15.

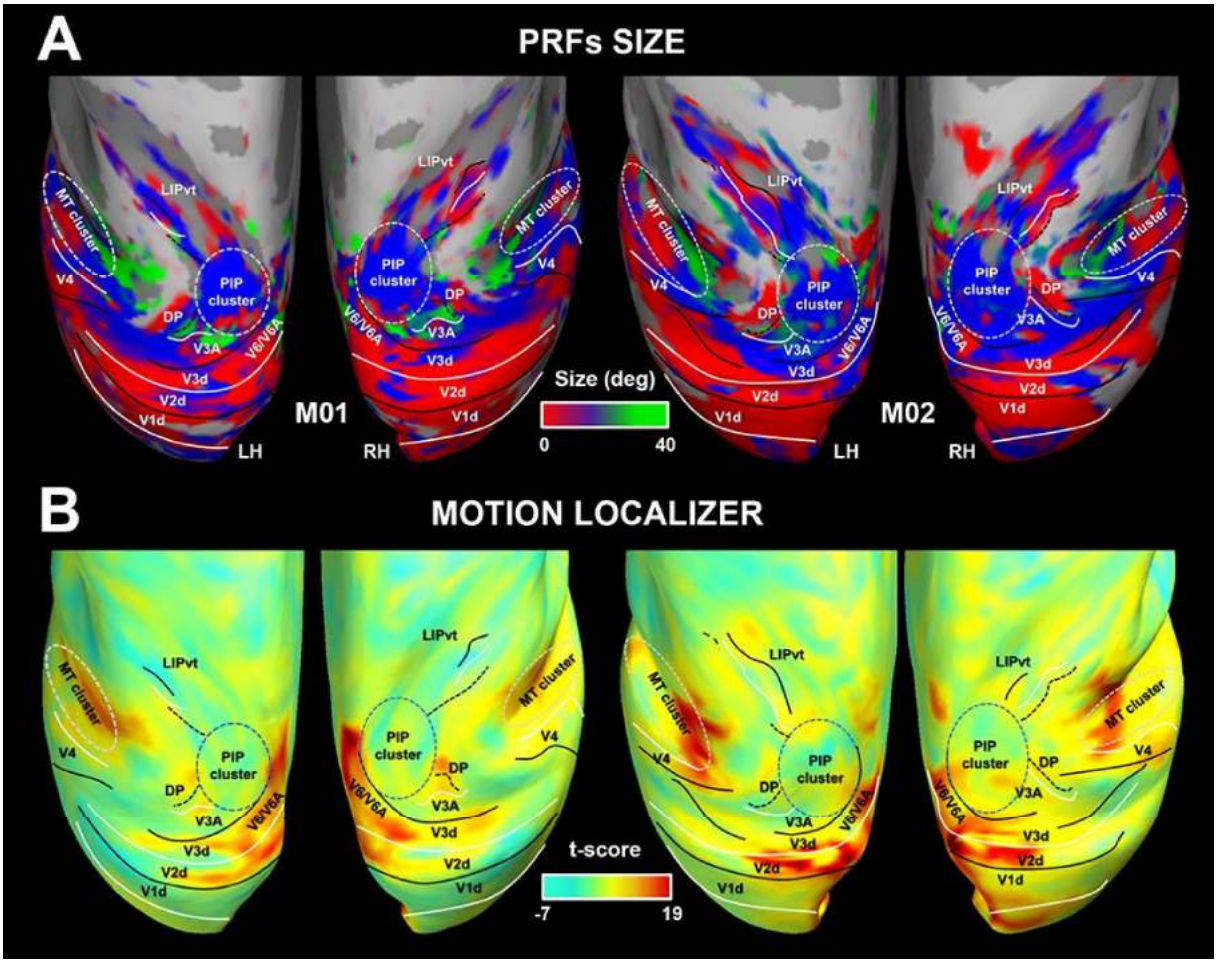

Figure 17. **Maps of PRFs size and motion sensitivity.** PRFs size (A) and T-score maps of motion sensitivity (B) on the surface reconstructions of the dorsal visual cortex for M01 (left) and M02 (right). (LH and RH stand for left and right hemispheres, respectively).

E.3.3.4 Parietal area LIP.

In all 4 hemispheres, a visuotopic organization was observed along most of the lateral bank of the intra-parietal sulcus, which is known to house the lateral intra-parietal (LIP) area. Consistently, this organization reveals an antero-posterior and slightly latero-medial gradient of eccentricity, with the antero-lateral and postero-medial sectors holding respectively representations of the central and peripheral visual field. Polar angle maps indicate that the lower and upper visual field quadrants are located antero-medially and postero-laterally, respectively. Overall, this visuotopic portion of LIP (LIPvt) fits quite well with those described in previous monkey fMRI studies (Patel et al., 2010; Arcaro et al., 2011). Its MNI coordinates and surface coverage are provided in Table 2.

E.3.3.5 Parietal cluster PIP: CIP1 & CIP2.

A major finding of Arcaro and colleagues (2011) concerned the existence of 2 new visuotopic areas in the caudal intra-parietal, CIP1 and CIP2, lying between V3A/DP posteriorly and LIPvt anteriorly. By studying the evolution of polar angle gradients between V3A and LIPvt, a succession of gradient reversals was robustly identified, marking the borders shared by those visuotopic areas. We confirmed this finding by using a similar approach, as illustrated in Figure 18. Small segments that run parallel to the polar angle gradient and perpendicular to the eccentricity gradients were drawn between V3A and LIPvt in all 4 hemispheres (yellow segments in maps' insets of Figure 18). The profiles shown in Figure 18 represent the progression along the segment paths, with each point providing the average polar angle values along a segment. To assess the reproducibility of the results, these polar angle profiles were assessed separately on odd (full line) and even (dashed lines) runs. Besides showing high consistency between the 4 hemispheres and between odd and even runs, those profiles are also strikingly similar to those shown in Figure 4 of Arcaro et al. (2011). Both V3A/CIP1 and CIP2/LIPvt share a representation of the UVM (Upper Vertical Meridian), while CIP1/CIP2 share a representation of the HM and thus mostly represent the upper quadrant of the contra-lateral hemi-field. Altogether, those polar angle analyses are highly consistent with those of Arcaro and colleagues and they bring firm confirmation for the existence of visuotopic

areas CIP1/2. However, these authors postulated that CIP1/2 share a foveal representation lying on the lateral bank of the IPS, while our results rather indicate a medial position, close to the fundus of the sulcus. This point is very important, since it suggests a more extended cluster, in which this foveal representation is shared not only by CIP1/2 laterally, but also by 2 additional and newly defined posterior intra-parietal areas, PIP1/2, extending medially. Evidences for this cluster organization are provided in the following section.

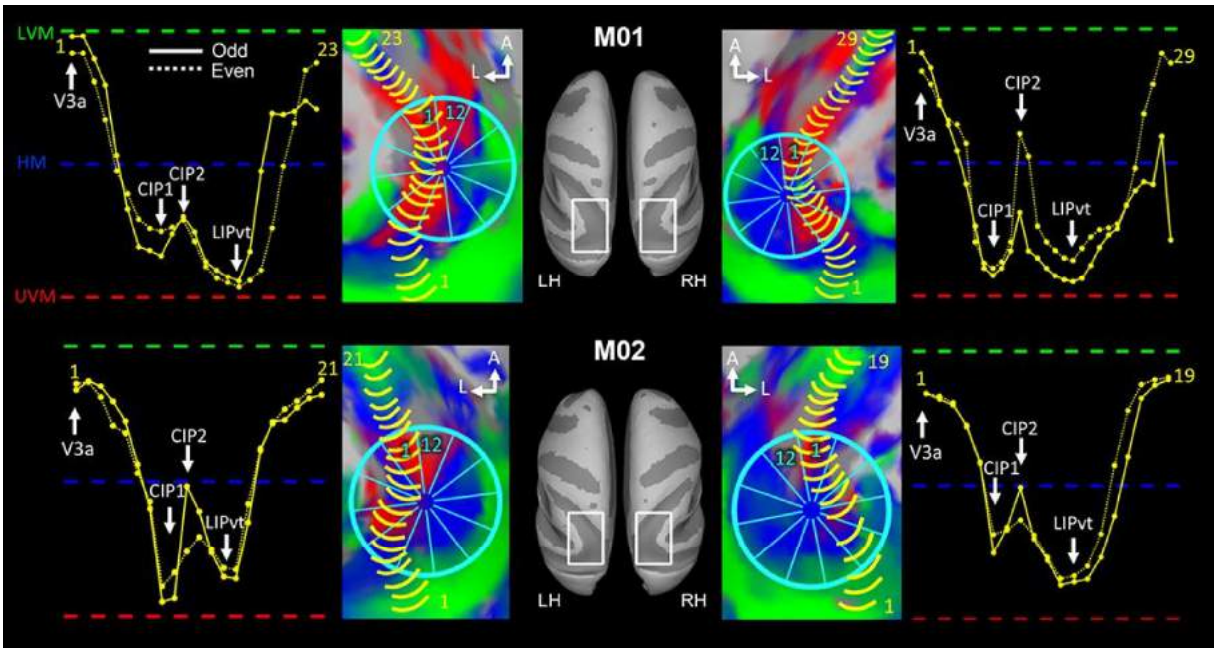

Figure 18. **Polar angle profiles from V3A to LIPvt in M01 (upper line) and M02 (lower line).** Line segments were drawn on top of the 4 cortical surfaces, forming paths going from V3A posteriorly to LIPvt anteriorly (yellow segments in the polar angle maps' inset). Polar angle profiles (in yellow) along those paths were highly consistent across animals, hemispheres, and between odd (full lines) and even (dotted lines) runs, with gradient inversions marking the frontiers between V3A/CIP1, CIP1/CIP2 and CIP2/LIPvt. The maps' inset also show the circular sectors (in cyan) used for the profiles in Figure 19.

E.3.3.6 Parietal cluster PIP: PIP1 & PIP2.

For each of the 4 hemispheres, we drew a circular area encompassing CIP1/2 laterally and centered on their medially-located central visual field representation, as illustrated in Figure 18. Circular polar angle profiles were then constructed by subdividing the circular area into 12 equal sectors and by averaging the polar angle values of all nodes encompassed within a sector, yielding 12 mean polar angle values. Figure 19A presents those profiles for odd (full lines) and even (dotted lines) runs in each of the 4 hemispheres. They clearly established that besides the gradient inversions defining the mirror upper quadrant representations of CIP1 and 2 laterally, other inversions reveal 2 mirror representations of the full contra-lateral hemi-field medially. We have named those newly identified visuotopic maps posterior intra-parietal areas 1 and 2 (PIP1/2). Both CIP1/PIP1 and CIP2/PIP2 share a UVM representation, while PIP1/PIP2 share a LVM representation. To further assert the cluster organization of these areas, surface nodes belonging to the lateral and medial aspects of the circular area drawn on each hemisphere were segregated before being subdivided in 3 groups depending on their small, intermediate or large distance with respect to the area's center (corresponding to the cluster's foveal confluence). Mean PRF eccentricity was computed for each of these 6 groups of nodes (Lateral/Medial * Small/Intermediate/Large distance). Figure 19B shows clear gradients of increasing eccentricity as distance of the surfaces' nodes from the foveal confluence increases, both laterally and medially. The wider range of retinal eccentricities covered by our mapping stimuli (40° against 15° in that previous study) may account for this elucidation of the eccentricity gradient.

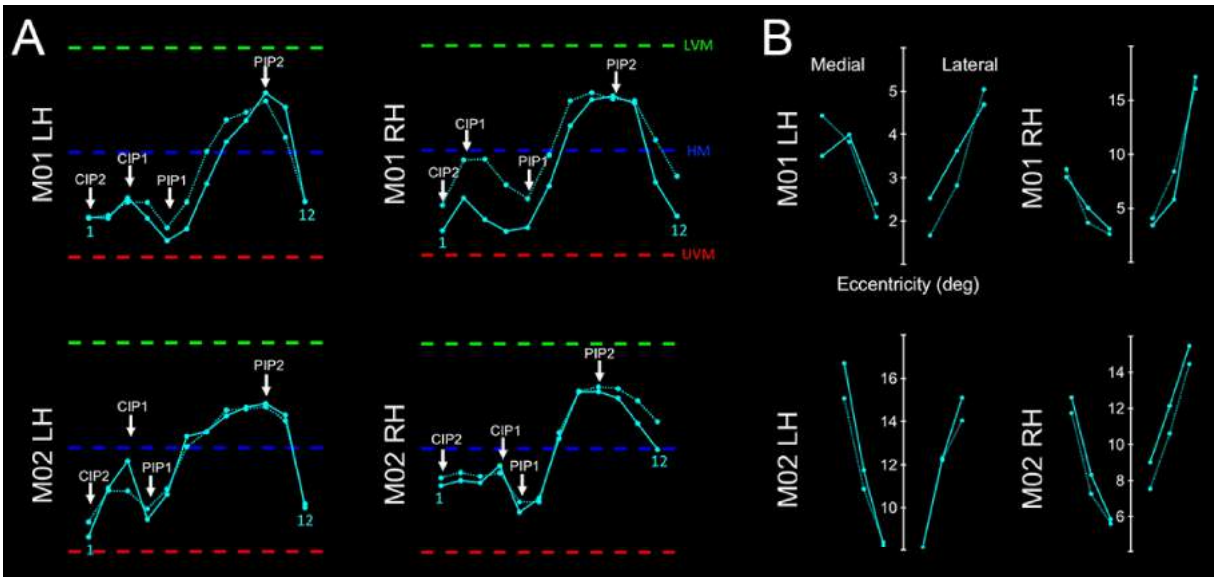

Figure 19. **Polar angle and eccentricity profiles within the PIP cluster in M01 (upper line) and M02 (lower line).** (A) Polar angle profiles along the wedge sectors shown in Figure 4, both odd (full lines) and even (dotted lines) runs (LH and RH stand for left and right hemispheres). Gradient inversions mark the frontiers between CIP2/CIP1, CIP1/PIP1, PIP1/PIP2 and PIP2/CIP2 when progressing from anterior-to-lateral-to-posterior-to-medial sectors. (B) Eccentricity gradients from the center toward the medial and lateral borders of the PIP cluster. In both directions, we observe an increase in mean eccentricity when surface nodes are divided in 3 groups of close, intermediate or far cortical distance from the foveal confluence.

E.3.3.7 Parietal cluster PIP: overall anatomo-functional definition.

Figure 20 presents enlarged views of this newly identified visuotopic cluster on top of the maps of polar angle (Figure 20A), eccentricity (Figure 20B), motion localizer (Figure 20C) and sulci/gyri definition (Figure 20D), with the star indicating foveal confluence. In most hemispheres, the external borders of the PIP cluster are defined both by representations of visual field meridians (i.e. it shares UVM representations with both V3A and LIPvt, and LVM representation with V3d/V6/V6A) and by eccentricity gradient inversions (i.e. peripheral field representations mark the borders with V3A laterally, LIPvt anteriorly, V3d/V6/V6A posteriorly and medially). Additionally, the postro-medial border between the PIP cluster and the V6/V6A complex is marked functionally by a strong motion sensitivity of V6/V6A, contrasting with the lack of motion sensitivity in PIP1/2. In Figure 21A, those visuotopic areas are finally shown on coronal sections of M01 and M02 brains. In the posterior-most sections (upper row), PIP1 and PIP2 occupy the fundus and medial bank of the parieto-occipital sulcus, capped by V6A in the dorso-medial

convexity. In more anterior sections (middle and bottom rows), they always occupy the fundus and medial bank of the intra-parietal sulcus, while CIP1 and CIP2 occupy the lateral bank of the IPS. As shown in Figure 21B, this visuotopic cluster occupies a position at the junction of the parieto-occipital and intra-parietal sulci, which is that attributed to the PIP area initially defined by Colby (Colby et al., 1988) on the basis of its myelo-architecture (Colby et al., 1988), and shown here in yellow as defined on the F99-M132 template (Van Essen et al., 2001b; Markov et al., 2014). In all 4 hemispheres, the lateral-most portion of the template-defined V6A is included in the cluster, while its medial aspect is in fine correspondence with our visuotopically-defined V6A. The stereotaxic coordinates and cortical surface coverage of these different visuotopic areas are provided in Table 2. The size of the PRFs is the third parameter provided by our analyses (in addition to the PRFs polar angle and eccentricity). In the PIP cluster, all areas have very large PRFs (median ~ 10-12°), with no significant difference between them. These sizes are about 10 times larger than those measured in V1 (median ~ 1.3°) and more surprisingly, also much larger than those measured in LIP (median ~ 6°) and in V6/V6A (median ~ 7°). Maps of PRF sizes are provided in Figure 17.

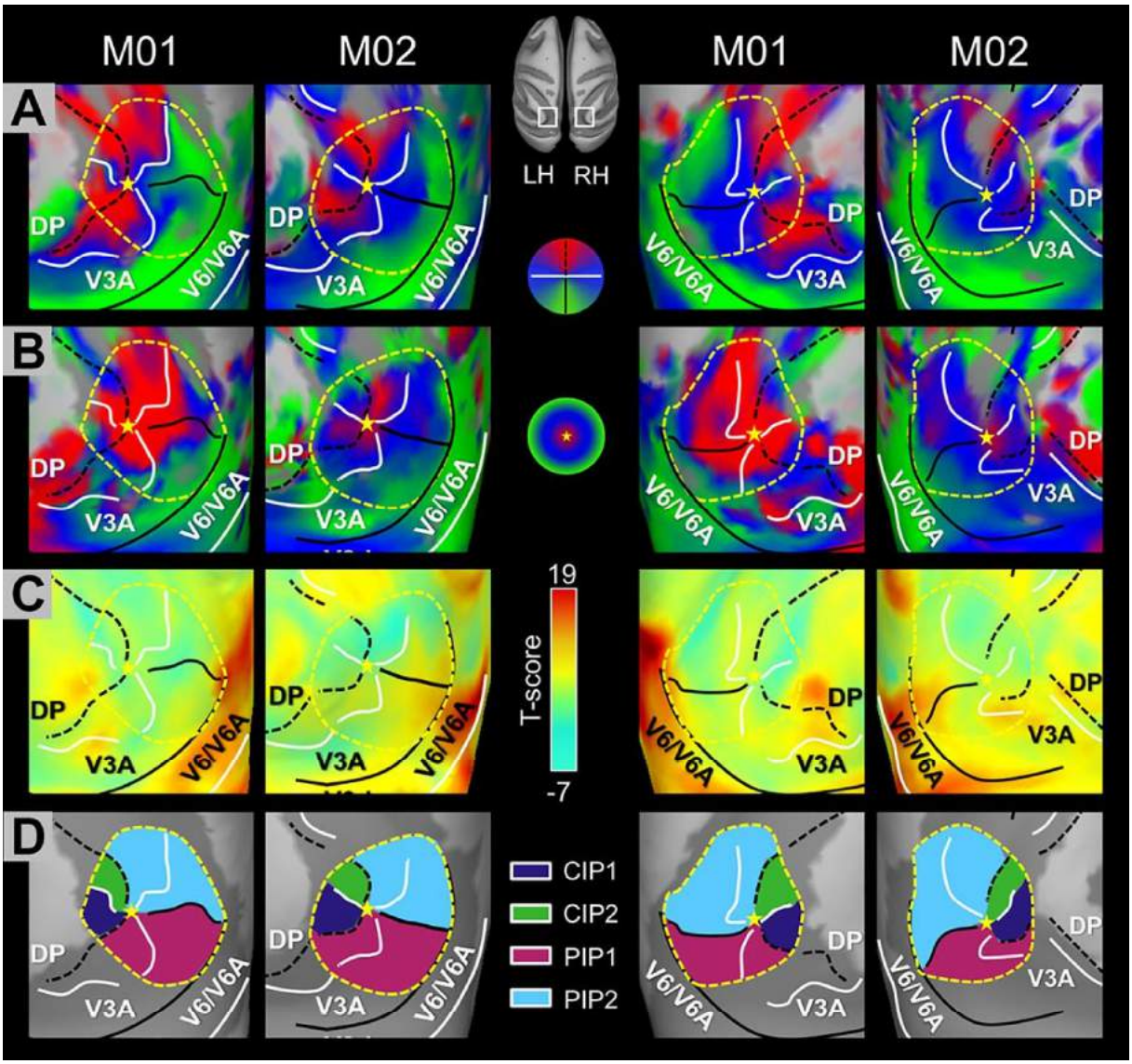

Figure 20. **Functional delineation of the PIP cluster.** In all 4 hemispheres, the PIP cluster defines by its external borders (yellow dotted ellipses), internal frontiers (meridian representations) and foveal confluence (yellow stars) is shown on top of the polar angle map (A), eccentricity map (B), motion sensitivity map (C) and sulci/gyri map (D).

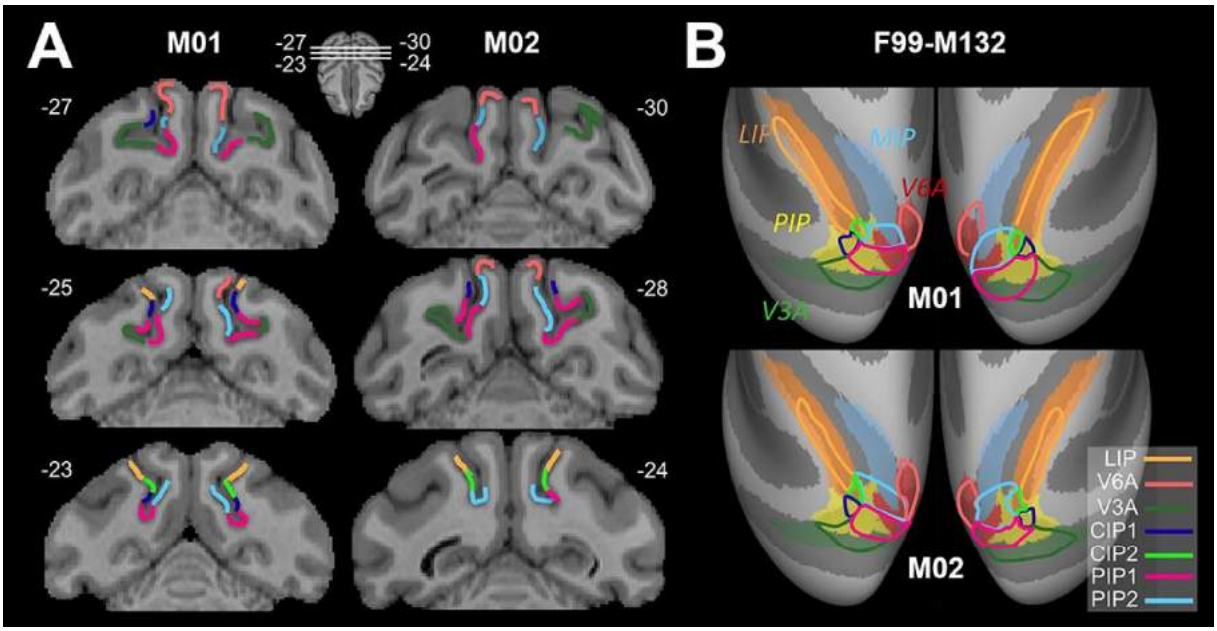

Figure 21. **Anatomical location of the PIP cluster.** (A) Coronal brain slices for M01 (left panels) and M02 (right panels) showing the anatomical location of the PIP cluster and neighbors visuotopic areas. (B) Representation of the same areas for all 4 hemispheres of M01 and M02 on top of some of the areas of the F99-M132 atlas. Our PIP cluster includes most of the atlas defined PIP region, along with the most lateral portion V6A and, to a lesser extent, the most posterior part of MIP.

Table 2. MNI coordinates (x, y, z in mm) and cortical surface coverage (mm2) for the PPC visuotopic areas in the left (LH) and right (RH) hemispheres of M01 and M02.

		LH				RH			
		X	Y	Z	mm2	X	Y	Z	mm2
PIP1	M01	-7	-5	25	42	7	-5	25	42
	M02	-9	-9	24	63	8	-8	25	47
PIP2	M01	-5	-3	28	62	6	-3	28	76
	M02	-6	-9	27	78	6	-8	28	59
CIP1	M01	-7	-6	30	11	8	-5	29	9
	M02	-8	-9	29	14	8	-8	29	8
CIP2	M01	-8	-3	30	18	7	-3	29	12
	M02	-7	-7	29	9	7	-6	30	13
LIP	M01	-14	1	38	62	14	3	31	71
	M02	-11	-3	32	54	12	-2	33	67
V6A	M01	-3	-9	31	56	4	-9	31	43
	M02	-4	-11	33	46	4	-11	33	36

E.3.4 Discussion

By using wide-field retinotopy with fMRI in two behaving macaques, we provide evidence for a new visuotopic cluster in a location previously defined histologically and anatomically as the posterior intra-parietal (PIP) area (Colby et al., 1988; Markov et al., 2014). This PIP cluster includes 4 visuotopic areas sharing a foveal confluence, an organization echoing that of the recently documented MT cluster (Kolster et al., 2009, 2014) and registering into the general category of "cloverleaf" clusters (Brewer and Barton, 2012).

The 2 smallest and lateral-most areas of this cluster, CIP1 and CIP2, have recently been described with classical retinotopy (Arcaro et al., 2011). In accordance with this previous study, we found that they house mainly upper visual field representations and that they are bordered by other visuotopic areas: V3A/DP posteriorly and LIP anteriorly. The 2 largest and medial-most areas, PIP1 and PIP2, are newly discovered areas with complete representations of the contralateral hemi-field. They are bordered posteriorly and medially by V3d/V6/V6A, whose visuotopic organizations are consistent with the descriptions drawn from single cell recordings (Gamberini et al., 2015). By introducing wide-field mapping, the present study complements the previous mapping study of Arcaro and colleagues (2011) and it offers a more exhaustive view of the visuotopic maps paving the PPC, notably by documenting a new visuotopic cluster and its relationship with surrounding visuotopic areas. One can point that in humans too, wide-field mapping has been shown to be necessary for detecting the potential human homologues of V6 (Pitzalis et al., 2006) and V6A (Pitzalis et al., 2013b) .

We have little elements to provide regarding the functional role(s) of CIP1/2 and PIP1/2, except that they do not seem to be particularly involved in processing visual motion, by contrast with the neighboring V6/V6A complex. Future investigations will have to clarify this issue but we can nevertheless speculate that CIP1 and/or CIP2 are likely to process 3D slants defined by binocular

disparity or other depth cues (Tsutsui et al., 2005; Durand et al., 2007; Rosenberg et al., 2013). Interestingly, neurons recorded in a location matching that of CIP1/2 have been shown to possess very large receptive fields (10-30°) (Tsutsui et al., 2005), in good agreement with the PRF sizes found in the present study. However, those single cell recordings failed to note any visuotopic organization, illustrating the higher sensitivity of fMRI for revealing large scale organization of the receptive fields in high-order areas (Patel et al., 2010). Recent findings suggest that PIP1 and/or PIP2 might also be involved in visuospatial functions (Premereur et al., 2015; Van Dromme et al., 2016).

Together, our results demonstrate that in macaques, as in humans, the PPC is largely visuotopic. Further engaging in a direct comparison between the large-scale organization of visuotopic maps between human and monkey PPC would remain very speculative, because the only human studies that have employed wide-field retinotopy have focused on the potential human homologues of V6 (Pitzalis et al., 2006) and V6A (Pitzalis et al., 2013b). We have detected robust motion sensitivity in the piece of parieto-occipital cortex in which V6/V6A have been previously reported. Furthermore, retinotopic mapping provides some elements that help the delineation of these areas. Notably, our data reveals that V6/V6A possess representations of far eccentricities (>20°), that they share borders with V3d and the PIP cluster, and that they are separated by an eccentricity gradient inversion. Non-generalizable, yet non negligible evidence allows us to speculate on a possible demarcation between V6 and V3d: in most hemispheres, the horizontal meridian that constitutes the limit between V2d and V3d is cut by a representation of the UVM. This occurring severance also seems to overlap with the limit of V6's motion sensitivity. Although no safe conclusions can be drawn from this observation, it encourages further investigation. It is interesting to indicate that for most of the visuotopic maps already documented in human PPC, the delineations rely almost exclusively on polar angle gradient inversions, since foveal representations and eccentricity gradients are notoriously ambiguous (Brewer and Barton, 2012). Our study

provides a good illustration that beyond the potential to divulge novel visuotopic maps, wide-field retinotopy also disambiguates the location of foveal representations and the direction of eccentricity gradients.

To conclude, our results deliver the most exhaustive view to date of the visuotopic organization of monkey PPC. They show a dense organization of abutting visual field maps, of which some are arranged in clusters. Generalizing wide-field mapping in both species will undoubtedly contribute to the thorough understanding of these large-scale visuotopic ensembles, which represents an essential step in the quest for establishing the functional homologies between the PPC of human and non-human primates (Orban et al., 2004, 2006; Sereno and Tootell, 2005).

F. Processing of egomotion-consistent optic flow in the rhesus macaque cortex

F.1 Introduction

In macaques, numerous regions of the cerebral cortex contain at least some neurons that are selectively responsive to the direction of motion of a moving visual stimulus. These regions have diverse locations including large parts of the occipital cortex, posterior portions of the temporal cortex, the inferior parietal cortex and even parts of the frontal cortex. Although the most obvious use of sensitivity to image motion is to specify the motion of external objects, it is also valuable for monitoring the animal's own movements. Two cortical regions in particular, the dorsal middle superior temporal area (MSTd) and the ventral intraparietal area (VIP), are associated with the specialized function of encoding visual cues to self-motion. Both contain many neurons that are selectively sensitive to specific components of the optic flow that occurs during self-motion, including direction of heading during locomotion (Tanaka et al., 1989; Duffy and Wurtz, 1991, 1995; Bremmer et al., 2002a). Electrical stimulation of these regions can influence heading judgments (Britten and Wezel, 2002; Zhang and Britten, 2011) suggesting that they contribute directly to perceptual awareness of self-motion, although this has recently been questioned in the case of VIP (Chen et al., 2016). Many MSTd and VIP neurons also receive vestibular input (Duffy et al., 1976; Gu et al., 2006; Chen et al., 2011a) and there is evidence that visual and vestibular cues are efficiently integrated by such neurons, with weightings based on cue reliability (Fetsch et al., 2012). Neurons that appear to encode optic flow have also been identified in Area 7a of the inferior parietal lobule (Motter and Mountcastle, 1981; Steinmetz et al., 1987) and recently in the frontal eye fields (Gu et al., 2015), where again many neurons also respond to vestibular stimuli.

Despite much research, it is not known exactly how visual responses to specific types of optic flow are constructed. The problem has proved challenging and although several sophisticated and biologically plausible models have been proposed (e.g. Perrone and Stone 1994; Grossberg et al. 1999; Yu et al. 2010; Mineault et al. 2012), the computations involved are still debated. However, signals encoding motion, which are initially encoded locally, must be spatially integrated in some

way. Self-motion generates full-field visual stimulation: when the animal moves, the entire retinal image moves. Receptive fields in MSTd and VIP are large enough (typically 10-50 degs, e.g. Komatsu and Wurtz 1988; Schaafsma and Duysens 1996; Mendoza-Halliday et al. 2014) to integrate local motion signals over a wide area, and in some cases a significant proportion of the visual field, but they are not large enough to integrate signals over the entire visual field. The question therefore arises: do the responses of flow-selective neurons having different receptive field locations combine to specify the overall optic flow, and if so how? Visual responses are usually studied with a simulated optic flow stimulus positioned such that all key features of the flow are contained within the receptive field. For example, in the case of expansion (forward motion), the center of expansion is typically placed within the receptive field being examined. The implicit assumption is that single neurons are concerned with optic flow only within their receptive fields and can therefore be expected to respond the same way to a given stimulus irrespective of whether the remainder of the visual field is consistent with the same optic flow. However, this has not been tested empirically and consequently we do not know whether neurons in MST and VIP respond (a) whenever what falls in their purview could be part of full-field optic flow, or (b) only, or at least more strongly, when signals from other parts of the visual field indicate that it actually is part of full-field flow. Whether MSTd and VIP encode optic flow per se, or localized flow components that can be used to derive overall optic flow, is a key unanswered question.

Surprisingly, perhaps, the above question has been better addressed in humans than in macaques. In the human brain, putative homologs of macaque MST (Dukelow et al., 2001; Huk et al., 2002; Kolster et al., 2010) and VIP (Bremmer et al., 2001) have been identified. These have been shown to be involved in encoding optic flow (Smith et al., 2006; Cardin et al., 2012a). Wall and Smith (2008) addressed the question of whether human MST and VIP are active whenever optic flow components are present in the image, or only when full-field flow is present. They presented an array of nine (3x3) optic flow patches. The patches were identical and each contained spiralling

flow that would be expected to provide a good stimulus for a macaque MST neuron if presented in its receptive field. However, the array as a whole was not consistent with self-motion and should not activate neurons that respond selectively to image motion caused by self-motion. Wall and Smith (2008) found that human MST (hMST) responded almost as strongly to the array as to a single large patch of the same total size, suggesting that it is not strongly sensitive to whether or not image motion reflects self-motion. In putative human VIP (pVIP), the response was about half that to a single patch, implying stronger selectivity for self-motion. A more extensive study using the same paradigm (Cardin and Smith, 2010) confirmed these findings and additionally identified two more visually responsive regions that respond at least twice as well to one patch as to an array. One was human V6 (hV6), a region identified in humans only quite recently (Pitzalis et al., 2006) and thought to be the homologue of macaque V6 (Galletti et al., 2001). The other was labelled PIVC (parieto-insular vestibular cortex) but was probably PIC (posterior insular cortex), a visual-vestibular region immediately posterior to human PIVC (Frank et al., 2014) that may be homologous to macaque VPS (Chen et al., 2011b). In macaques, both V6 (Fan et al., 2015) and VPS (Chen et al., 2011b) contain neurons that are tuned for visually simulated direction of heading. In both the above human fMRI studies (Wall and Smith, 2008; Cardin and Smith, 2010), the strongest specificity to visual self-motion occurred in a region not previously studied in any detail, the cingulate sulcus visual area (CSv). Here, a strong response could be elicited by a single optic flow patch but the response was almost completely abolished when an array of optic flow patches was used as substitute. Recent studies (Antal et al., 2008; Fischer et al., 2012) confirm the role of CSv in self-motion processing and an additional piece of evidence implicating CSv in self-motion processing is that it receives vestibular as well as visual input (Smith et al., 2012). Thus, population responses in human visual cortex show a hierarchy of sensitivity to whether the overall visual image is likely to reflect self-motion, from hMST (weakest sensitivity), through hV6 and hVIP (substantial sensitivity), to PIC and CSv (strongest sensitivity).

There have been no single-unit studies in macaques that used either the multi-patch approach or, to our knowledge, any other approach to distinguish responses to true, full-field optic flow from responses to the mere presence of optic flow segments in the receptive field. Before undertaking such studies, it would be valuable to establish with fMRI which macaque visual areas, if any, show such differentiation on a macroscopic scale. This would guide physiological experimentation and also provide a much stronger link with the relevant human fMRI literature. There are numerous important species differences that could make human fMRI studies an unreliable guide to macaque physiology. Not least, area CSv has not been identified in macaques. We have therefore employed the multi-patch paradigm during fMRI in alert fixating macaques with the aim of establishing candidate visual regions for true self-motion specialization, in the sense discussed above.

F.2 Material and methods

F.2.1 Animal model

Three female rhesus macaques: M01, M02, and M03 (age: 5–7 years; weight: 4.5–6.5 kg) were involved in this study. Animal housing, handling, and all experimental protocols (surgery, behavioral training, and MRI (magnetic resonance imaging) recordings) followed the guidelines of the European Union legislation (2010/63/UE) and of the French Ministry of Agriculture (décret 2013–118). The project was approved by a local ethics committee (CNREEA code: C2EA – 14) and received authorization from the French Ministry of Research (MP/03/34/10/09). The 3 animals were housed together in a large, enriched enclosure and could thus develop social and foraging behaviors. They returned to their individual cages to be fed twice a day, with standard primate biscuits supplemented with various types of fruits and vegetables. Health inspections were carried out quarterly on these animals. Details about the animals' surgical preparation and behavioral training are provided in Section C.

F.2.2 Optic flow stimuli

The stimuli were identical to those used in previous human studies (Wall and Smith, 2008; Cardin and Smith, 2010). They consisted of 800 moving dots arranged in an egomotion-consistent (EC) or egomotion-inconsistent (EI) pattern (Figure 22b). The EC condition consisted of a 40° × 40° square field of dots moving in a coherent optic flow pattern containing expansion/contraction and rotation components that varied over time, consistent with self-motion on a varying spiral trajectory (Morrone et al., 2000), displayed at 60 fps. For a given dot with radius r, angle θ and local speed v, its trajectory was defined by:

Equation 7 $$\frac{dr}{dt} = v\cos\phi$$

Equation 8 $$\frac{d\theta}{dt} = (v\sin\phi)/r$$

Radial and angular velocities are defined by dr/dt and dθ/dt, respectively. The direction of optic flow was defined by ϕ, which varied over time from −π to π generating stimuli with radial, circular, and spiral motion. The EI stimulus consisted of a 3 × 3 array of 9 identical panels, each containing a smaller version of the EC stimulus. Although the individual panels contain optic flow, the overall pattern is not consistent with egomotion because flow induced by observer motion can have only one center of motion. In true optic flow stimuli, the size and speed of motion of the features in the image increase with eccentricity. Because the introduction of these scaling factors would result in different distributions of dot size and speed in our 2 stimuli, and potentially spurious results, we kept the dot size, dot speed, and number of dots in the whole array identical across conditions in order to equate low-level visual characteristics. As a result, our stimulus does not accurately simulate "true" optic flow in terms of the scaling of size and speed with eccentricity typical of motion through a cloud of dots. The use of time-varying flow ensured that all locations were stimulated by all dot directions during the stimulus cycle. It also provides larger responses than

continuous expansion because multiple flow-sensitive neurons are stimulated. Finally, it ensures that adaptation at any one local direction is minimal.

F.2.3 MRI recordings

Images were acquired on a 3 Tesla clinical MR scanner (Phillips Achieva) using a custom 8 channel phased array coil (RapidBiomed) specially designed to fit the skull of macaques while preserving their field of view.

F.2.3.1 Recordings for individual templates.

For each individual, anatomical and functional brain templates were built from acquisitions made in a single session on slightly anaesthetised animals (Zoletil 100: 10 mg/kg and Domitor: 0.04 mg/kg). The animals' constants were monitored during the whole session (about 1 hour) with an MR compatible oximeter. During that session, we acquired 4 T1-weighted anatomical volumes (MPRAGE; repetition time [TR] = 10.3 ms; echo time [TE] = 4.6 ms, flip angle = 8°; voxel size = 0.5 x 0.5 x 0.5 mm; 192 slices), and 300 functional volumes (GE-EPI; TR = 2000 ms, TE = 30 ms, flip angle = 90°, SENSE factor = 1.6; voxel size = 1.25 × 1.25 × 1.5 mm, 32 axial slices).

F.2.3.2 Recordings for functional sessions.

The functional scanning sessions were performed on awake behaving animals on a daily basis and lasted for about one hour (8 to 12 runs). EC and EI stimuli were presented using a block-design. Each run consisted of 224s (112 TRs) divided into 7 identical cycles of 32s (16 TRs). In half of the runs, a cycle started with a baseline of 10s (5 TRs) where only the fixation point was present. It was followed by 6s (3 TRs) of the EC condition, then by another 10s of blank and finally by 6s of the EI condition (Figure 22). In the other half of the runs, the EC and EI conditions were reversed within a cycle (i.e. a cycle had 10s of blank, 6s of the EI condition, 10s of blank and finally 6 of the EC condition). Video display and reward for correct fixation were controlled using the V-Cortex software.

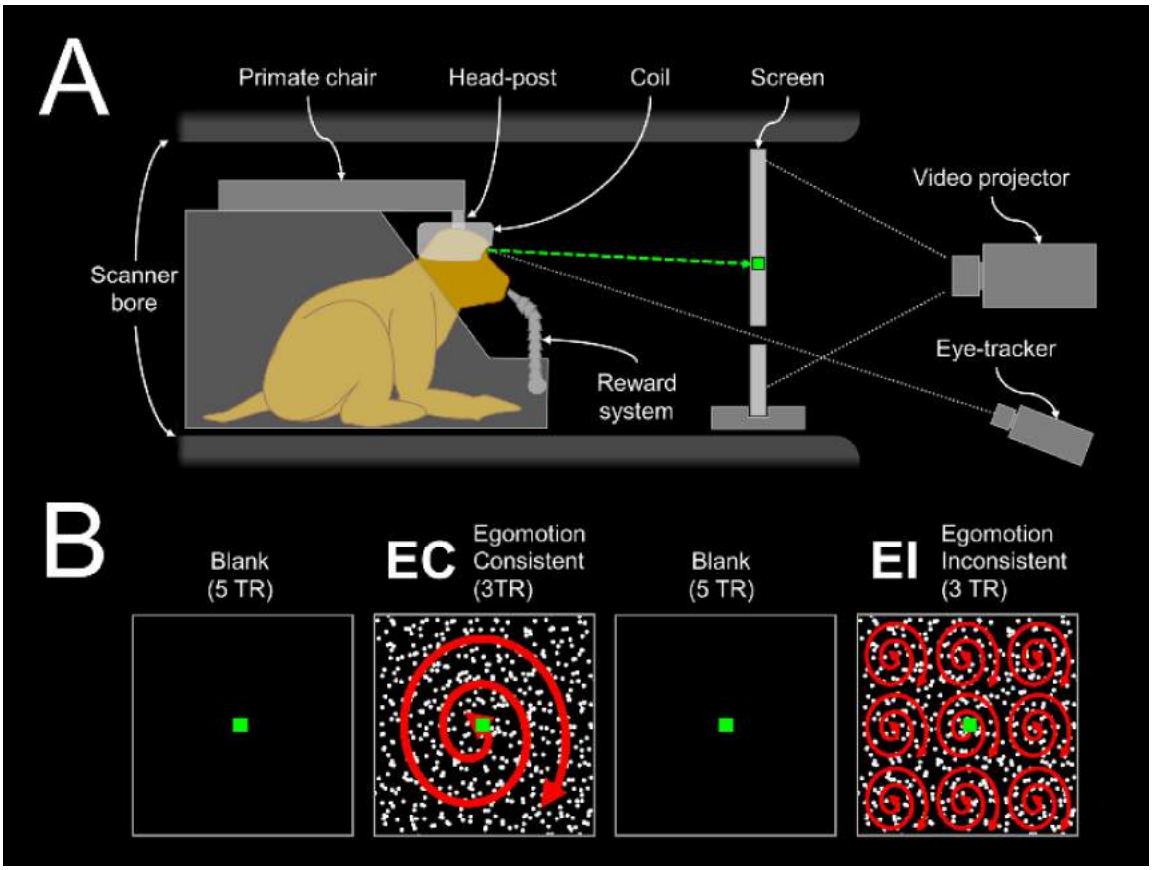

Figure 22. **A. Schematic representation of the monkey fMRI set-up. B. Illustration of the stimuli and experimental design.** The egomotion consistent (EC) stimulus consisted of a square field of dots moving in a coherent optic flow pattern containing expansion/contraction and rotation components that varied over time, consistent with self-motion on a varying spiral trajectory. The egomotion inconsistent (EI) stimulus consisted of a 3 × 3 array of 9 identical panels, each containing a smaller version of the EC stimulus. Recordings were performed using a block design, with the alternation of EC and EI flow stimuli, separated by blank periods. Each run contained 7 repetitions of such blocks (112 TR in total). EC conditions were shown first in half of the runs and EI conditions appeared first in the other half of the runs.

F.2.4 Data processing

F.2.4.1 Preprocessing of the functional data.

In total, 36 runs per animal were kept for further analyses (18 runs with the EC condition first during the blocks and 18 runs with the EI condition first). All those runs were selected based on the quality of fixation (percentage of correct fixation > 85%) to minimize the influence of eye movements in BOLD signal fluctuations for an additional control on the influence of eye position on our results. To control that our results are not corrupted by differences in eye position during the presentations of the egomotion-consistent (EC) and egomotion-inconsistent (EI) optic flow stimuli, we analyzed the percentage of correct fixation (i.e. when the eye position was less than 1° away from the fixation point) during the EC and EI conditions. For each of the 3 monkeys, the distributions of these percentages across runs are provided in Figure 23A. Using paired t-tests, we did not find any significant differences between the distributions corresponding to the EC and EI conditions. To go further, we characterized the stability of eye position during correct fixation for these two conditions. This was done by computing the ratio between the standard deviation of correct eye position during the EC (in blue) or EI (in green) conditions versus during the baseline. The distributions of these fixation ratios across runs are provided in Figure 23B. Here again, paired t-tests did not reveal any significant differences between the ratios corresponding to the 2 conditions. We conclude that the results of our study (i.e. the contrast between the responses to the EC vs EI conditions) are not affected by eye position or fixation stability. Within each run, volumes were rigidly realigned with each other on a slice-by-slice basis using a subpixel cross-correlation algorithm (Guizar-Sicairos et al., 2008). This was followed by slice-time correction. A mean image of the functional volumes was then computed for each run and used for normalization on the functional template of the same individual. Those run-dependent normalization parameters were combined to the run-independent parameters linking the functional template to the anatomical one in a single deformation step, during which the functional volumes were resampled

at 1 x 1 x 1 mm and slightly smoothed with a spatial Gaussian kernel (FWHM = 1.5 x 1.5 x 1.5 mm).

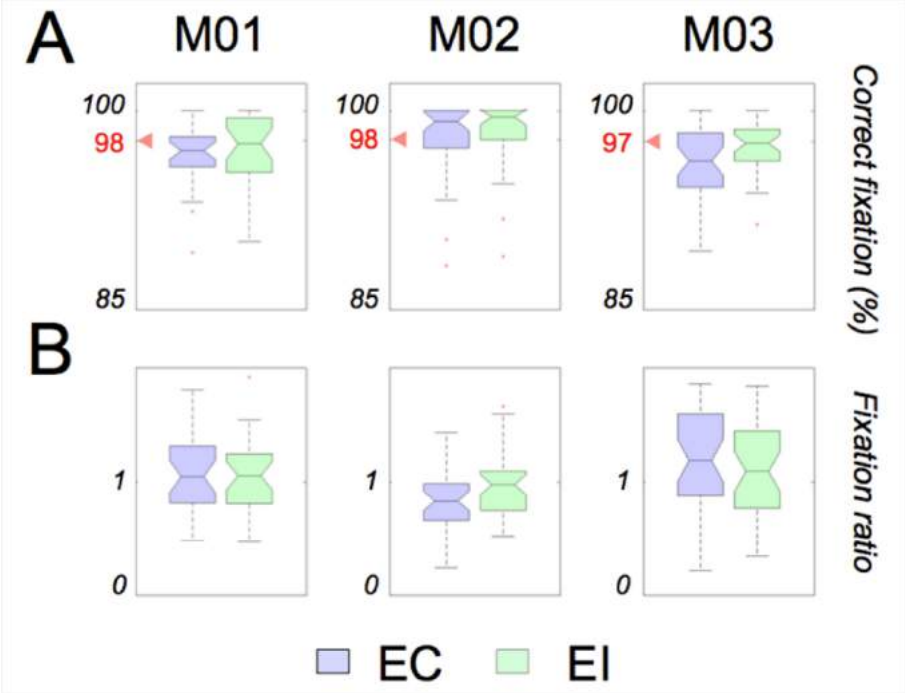

Figure 23. **Ocular fixation and stability of the 3 monkeys during the 2 experimental conditions.** A) Percentage of correct fixation (i.e. less than 1° away from the fixation point) during the EC (in blue) EI conditions. The boxplots give the distribution of these values across runs. Each box provides the 25 and 75 percentiles of the distribution (lower and upper border of the box), its median and the associated 95% intervals. Numbers and arrows in red provide the median values of the percentage of correct fixation during baseline. B) Ratio between the standard deviation of correct eye position during the EC (in blue) or EI (in green) conditions versus during the baseline.

F.2.4.2 General linear model

Voxel-wise statistics were computed by fitting a GLM to the BOLD signal. The model contained 3 main regressors, representing the 3 experimental conditions: EC, EI and blank periods (Figure 22b). Those regressors were convolved with the HRF estimated from each of the 3 monkeys (see Section D). In addition, 4 motion regressors were included in the model. For each run, the slice-by-slice rigid realignment yielded 32 vectors of lateral displacements and 32 vectors of antero-posterior (Y) displacements: one for each slice of the functional volume. The principal component analysis was used to derive 2 lateral and 2 antero-posterior motion regressors, which were entered

in the model as nuisance regressors (Vanduffel and Farivar, 2014). Both the preprocessing steps and GLM analyses were implemented in Matlab, with the SPM12 software and custom scripts.

F.2.4.3 Statistics and results presentation

As a first step for identifying potential regions of interest (i.e. regions with consistent BOLD response differences between the EC and EI conditions), the volumetric statistical parametric maps obtained for the EC>EI and EI>EC contrasts in the individual GLM analyses were thresholded at $p<10^{-3}$ uncorrected (t value > 3.1) and spatially normalized for projection onto the cortical surface of the F99 template. Cortical regions showing significant differences in the same direction between the EC and EI conditions in at least 2 individuals were all considered as potential regions of interest. In a second step, 2 new GLM analyses were performed on each individual after splitting the runs into 2 equal parts (18 runs per GLM, 9 of them with the EC condition first). One GLM was used to look for the presence of individual statistical local maxima in the potential regions of interest or in their immediate vicinity. This search was performed at a relaxed statistical threshold of $p<10^{-2}$ uncorrected. The GLM performed with the other half of the runs was then used to extract the percent BOLD signal changes (PSC) in cubes of 3 x 3 x 3 voxels centered on the local maxima found with the first GLM. This method avoids the "double dipping" that arises when the same data are used both for identifying ROIs and for measuring activity within them. Small cubes were favored over patches determined by anatomical and/or statistical considerations, because anatomical borders between areas are difficult to determine precisely and, as we will see below, our contrasts (EC>EI but also EC+EI>baseline) lead to extended activations that cannot be accurately divided into clusters corresponding to different functional regions.

Our approach is more conservative and avoids subjectivity when dealing with borders between areas. As we will see in the results sections (MNI coordinates provided in Table 3), our local maxima are separated enough that we were able to associate a single local maximum with each region and with no overlap between the cubes corresponding to the different regions. Importantly,

we assessed that the precise size of those cubes (1, 3 or 5 voxels size) did not have significant impact on the extracted results. For these cubes, we estimated percent BOLD signal changes (PSC) for the EC and EI conditions relative to the Blank condition as follows:

Equation 9 $$\mathbf{PSC_{EC}} = \mathbf{100}\left(\frac{\boldsymbol{\beta_{EC}} - \boldsymbol{\beta_{blank}}}{\boldsymbol{\beta_{constant}}}\right)$$

Equation 10 $$\mathbf{PSC_{EC}} = \mathbf{100}\left(\frac{\boldsymbol{\beta_{EI}} - \boldsymbol{\beta_{blank}}}{\boldsymbol{\beta_{constant}}}\right)$$

where β_{EC} β_{EI}, β_{blank} and $\beta_{constant}$ represent the regressor coefficients provided by the GLM analyses. For each region of interest, PSC_{EC} and PSC_{EI} were computed for each run independently, and thus expressed as mean ± standard error across the runs included in the second GLM (18 runs per monkey). Only regions where PSCs were significantly stronger for the EC than for the EI condition (t-tests with p-value < 0.05 and a confidence interval for the difference distribution that does not include 0) were considered for further analysis. Given our number of animals (n=3), there is no statistical test of generalizability. We therefore present the data on each individual and focus on regions that were consistently found in all the macaques (in at least one hemisphere). In these regions, specificity of the BOLD responses to EC versus EI conditions was quantified by computing a sensitivity ratio of the mean PSC_{EC} and PSC_{EI} with the following formula:

Equation 11 $$\boldsymbol{Sensitivity\ Ratio}\ (\%) = \mathbf{100}\left(\frac{\boldsymbol{PSC_{EC} - PSC_{EI}}}{\boldsymbol{PSC_{EC}}}\right)$$

F.2.4.4 Emergence of specificity for consistent versus inconsistent optic flow

To complement our analyses, we seek to better understand how specificity for EC over EI stimuli emerges by comparing our results with sensitivity ratios derived from earlier visual areas. Anatomical regions of interest (ROIs) are available in the Caret software for V1, V2, V3, V3A, MT, FST and V4t, based on the definitions provided by Lewis and Van Essen (2000). These ROIs are shown in Figure 31. For each ROI, we used the first half of the data (see details in the text) to determine all its voxels that were significantly activated by visual stimulation (using the EC + EI > Baseline contrast shown in Figure 24). We then computed the average sensitivity ratio across these voxels on the second half of the data. The results in areas MT, FST, V4T and MST are shown in Figure 27. If preferences for the EC condition exist in MT, V4T and FST (average sensitivity ratios of 13%, 8% and 6% respectively), they remain small and are significantly weaker than those observed in area MSTd (30%, a value that is actually very close to the ratio of 29% obtained with our main analysis). These results confirm that the activations found in the temporal sulcus for the EC > EI contrast more likely correspond to area MSTd and not to neighboring regions. Figure 31C shows the responses obtained in areas V1, V2, V3 and V3A. While V1 seems to marginally prefer the EI condition, this preference is gradually reversed when progressing through V2, V3 and V3A. Even in V3A the ratio is only 8%, so there is little evidence for an EC preference in any of these areas (and none in V1/V2). Also included in Figure 31C is area V6, which is available in Caret based on the definition of Galletti et al. (1999). In this ROI, we found a ratio of 20%. This result suggests that selectivity for the EC condition might exist in V6. However, this selectivity remains not reliable across runs because 1) it did not permit to extract local maxima on the first half of the data for M03 and 2) activations around the local maxima found for M01 and M02 were not significantly stronger for the EC condition in the second half of the data.

F.3 Results

F.3.1 Cortical network involved in processing optic flow

In the present study, monkey fMRI techniques are used to characterize the cortical network involved in processing optic flow signals generated by self-motion in non-human primate. To that end, 3 macaque monkeys were exposed to optic flow stimuli (moving random dots pattern) either consistent or inconsistent with egomotion (EC and EI conditions respectively; see Material and Methods). The experimental design is similar to that developed by Smith and colleagues in their human fMRI studies (Wall and Smith, 2008; Cardin and Smith, 2010), allowing a direct comparison of the cortical networks processing optic flow in the two primate species (Orban, 2002; Orban et al., 2004).

We first assessed the changes in blood-oxygen-level dependent (BOLD) signal evoked by the visual conditions (EC and EI) relative to baseline (blank screen with fixation point only). These flow stimuli were found to elicit strong statistical increases in BOLD signal across most of the visual cortex in all 3 monkeys (Figure 24A), with a very high degree of overlap between individuals (Figure 24B). This first analysis indicates that studying the more specific contrast between the egomotion-consistent and inconsistent conditions is not hampered by a lack of statistical power in any of the individuals. Figure 24A shows the statistical parametric maps (t-values) based on all the available data (36 runs/animal) for the EC versus EI contrast in monkeys M01, M02 and M03, projected on dorsal, lateral and medial views of the individuals left and right cortical hemispheres (see Methods). Hot colors (orange to yellow) indicate significantly stronger BOLD responses for EC than for EI condition ($p<10\text{-}3$ uncorrected), while cold colors (dark to pale blue) signal the opposite. Despite differences in the extent of the activation patterns observed in the 3 animals (e.g. monkey M02 is generally more responsive than monkeys M01 and M03), preference for the consistent flow (EC>EI) defines a cortical network encompassing the occipital, parietal, temporal and frontal lobes in all the monkeys. Many nodes of this network are found consistently across the 3 individuals, as

revealed in Figure 24B by overlapping the activations observed in at least 2 of the 3 individuals after normalization on the F99 template (Van Essen, 2002). Regions color-coded in orange and yellow are those in which EC evokes significantly stronger activations than EI in 2/3 and 3/3 of the monkeys respectively. Regions with stronger activations for the EI condition are color-coded in dark and pale blue, depending on whether they are found in 2 or 3 animals.

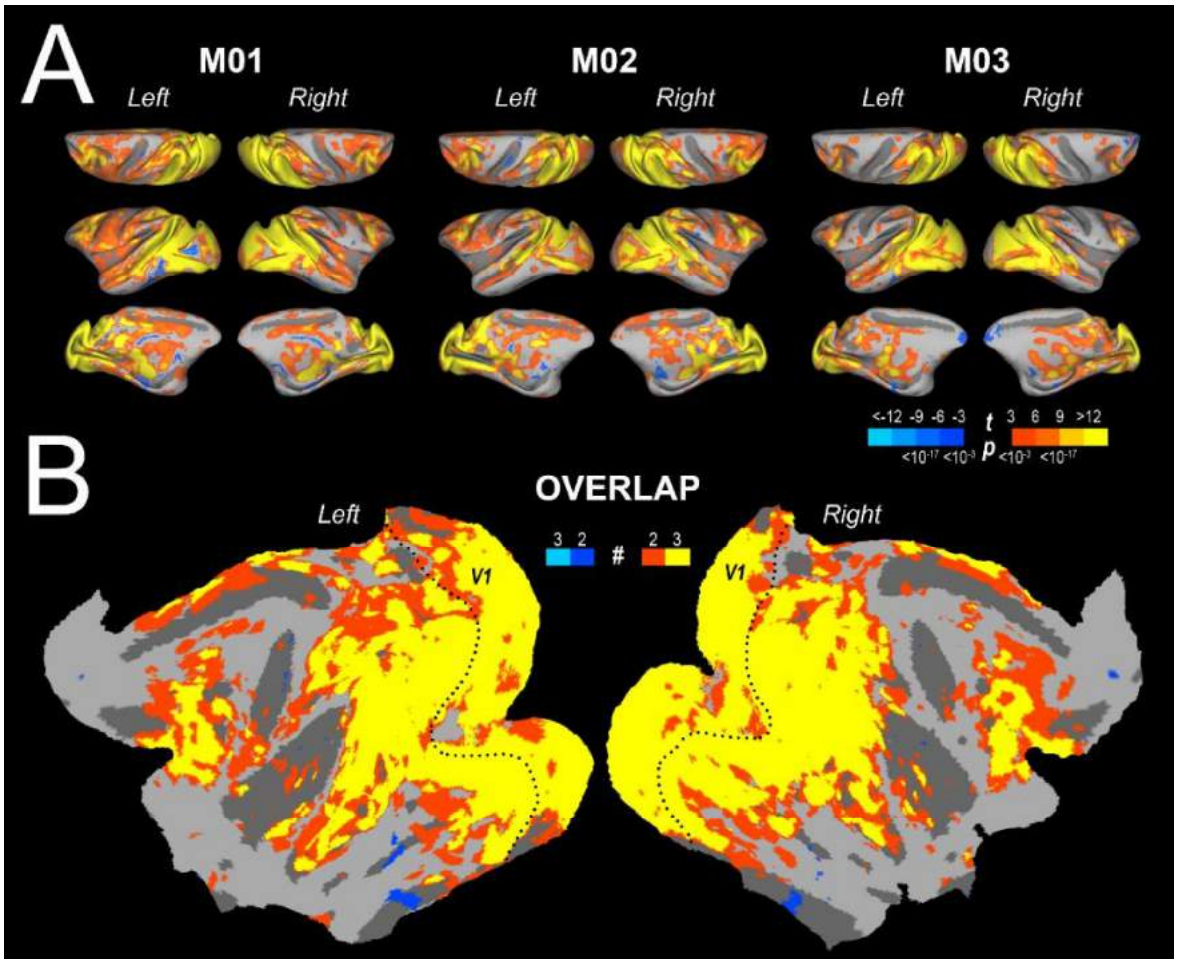

Figure 24. **A. Statistical parametric maps for the contrast Vision (EC+EI) versus Baseline (blank) in monkeys M01, M02 and M03.** Results are projected on dorsal, lateral and medial views of the left and right hemispheres of the individual cortices. The color code reflects the contrast t-values and indicates statistically significant differences in BOLD responses (p<10-3 uncorrected). Hot (orange to yellow) and cold (dark to pale blue) colors indicate stronger responses to Vision and to Baseline respectively. **B. Map of overlap between significant activations in the Vision versus Baseline contrast across the 3 monkeys.** Only activation sites found in at least 2 individuals are shown. Results are projected on the flattened representations of the left and right hemispheres of the F99 template. Orange and yellow indicate cortical sites significantly more activated by Vision than by Baseline in 2/3 and 3/3 of the subjects, respectively. Dark and pale blue show regions more activated during Baseline than during Vision in 2/3 and 3/3 of the subjects, respectively.

ROI	M01			M02			M03			Average		
	x	y	z	x	y	z	x	y	z	x	y	z
MSTd												
L	−18	−2	27	−14	−6	29	−13	−4	24	−15	−4	27
R	16	−1	26	14	−4	29	14	−4	26	15	−3	27
FEFsem												
L	−14	23	27	−15	24	29	−15	26	27	−15	24	28
R	13	23	26	12	25	28	–	–	–	13	24	27
VPS												
L	−17	1	28	−19	−3	29	−15	2	27	−17	1	28
R	17	3	27	20	−2	30	–	–	–	19	1	29
7a												
L	−14	−4	30	−15	−7	32	−15	−6	30	−15	−6	31
R	–	–	–	12	−7	34	17	−5	31	15	−6	33
STPm												
L	–	–	–	−20	1	17	−17	2	17	−19	2	17
R	17	2	18	20	0	18	17	1	20	18	1	19
VIP												
L	−8	3	24	−13	3	29	−11	1	27	−11	2	27
R	13	7	27	13	3	29	9	1	24	12	4	27
LIPd												
L	–	–	–	−15	1	33	−15	1	32	−15	1	33
R	–	–	–	14	2	32	16	2	31	15	2	32
FEFsac												
L	−13	23	22	−19	28	21	−15	27	20	−16	26	21
R	–	–	–	17	25	20	–	–	–	17	25	20
pmCSv												
L	−4	15	28	−3	13	27	−3	15	27	−4	14	27
R	–	–	–	2	16	28	–	–	–	2	16	28

Table 3. **Cortical areas activated in at least 3 animals.** Coordinates in MNI space (mm) are those of the statistical local maxima in the left (L) and right (R) hemispheres. Local maxima were determined from the first half of the data and significant selectivity for the EC condition were evaluated from the second half (see details in the Methods).

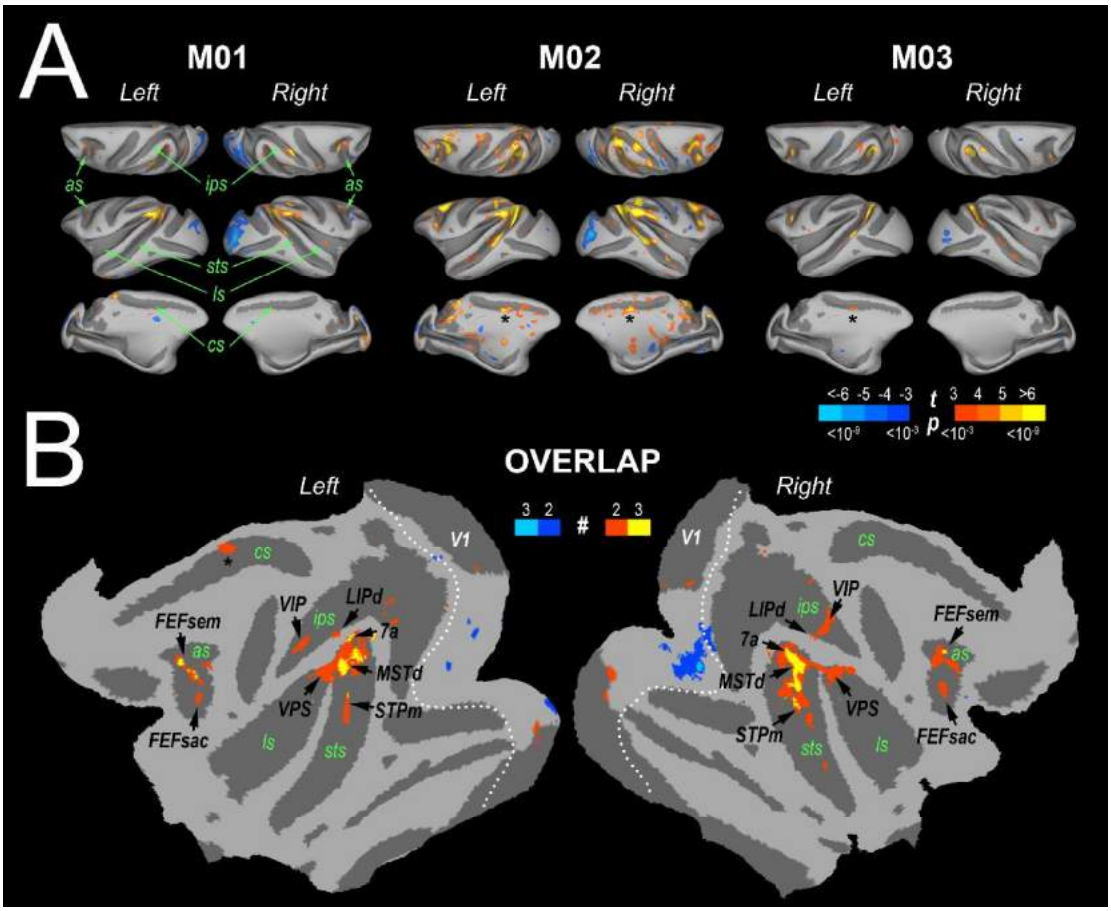

Figure 25. **A. Statistical parametric maps for the EC versus EI contrast in monkeys M01, M02 and M03**. Results are projected on dorsal, lateral and medial views of the left and right hemispheres of the individual cortices. The color code reflects the contrast t-values and indicates statistically significant differences between BOLD responses evoked by the EC and EI conditions (p<10-3 uncorrected). Hot (orange to yellow) and cold (dark to pale blue) colors indicate stronger responses to EC and to EI respectively. **B. Map of overlap between significant activations in the EC versus EI contrast across the 3 monkeys.** Only activation sites found in at least 2 individuals are shown. Results are projected on the flattened representations of the left and right hemispheres of the F99 template. Orange and yellow indicate cortical sites significantly more activated by EC than by EI in 2/3 and 3/3 of the subjects, respectively. Dark and pale blue show regions more activated by EI than by EC in 2/3 and 3/3 of the subjects, respectively. Seven cortical were significantly activated in our three macaques: MSTd, 7a, STPm, VIP, VPS, FEFsem and FEFsac. Black stars indicate a region of the cingulate sulcus (pmCSv) that was found in the three animals in the left hemisphere and in one animal on the right hemisphere. White stars indicate a region of the parieto-occipital sulcus (POS) were significant activations were found in two animals. Borders of the primary visual area (V1) are shown as white dotted lines (Lewis and Van Essen, 2000). (as: arcuate sulcus; cs: cingulate sulcus; ips: intraparietal sulcus; ls: lateral sulcus; sts: superior temporal sulcus).

We chose a relaxed threshold to avoid the risk of false negatives while using only half of the full dataset. However, the robustness of those activation sites was tested by running paired t-tests on the BOLD signal change profiles obtained at the same sites in the EC and EI conditions in the other half of the runs. In the following, we describe the activation sites that were identified with the above method in at least one hemisphere in each of the 3 individuals. Two cortical activation sites were found to prefer egomotion-consistent flow (EC) in both hemispheres of all our macaques. The most significant one according to the EC versus EI contrast (i.e. global statistical maximum in all 6 hemispheres) was located in the dorso-caudal portion of the superior temporal sulcus (STS), a location corresponding to the dorsal Medial Superior Temporal (MSTd) area. The second site, located within the intra-parietal sulcus, matches the location of the Ventral Intra-Parietal area (VIP). Both MSTd and VIP areas have been repeatedly shown to play a central role in optic flow processing. Note that for VIP, the activation found in M03 did not overlap those found in M01 and M02, although the local maxima were very close between the 3 animals (see Figure 25B).

Four other sites were observed in 5 out of 6 hemispheres. One of them was found in the caudal portion of the lateral sulcus (ls), in a location matching that of the Visual Posterior Sylvian area (VPS; Chen et al. 2011b). Another site was located dorsally in the arcuate sulcus (as), in a portion of the Frontal Eye Field involved in smooth pursuit eye movements (FEFsem) and also recently shown to house neurons responsive to optic flow stimuli (Gu et al., 2015). The third site, in the postero-ventral portion of the inferior parietal lobule, slightly above MSTd, seems to correspond to posterior area 7a, a region that is known to contain neurons that respond to optic flow (e.g. Siegel & Reid, 1997). Finally, the fourth site lay in the fundus of the STS, anterior to MSTd. This could be part of the superior temporal polysensory area (STP), which also contains motion-sensitive cells with large receptive fields (e.g. Bruce et al. 1981), although STP occupies primarily

the upper bank of the sulcus. We tentatively refer to it as STPm after Nelissen et al. (2006) who report motion-sensitive activity at a similar location with fMRI.

Two further sites were found in all three individuals, but less reliably across hemispheres (in 4 out of 6 hemispheres). One of them was located in the arcuate sulcus, slightly more anterior and lateral than FEFsem, in a location described as a portion of the Frontal Eye Field involved in saccadic eye movements (FEFsac; Gu et al. 2015). Finally, consistent activations were observed within the postero-ventral lip of the cingulate sulcus (black asterisks in Figure 25A and Figure 25B), in a region which had not been documented previously as being involved in optic flow processing in monkeys. However, the location of this region echoes that of the recently discovered Cingulate Sulcus visual (CSv) area in human, which has been shown to be highly selective for the egomotion-compatible optic flow stimuli used in the present study (Wall and Smith, 2008; Cardin and Smith, 2010). For that reason, we will refer to this cingulate activation site as putative macaque homologue of CSv (pmCSv; see Figure 25B). Overlapping activations and corresponding local maxima were also identified in 2 out of 3 animals along the dorsal lip of the intra-parietal sulcus (LIPd) and within the parieto-occiptal sulcus (pos; white asterisks in Figure 25B). However, only the LIPd maxima were associated with significant differences between the BOLD signals evoked by the EC and EI conditions in both animals. MNI coordinates of the statistical local maxima for the different areas described above are provided in Table 3. Note that we also found consistent responses for the EI>EC contrast, but they remained largely restricted to the early visual cortex (see blue patches in 24B). These activations are not caused by local motion characteristics since they are well matched between the two conditions. They might be due to the detection of kinetic boundaries (Reppas et al., 1997).

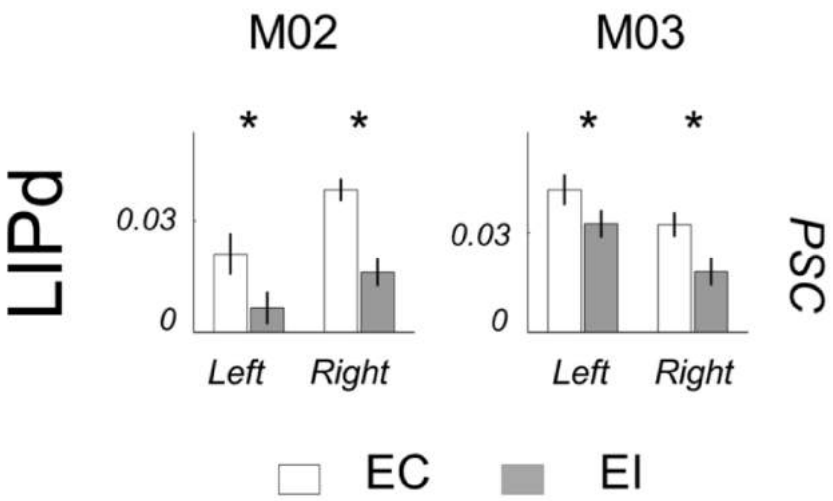

Figure 26. **Activity profiles in area LIPd.** Percent BOLD signal for the EC and EI conditions with respect to baseline. Other details as in Figure 25.

F.3.2 Quantitative analysis of egomotion selectivity

In the following, we characterize in more detail the BOLD response profiles in the cortical regions enumerated above. For each region, the statistical local maximum was localized based on the GLMs performed in half of the runs for each monkey. The response profiles were estimated with the GLMs performed on the other half of the runs (see Materials and Methods). These response profiles correspond to the average responses within cubes of 27 (3 × 3 × 3) voxels centered on the local max- ima localized on the first GLMs. Figure 28 and Figure 29 show the percentage of BOLD signal changes evoked by the EC and EI conditions with respect to the Blank condition within the 8 areas that were activated in all 3 individuals (areas MSTd, VIP, VPS, FEFsem, 7a, STPm, FEFsac, and pmCSv). Voxel-wise statistical parametric maps obtained for the EC > EI contrast in each individual, superimposed on horizontal sections of the individual anatomical templates, are shown in Figure 28A (areas MSTd, VPS, VIP, pmCSV, and FEFsem), 29A (area 7a), and 29C (areas STPm and FEFsac). Their corresponding BOLD profiles are presented in Figure 28B, Figure 29B and D. The asterisks above the profiles indicate statistically significant differences (paired t-test, $P < 10-2$) between the BOLD responses evoked by the EC (white bars) and EI (gray bars) conditions. The percentages of BOLD signal change in area LIPd are shown in Figure 27 for the 2 animals (M02

and M03) that had significantly stronger responses for the EC than for the EI condition in this area. In order to characterize the strengths of the BOLD responses elicited by the EC stimulus relative to those evoked by the EI stimulus, we computed a sensitivity ratio (in percentage) between the percentages of signal change obtained for these 2 conditions relative to baseline (see the "Materials and Methods" section). These ratios are shown in Figure 30A for all the 8 areas reported above and their respective locations are illustrated on the cortical surface of the F99 template in Figure 30B (the positions of these ROIs on the individual cortical surfaces are provided in Figure 31A). In Figure 31A, the areas are ranked from the highest to the lowest specificity for the EC condition. This analysis reveals that 2 regions, pmCSv and VPS, emerge as being clearly the most specific for flow stimuli compatible with egomotion, with a near absence of BOLD responses evoked by the egomotion-incompatible stimuli (see also Figure 29B). In both regions, the mean ratio (across the 3 animals) was above 70% (77% in pmCSv and 70% in VPS), revealing a nearly 4 times larger response for the egomotion-compatible stimuli. Ratios were much lower but still impressive in areas VIP (43%), FEFsac (43%), and FEFsem (39%), and lower still in MSTd (29%), 7a (21%), and STPm (15%). In LIPd (not shown because it was found in only 2 of the 3 individuals), we observed an intermediate ratio of 47%. Note that these sensitivity ratios are robust to changes in the size of the cubes used to define the ROIs (see Figure 31B). Finally, we estimated differential sensitivity to egomotion-compatible flow within a number of pre-defined visual ROIs taken from the Caret atlas. This enabled us to cross-check our results for regions such as MSTd and also to check that in visual regions such as V1–V3 and MT, where specificity is not expected, it is not seen. The results, shown in Figure 31, confirmed that selectivity for EC stimuli is seen in MSTd but not in MT, FST (Fundus of the Superior Temporal sulcus), or V4t and was not seen in V1–V3 or V3A. V6 showed weak selectivity (see Discussion).

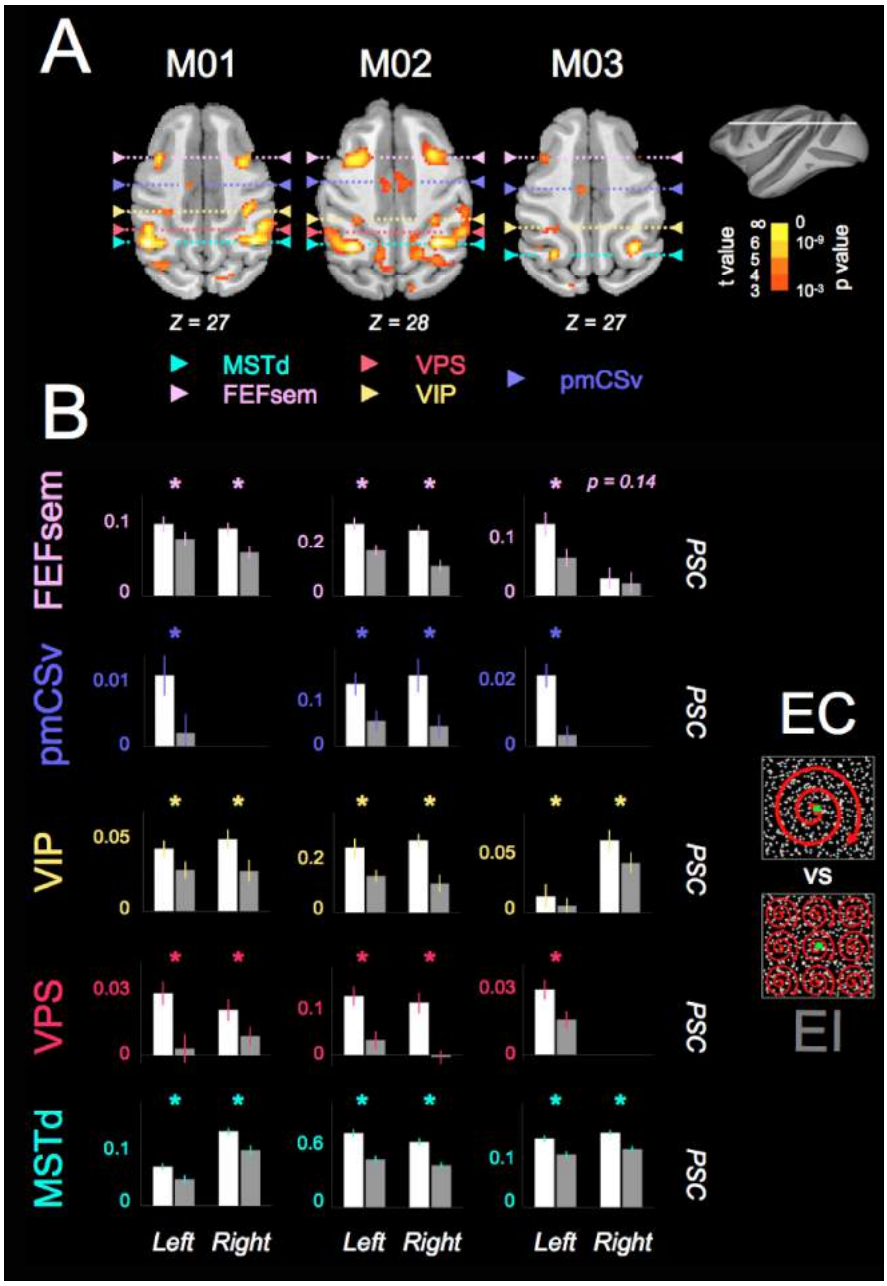

Figure 27. **Activity profiles in areas MSTd, VPS, VIP, pmCSv and FEFsem.** A. Statistical results of the EC>EI contrast shown on axial sections for monkeys M01, M02 and M03 (neurological convention). Areas are indicated by arrows on the 3 monkeys. B. Percent BOLD signal change (PSC) in these 5 areas for the EC and EI conditions with respect to baseline (blank condition) in both hemispheres of the 3 macaques. The first half of the data was used to define ROIs around the local maxima of these areas and the second half was used to compute PSC (see details in the text). The error bars provide the standard errors across runs (n = 36). Stars indicate areas whose PSCs during the EC condition were significantly stronger than during the EI condition (t-tests, $p < 0.05$). P-values of the t-tests are provided for areas that did not pass significance.

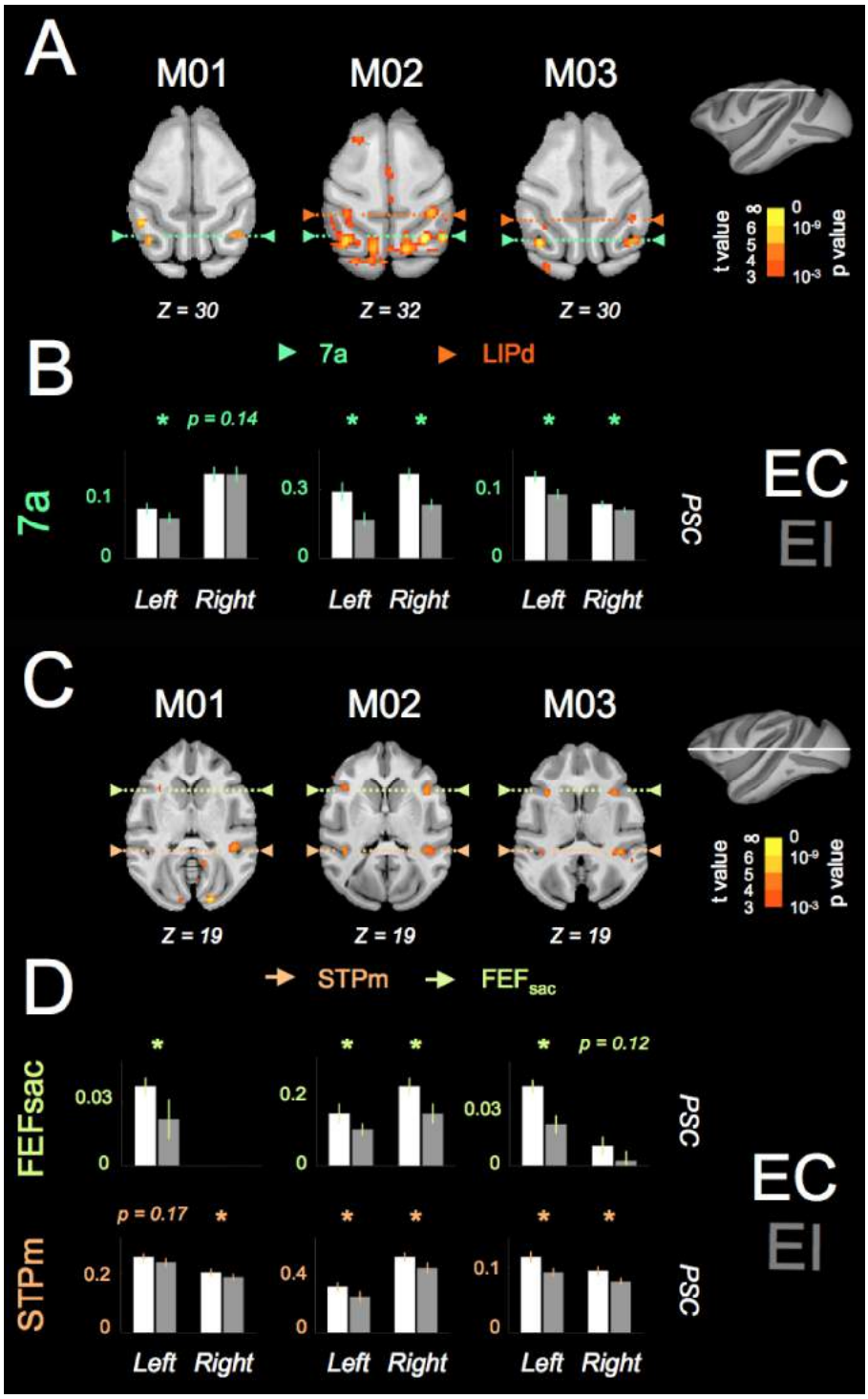

Figure 28. **Activity profiles in areas 7a, FEFsac and STPm.** A. Statistical results of the EC>EI contrast shown on axial sections for the 3 monkeys. Areas 7a (in all monkeys) and LIPd (in M02 and M03) are indicated by arrows. B. Percent BOLD signal change in area 7a for the EC and EI conditions with respect to baseline. C. Statistical results of the EC>EI contrast shown on axial sections for the 3 monkeys. Areas STPm and FEFsac are indicated by arrows. D. Percent BOLD signal change in areas FEFsac and STPm for the EC and EI conditions with respect to baseline.

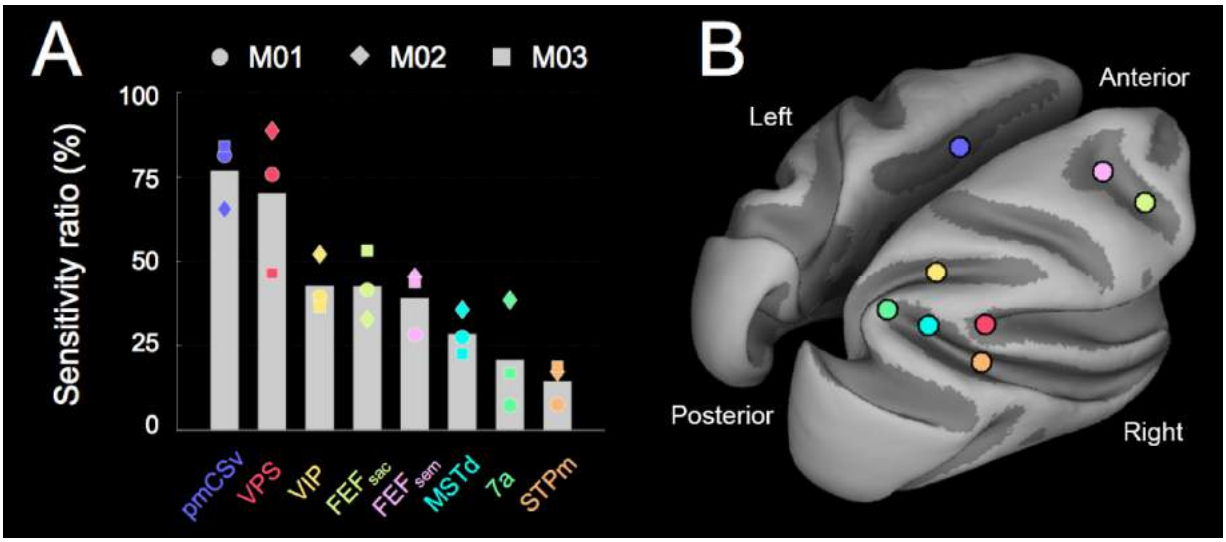

Figure 29. **A. Average sensitivity ratio (%) between the responses to the EC and EI conditions.** The ratio (defined in the text) may be thought of as the reduction in response that occurs when an EC stimulus is replaced with EI. As for the percent BOLD signal change, ratios were computed on the second half of the data (see details in the text). Only areas with significant responses in the three animals are shown. Areas were sorted according to their mean sensitivity ratio. Markers provide the individual data corresponding to M01 (circles), M02 (diamonds) and M03 (squares). **B. Schematic localization of the 8 areas on the F99 template.**

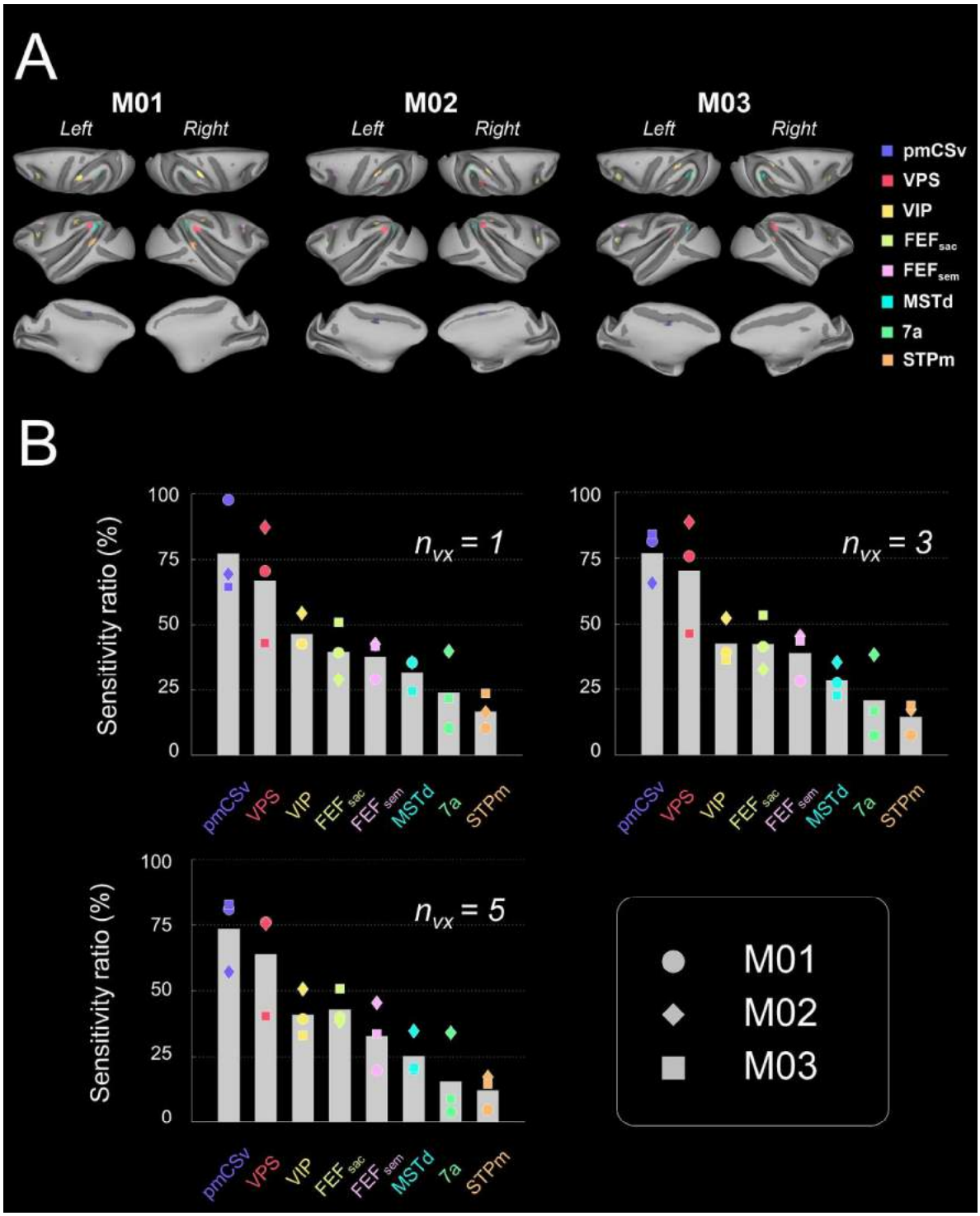

Figure 30. **A. Projection of the ROIs on the individual surfaces of each macaque. B. Average sensitivity ratio (%) between the responses to the EC and EI conditions for different area sizes.** Areas were defined from cubes of 1x1x1 voxel (1mm^3 with voxels resampled at 1x1x1, n_{vx} = 1) in the upper-left panel, 3x3x3 voxels (27 mm^3, n_{vx} = 3) in the upper-right panel and 5x5x5 voxels (125 mm^3, n_{vx} = 5) in the lower-left panel. See figure 5 for the details of the legend.

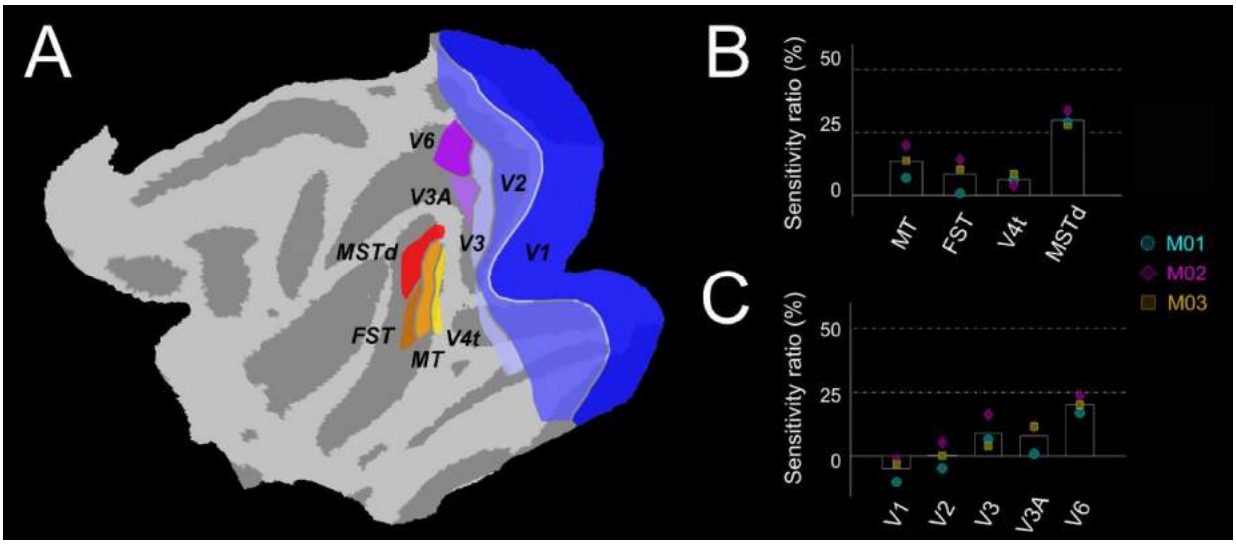

Figure 31. **Average sensitivity ratio (%) between the responses to the EC and EI conditions across anatomical ROIs.** A. Representation of the anatomical ROIs used in the present analysis. These ROIs are available in the Caret software for the F99 template, and are based on the works of Lewis and VanEssen (2000; for V1, V2, V3, V3A, MT, V4t, FST and MSTd) and Galletti and colleagues (1999; for V6). B. Mean sensitivity profiles across the voxels belonging to MT, FST, V4t and MSTd. The color code is the same as that of Figure 5. C. Idem for V1, V2, V3, V3A and V6.

F.4 Discussion

F.4.1 Overview

The aim of present study was to identify, in non-human primates, the cortical areas involved in processing visual motion produced by self-displacements, i.e. egomotion-consistent optic flow. To that end, we recorded whole-brain BOLD responses from 3 behaving macaques while they were exposed to optic flow stimuli either consistent or inconsistent with egomotion (Figure 22). The visual stimuli and experimental design were similar to those used in previous human fMRI studies (Wall and Smith, 2008; Cardin and Smith, 2010), allowing a direct comparison of the cortical networks between human and non-human primates. Our results reveal that in macaque, as in human, many cortical areas are more strongly activated by egomotion-consistent optic flow stimuli. Those regions are broadly distributed, encompassing the temporal, parietal, frontal and cingulate cortices (Figure 26). They are now discussed in more detail.

F.4.2 Activations in temporal cortex: MSTd and STPm

In all 6 recorded hemispheres, the most statistically significant activations for the contrast between egomotion consistent and inconsistent stimuli was found in a dorso-caudal portion of the superior temporal sulcus, which corresponds in macaque to area MSTd (Figure 26). In order to check that these activations were well localized in MSTd and did not overlap with adjacent areas like MT, FST or V4t, we performed an additional analysis from anatomical atlases provided in the Caret software (see Figure 32). This analysis confirmed that our activations are specific to MSTd. Numerous electrophysiological studies have shown that MSTd houses neurons selective to optic flow stimuli presented in their receptive fields (e.g. Tanaka et al. 1989; Duffy and Wurtz 1991), as well as to inertial vestibular stimulation (e.g. Duffy 1998; Takahashi et al. 2007). Moreover, both microstimulation and reversible inactivation indicate a causal role for MSTd in heading perception (Britten and Wezel, 2002; Gu et al., 2012). Together, these characteristics point to a central role for MSTd in processing visual motion produced by self-displacements. Our data also revealed that the

sensitivity ratio between responses to consistent and inconsistent flow stimuli is not very high (29%; see Figure 30), suggesting that flow stimuli that are not consistent with self-displacements can nevertheless evoke strong responses in MSTd neurons. Interestingly, our results are in broad agreement with those obtained in human area MST (hMST) using the same experimental protocol (Wall and Smith, 2008). These authors reported about 15% reduction in response to incompatible flow in hMST, compared to about 30% found here in macaque MSTd. This difference is consistent and could reflect a species difference, suggesting greater specialization in macaque than human MST. However, it should be remembered that hMST in humans, which is defined simply in terms of the presence of strong ipsilateral drive (absent in hMT), probably does not correspond exactly to MSTd and may include other motion-sensitive regions with large receptive fields. It is therefore unsafe to make a direct comparison of results. Our results leave open the possibility that hMST, or some part of it, is homologous with MSTd for optic flow processing.

Another temporal activation site was observed in all the animals (5/6 hemispheres), situated more anteriorly along the fundus and the dorsal lip of the superior temporal sulcus. This site may correspond to a sub-region of the superior temporal polysensory (STP) area, in which neurons selective to optic flow stimuli have been reported (Bruce et al., 1981; Anderson and Siegel, 1999), although neurophysiological studies describe STP as located in the upper bank and fundus of STS whereas our cases show activity mainly in the lower bank (Figure 26B), albeit with overlap across animals mainly in the fundus (Figure 26B). In a recent monkey fMRI study, Nelissen and colleagues (2006) confirmed the existence of an optic-flow sensitive region in STP, that they named STPm and whose location is close to that found in the present study (Figure 26), although again STPm is mainly in the upper bank of the sulcus. Interestingly, Nelissen and colleagues noted that responses to optic flow stimuli in STPm are similar to those of MSTd, except that the amplitude is lower. This difference is also found in the present study, together with a slightly lower sensitivity ratio (15%) of STPm. In human, a region within the superior temporal sulcus (STS) and anterior to the

hMT+ complex has been recently proposed as a putative homologue of macaque STP (Beauchamp et al., 2004b; Smith et al., 2012). This region was named STSms (superior temporal sulcus multi-sensory) because of its multi-sensory responses (Beauchamp et al., 2004a, 2004b, 2008). Among other modalities, STSms is activated by visual (Beauchamp et al., 2004b) and vestibular (Smith et al., 2012) signals. Therefore, it might be involved in the processing of egomotion-consistent optic flow. However, STSms was not significantly activated by our contrast in two human studies based on the same experimental protocol (Wall and Smith, 2008; Cardin and Smith, 2010). How can this be explained? One possibility might be simply that differential activity was missed in human STSms because of sensitivity limitations (e.g. the human studies used considerably fewer stimulus repetitions). Another is that STSms is not in fact homologous with STPm, or is broadly homologous but differs in its degree of specialization. Further investigations will be needed to clarify this point.

F.4.3 Activations in parietal cortex: VIP, 7a and LIPd

In our 3 animals (6/6 hemispheres), we found statistically significant activation for the egomotion-consistent versus egomotion-inconsistent contrast in the fundus of the intraparietal sulcus, which houses area VIP in macaque (Figure 28). Together with MSTd, VIP is generally considered as playing a central role in processing heading information provided by both visual and vestibular signals (Bremmer et al., 2002a, 2002b). VIP and MSTd neurons seem to share many characteristics in the way they code both visual and inertial movements (Schaafsma and Duysens, 1996; Chen et al., 2011a). However, the mean sensitivity ratio we measured in VIP (43%) was greater than that found in MSTd (Figure 30). In human, the same contrast significantly activates a region within the anterior part of the intra-parietal sulcus (see e.g. Wall and Smith, 2008) whose coordinates are very close to those of the polysensory motion sensitive area originally described by Bremmer and colleagues (Bremmer et al., 2001) and proposed as a putative homologue of macaque VIP (hVIP). Wall & Smith (2008) reported a 46% response reduction for EI stimuli, very similar to our result

for macaque VIP. Our data are therefore consistent with the hypothesis of a correspondence between these two areas, although caution is needed because the intraparietal sulcus is organized differently in humans and macaques, with several more areas in humans.

Besides VIP, a consistent site of parietal activation, observed in all our monkeys (5/6 hemispheres), was located within area 7a, which occupies an elongated posterior portion of the inferior parietal lobule (Figure 29). Area 7a is involved in spatial vision, through the integration of visual and oculomotor signals (Mishkin et al., 1982; Anderson and Siegel, 1999). Both electrophysiological and optical imaging studies have shown that 7a neurons respond selectively to optic flow stimuli (Siegel and Read, 1997; Phinney and Siegel, 2000; Merchant et al., 2001; Raffi and Siegel, 2007). More recently, cytoarchitectonic differences along the inferior parietal lobule have led to its subdivision into 4 sectors: PF, PFG, PG and Opt (Pandya and Seltzer, 1982; Gregoriou et al., 2006). The posterior location of our activation site, together with the fact that it extends ventrally into the dorsal bank of the superior temporal sulcus, strongly suggest that it corresponds to the caudal-most region Opt (Gregoriou et al., 2006). Interestingly, tracer injections in Opt (Rozzi et al., 2006) revealed strong connections with the temporal areas that we found to be involved in processing egomotion-compatible optic flow: MSTd and STP, and much weaker connections with the neighbouring temporal areas MT and FST. The same study revealed that Opt is also connected to LIP in the intra-parietal sulcus and to area 23, in the cingulate sulcus, two sites that also responded more strongly to consistent than inconsistent optic flow stimuli in a majority of recorded hemispheres, as will be discussed below.

The dorsal part of the lateral intraparietal (LIPd) area was the third site of parietal activation evidenced in the present study (see Figure 28). Results were less systematic than those of area 7a/Opt, with 4 out of 6 hemispheres, but closely resembled those found in VIP (with an average sensitivity ratio of 47%). To our knowledge, there is no previous study linking LIPd to the specific processing of egomotion-compatible optic flow. However, the present results, together with the

fact that LIPd is connected to 7a/Opt, argue that the possible role of LIPd in optic flow processing deserves further investigation.

Several studies have reported the existence of a possible homologue of macaque area LIP in the human superior parietal cortex (Sereno et al., 2001; Shikata et al., 2008). To our knowledge, the human homologue of area 7a has not been firmly established. In any case, the only robust and reliable activations that were found near intra-parietal sulcus in human using the same protocol corresponded to area hVIP (see above). Our results therefore suggest that processing of optic flow in 7a (and LIPd, if confirmed) may be specific to macaque.

F.4.4 Activation in parieto-insular cortex: VPS

In our 3 individuals (5/6 hemispheres) stronger BOLD responses for the egomotion-consistent optic flow stimuli were observed in the caudal portion of the sylvian fissure (Figure 28). The location of this activation site corresponds to the visual posterior sylvian (VPS) area, which is posterior to the parieto-insular vestibular cortex (PIVC) from which it receives vestibular inputs. VPS is also connected to MSTd (Guldin et al., 1992), which may feed VPS with visual optic flow information. In agreement with this view, VPS neurons have been shown to integrate heading-related information from both visual optic-flow and vestibular signals (Chen et al., 2011b). Importantly, our results revealed that after pmCSv, VPS is actually the cortical region exhibiting the greatest sensitivity ratio for egomotion-consistent stimuli (70%, see Figure 30), much higher than those found in the temporal and parietal activation sites described so far. In human, the same contrast (Cardin and Smith, 2010) also revealed a parieto-insular region, PIC (that was originally mistakenly labelled as PIVC), sharing most of the properties described here for VPS and notably its responsiveness to vestibular inputs (Smith et al., 2012). The sensitivity ratio in PIC is very high (~80%; Cardin and Smith, 2010) and close to the one we found in macaque VPS. Altogether, these results further support the idea that these two regions are homologous.

F.4.5 Activations in frontal cortex: FEFsem and FEFsac

In 3 animals (5/6 hemispheres), strong activations were found in the dorsal part of the arcuate sulcus (Figure 3). This location matches that of FEFsem, a sub-region of the frontal eye field involved in the control of smooth pursuit eye movements (Lynch, 1987; MacAvoy et al., 1991). The average sensitivity ratio we found in FEFsem (39%) was about the same as those of MSTd, VIP and 7a/Opt, which all share strong recurrent connections with FEFsem (Boussaoud et al., 1990; Maioli et al., 1998; Stanton et al., 2005). Recently, FEFsem neurons have been shown to respond selectively to visual and vestibular signals induced by self-displacements (Gu et al., 2015). Thus, the present results provide further evidence that FEFsem processes heading information.

In 4/6 hemispheres, (3 individuals), a second site of activation was observed within the arcuate sulcus. Located slightly more anterior and lateral than FEFsem, within the fundus and anterior branch of the arcuate sulcus (Figure 29), it nicely fits the anatomical location reported for another sub-region of the frontal eye field, FEFsac, which is involved in saccadic eye movements (MacAvoy et al., 1991; Gu et al., 2015). Our analyses of eye movements reveal differences neither in the quality of fixation nor in the number of saccades evoked by egomotion consistent and inconsistent stimuli, in any of the 3 individuals (see Figure 24). Thus, the present results argue for a secondary role of FEFsac in the processing of visual motion induced by self-displacements.

In human, studies that used the same experimental protocol (Wall and Smith, 2008; Cardin and Smith, 2010) did not report any significant activation in or around the frontal eye field region. A re-examination of these data revealed that a few subjects (<20%) actually had significant responses in FEF. This low proportion makes it difficult to determine whether these activations were false positive. Either way, this comparison across species supports the idea that the implication of the FEFsem and FEFsac regions in optic flow processing is at least more pronounced in macaque.

F.4.6 Activation in cingulate cortex: pmCSv

In human, a growing number of fMRI studies have described a region within the cingulate sulcus, CSv, which is significantly activated by complex motion patterns (Wall and Smith, 2008; Fischer et al., 2012; Pitzalis et al., 2013a; Schindler and Bartels, 2016). Using the stimuli of the present study, Cardin and Smith (2010) reported that this region had the greatest specificity for egomotion-consistent optic flow, in virtually all the tested subjects. In all our animals (4/6 hemispheres), we measured strong responses in the posterior cingulate sulcus (Figure 28). Atlas-based comparison in Caret software indicates that this activation site belongs to area 23c (Vogt et al., 2005), which is thought to be involved in spatial vision notably through its connection to area 7a/Opt (Vogt et al., 1992; Rozzi et al., 2006). A striking feature of the activity profiles for the 4 significant hemispheres is the near absence of response to egomotion-inconsistent stimuli which leads to a very high sensitivity ratio (77%, see figure 5), as has been found in human CSv (Wall and Smith, 2008). Although other studies will be needed to confirm the possible homology between pmCSV and CSv, the identification of pmCSv provides new opportunities to understand activations in human CSv by reference to electrophysiological explorations in macaque.

F.4.7 Homologies with the human EC-selective areas V6, Pc and 2v?

In human, the contrast used in this study leads to consistent activations in the parieto-occipital cortex (Cardin and Smith, 2010), in a site that both retinotopic mapping and response properties point to as the human homologue of macaque area V6 (Pitzalis et al., 2006, 2010; Cardin et al., 2012b). In the present study, our voxel-wise analysis did not reveal any evidence that V6 prefers egomotion-consistent optic flow. However, a suggestive trend was observed in the atlas-based approach which shows a sensitivity ratio for V6 of about 20% that is consistent across the 3 animals. This leaves open the possibility that V6 does possess EC selectivity but that this was not reliable enough to be detected at the voxel level. It is also possible that there is no such selectivity and the trend arises from erroneous inclusion of parts of neighboring visual regions, although the immediate neighbors V2, V3 and V3A do not themselves show strong specificity. Whatever the

explanation, our results indicate that selectivity to the EC condition in macaque V6 is not as robust as in human V6. One possible interpretation of this discrepancy might be that human and monkey V6 differ regarding their involvement in heading processing, the involvement being greater in humans. More generally, this observation reinforces the view that the cortical processing of visual motion might differ in several aspects between these 2 primate species (Vanduffel et al., 2002; Orban et al., 2003).

Finally, it should be noted that two other human cortical regions have been reported to show selective responses to EC stimuli (Cardin & Smith, 2010) that do not appear to do so in macaque. The first is a possible homologue of macaque area 2v in anterior parietal cortex, which has been shown to receive vestibular afferents and may therefore process self-motion. The second is an anterior region of the precuneus, termed Pc by these authors. Since little is known about either region, it is difficult to interpret these differences. At least in Pc, and possibly also in putative human 2v, the difference between EC and EI reflects differences in visual suppression rather than visual responses.

F.5 Conclusion

Overall, our results are in excellent agreement with the electrophysiological and anatomical data collected over recent decades in macaque monkey. They demonstrate that a simple contrast between **optic** flow stimuli that are consistent or inconsistent with self-displacements can reveal the vast majority of cortical areas known to be involved in processing heading information through optic flow, including those also thought to integrate vestibular inputs. An advantage of the monkey fMRI approach is that it allows a direct comparison with results obtained in several human studies based on the same contrast (Wall and Smith, 2008; Cardin and Smith 2010). Together, the data collected in the two species suggest that although the networks processing optic flow in human and macaque share some properties (i.e. possible homologies between areas MST/hMST,

VIP/hVIP, VPS/PIC and pmCSv/CSv), they nonetheless remain different. On the one hand, some of the significantly activated areas in macaque (7a, STPm, FEFsem and also FEFsac) were not found in human. On the other hand, some areas robustly found in humans (V6, P2v, Pc) did not show significant activations in the present study.

G.General discussion & Conclusion

G.1 Summary of results

The goal of this thesis was to investigate the visuotopic organization the dorsal visual pathway and its sensitivity to optic flow in macaque monkeys using fMRI. To reach this objective we secured many milestones to develop the monkey fMRI technique in Toulouse and implement routine procedures of surgery, conditioning and data acquisition and processing. The technique was then used to conduct 3 studies. The first study used a visual impulse and a Fourrier analysis to isolate visually responsive voxels from which we modeled HRF responses for each monkey individually. In the second study, we used wide-field retinotopy with behaviorally salient 2D stimuli coupled with surface based analysis of population receptive fields, to uncover a novel cluster within the posterior parietal cortex. This new PIP cluster includes 2 previously described regions CIP1/2 ((Arcaro et al., 2011) and 2 new regions PIP1/2. The third study characterized the functional network involved in processing egomotion compatible optic flow. The revealed network comprised of an extended set of cortical areas: MSTd, VIP, VPS, pmCSv, STPm, 7a and LIP, echoing that described in humans with the same protocol.

G.2 Considerations pertaining to the awake monkey fMRI technique

My involvement in the implementation of the monkey fMRI technique in our lab revealed important insight on the obstacles that one most probably will encounter when embarking on such an endeavor. It is thus elementary that I provide some recommendations. A crucial element for monkey conditioning is to insure a constant, secure and comfortable work environment for both the researcher and the monkey. Any stressful factors, such as unrecognized noise and smells can hinder monkey conditioning. Furthermore, novel objects, stimuli and procedures must be introduced progressively, otherwise it will distract the monkey quite a bit. Another key factor in monkey conditioning for fMRI, which is common to any research with behaving animals, is knowledge of the animal's motivating drive. The precise control of water intake and the animal's

weight are default solutions to manipulating a monkey's motivation to perform a task. Some monkeys do not require water scheduling, as finding the proper reward, such as sweet juice, which would be exclusively delivered during task performance, is enough to make them cooperate fully. Monkeys should also be exposed lengthily to the MR environment, to gain confidence and perform required tasks without being on edge.

Another important variable, which some seek to reduce as much as possible is the time of post-surgical recovery. Enough post-surgical time is not only required for proper healing of surgery wounds, but also for consolidating the skull implant. The necessary time for implant consolidation also allows the monkey to become habituated to its new body part, thus integrating it to its schema, which reduces collisions with its surrounding environment. Furthermore, the animal is likely to fidget with the cement and the wound. Such behavior shouldn't be a problem as long as it doesn't hinder proper healing. Otherwise, one could consider fitting the monkey with a thermoplastic helmet which restricts the animal's access to the implant. By ensuring enough time for healing, maximum contact between cement and skull, proper screw length and maintenance, a skull implant can last well beyond 5 years.

The skull implant is a practical and efficient solution for immobilizing a monkey's head. Nevertheless, it remains an invasive method that exposes the animal to dangers of infection of bone corrosion. Ideally, it would be desirable to shift from a skull implant to a non-invasive head holding apparatus. Many labs around the world have tried implementing such a device. Howell and colleagues developed a plastic helmet filled with expandable foam that fits snugly to the monkey's head. This method allowed PET scanning of alert monkey (Howell et al., 2001). The drawback of this method is that the foaming did not allow visual stimulation. Another study used a custom-fitted plastic helmet (Srihasam et al., 2010), a chin strap and mild suction supplied by a vacuum blower to immobilize the monkey's head during scanning. Although the authors state that the immobilization was comparable to a conventional skull implant, the suction device remains a heavy

apparatus and a stressful factor for the monkey. A recent paper published by Slater and colleagues, describes a non-invasive head immobilization system that makes use of individual custom face masks (Slater et al., 2016). The face mask can be used in combination with a rear mask to make a full helmet. Their facemask was integrated into an automated voluntary training system, that allowed the monkey to familiarize with the apparatus at its own pace. Results of comparison with existing methods indicate that comparable immobilization capabilities with tradition skull implants. The apparatus seems to be highly advantageous if no invasive neuronal recordings are required. This system could well be an alternative to surgical implants for fMRI scanning. Our team is also developing similar equipment designed to restrain head movement within the horizontal primate chair.

A significant dilemma we faced was the use of contrast agents. While the norm of the field is to conduct IRON imaging in monkeys, we could demonstrate that acquiring a reliable BOLD signal with high SNR is possible with a multichannel phase array, monkey head coil. Not being obliged to use dangerous chemicals constituted a relief. Indeed, in addition to the prohibitive price and its restricted availability, the daily injections of MION and chelation agent are stressful for animals and can become an inconvenience, especially when certain subjects have small veins. Furthermore, excess iron deposits in the brain become a health hazard for the animal. Healthy animals are cooperative animals, and being able to maintain a healthy animal for as many experiments as possible is a major benefit because a lot of time and resources are invested to have reliable data from an animal. Animals that gain experience, are animals that are easier to train to perform new tasks, they are less likely to move in the scanner, and provide data that is less contaminated by noise. Animals that are kept for a long time are also good candidates for longitudinal studies, as one can imagine studying the evolution of cortical visual maps and functional networks as the animal gets older.

G.3 Considerations pertaining to the measurement of the HRF

The HRF study provided important insight on the BOLD HRF of monkeys and its necessity for proper analysis of fMRI data. Results show that monkey HRF is quite different from that of humans, and that it also varies across individuals of the same species. An accurate estimation of the HRF model can make all the difference in detecting functional areas and visuotopic maps. One must note though, that we are estimating a monkey HRF model from the average activity of voxels that where significantly activated by the visual impulse. Nevertheless, vasculature is quite different across areas of the visual cortex, which implies that each voxel possesses its own hemodynamic signature. Applying a meticulous method would mean defining a model of the HRF for each voxel in the brain, or at least for each cortical area, and for different visual impulse latencies, and presentation eccentricities. This will have to be done in the future if one wants to exploit optimally the monkey fMRI approach.

G.4 Considerations pertaining to the visuotopic mapping of the dorsal visual pathway

The results of this study bring a fresh view to the organization of the posterior parietal cortex. The newly uncovered maps in the PPC provide additional proof that visually activated areas that are higher in the chain of visual processing must conserve the visuotopic organization of the lower areas, although coarser, and that revealing the maps requires a reassessment of the nature and size of the stimulus, as well as the analysis method. These results partly agree with the current understanding of the organization of the monkey PPC. On one hand, they confirm the locations and visuotopic organization of the V6/V6A complex, and its location relatively to V3d (Gamberini et al., 2015). On the other hand, there is a clear discrepancy with the definition of the ventral part of V6A as branching into V3A (Gamberini et al., 2011; Pitzalis et al., 2013b), since it interposes between these two regions the newly discovered PIP cluster. The new PIP cluster is in good

matching with the area defined by ((Colby et al., 1988). Settling for one alternative requires the definition of the functional differences between the neighboring areas. As expected our motion localizer revealed motion sensitivity for V6/V6A but not for the PIP cluster. CIP and PIP have been demonstrated to be involved in the processing of 3D structure and position (Durand et al., 2007). The same study shows that a small area of PIP also shows sensitivity to structural depth from motion. A recent study (Van Dromme et al., 2016), investigated the interaction between area CIP and the inferior temporal cortex (ITC), by combining focal perturbations of CIP (reversible inactivation and electrical microstimulation). They reveal that the inactivation of CIP caused a perceptual deficit in a depth-structure categorization task. Moreover, they provide evidence of decreased fMRI activations in the PPC caused by the inactivation of CIP. Surprisingly, concomitant reduction of activation was also observed in ITC. This study corroborates the initial findings of Durand et al. (2007) et demonstrates the complementarity of fMRI and focal perturbations.

The use of wide-field retinotopy can be modified to include more complex shapes, motion and stereoscopic depth components to drive other visually responsive areas. Possibilities include but are not limited to the use of slanted wedges and rings, to appear that the wedges are rotating either close to or away from the subject, and rings expanding towards or away from them. Previous studies used faces to create the probabilistic maps of face processing areas (Janssens et al., 2014) and videos to map higher order areas such as V6 (Pitzalis et al., 2006).

Further research should investigate in detail the functional properties of the areas of this cluster.

G.5 Considerations pertaining to the motion sensitivity of the dorsal visual pathway.

Mapping the visuotopic organization of the dorsal visual stream does not provide information about the functional properties of this subsystem, we thus sought to investigate the functional network processing optic flow that is coherent with self-motion in macaques. We employed a similar paradigm previously used in humans to investigate the same network. The comparison of human and monkey networks revealed homologies but also striking differences, with the notable lack of activation in macaque V6. Nevertheless, V6 was found to be motion sensitive (Fattori et al., 2009) using our motion localizer, and it could be mapped using wide-field retinotopy except for its border with V3d. Another notable difference between macaques and humans in motion processing along the dorsal pathway is area V3A, which is much more motion sensitive in the latter than in the former (Orban et al., 2003).

To speculate on the origin of such differences, one must bear in mind that macaques and humans move around differently. A normally walking human being will rarely witness rapid translational optic flow, as most of a human's displacements are done on foot, or in vehicles with front facing apertures, which means that the point of focus of the optic flow on the retina virtually constant, unless sudden changes of direction occur. On the other hand, macaques rarely spend time on the ground and mostly travel between levels of different heights. Which implies that in addition to witnessing an expanding component of optic flow, the translational (up/down, side-to-side) and rotational components are very present. Thus, compared to humans the point of focus of the optic flow on the retina changes a lot during the macaque's movement. This difference in the frequency of alternation between one focal point and the other may explain some of the discrepancies in the functional network processing optic-flow that is coherent with self-motion. To simulate more natural stimuli of self-motion consistent optic flow, one could devise an apparatus, mounted on

human or monkey subjects, with stereoscopic cameras that would record videos while the subject is naturally moving around. Stereoscopic optic flow can then be derived from the videos and presented to subjects while recording fMRI signals.

G.6 Perspectives

In the future, my main objective would be to use the monkey fMRI technique in conjunction with invasive methods, as I have done during my Master's thesis. Mainly, I would like to continue the investigation on the effect of reward on perception. One prospective experiment would be to specifically target dopaminergic neurons in the VTA of the macaque monkey using optogenetics, where fMRI would be used to precisely target this area. Some questions I am eager to answer are, how does the optogenetic stimulation of VTA (VTA-OS) affects visual perception? Can VTA-OS affect perceptual learning? If so, how? How is the dopamine projection network involved in visual decision-making and reinforcement learning? Can this knowledge help us build better neural networks?

If dopaminergic stimulation had an impact on visual perception, this could be measured behaviorally through multiple tests of psychophysics, ranging from simple discrimination tasks, to the ability to control dominant percepts during monocular and binocular rivalry. The confirmation of such effects would encourage the use of concomitant VTA-OS and retinotopic mapping to tell us more about how dopaminergic projections may affect the cortical encoding of visual space. Furthermore, one could combine VTA-OS with electrophysiological recordings to inspect the effect of dopaminergic projections on information processing at the level of a single neuron or a small population of neurons. The possibilities are endless, and the limit of our knowledge of the brain can be pushed by combining all available techniques. Creativity is also essential.

H.Bibliography

Aguirre GK, Zarahn E, D'Esposito M (1998) The Variability of Human, BOLD Hemodynamic Responses. Neuroimage 8:360–369 Available at: http://linkinghub.elsevier.com/retrieve/pii/S105381199890369X.

Alvarez I, de Haas B, Clark CA, Rees G, Schwarzkopf DS (2015) Comparing different stimulus configurations for population receptive field mapping in human fMRI. Front Hum Neurosci 9:96 Available at: http://journal.frontiersin.org/article/10.3389/fnhum.2015.00096/abstract.

Amano K, Wandell BA, Dumoulin SO (2009) Visual Field Maps, Population Receptive Field Sizes, and Visual Field Coverage in the Human MT+ Complex. J Neurophysiol 102:2704–2718 Available at: http://www.ncbi.nlm.nih.gov/pmc/articles/PMC2777836/.

Andersen RA, Asanuma C, Essick G, Siegel RM (1990) Corticocortical connections of anatomically and physiologically defined subdivisions within the inferior parietal lobule. J Comp Neurol 296:65–113.

Andersen RA, Musallam S, Pesaran B (2004) Selecting the signals for a brain-machine interface. Curr Opin Neurobiol 14:720–726.

Anderson KC, Siegel RM (1999) Optic flow selectivity in the anterior superior temporal polysensory area, STPa, of the behaving monkey. J Neurosci 19:2681–2692.

Antal A, Baudewig J, Paulus W, Dechent P (2008) The posterior cingulate cortex and planum temporale/parietal operculum are activated by coherent visual motion. Vis Neurosci 25:17–26.

Arcaro MJ, Pinsk MA, Li X, Kastner S (2011) Visuotopic organization of macaque posterior parietal cortex: a functional magnetic resonance imaging study. J Neurosci 31:2064–2078 Available at: http://www.ncbi.nlm.nih.gov/entrez/query.fcgi?cmd=Retrieve&db=PubMed&dopt=Citation&list_uids=21307244.

Arsenault JT, Rima S, Stemmann H, Vanduffel W (2014) Role of the primate ventral tegmental area in reinforcement and motivation. Curr Biol 24:1347–1353 Available at: http://www.ncbi.nlm.nih.gov/pubmed/24881876 [Accessed September 27, 2014].

Attwell D, Iadecola C (2002) The neural basis of functional brain imaging signals. Trends Neurosci 25:621–625 Available at: http://www.ncbi.nlm.nih.gov/pubmed/12446129.

Attwell D, Laughlin SB (2001) An Energy Budget for Signaling in the Grey Matter of the Brain. J Cereb Blood Flow Metab:1133–1145 Available at: http://jcb.sagepub.com/lookup/doi/10.1097/00004647-200110000-00001.

Bailey J, Taylor K (2016) Non-human primates in neuroscience research : The case against its scientific necessity Non-human Primates in Neuroscience Research : The Case Against its Scientific Necessity. Altern to Lab Anim 44:43–69.

Bandettini PA, Jesmanowicz A, Wong EC, Hyde JS (1993) Processing strategies for time-course data sets in functional MRI of the human brain. Magn Reson Med 30:161–173.

Bartels a, Zeki S (2000) The architecture of the colour centre in the human visual brain: new results and a review. Eur J Neurosci 12:172–193.

Beauchamp MS, Argall BD, Bodurka J, Duyn JH, Martin A (2004a) Unraveling multisensory integration: patchy organization within human STS multisensory cortex. Nat Neurosci 7:1190–1192.

Beauchamp MS, Lee KE, Argall BD, Martin A (2004b) Integration of Auditory and Visual Information about Objects in Superior Temporal Sulcus. Neuron 41:809–823.

Beauchamp MS, Yasar NE, Frye RE, Ro T (2008) Touch, sound and vision in human superior temporal sulcus. Neuroimage 41:1011–1020.

Ben Hamed S, Duhamel JR, Bremmer F, Graf W (2001) Representation of the visual field in the lateral intraparietal area of macaque monkeys: a quantitative receptive field analysis. ExpBrain Res 140:127–144.

Bird CM, Castelli F, Malik O, Frith U, Husain M (2004) The impact of extensive medial frontal lobe damage on "Theory of Mind" and cognition. Brain 127:914–928.

Blatt GJ, Andersen RA, Stoner GR (1990) Visual receptive field organization and cortico-cortical connections of the lateral intraparietal area (area LIP) in the macaque. J Comp Neurol 299:421–445 Available at: http://dx.doi.org/10.1002/cne.902990404.

Boussaoud D, Ungerleider LG, Desimone R (1990) Pathways for motion analysis: Cortical connections of the medial superior temporal and fundus of the superior temporal visual areas in the macaque. J Comp Neurol 296:462–495.

Boynton GM, Engel SA, Glover GH, Heeger DJ (1996) Linear systems analysis of functional magnetic resonance imaging in human V1. J Neurosci 16:4207–4221.

Bremmer F, Duhamel J-R, Ben Hamed S, Graf W (2002a) Heading encoding in the macaque ventral intraparietal

area (VIP). Eur J Neurosci 16:1554–1568.

Bremmer F, Klam F, Duhamel J-R, Ben Hamed S, Graf W (2002b) Visual-vestibular interactive responses in the macaque ventral intraparietal area (VIP). Eur J Neurosci 16:1569–1586.

Bremmer F, Schlack A, Shah NJ, Zafiris O, Kubischik M, Hoffmann K-P, Zilles K, Fink GR (2001) Polymodal Motion Processing in Posterior Parietal and Premotor Cortex: A Human fMRI Study Strongly Implies Equivalencies between Humans and Monkeys. Neuron 29:287–296.

Brewer A a, Barton B (2012) Visual Field Map Organization in Human Visual Cortex. Vis Cortex - Curr Status Perspect:29–60.

Bridge H (2011) Mapping the visual brain: how and why. Eye 25:291–296 Available at: http://www.nature.com/doifinder/10.1038/eye.2010.166.

Britten KH, Wezel RJA van (2002) Area MST and Heading Perception in Macaque Monkeys. Cereb Cortex 12:692–701.

Bruce C, Desimone R, Gross CG (1981) Visual properties of neurons in a polysensory area in superior temporal sulcus of the macaque. J Neurophysiol 46:369–384.

Buneo CA, Andersen RA (2006) The posterior parietal cortex: Sensorimotor interface for the planning and online control of visually guided movements. Neuropsychologia 44:2594–2606.

Cardin V, Hemsworth L, Smith AT (2012a) Adaptation to heading direction dissociates the roles of human MST and V6 in the processing of optic flow. J Neurophysiol 108:794–801.

Cardin V, Sherrington R, Hemsworth L, Smith AT (2012b) Human V6: Functional Characterisation and Localisation Yacoub E, ed. PLoS One 7:e47685.

Cardin V, Smith AT (2010) Sensitivity of human visual and vestibular cortical regions to egomotion-compatible visual stimulation. Cereb Cortex 20:1964–1973 Available at: http://cercor.oxfordjournals.org/content/20/8/1964 [Accessed May 29, 2015].

Carmena JM, Lebedev MA, Crist RE, O'Doherty JE, Santucci DM, Dimitrov DF, Patil PG, Henriquez CS, Nicolelis MAL (2003) Learning to control a brain-machine interface for reaching and grasping by primates. PLoS Biol 1.

Chafee M V, Goldman-Rakic PS (2000) Inactivation of parietal and prefrontal cortex reveals interdependence of

neural activity during memory-guided saccades. J Neurophysiol 83:1550–1566 Available at: http://www.ncbi.nlm.nih.gov/pubmed/10712479.

Chen A, DeAngelis GC, Angelaki DE (2011a) Representation of vestibular and visual cues to self-motion in ventral intraparietal cortex. J Neurosci 31:12036–12052.

Chen A, DeAngelis GC, Angelaki DE (2011b) Convergence of vestibular and visual self-motion signals in an area of the posterior sylvian fissure. J Neurosci 31:11617–11627.

Chen A, Gu Y, Liu S, DeAngelis GC, Angelaki DE (2016) Evidence for a Causal Contribution of Macaque Vestibular, But Not Intraparietal, Cortex to Heading Perception. J Neurosci 36:3789–3798.

Cheng K, Waggoner R a, Tanaka K (2001) Human ocular dominance columns as revealed by high-field functional magnetic resonance imaging. Neuron 32:359–374.

Christel MI, Billard A (2001) Article in press. 0:1–16.

Cohen D (1968) Magnetoencephalography: Evidence of Magnetic Fields Produced by Alpha-Rhythm Currents. Science (80-) 161:784 LP-786 Available at: http://science.sciencemag.org/content/161/3843/784.abstract.

Colby CL, Gattass R, Olson CR, Gross CG (1988) Topographical organization of cortical afferents to extrastriate visual area PO in the macaque: a dual tracer study. J Comp Neurol 269:392–413.

Cowan WM, Harter DH, Kandel ER (2000) The Emergence of Modern Neuroscience: Some Implications for Neurology and Psychiatry. Annu Rev Neurosci 23:343–391 Available at: http://www.annualreviews.org/doi/10.1146/annurev.neuro.23.1.343.

Dale AM, Fischl B, Sereno MI (1999) Cortical surface-based analysis. I. Segmentation and surface reconstruction. Neuroimage 9:179–194 Available at: http://www.ncbi.nlm.nih.gov/pubmed/9931268.

Denys K (2004) The Processing of Visual Shape in the Cerebral Cortex of Human and Nonhuman Primates: A Functional Magnetic Resonance Imaging Study. J Neurosci 24:2551–2565 Available at: http://www.jneurosci.org/cgi/doi/10.1523/JNEUROSCI.3569-03.2004.

Devor A, Sakadzic S, Saisan PA, Yaseen MA, Roussakis E, Srinivasan VJ, Vinogradov SA, Rosen BR, Buxton RB, Dale AM, Boas DA (2011) "Overshoot" of O2 Is Required to Maintain Baseline Tissue Oxygenation at Locations Distal to Blood Vessels. J Neurosci 31:13676–13681 Available at: http://www.jneurosci.org/cgi/doi/10.1523/JNEUROSCI.1968-11.2011.

DeYoe E a, Carman GJ, Bandettini P, Glickman S, Wieser J, Cox R, Miller D, Neitz J (1996) Mapping striate and extrastriate visual areas in human cerebral cortex. Proc Natl Acad Sci U S A 93:2382–2386.

Di Bono MG, Begliomini C, Castiello U, Zorzi M (2015) Probing the reaching-grasping network in humans through multivoxel pattern decoding. Brain Behav 5:1–18.

Drury HA, Van Essen DC, Anderson CH (2000) Surefit: Software for segmenting the cerebral cortex and generating surface reconstructions. Neuroimage 11:S914 Available at: http://www.sciencedirect.com/science/article/pii/S1053811900918421.

Drury HA, Van Essen DC, Anderson CH, Lee CW, Coogan TA, Lewis JW (1996) Computerized Mappings of the Cerebral Cortex: A Multiresolution Flattening Method and a Surface-Based Coordinate System. J Cogn Neurosci 8:1–28 Available at: http://www.mitpressjournals.org/doi/10.1162/jocn.1996.8.1.1.

Dubowitz DJ, Chen DY, Atkinson DJ, Grieve KL, Gillikin B, Bradley Jr. WG, Andersen RA (1998) Functional magnetic resonance imaging in macaque cortex. Neuroreport 9:2213–2218 Available at: http://www.ncbi.nlm.nih.gov/entrez/query.fcgi?cmd=Retrieve&db=PubMed&dopt=Citation&list_uids=9694202.

Duffy CJ (1998) MST neurons respond to optic flow and translational movement. J Neurophysiol 80:1816–1827.

Duffy CJ, Wurtz RH (1991) Sensitivity of MST neurons to optic flow stimuli. I. A continuum of response selectivity to large-field stimuli. J Neurophysiol 65:1329–1345.

Duffy CJ, Wurtz RH (1995) Response of monkey MST neurons to optic flow stimuli with shifted centers of motion. J Neurosci 15:5192–5208.

Duffy FH, Burchfiel JL, Conway JL (1976) Bicuculline reversal of deprivation amblyopia in the cat. Nature 260:256–257.

Dukelow SP, DeSouza JF, Culham JC, van den Berg A V, Menon RS, Vilis T (2001) Distinguishing subregions of the human MT+ complex using visual fields and pursuit eye movements. J Neurophysiol 86:1991–2000.

Dumoulin SO, Wandell BA (2008) Population receptive field estimates in human visual cortex. Neuroimage 39:647–660 Available at: http://www.pubmedcentral.nih.gov/articlerender.fcgi?artid=3073038&tool=pmcentrez&rendertype=abstract [Accessed November 6, 2013].

Durand JB, Nelissen K, Joly O, Wardak C, Todd JT, Norman JF, Janssen P, Vanduffel W, Orban GA (2007) Anterior Regions of Monkey Parietal Cortex Process Visual 3D Shape. Neuron 55:493–505.

Durand JB, Peeters R, Norman JF, Todd JT, Orban GA (2009) Parietal regions processing visual 3D shape extracted from disparity. Neuroimage 46:1114–1126 Available at: http://dx.doi.org/10.1016/j.neuroimage.2009.03.023.

Ekstrom LB, Roelfsema PR, Arsenault JT, Bonmassar G, Vanduffel W (2008) Bottom-up dependent gating of frontal signals in early visual cortex. Science 321:414–417 Available at: http://www.pubmedcentral.nih.gov/articlerender.fcgi?artid=3011100&tool=pmcentrez&rendertype=abstract [Accessed March 11, 2013].

Engel SA, Glover GH, Wandell BA (1997) Retinotopic organization in human visual cortex and the spatial precision of functional MRI. Cereb Cortex 7:181–192.

Engel SA, Rumelhart BA, Wandell BA, Lee AT, Glover GH, Chichilnisky EJ, Shadlen MN (1994) fMRI of human visual cortex. Nature 369:525.

Fan RH, Liu S, DeAngelis GC, Angelaki DE (2015) Heading Tuning in Macaque Area V6. J Neurosci 35:16303–16314.

Fattori P, Breveglieri R, Bosco A, Gamberini M, Galletti C (2017) Vision for Prehension in the Medial Parietal Cortex. Cereb Cortex 27:1149–1163 Available at: http://dx.doi.org/10.1093/cercor/bhv302.

Fattori P, Pitzalis S, Galletti C (2009) The cortical visual area V6 in macaque and human brains. J Physiol Paris 103:88–97 Available at: http://dx.doi.org/10.1016/j.jphysparis.2009.05.012.

Felleman DJ, Van Essen DC (1991) Distributed hierachical processing in the primate cerebral cortex. Cereb Cortex 1:1–47 Available at: http://cercor.oxfordjournals.org/cgi/doi/10.1093/cercor/1.1.1.

Fetsch CR, Pouget A, DeAngelis GC, Angelaki DE (2012) Neural correlates of reliability-based cue weighting during multisensory integration. Nat Neurosci 15:146–154.

Filimon F (2010a) Human Cortical Control of Hand Movements: Parietofrontal Networks for Reaching, Grasping, and Pointing. Neurosci 16:388–407 Available at: http://dx.doi.org/10.1177/1073858410375468.

Filimon F (2010b) Human Cortical Control of Hand Movements: Parietofrontal Networks for Reaching, Grasping, and Pointing. Neurosci 16:388–407.

Fischer E, Bülthoff HH, Logothetis NK, Bartels A (2012) Visual motion responses in the posterior cingulate sulcus: a comparison to V5/MT and MST. Cereb Cortex 22:865–876.

Fize D, Vanduffel W, Nelissen K, Denys K, Chef d'Hotel C, Faugeras O, Orban G a (2003) The retinotopic organization of primate dorsal V4 and surrounding areas: A functional magnetic resonance imaging study in awake monkeys. J Neurosci 23:7395–406 Available at: http://www.ncbi.nlm.nih.gov/entrez/query.fcgi?cmd=Retrieve&db=PubMed&dopt=Citation&list_uids=12917375.

Fogassi L, Gallese V, Gentilucci M, Chieffi S, Rizzolatti G (1991) [Kinematic study of reaching-grasping movements in the monkey]. Boll Soc Ital Biol Sper 67:715–721 Available at: http://europepmc.org/abstract/MED/1818597.

Fox PT, Raichle ME (1986) Focal physiological uncoupling of cerebral blood flow and oxidative metabolism during somatosensory stimulation in human subjects. Proc Natl Acad Sci U S A 83:1140–1144 Available at: http://www.pubmedcentral.nih.gov/articlerender.fcgi?artid=323027&tool=pmcentrez&rendertype=abstract.

Fox PT, Raichle ME, Mintun MA, Dence C (1988) Nonoxidative glucose consumption during focal physiologic neural activity. Science 241:462–464 Available at: http://www.ncbi.nlm.nih.gov/sites/entrez?Db=pubmed&DbFrom=pubmed&Cmd=Link&LinkName=pubmed_pubmed&LinkReadableName=Related Articles&IdsFromResult=3260686&ordinalpos=3&itool=EntrezSystem2.PEntrez.Pubmed.Pubmed_ResultsPanel.Pubmed_RVDocSum.

Frank SM, Baumann O, Mattingley JB, Greenlee MW (2014) Vestibular and visual responses in human posterior insular cortex. J Neurophysiol 112:2481–2491.

Friston KJ, Holmes a P, Worsley KJ, Poline J-B, Frith CD, Frackowiak RS (1995) Statistical parametric maps in functional imaging: a general linear model approach. Hum Brain Mapp 2:189–210.

Gallese V, Murata A, Kaseda M, Niki N, Sakata H (1994) Deficit of hand preshaping after muscimol injection in monkey parietal cortex. Neuroreport 5:1525–1529 Available at: http://content.wkhealth.com/linkback/openurl?sid=WKPTLP:landingpage&an=00001756-199407000-00029.

Galletti C, Fattori P, Gamberini M, Kutz DF (1999) The cortical visual area V6: Brain location and visual

topography. Eur J Neurosci 11:3922–3936.

Galletti C, Gamberini M, Kutz DF, Fattori P, Luppino G, Matelli M (2001) The cortical connections of area V6: An occipito-parietal network processing visual information. Eur J Neurosci 13:1572–1588.

Gamberini M, Fattori P, Galletti C (2015) The medial parietal occipital areas in the macaque monkey. Vis Neurosci 32:E013 Available at: http://www.journals.cambridge.org/abstract_S0952523815000103.

Gamberini M, Galletti C, Bosco A, Breveglieri R, Fattori P (2011) Is the medial posterior parietal area V6A a single functional area? J Neurosci 31:5145–5157 Available at: http://www.ncbi.nlm.nih.gov/pubmed/21451050.

Gardner EP, Babu KS, Reitzen SD, Ghosh S, Brown AS, Chen J, Hall AL, Herzlinger MD, Kohlenstein JB, Ro JY, Ep G, Ks B, Sd R, Ghosh S, As B, Chen J, Al H, Jb K, Neurophysiology RJY (2007) Neurophysiology of Prehension . I . Posterior Parietal Cortex and Object- Oriented Hand Behaviors. New York:387–406.

Georgieva S, Peeters R, Kolster H, Todd JT, Orban GA (2009a) The Processing of Three-Dimensional Shape from Disparity in the Human Brain. J Neurosci 29:727–742 Available at: http://www.jneurosci.org/cgi/doi/10.1523/JNEUROSCI.4753-08.2009.

Georgieva S, Peeters R, Kolster H, Todd JT, Orban GA (2009b) The Processing of Three-Dimensional Shape from Disparity in the Human Brain. J Neurosci 29:727–742.

Gerits A, Farivar R, Rosen BR, Wald LL, Boyden ES, Vanduffel W (2012) Optogenetically induced behavioral and functional network changes in primates. Curr Biol 22:1722–1726 Available at: http://www.ncbi.nlm.nih.gov/pubmed/22840516 [Accessed May 23, 2013].

Goense JBM, Logothetis NK (2008) Neurophysiology of the BOLD fMRI Signal in Awake Monkeys. Curr Biol 18:631–640.

Grafton ST, Fagg AH, Woods RP, Arbib MA (1996) Functional anatomy of pointing and grasping in humans. Cereb Cortex 6:226–237.

Gregoriou GG, Borra E, Matelli M, Luppino G (2006) Architectonic organization of the inferior parietal convexity of the macaque monkey. J Comp Neurol 496:422–451.

Grossberg S, Mingolla E, Pack C (1999) A Neural Model of Motion Processing and Visual Navigation by Cortical Area MST. Cereb Cortex 9:878–895.

Gu Y, Cheng Z, Yang L, DeAngelis GC, Angelaki DE (2015) Multisensory Convergence of Visual and Vestibular Heading Cues in the Pursuit Area of the Frontal Eye Field. Cereb Cortex.

Gu Y, DeAngelis GC, Angelaki DE (2012) Causal Links between Dorsal Medial Superior Temporal Area Neurons and Multisensory Heading Perception. J Neurosci 32:2299–2313.

Gu Y, Watkins P V., Angelaki DE, DeAngelis GC (2006) Visual and Nonvisual Contributions to Three-Dimensional Heading Selectivity in the Medial Superior Temporal Area. J Neurosci 26:73–85.

Guizar-Sicairos M, Thurman ST, Fienup JR (2008) Efficient subpixel image registration algorithms. Opt Lett 33:156 Available at: https://www.osapublishing.org/abstract.cfm?URI=ol-33-2-156.

Guldin WO, Akbarian S, Grüsser O-J (1992) Cortico-cortical connections and cytoarchitectonics of the primate vestibular cortex: A study in squirrel monkeys (*Saimiri sciureus*). J Comp Neurol 326:375–401.

Handwerker DA, Ollinger JM, D'Esposito M (2004) Variation of BOLD hemodynamic responses across subjects and brain regions and their effects on statistical analyses. Neuroimage 21:1639–1651.

Heider B, Jandó G, Siegel RM (2005) Functional architecture of retinotopy in visual association cortex of behaving monkey. Cereb Cortex 15:460–478.

Herscovitch P, Markham J, Raichle ME (1983) Brain Blood Flow Measured with Intravenous H215O.: I. Theory and Error Analysis . J Nucl Med 24:782–789 Available at: http://jnm.snmjournals.org/content/24/9/782.short.

Howell LL, Hoffman JM, Votaw JR, Landrum AM, Jordan JF (2001) An apparatus and behavioral training protocol to conduct positron emission tomography (PET) neuroimaging in conscious rhesus monkeys. J Neurosci Methods 106:161–169.

Huk AC, Dougherty RF, Heeger DJ (2002) Retinotopy and functional subdivision of human areas MT and MST. J Neurosci 22:7195–7205.

Huster RJ, Debener S, Eichele T, Herrmann CS (2012) Methods for Simultaneous EEG-fMRI: An Introductory Review. J Neurosci 32:6053–6060 Available at: http://www.jneurosci.org/cgi/doi/10.1523/JNEUROSCI.0447-12.2012.

Janssens T, Keil B, Farivar R, McNab J a, Polimeni JR, Gerits a, Arsenault JT, Wald LL, Vanduffel W (2012) An implanted 8-channel array coil for high-resolution macaque MRI at 3T. Neuroimage 62:1529–1536 Available at: http://www.ncbi.nlm.nih.gov/pubmed/22609793 [Accessed April 25, 2013].

Janssens T, Zhu Q, Popivanov ID, Vanduffel W (2014) Probabilistic and single-subject retinotopic maps reveal the topographic organization of face patches in the macaque cortex. J Neurosci 34:10156–10167 Available at: http://www.ncbi.nlm.nih.gov/pubmed/25080579.

Jeannerod M, Arbib MA, Rizzolatti G, Sakata H (1995) Grasping objects: the cortical mechanisms of visuomotor transformation. Trends Neurosci 18:314–320.

Jin T, Kim S-GSG (2008) Cortical layer-dependent dynamic blood oxygenation, cerebral blood flow and cerebral blood volume responses during visual stimulation. Neuroimage 43:1–9 Available at: http://www.ncbi.nlm.nih.gov/pubmed/18655837%5Cnhttp://www.sciencedirect.com/science/article/pii/S1053811908007751.

Jindrich DL, Courtine G, Liu JJ, McKay HL, Moseanko R, Bernot TJ, Roy RR, Zhong H, Tuszynski MH, Reggie Edgerton V (2011) Unconstrained three-dimensional reaching in Rhesus monkeys. Exp Brain Res 209:35–50.

Kaas JH (2006) The Evolution of Visual Cortex in Primates. In: The Primate Visual System, pp 267–283. John Wiley & Sons, Ltd. Available at: http://dx.doi.org/10.1002/0470868112.ch9.

Kaas JH, Stepniewska I (2016) Evolution of posterior parietal cortex and parietal-frontal networks for specific actions in primates. J Comp Neurol 524:595–608.

Kastner S, Chen Q, Jeong SK, Mruczek REB (2017) Neuropsychologia A brief comparative review of primate posterior parietal cortex : A novel hypothesis on the human toolmaker. Neuropsychologia:0–1 Available at: http://dx.doi.org/10.1016/j.neuropsychologia.2017.01.034.

Kay KN, Rokem A, Winawer J, Dougherty RF, Wandell BA (2013a) GLMdenoise: A fast, automated technique for denoising task-based fMRI data. Front Neurosci 7:1–15.

Kay KN, Winawer J, Mezer A, Wandell BA (2013b) Compressive spatial summation in human visual cortex. J Neurophysiol 110:481–494 Available at: http://www.pubmedcentral.nih.gov/articlerender.fcgi?artid=3727075&tool=pmcentrez&rendertype=abstract.

Kay KN, Winawer J, Mezer A, Wandell BA (2013c) Compressive spatial summation in human visual cortex. J Neurophysiol 110.

Kennan RP, Scanley BE, Innis RB, Gore JC (1998) Physiological basis for BOLD MR signal changes due to neuronal stimulation: separation of blood volume and magnetic susceptibility effects. Magn Reson Med

40:840–846.

Kim S-G, Harel N, Jin T, Kim T, Lee P, Zhao F (2014) Cerebral Blood Volume MRI with Intravascular Superparamagentic Iron Oxide Nanoparticles. 26:949–962.

Klein C, Evrard HC, Shapcott KA, Haverkamp S, Logothetis NK, Schmid MC, Klein C, Evrard HC, Shapcott KA, Haverkamp S, Logothetis NK (2016) Cell-Targeted Optogenetics and Electrical Microstimulation Reveal the Primate Koniocellular Projection to Supra-granular Visual Cortex Article Cell-Targeted Optogenetics and Electrical Microstimulation Reveal the Primate Koniocellular Projection to Supra-. Neuron 90:143–151 Available at: http://dx.doi.org/10.1016/j.neuron.2016.02.036.

Kolster H, Janssens T, Orban GA, Vanduffel W (2014) The retinotopic organization of macaque occipitotemporal cortex anterior to V4 and caudoventral to the middle temporal (MT) cluster. J Neurosci 34:10168–10191 Available at: http://www.pubmedcentral.nih.gov/articlerender.fcgi?artid=4115132&tool=pmcentrez&rendertype=abstract.

Kolster H, Mandeville JB, Arsenault JT, Ekstrom LB, Wald LL, Vanduffel W (2009) Visual field map clusters in macaque extrastriate visual cortex. J Neurosci 29:7031–7039 Available at: http://www.pubmedcentral.nih.gov/articlerender.fcgi?artid=2749229&tool=pmcentrez&rendertype=abstract [Accessed March 17, 2013].

Kolster H, Peeters R, Orban GA (2010) The Retinotopic Organization of the Human Middle Temporal Area MT/V5 and Its Cortical Neighbors. J Neurosci 30:9801–9820.

Komatsu H, Wurtz RH (1988) Relation of cortical areas MT and MST to pursuit eye movements. I. Localization and visual properties of neurons. J Neurophysiol 60:580–603.

Konen CS, Kastner S (2008) Representation of eye movements and stimulus motion in topographically organized areas of human posterior parietal cortex. J Neurosci 28:8361–8375.

Ku SP, Tolias AS, Logothetis NK, Goense J (2011) FMRI of the Face-Processing Network in the Ventral Temporal Lobe of Awake and Anesthetized Macaques. Neuron 70:352–362 Available at: http://dx.doi.org/10.1016/j.neuron.2011.02.048.

Larsson J, Heeger DJ (2006) Two Retinotopic Visual Areas in Human Lateral Occipital Cortex. J Neurosci 26:13128–13142 Available at: http://www.jneurosci.org/cgi/doi/10.1523/JNEUROSCI.1657-06.2006.

Leite FP, Tsao D, Vanduffel W, Fize D, Sasaki Y, Wald LL, Dale AM, Kwong KK, Orban G a, Rosen BR, Tootell RBH, Mandeville JB (2002) Repeated fMRI using iron oxide contrast agent in awake, behaving macaques at 3 Tesla. Neuroimage 16:283–294 Available at: http://www.ncbi.nlm.nih.gov/pubmed/12030817 [Accessed March 3, 2013].

Lewis JW, Van Essen DC (2000) Corticocortical connections of visual, sensorimotor, and multimodal processing areas in the parietal lobe of the macaque monkey. J Comp Neurol 428:112–137.

Lindquist MA, Loh JM, Atlas LY, Wager TD (2009) Modeling the Hemodynamic Response Function in fMRI: Efficiency, Bias and Mis-modeling. Neuroimage 45:S187–S198 Available at: http://www.ncbi.nlm.nih.gov/pmc/articles/PMC3318970/.

Logothetis N, Merkle H, Augath M, Trinath T, Ugurbil K (2002) Ultra high-resolution fMRI in monkeys with implanted RF coils. Neuron 35:227–242 Available at: http://www.ncbi.nlm.nih.gov/pubmed/12160742.

Logothetis N, Pauls J, Logothetis NK, Guggenberger H, Peled S, Pauls J (1999) Functional imaging of the monkey brain Functional imaging of the monkey brain.

Logothetis NK (2002) The neural basis of the blood-oxygen-level-dependent functional magnetic resonance imaging signal. Philos Trans R Soc Lond B Biol Sci 357:1003–1037 Available at: http://www.ncbi.nlm.nih.gov/pubmed/12217171%5Cnhttp://www.pubmedcentral.nih.gov/articlerender.fcgi?artid=PMC1693017.

Logothetis NK, Pauls J, Augath M, Trinath T, Oeltermann A (2001) Neurophysiological investigation of the basis of the fMRI signal. Nature 412:150–157 Available at: http://www.ncbi.nlm.nih.gov/pubmed/11449264.

Logothetis NK, Wandell BA (2004) Interpreting the BOLD Signal. Annu Rev Physiol 66:735–769 Available at: http://www.annualreviews.org/doi/10.1146/annurev.physiol.66.082602.092845.

Loh JM, Lindquist M a, Wager TD (2008) Residual Analysis for Detecting MIS-Modelling in fMRI. Stat Sin 18:1421–1448.

Lomber SG (1999) The advantages and limitations of permanent or reversible deactivation techniques in the assessment of neural function. J Neurosci Methods 86:109–117.

Lynch JC (1987) Frontal eye field lesions in monkeys disrupt visual pursuit. Exp Brain Res 68:437–441.

MacAvoy MG, Gottlieb JP, Bruce CJ (1991) Smooth-Pursuit Eye Movement Representation in the Primate Frontal

Eye Field. Cereb Cortex 1:95–102.

Maioli MG, Squatrito S, Samolsky-Dekel BG, Riva Sanseverino E (1998) Corticocortical connections between frontal periarcuate regions and visual areas of the superior temporal sulcus and the adjoining inferior parietal lobule in the macaque monkey. Brain Res 789:118–125.

Mandeville JB (2012) IRON fMRI measurements of CBV and implications for BOLD signal. Neuroimage 62:1000–1008 Available at: http://www.ncbi.nlm.nih.gov/pubmed/22281669 [Accessed April 10, 2013].

Mandeville JB, Marota JJA, Kosofsky BE, Keltner JR, Weissleder R, Rosen BR, Weisskoff RM (1998) Dynamic Functional Imaging of Relative Cerebral Blood Volume During Forepaw Stimulation. Magn Reson Med 39:615–624.

Markov NT et al. (2014) A weighted and directed interareal connectivity matrix for macaque cerebral cortex. Cereb Cortex 24:17–36.

Mcintyre M, Richter W, Morden D, Wennerberg A, Frankenstein U (2003) Blood oxygenation level dependent functional magnetic resonance imaging. Concepts Magn Reson 16A:5–15 Available at: http://doi.wiley.com/10.1002/cmr.a.10049.

Mendoza-Halliday D, Torres S, Martinez-Trujillo JC (2014) Sharp emergence of feature-selective sustained activity along the dorsal visual pathway. Nat Neurosci 17:1255–1262.

Merchant H, Battaglia-Mayer A, Georgopoulos AP (2001) Effects of optic flow in motor cortex and area 7a. J Neurophysiol 86:1937–1954.

Mineault PJ, Khawaja FA, Butts DA, Pack CC (2012) Hierarchical processing of complex motion along the primate dorsal visual pathway. Proc Natl Acad Sci 109:E972–E980.

Miranda-Dominguez O, Mills BD, Grayson D, Woodall A, Grant KA, Kroenke CD, Fair DA (2014) Bridging the Gap between the Human and Macaque Connectome: A Quantitative Comparison of Global Interspecies Structure-Function Relationships and Network Topology. J Neurosci 34:5552–5563 Available at: http://www.jneurosci.org/cgi/doi/10.1523/JNEUROSCI.4229-13.2014.

Mishkin M, Lewis ME, Ungerleider LG (1982) Equivalence of parieto-preoccipital subareas for visuospatial ability in monkeys. Behav Brain Res 6:41–55.

Morrone MC, Tosetti M, Montanaro D, Fiorentini A, Cioni G, Burr DC (2000) A cortical area that responds

specifically to optic flow, revealed by fMRI. Nat Neurosci 3:1322–1328.

Motter BC, Mountcastle VB (1981) The functional properties of the light-sensitive neurons of the posterior parietal cortex studied in waking monkeys: foveal sparing and opponent vector organization. J Neurosci 1:3–26.

Mullinger K, Bowtell R (2011) Combining EEG and fMRI. In: Magnetic Resonance Neuroimaging: Methods and Protocols (Modo M, Bulte JWM, eds), pp 303–326. Totowa, NJ: Humana Press. Available at: http://dx.doi.org/10.1007/978-1-61737-992-5_15.

Murata A, Gallese V, Luppino G, Kaseda M, Sakata H (2000) Selectivity for the Shape, Size, and Orientation of Objects for Grasping in Neurons of Monkey Parietal Area AIP. J Neurophysiol 83:2580–2601.

Mushiake H, Inase M, Tanji J (1991) Neuronal activity in the primate premotor, supplementary, and precentral motor cortex during visually guided and internally determined sequential movements. J Neurophysiol 66:705 LP-718 Available at: http://jn.physiology.org/content/66/3/705.abstract.

Nelissen K, Fiave PA, Vanduffel W (2017) Decoding Grasping Movements from the Parieto-Frontal Reaching Circuit in the Nonhuman Primate. Cereb Cortex:1–15 Available at: http://dx.doi.org/10.1093/cercor/bhx037.

Nelissen K, Vanduffel W (2011) Grasping-related functional magnetic resonance imaging brain responses in the macaque monkey. J Neurosci 31:8220–8229 Available at: http://www.pubmedcentral.nih.gov/articlerender.fcgi?artid=3117146&tool=pmcentrez&rendertype=abstract [Accessed March 11, 2013].

Nelissen K, Vanduffel W, Orban GA (2006) Charting the Lower Superior Temporal Region, a New Motion-Sensitive Region in Monkey Superior Temporal Sulcus. J Neurosci 26:5929–5947.

Nicolas-alonso LF, Gomez-gil J (2012) Brain Computer Interfaces, a Review. :1211–1279.

Nobre AC, Mccarthy G (1995) Language-Related Field Potentials in the Anterior-Medial Temporal-Lobe .2. Effects of Word Type and Semantic Priming. J Neurosci 15:1090–1098.

Ogawa S, Lee TM, Kay AR, Tank DW (1990) Brain magnetic resonance imaging with contrast dependent on blood oxygenation. Proc Natl Acad Sci U S A 87:9868–9872 Available at: http://www.pubmedcentral.nih.gov/articlerender.fcgi?artid=55275&tool=pmcentrez&rendertype=abstract.

Orban GA (2002) Functional MRI in the awake monkey: the missing link. J Cogn Neurosci 14:965–969.

Orban GA (2016) Functional definitions of parietal areas in human and non-human primates. Proc Biol Sci 283 Available at: http://www.ncbi.nlm.nih.gov/pubmed/27053755.

Orban GA, Claeys K, Nelissen K, Smans R, Sunaert S, Todd JT, Wardak C, Durand JB, Vanduffel W (2006) Mapping the parietal cortex of human and non-human primates. Neuropsychologia 44:2647–2667.

Orban GA, Fize D, Peuskens H, Denys K, Nelissen K, Sunaert S, Todd J, Vanduffel W (2003) Similarities and differences in motion processing between the human and macaque brain: evidence from fMRI. Neuropsychologia 41:1757–1768.

Orban GA, Van Essen D, Vanduffel W (2004) Comparative mapping of higher visual areas in monkeys and humans. Trends Cogn Sci 8:315–324.

Pandya DN, Seltzer B (1982) Intrinsic connections and architectonics of posterior parietal cortex in the rhesus monkey. J Comp Neurol 204:196–210 Available at: http://www.ncbi.nlm.nih.gov/pubmed/6276450.

Passingham R (2009) How good is the macaque monkey model of the human brain? Curr Opin Neurobiol 19:6–11.

Patel GH, Shulman GL, Baker JT, Akbudak E, Snyder AZ, Snyder LH, Corbetta M (2010) Topographic organization of macaque area LIP. Proc Natl Acad Sci U S A 107:4728–4733 Available at: http://www.pubmedcentral.nih.gov/articlerender.fcgi?artid=2842044&tool=pmcentrez&rendertype=abstract.

Paulson OB, Hasselbalch SG, Rostrup E, Knudsen GM, Pelligrino D (2010) Cerebral Blood Flow Response to Functional Activation. J Cereb Blood Flow Metab 30:2–14 Available at: http://journals.sagepub.com/doi/10.1038/jcbfm.2009.188.

Perrone JA, Stone LS (1994) A model of self-motion estimation within primate extrastriate visual cortex. Vision Res 34:2917–2938.

Pfeuffer J, Shmuel A, Keliris GA, Steudel T, Merkle H, Logothetis NK (2007) Functional MR imaging in the awake monkey: effects of motion on dynamic off-resonance and processing strategies. Magn Reson Imaging 25:869–882.

Phinney RE, Siegel RM (2000) Speed selectivity for optic flow in area 7a of the behaving macaque. Cereb Cortex 10:413–421.

Pitzalis S, Galletti C, Huang RS, Patria F, Committeri G, Galati G, Fattori P, Sereno MI (2006) Wide-field retinotopy defines human cortical visual area v6. J Neurosci 26:7962–7973.

Pitzalis S, Sdoia S, Bultrini A, Committeri G, Di Russo F, Fattori P, Galletti C, Galati G (2013a) Selectivity to Translational Egomotion in Human Brain Motion Areas Engelmann J, ed. PLoS One 8:e60241.

Pitzalis S, Sereno MI, Committeri G, Fattori P, Galati G, Patria F, Galletti C (2010) Human v6: the medial motion area. Cereb Cortex 20:411–424.

Pitzalis S, Sereno MI, Committeri G, Fattori P, Galati G, Tosoni A, Galletti C (2013b) The human homologue of macaque area V6A. Neuroimage 82:517–530 Available at: http://dx.doi.org/10.1016/j.neuroimage.2013.06.026.

Pouydebat E, Fragaszy D, Kivell TL (2014) Grasping in primates: for feeding, moving and human specificities. Bmsap 26:129–133 Available at: http://link.springer.com/10.1007/s13219-014-0100-7.

Premereur E, Van Dromme IC, Romero MC, Vanduffel W, Janssen P (2015) Effective Connectivity of Depth-Structure–Selective Patches in the Lateral Bank of the Macaque Intraparietal Sulcus. PLoS Biol 13:1–20.

Quiroga RQ, Reddy L, Kreiman G, Koch C, Fried I (2005) Invariant visual representation by single neurons in the human brain. Nature 435:1102–1107 Available at: http://www.nature.com/doifinder/10.1038/nature03687.

Raffi M, Siegel RM (2007) A functional architecture of optic flow in the inferior parietal lobule of the behaving monkey. PLoS One 2:e200.

Rainer G, Rao SC, Miller EK (1999) Prospective coding for objects in primate prefrontal cortex. J Neurosci 19:5493–5505 Available at: http://www.ncbi.nlm.nih.gov/pubmed/10377358.

Reppas JB, Niyogi S, Dale AM, Sereno MI, Tootell RB (1997) Representation of motion boundaries in retinotopic human visual cortical areas. Nature 388:175–179.

Rice NJ, Tunik E, Grafton ST (2006) The Anterior Intraparietal Sulcus Mediates Grasp Execution, Independent of Requirement to Update: New Insights from Transcranial Magnetic Stimulation. J Neurosci 26:8176–8182 Available at: http://www.jneurosci.org/cgi/doi/10.1523/JNEUROSCI.1641-06.2006.

Rogers BP, Morgan VL, Newton AT, Gore JC (2007) Assessing Functional Connectivity in the Human Brain by FMRI. Magn Reson Imaging 25:1347–1357 Available at: http://www.ncbi.nlm.nih.gov/pmc/articles/PMC2169499/.

Rosenberg A, Cowan NJ, Angelaki DE (2013) The Visual Representation of 3D Object Orientation in Parietal Cortex. J Neurosci 33:19352–19361 Available at:

http://www.jneurosci.org/content/33/49/19352%5Cnhttp://www.jneurosci.org/content/33/49/19352.full.pdf%5Cnhttp://www.jneurosci.org/content/33/49/19352.short.

Roy AC, Paulignan Y, Farnè A, Jouffrais C, Boussaoud D (2000) Hand kinematics during reaching and grasping in the macaque monkey. Behav Brain Res 117:75–82.

Roy AC, Paulignan Y, Meunier M, Boussaoud D (2006) Prehension movements in the macaque monkey: Effects of perturbation of object size and location. Exp Brain Res 169:182–193.

Rozzi S, Calzavara R, Belmalih A, Borra E, Gregoriou GG, Matelli M, Luppino G (2006) Cortical connections of the inferior parietal cortical convexity of the macaque monkey. Cereb Cortex 16:1389–1417.

Rozzi S, Coudé G (2015) Grasping actions and social interaction: neural bases and anatomical circuitry in the monkey. Front Psychol 6:1–19 Available at: http://journal.frontiersin.org/Article/10.3389/fpsyg.2015.00973/abstract.

Sabatinelli D, Lang PJ, Keil A, Bradley MM (2007) Emotional perception: Correlation of functional MRI and event-related potentials. Cereb Cortex 17:1085–1091.

Sacrey LAR, Alaverdashvili M, Whishaw IQ (2009) Similar hand shaping in reaching-for-food (skilled reaching) in rats and humans provides evidence of homology in release, collection, and manipulation movements. Behav Brain Res 204:153–161.

Sakata H, Taira M, Murata A, Mine S (1995) Neural Mechanisms of Visual Guidance of Hand Action in the Parietal Cortex of the Monkey. :429–438.

Sawamura H (2005) Using Functional Magnetic Resonance Imaging to Assess Adaptation and Size Invariance of Shape Processing by Humans and Monkeys. J Neurosci 25:4294–4306 Available at: http://www.jneurosci.org/cgi/doi/10.1523/JNEUROSCI.0377-05.2005.

Schaafsma SJ, Duysens J (1996) Neurons in the ventral intraparietal area of awake macaque monkey closely resemble neurons in the dorsal part of the medial superior temporal area in their responses to optic flow patterns. J Neurophysiol 76:4056–4068.

Schicke T, Muckli L, Beer AL, Wibral M, Singer W, Goebel R, Rösler F, Röder B (2006) Tight covariation of BOLD signal changes and slow ERPs in the parietal cortex in a parametric spatial imagery task with haptic acquisition. Eur J Neurosci 23:1910–1918.

Schindler A, Bartels A (2016) Connectivity Reveals Sources of Predictive Coding Signals in Early Visual Cortex During Processing of Visual Optic Flow. Cereb Cortex.

Schluppeck D, Glimcher P, Heeger DJ (2005) Topographic organization for delayed saccades in human posterior parietal cortex. J Neurophysiol 94:1372–1384 Available at: http://www.ncbi.nlm.nih.gov/pubmed/15817644%5Cnhttp://jn.physiology.org/content/94/2/1372.full.pdf.

Schmid MC, Oeltermann A, Juchem C, Logothetis NK, Smirnakis SM (2006) Simultaneous EEG and fMRI in the macaque monkey at 4.7 Tesla. Magn Reson Imaging 24:335–342.

Selimbeyoglu A (2010) Electrical stimulation of the human brain: perceptual and behavioral phenomena reported in the old and new literature. Front Hum Neurosci Available at: http://journal.frontiersin.org/article/10.3389/fnhum.2010.00046/abstract.

Sereno M, Dale A, Reppas J, Kwong K, Belliveau J, Brady T, Rosen B, Tootell R (1995a) Borders of multiple visual areas in humans revealed by functional magnetic resonance imaging. Science (80-) 268:889–893 Available at: http://www.ncbi.nlm.nih.gov/pubmed/7754376.

Sereno MI (2001) Mapping of Contralateral Space in Retinotopic Coordinates by a Parietal Cortical Area in Humans. Science (80-) 294:1350–1354 Available at: http://dx.doi.org/10.1126/science.1063695%5Cnhttp://www.sciencemag.org/cgi/doi/10.1126/science.1063695.

Sereno MI, Dale a M, Reppas JB, Kwong KK, Belliveau JW, Brady TJ, Rosen BR, Tootell RBH, Series N, May N (1995b) Borders of Multiple Visual Areas in Humans Revealed by Functional Magnetic Resonance Imaging Borders of Multiple Visual Areas in Humans Revealed by Functional Magnetic Resonance Imaging. 268:889–893.

Sereno MI, Dale AM, Liu A, Tootell RBH (1996) Surface-based coordinate system for a canonical human neocortex. Soc Neurosci Abstr 22:1060.

Sereno MI, Pitzalis S, Martinez A (2001) Mapping of contralateral space in retinotopic coordinates by a parietal cortical area in humans. Science 294:1350–1354.

Sereno MI, Tootell RBH (2005) From monkeys to humans: What do we now know about brain homologies? Curr Opin Neurobiol 15:135–144.

Shikata E, McNamara A, Sprenger A, Hamzei F, Glauche V, Büchel C, Binkofski F (2008) Localization of human intraparietal areas AIP, CIP, and LIP using surface orientation and saccadic eye movement tasks. Hum Brain Mapp 29:411–421.

Shima K, Tanji J (2011) Both Supplementary and Presupplementary Motor Areas Are Crucial for the Temporal Organization of Multiple Movements happens Both Supplementary and Presupplementary Motor Areas Are Crucial for the Temporal Organization of Multiple Movements. Am Physiol Soc:3247–3260.

Siegel RM, Read HL (1997) Analysis of optic flow in the monkey parietal area 7a. Cereb Cortex 7:327–346.

Silver M a, Ress D, Heeger DJ, Michael A, Topographic DJH (2005) Topographic Maps of Visual Spatial Attention in Human Parietal Cortex. J Neurophysiol 94:1358–1371.

Silver MA, Kastner S (2009) Topographic maps in human frontal and parietal cortex. Trends Cogn Sci 13:488–495.

Slater H, Milne AE, Wilson B, Muers RS, Balezeau F, Hunter D, Thiele A, Griffiths TD, Petkov CI (2016) Individually customisable non-invasive head immobilisation system for non-human primates with an option for voluntary engagement. J Neurosci Methods 269:46–60 Available at: http://dx.doi.org/10.1016/j.jneumeth.2016.05.009.

Smith AT, Wall MB, Thilo K V (2012) Vestibular inputs to human motion-sensitive visual cortex. Cereb Cortex 22:1068–1077.

Smith AT, Wall MB, Williams AL, Singh KD (2006) Sensitivity to optic flow in human cortical areas MT and MST. Eur J Neurosci 23:561–569.

Soares JM, Marques P, Alves V, Sousa N (2013) A hitchhiker's guide to diffusion tensor imaging. Front Neurosci 7:1–14.

Sparing R, Mottaghy FM (2008) Noninvasive brain stimulation with transcranial magnetic or direct current stimulation (TMS/tDCS)-From insights into human memory to therapy of its dysfunction. Methods 44:329–337.

Srihasam K, Sullivan K, Savage T, Livingstone MS (2010) Non-invasive functional MRI in alert monkeys. Neuroimage 51:267–273 Available at: http://www.ncbi.nlm.nih.gov/pmc/articles/PMC2847050/.

Srivastava S, Orban GA, Mazie PA De, Janssen P (2009) A Distinct Representation of Three-Dimensional Shape in Macaque Anterior Intraparietal Area : Fast , Metric , and Coarse. 29:10613–10626.

Stanton GB, Friedman HR, Dias EC, Bruce CJ (2005) Cortical afferents to the smooth-pursuit region of the macaque monkey's frontal eye field. Exp Brain Res 165:179–192.

Stefanacci L, Reber P, Costanza J, Wong E, Buxton R, Zola S, Squire L, Albright T (1998) fMRI of monkey visual cortex. Neuron 20:1051–1057.

Steinmetz MA, Motter BC, Duffy CJ, Mountcastle VB (1987) Functional properties of parietal visual neurons: radial organization of directionalities within the visual field. J Neurosci 7:177–191.

Stephan KE (2004) On the role of general system theory for functional neuroimaging. J Anat 205:443–470 Available at: http://dx.doi.org/10.1111/j.0021-8782.2004.00359.x.

Swartz BE (2017) The advantages of digital over analog recording techniques. Electroencephalogr Clin Neurophysiol 106:113–117 Available at: http://dx.doi.org/10.1016/S0013-4694(97)00113-2.

Swisher JD, Halko M a, Merabet LB, McMains S a, Somers DC (2007) Visual topography of human intraparietal sulcus. J Neurosci 27:5326–5337 Available at: http://www.ncbi.nlm.nih.gov/pubmed/17507555.

Taira M, Mine S, Georgopoulos AP, Murata A, Sakata H (1990) Parietal cortex neurons of the monkey related to the visual guidance of hand movement. Exp Brain Res 83:29–36 Available at: http://link.springer.com/10.1007/BF00232190.

Takahashi K, Gu Y, May PJ, Newlands SD, DeAngelis GC, Angelaki DE (2007) Multimodal Coding of Three-Dimensional Rotation and Translation in Area MSTd: Comparison of Visual and Vestibular Selectivity. J Neurosci 27:9742–9756.

Takechi H, Onoe H, Shizuno H, Yoshikawa E, Sadato N, Tsukada H, Watanabe Y (1997) Mapping of cortical areas involved in color vision in non-human primates. Neurosci Lett 230:17–20.

Takeda K, Funahashi S (2004) Population vector analysis of primate prefrontal activity during spatial working memory. Cereb Cortex 14:1328–1339.

Tanaka K, Fukada Y, Saito HA (1989) Underlying mechanisms of the response specificity of expansion/contraction and rotation cells in the dorsal part of the medial superior temporal area of the macaque monkey. J Neurophysiol 62:642–656.

Tanji J, Shima K (1994) Role for supplementary motor area cells in planning several movements ahead. Nature 371:413–416 Available at: http://www.nature.com/doifinder/10.1038/371413a0.

Ts'o D, Frostig R, Lieke E, Grinvald A (1990) Functional organization of primate visual cortex revealed by high resolution optical imaging. Science (80-) 249:417–420 Available at: http://www.sciencemag.org/cgi/doi/10.1126/science.2165630.

Tsao DY, Vanduffel W, Sasaki Y, Fize D, Knutsen TA, Mandeville JB, Wald LL, Dale AM, Rosen BR, Essen DC Van, Livingstone MS, Orban GA, Tootell RBH, Louis S (2003) Stereopsis Activates V3A and Caudal Intraparietal Areas in Macaques and Humans. 39:555–568.

Tsutsui KI, Taira M, Sakata H (2005) Neural mechanisms of three-dimensional vision. Neurosci Res 51:221–229.

van Bruggen N, Busch E, Palmer JT, Williams SP, de Crespigny a J (1998) High-resolution functional magnetic resonance imaging of the rat brain: mapping changes in cerebral blood volume using iron oxide contrast media. J Cereb Blood Flow Metab 18:1178–1183.

Van Dromme IC, Premereur E, Verhoef BE, Vanduffel W, Janssen P (2016) Posterior Parietal Cortex Drives Inferotemporal Activations During Three-Dimensional Object Vision. PLoS Biol 14:1–26.

Van Essen DC (2002) Surface-based atlases of cerebellar cortex in the human, macaque, and mouse. Ann N Y Acad Sci 978:468–479.

Van Essen DC (2004) Organization of visual areas in macaque and human cerebral cortex. In: The Visual Neurosciences (Chalupa L, Werner J., eds), pp 507–521. MIT Press.

Van Essen DC, Drury H a., Dickson J, Harwell J, Hanlon D, Anderson CH (2001a) An Integrated Software Suite for Surface-based Analyses of Cerebral Cortex. J Am Med Informatics Assoc 8:443–459.

Van Essen DC, Lewis JW, Drury H a, Hadjikhani N, Tootell RB, Bakircioglu M, Miller MI (2001b) Mapping visual cortex in monkeys and humans using surface-based atlases. Vision Res 41:1359–1378 Available at: http://www.ncbi.nlm.nih.gov/pubmed/11322980.

Vanduffel W, Farivar R (2014) Functional MRI of Awake Behaving Macaques Using Standard Equipment. In: Advanced Brain Neuroimaging Topics in Health and Disease - Methods and Applications. InTech.

Vanduffel W, Fize D, Peuskens H, Denys K, Sunaert S, Todd JT, Orban GA (2002) Extracting 3D from motion: differences in human and monkey intraparietal cortex. Science 298:413–415.

Vanduffel W, Mandeville JB, Fize D, Nelissen K, Rosen BR, Tootell RBH, Hecke P Van, Orban GA (2001) Visual Motion Processing Investigated Using Contrast Agent- Enhanced fMRI in Awake Behaving Monkeys.

Neurotechnique 624:565–577.

Vanduffel W, Zhu Q, Orban GA (2014) Monkey Cortex through fMRI Glasses. Neuron 83:533–550 Available at: http://dx.doi.org/10.1016/j.neuron.2014.07.015.

Verhoef B-E, Vogels R, Janssen P (2016) Binocular depth processing in the ventral visual pathway. Philos Trans R Soc Lond B Biol Sci 371 Available at: http://www.ncbi.nlm.nih.gov/pubmed/27269602.

Vingerhoets G (2014) Contribution of the posterior parietal cortex in reaching, grasping, and using objects and tools. Front Psychol 5:1–17.

Vogt BA, Finch DM, Olson CR (1992) Functional Heterogeneity in Cingulate Cortex: The Anterior Executive and Posterior Evaluative Regions. Cereb Cortex 2:435–443.

Vogt BA, Vogt L, Farber NB, Bush G (2005) Architecture and Neurocytology of Monkey Cingulate Gyrus. J Comp Neurol 485:218–239.

Waldorp L (2009) Robust and unbiased variance of glm coefficients for misspecified autocorrelation and hemodynamic response models in fMRI. Int J Biomed Imaging 2009.

Wall MB, Smith AT (2008) The Representation of Egomotion in the Human Brain. Curr Biol 18:191–194 Available at: http://www.sciencedirect.com/science/article/pii/S0960982207024852 [Accessed November 18, 2013].

Wallis JD, Miller EK (2003) Neuronal activity in primate dorsolateral and orbital prefrontal cortex during performance of a reward preference task. Eur J Neurosci 18:2069–2081.

Wandell B a, Dumoulin SO, Brewer AA (2007) Visual field maps in human cortex. Neuron 56:366–383 Available at: http://www.ncbi.nlm.nih.gov/pubmed/17964252 [Accessed November 7, 2013].

Wandell BA, Winawer J (2011) Imaging retinotopic maps in the human brain. Vision Res 51:718–737 Available at: http://dx.doi.org/10.1016/j.visres.2010.08.004.

Wandell BA, Winawer J (2017) Computational neuroimaging and population receptive fields. Trends Cogn Sci 19:349–357 Available at: http://dx.doi.org/10.1016/j.tics.2015.03.009.

Worsley KJ, Friston KJ (1995) Analysis of fMRI Time-Series Revisited—Again. Neuroimage 2:173–181 Available at: http://linkinghub.elsevier.com/retrieve/pii/S1053811985710233.

Yablonskiy DA, Ackerman JJ, Raichle ME (2000) Coupling between changes in human brain temperature and

oxidative metabolism during prolonged visual stimulation. Proc Natl Acad Sci U S A 97:7603–7608 Available at: http://www.pubmedcentral.nih.gov/articlerender.fcgi?artid=16592&tool=pmcentrez&rendertype=abstract.

Yacoub E, Shmuel A, Logothetis N, Uğurbil K (2007) Robust detection of ocular dominance columns in humans using Hahn Spin Echo BOLD functional MRI at 7 Tesla. Neuroimage 37:1161–1177.

Young MP (1992) Objective analysis of the topological organization of the primate cortical visual system. Nature 358:152–155 Available at: http://dx.doi.org/10.1038/358152a0.

Young MP (1993) The organization of neural systems in the primate cerebral cortex. Proc Biol Sci 252:13–18.

Yu CP, Page WK, Gaborski R, Duffy CJ (2010) Receptive field dynamics underlying MST neuronal optic flow selectivity. J Neurophysiol 103:2794–2807.

Yu M, Huang S, Yu KJ, Clyne AM (2012) Dextran and polymer polyethylene glycol (PEG) coating reduce both 5 and 30 nm iron oxide nanoparticle cytotoxicity in 2D and 3D cell culture. Int J Mol Sci 13:5554–5570.

Zeidman P (2016) Bayesian Population Receptive Field Modelling. :17–19.

Zhang T, Britten KH (2011) Parietal Area VIP Causally Influences Heading Perception during Pursuit Eye Movements. J Neurosci 31:2569–2575.

Zhao F, Wang P, Hendrich K, Ugurbil K, Kim SG (2006) Cortical layer-dependent BOLD and CBV responses measured by spin-echo and gradient-echo fMRI: Insights into hemodynamic regulation. Neuroimage 30:1149–1160.

Zuiderbaan W, Harvey BM, Dumoulin SO (2012) Modeling center – surround configurations in population receptive fields using fMRI. J Vis 12:1–15.

I. Annex 1

REWARDING OBJECTS APPEAR LARGER BUT NOT BRIGHTER

Samy Rima[1,2], Mylène Poujade[1,2], Marcello Maniglia[1,2,3] & Jean-Baptiste Durand[1,2*]

[1] Université de Toulouse, Centre de Recherche Cerveau et Cognition, Toulouse, France

[2] Centre National de la Recherche Scientifique, Toulouse Cedex, France

[3] Department of Psychology, University of California, Riverside, Riverside, CA, USA

* Corresponding author

ABSTRACT

The fact that rewarding objects might be perceptually accentuated, *i.e.* seen larger than they really are, is a long-standing and controversial question. Here, we revisit this issue with a novel 2-alternative forced-choice paradigm combining asymmetric reward schedule and task reversal. In a first experiment, participants (n=27) had to choose the larger of two unequally rewarded objects in some sessions and the smaller one in other sessions. Response biases differed significantly between the reversed tasks, revealing an influence of reward on perceived sizes. In a second, control experiment, participants (n=27) indicated either the brighter or darker object. By contrast with the first experiment, response biases toward the most rewarding object were similar between those reversed tasks, indicating that the perceived luminance is immune to reward manipulation. Together, these results reveal that more

rewarding objects are perceived larger, but not brighter, than less rewarding ones.

INTRODUCTION

In 1947, Jerome Bruner and Cecile Goodman published “Value and need as organizing factors in perception”, in which they reported that 10-year-old children tend to largely over-estimate the size of coins but not that of similarly-sized wooden disks. The effect was stronger for coins of higher monetary value and further pronounced among the poorest children, leading the authors to claim that value and need trigger the perceptual accentuation of desirable objects. This seminal work ignited the “New Look” movement, a collective effort among psychologists for collecting evidences that perception is penetrated by affective, motivational and cognitive factors, rather than immune to them (Bruner 1957). The movement progressively vanished in the 70’s, with the raise of criticisms pointing both weaknesses in the experimental findings and biases in their interpretation. However, the last 2 decades have witnessed a strong resurgence of the debate around the ideas advocated by the “New Look” movement (Balcetis and Lassiter 2010; Firestone and Scholl 2016). Among the studies most directly related to the seminal work of Bruner and Goodman, one claims that objects useful for reaching a goal look bigger (Veltkamp et al. 2008). Others, in the same vein, report that muffins seem larger to food-primed dieters (van Koningsbruggen et al. 2011) and women’s breast to sex-primed men (Den Daas et al. 2013). Rewarding objects might also look closer (Balcetis and Dunning 2010) and more salient in ambiguous figures (Balcetis and Dunning 2006). Altogether, those few example studies seem to largely confirm the perceptual accentuation hypothesis.

However, most of the above-mentioned studies rely on simple perceptual judgement tasks: participants report a judgement/response bias of their perceptual experience. Consequently, Firestone and Scholl (Firestone and Scholl 2016) have objected that in most cases, the accentuation might arise at the judgmental level rather than at the

perceptual level. In other words, the rewarding status of an object would not affect how this latter is perceived, but rather how we decide to respond to it. According to the authors, simple perceptual tasks in which there is no criterion for classifying responses as correct or incorrect should be avoided, because loosening the link between perception and judgement cannot be penalized.

In the present study, we thus decided to revisit the perceptual accentuation hypothesis with a new paradigm that allows dissociating the respective contribution of the perceptual and judgmental levels. This paradigm was used both to ask whether rewarding objects are actually perceived larger than less rewarding ones (first experiment) and whether this potential accentuation could extend into the luminance domain (second experiment). The paradigm relies on the 2-alternative forced-choice (2AFC) task, which is a performance-based procedure known to discourage response biases and promote accuracy (Macmillan and Creelman 2004). Reward was manipulated by allocating distinct amounts of monetary gain for the 2 alternatives: gains for correct responses towards one alternative were higher than those for correct responses towards the other alternative. In the first experiment, participants were asked to indicate the larger alternative in some sessions and the smaller alternative in others. In the second experiment, they had to indicate the brighter alternative in some sessions and the darker one in others.

How such a “task-reversal” 2AFC (TR-2AFC) paradigm allows disentangling the respective contribution of judgement and perception in the response biases induced by asymmetric reward? This is illustrated in **Figure 1** by considering a case in which the 2 alternatives (*i.e.* the 2 discs simultaneously presented to the left and right of the central fixation target) are strictly similar, so that the only difference is the amount of

monetary reward attached to each alternative (**Figure 1a**). Whatever the task at hand ("which is the larger/brighter?" versus "which is the smaller/darker?"; **Figure 1b**), if reward does not affect how the discs are seen (**Figure 1c**), perceptual evidences are absent but a reward-optimization strategy should bias responses towards the most rewarding alternative (Bogacz et al. 2006). When perceptual judgement is uncertain, it is better to bet on the option that can provide the highest gain. Similar response biases toward the most rewarding alternative are thus expected for both reversed tasks (**Figure 2d**). By contrast, the perceptual accentuation hypothesis posits that the most rewarding alternative might be perceptually accentuated (**Figure 2e**). Thus, when the task calls for indicating the more salient (larger/brighter) alternative, both perceptual evidences and reward-optimization strategy tip the balance towards the more rewarding alternative. However, when the task is to indicate the less salient (smaller/darker) alternative, perceptual evidences should point toward the less rewarding alternative while the reward-optimization strategy should continue favoring the more rewarding one (**Figure 2f**). Consequently, the perceptual accentuation hypothesis uniquely predicts distinct response biases between the reversed tasks.

In the following, it will be shown that size, but not luminance, fulfills the prediction of the perceptual accentuation hypothesis. However, the reward-induced accentuation of visual size is much weaker than that previously described with simple perceptual judgement tasks. Potential mechanisms underlying this phenomenon and its ecological importance will be finally discussed.

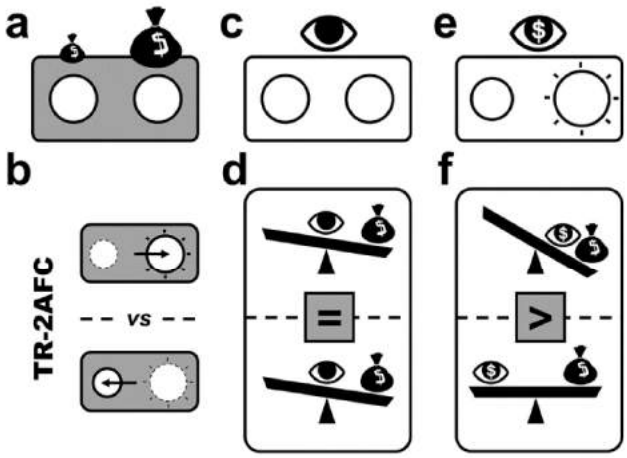

Figure 1. The task-reversal 2-alternative forced choice (TR-2AFC) procedure. (a) Example case with two unequally-rewarded but otherwise identical alternatives. **(b)** Illustration of the TR-2AFC procedure. **(c)** Absence of reward-induced perceptual accentuation. **(d)** Similar response biases toward the most rewarding alternative are expected for both reversed tasks, reflecting a simple reward-optimization strategy. **(e)** Presence of perceptual accentuation: the most rewarding alternative is seen as more salient. **(f)** Reward-induced perceptual salience and reward-optimization strategy should add-up when the task is to indicate the more salient alternative, but contradict each other when the task is to indicate the less salient alternative. Therefore, reward-induced response biases should differ between the reversed tasks.

MATERIAL AND METHODS

Participants

54 participants aged between 20 and 30 years old were recruited for the present study. Twenty-seven participants (18 females) were involved in the first experiment on size discrimination and 27 (12 females) participated in the second experiment on size discrimination. All participants were volunteers and declared having normal or corrected-to-normal vision. They were naïve about the purpose of the experiment and were only informed about the task to perform. They were also informed that the total amount of earned money would depend on their performances in the task (ranging from 13 euros/session for performances at chance level to 26 euros/session for optimal performances). Participants signed an informed consent form in which all those details were provided. The experiment met the ethical standards of the Helsinki Declaration and was approved by our local ethic committee (CLERIT).

Apparatus

Participants sat in a chair, legs uncrossed, hands on a table, within a dark experimental box. They positioned their heads within a head-support device clamped on top of the table and equipped with both chin and forehead supports. The uprights were further covered with sheets of dense foam in order minimize head movements during the experiment. Participants faced a video (LCD?) screen subtending 44 x 26 deg of visual angle at a viewing distance of 63 cm, with a resolution of 1920x1080 pixels and a refresh rate of 60 Hz. The experiment was controlled by the EventIDE software (OkazoLab), running on an Intel Core i5 based computer. A video-based binocular eye tracker (Eye Link 1000) placed 35 cm in front of the participants was used to record binocular eye movements at 1 kHz per eye during the experiment.

Experiment 1: Size discrimination

Each of the 27 participants involved in the first experiment performed 4 distinct sessions across different days, as illustrated in **Figure 2a**. In two successive sessions, participants were asked to indicate in each trial the larger of two simultaneously presented discs while in the two remaining sessions, they had to indicate the smaller disc. The order of those reversed tasks was alternated between participants. For both tasks, the higher monetary reward was attached to the left alternative in one session and to the right alternative in the other session, to dissociate reward-induced response biases from potential leftward or rightward response biases. High and low amount of reward corresponded to 5 and 1 cents of euro for each correct trial, respectively. The discs had similar luminance (180 cd/m^2) but across trials, they differed in their diameter by 2%, 4% 8% or 16% (reference disc diameter=6°) with equal probability for the larger and smaller discs to be located rightward and leftward (50%).

Each session started with the calibration of the eye tracker. In each trial, the central fixation cross appeared first and participants had to maintain fixation on that target for a period jittering randomly between 1500 and 3000 msec. Successful fixation was followed by the simultaneous appearance of the 2 alternatives (i.e. the 2 discs) that remained on the screen. Participants had 2300 ms to move their gaze toward the chosen disc (i.e. the brighter or darker one, depending on the task at hand). Beyond this time limit, the trial was aborted and text which indicated to the subjects that they were too late was shown for 500 ms. Correct trials were signaled by the image of a 5 cents coin or a 1 cent coin, depending on the reward associated with the chosen disc, accompanied by the sound of a cash machine, either brief or long depending on the

small and high monetary gain. Incorrect trials were marked by the image of a stop sign and the sound of a buzzer, indicating the absence of gain. A new trial was initiated 200 ms after that feedback. Each session consisted of 6 blocks of 72 trials (9 repetitions of each condition per block). Participants were free to rest between each block.

Experiment 2: Luminance discrimination

As for the first experiment, each of the 27 participants involved in the second experiment performed 4 distinct sessions with task reversal (indicate the brighter disc *versus* indicate the darker disc) and reward asymmetry reversal, as shown in **Figure 2a.** The discs had a fixed diameter of 6° of visual angle and their centers were separated horizontally from the central fixation target by 6°. The discs and grey background had mean luminance of 155 and 30 cd/m^2, respectively. Difference in luminance between the discs varied pseudo-randomly across trials with possible values of 2%, 8%, 16% or 32% and equal probability for the brighter and darker discs to be located rightward and leftward (50%). As for the first experiment, each session consisted of 6 blocks of 72 trials (9 repetitions of each experimental condition per block). Participants were free to rest between each block.

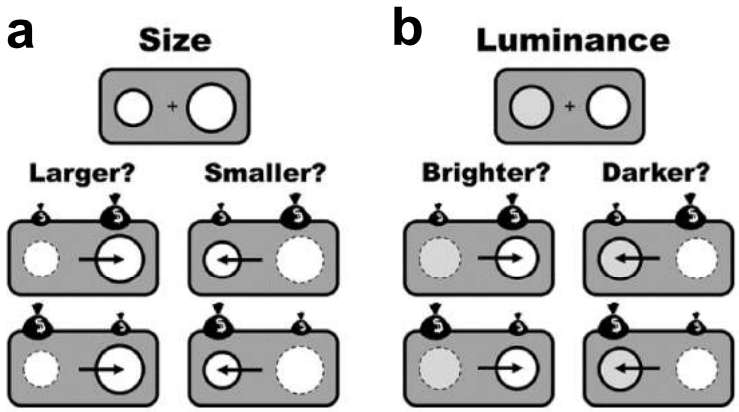

Figure 2. Experimental design. For both the size discrimination experiment **(a)** and the luminance discrimination experiment **(b)**, participants performed 4 distinct sessions. In 2 successive sessions, they had to indicate the brighter/larger one) and in the 2 other sessions, they had to indicate the smaller/darker. For each of those reversed tasks, the more rewarding alternative was located rightward in one session and leftward in the other session.

Data analysis

For each participant, we first evaluated whether introducing unequal monetary reward for the two alternatives induced significant response biases toward the most rewarding alternative. This was done to consider the fact that the subjective value of monetary reward can vary greatly among participants. Incorrect responses from the first 2 blocks of each session were summed and used to compute the proportions of incorrect responses toward the most and least rewarding alternatives. Participants were considered as sensitive to the manipulation of monetary reward if the proportion of incorrect responses was significantly greater for the most rewarding alternative than for the least rewarding one (Binomial test, $p<0.05$).

For each participant and each session, psychometric curves were constructed from the 4 remaining blocks, by computing the proportion of rightward saccades for each experimental condition (*i.e.* for each difference in luminance or size between the 2

discs). Those psychometric curves were then parametrized by fitting them with a cumulative Gaussian function (Wichmann and Hill 2001) of the form:

$$Y = \gamma+(1-\gamma-\lambda) \times 0.5 \times (1+erf((X-\mu)/\sqrt{(2\times\sigma^2)})),$$

where Y is the proportion of rightward saccades, X is the difference in luminance or size expressed as a percentage, γ and λ denote deviations of the curves' floor and ceiling from 0 and 1 respectively, while μ and σ represent the mean and standard deviation of the error function (*erf*). Those last 2 parameters are closely related to the point of subjective equality (PSE; *i.e.* the condition for which the 2 alternatives look the same), and to the just-noticeable-difference (JND; *i.e.* the minimal difference that can be detected between the alternatives), respectively.

The goodness of fit was evaluated from adjusted r^2 values, indicating how much of the psychometric curves' variance can be explained by the cumulative Gaussian function. Across all curves measured in the present study, the minimum r^2 value was 96.4%, indicating that this model nicely describes our whole data set.

RESULTS

Experiment 1: reward & perceived size

The sensitivity of each participant to the manipulation of monetary reward was evaluated by computing the relative proportion of incorrect responses toward the most rewarding alternative across the first 2 blocks of all 4 sessions (see Methods). As shown in **Figure 3a**, reward-induced response biases varied greatly among participants. Overall, 12 participants exhibited statistically significant bias (in black), while the 15 others did not show any significant bias (in gray). For both groups (sensitive/insensitive to reward manipulation), mean psychometric curves were computed from the remaining 4 blocks; they are shown in **Figure 3b**. As expected for the insensitive group (lower panels), no response bias toward the most rewarding alternative was observed. Placing the high monetary reward to the right (open squares) or to the left (filled circles) had no influence on the mean psychometric curves, which overlapped for both the larger task (left panel) and smaller task (right panel). By contrast, a shift of the psychometric curves was observed in the reward-sensitive group. However, this response bias was restricted to the larger task (**Figure 3b**; upper left panel) and virtually absent in the smaller task (upper right panel). This important point was confirmed by the analysis of the points of subjective equality (PSE; **Figure 3c**), since the larger task was the only one inducing a shift of the psychometric curves among the reward-sensitive participants (mean shift of ~1%). PSE shifts measured for the larger and smaller tasks were not correlated across participants ($r=-0.00$, $p=0.96$), confirming that those reversed tasks evoke distinct response biases. Those observations argue in favor of the perceptual accentuation hypothesis (**Figure 1f**). Finally, performances of the participants were quantified with the just-noticeable-

difference (JND). As shown in **Figure 3d**, they differed neither between the reversed (larger and smaller) tasks, nor between the reward-sensitive and insensitive groups, with an overall mean JND of ~4%.

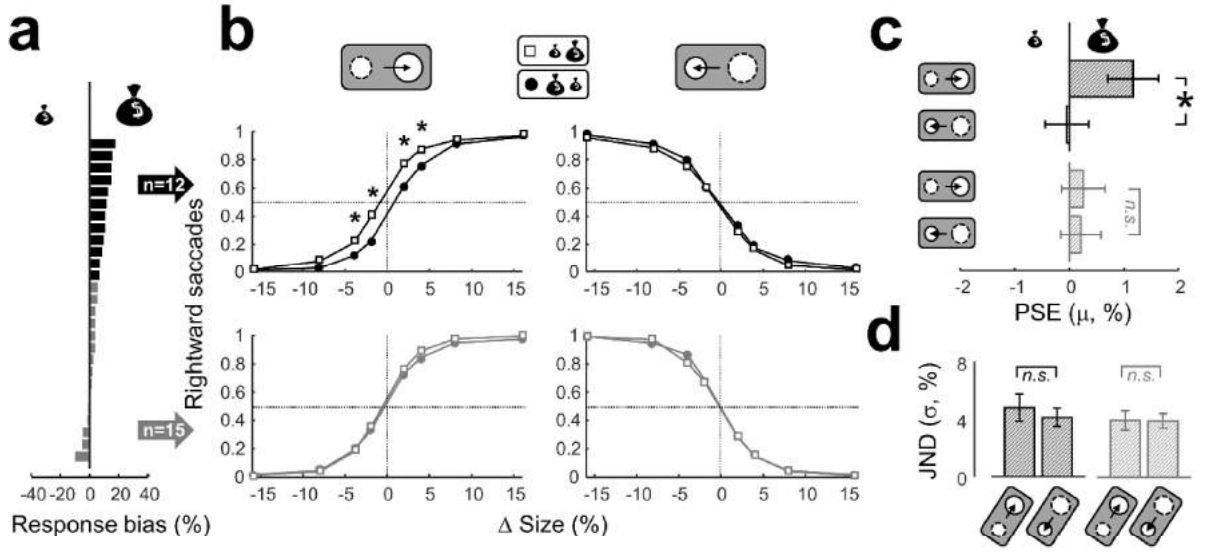

Figure 3. Results of the size discrimination task. (a) Response bias for the 27 participants. Those showing significant response bias toward the most rewarding alternative are shown in black (n=12), the others are shown in grey (n=15). **(b)** Mean population psychometric curves for the reversed tasks: larger (left column) *versus* smaller (right column), for participants with significant response bias (upper line, in black) and for the other participants (lower line, in grey).. **(c-d)** Mean point of subjective equality (PSE) and mean just-noticeable-differences (JND) with their 95% confidence intervals in each task for participants with significant response bias (in black) and for the other participants (in grey). Stars indicate significant differences in paired t-test, with a threshold set at p<0.01 (*n.s.* stands for non-significant difference).

Experiment 2: reward & perceived luminance

As in the first experiment, response biases in the first 2 blocks were used to distinguish the reward-sensitive (n=13) and insensitive (n=14) participants (**Figure 4a**). In the insensitive group (**Figure 4b**, lower panels), no response bias toward the most rewarding alternative was observed. By contrast, response biases toward the most rewarding alternative were clearly visible in the sensitive group (upper panels), taking the form of a statistically significant shift between the psychometric curves for both the brighter and darker tasks. Analysis of the individual psychometric curves revealed that PSE were shifted toward the most rewarding alternative by about 3% in the sensitive group (**Figure 4c**), while confirming the absence of significant shift for the insensitive group. Crucially, we did not find any difference between the PSE measured for the brighter and darker tasks in the sensitive group, which were highly correlated across participants ($r=0.68$, $p<10^{-4}$), revealing that the response biases can be accounted for by invoking solely a reward optimization strategy (*cf.* **Figure 1d**). As for the first experiment, performances differed significantly neither between the tasks nor between the groups, with an overall mean JND of about 7%.

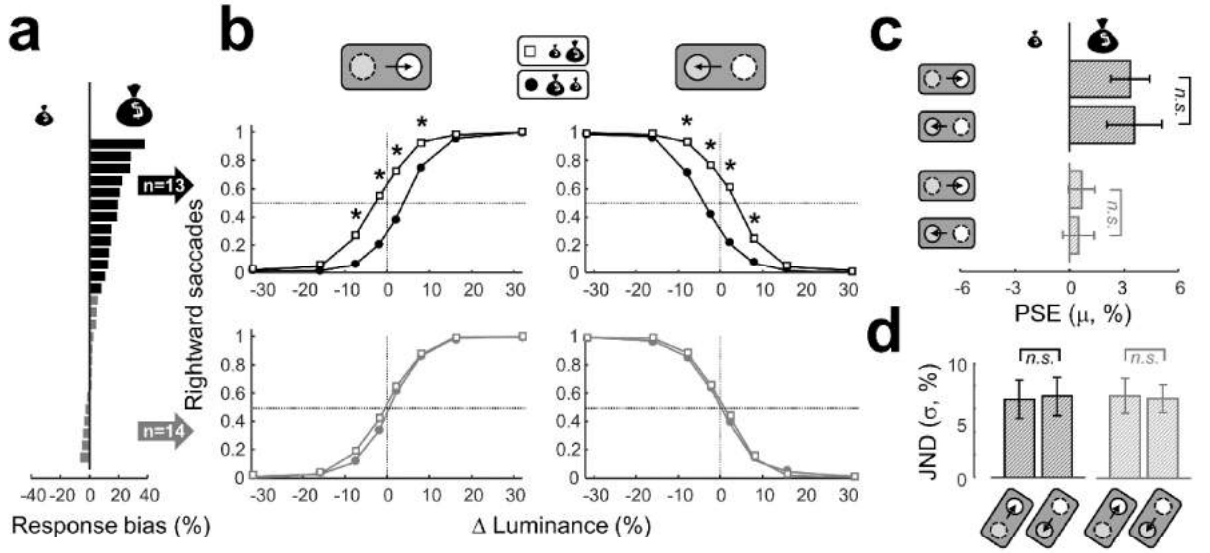

Figure 4. Results of the luminance discrimination task. (a) Response bias for the 27 participants. Those showing significant response bias toward the most rewarding alternative are shown in black (n=12), the others are shown in grey (n=15). **(b)** Mean population psychometric curves for the reversed tasks: brighter (left column) *versus* darker (right column), for participants with significant response bias (upper line, in black) and for the other participants (lower line, in grey). **(c-d)** Mean PSE and mean JND with their 95% confidence intervals in each task for participants with significant response bias (in black) and for the other participants (in grey). Stars indicate significant differences in paired t-test, with a threshold set at $p<0.01$ (*n.s.* stands for non-significant difference).

DISCUSSION

The objective of the present study was to re-evaluate the perceptual accentuation hypothesis (Bruner, 1957), according to which valuable objects might be seen larger than they really are. To that end, we developed a new task-reversal 2-alternative forced-choice (TR-2AFC) paradigm, that allows disentangling the respective contribution of the judgmental and perceptual levels in reward-induced response biases. With TR-2AFC, response biases toward the most rewarding alternative are expected to be similar between reversed tasks if they solely reflect a reward-optimization strategy (judgment bias) and to be distinct if they additionally reflect a perceptual accentuation of the most rewarding alternative (perceptual bias).

In a first experiment, the perceptual accentuation hypothesis was tested in the size domain on 27 participants, each one being tested across 4 distinct sessions. We found that among participants that were sensitive to monetary reward, response biases differed significantly between the reversed tasks (indicating the larger/smaller alternative): they were significant in the larger task, but virtually absent in the smaller task. This pattern of results fits with the perceptual accentuation hypothesis: more rewarding objects are perceived slightly larger than less rewarding ones. In a second experiment with another pool of 27 participants, we tested whether this perceptual accentuation extend to the luminance domain. However, we found that response biases toward the most rewarding alternative were similar between the reversed tasks (indicating the brighter/darker alternative). These results argue against the perceptual accentuation hypothesis in the luminance domain: more rewarding objects are not perceived brighter than less rewarding ones.

Our results seem to agree with those of previous studies documenting an effect of motivational factors on the perceived size of visual objects (Bruner and Goodman 1947; Veltkamp et al. 2008; van Koningsbruggen et al. 2011; Den Daas et al. 2013). However, it is important to note that the effect of reward we found is rather small when compared to those previous studies. If perceptual accentuation and reward optimization sum up to produce the response bias in the larger task (*i.e.* a shift of PSE of ~1%) and cancel each other in the smaller task (*i.e.* a shift of PSE of ~0%), one can infer that those perceptual and judgmental levels both contribute for ~0.5%. Phrased differently, the perceptual accentuation *per se* accounts for an increase of perceived size of ~0.5% for the more rewarding alternative. By contrast, previously reported effects are ~12% in Den Daas et al. (2013), ~25% in Bruner and Goodman (1947), ~35% in Veltkamp et al. (2008), ~40% in van Koningsbruggen et al. (2011). How much of the effects reported in those previous studies can be safely attributed to the perceptual level, and not to the judgmental level, remains an open question.

By contrast with the above-mentioned studies, we did not compare behavioural responses to objects of distinct intrinsic values (e.g. coins versus wooden discs in Bruner and Goodman, 1957) or from groups of participants with supposedly distinct motivational states (e.g. food-primed versus flower-primed dieters in Vletkamp et al., 2008). Our contrast targets within-subject differences between tasks involving intrinsically neutral and identical objects (i.e. luminance-defined discs). As such, we can rule out low-level differences and familiarity effects with the visual stimuli (Firestone and Scholls, 2016), but also other between-group differences, as confounding variables.

However, because the rewarding signal was attached to a spatial location, we cannot adress wether reward signals act directly on visual perception or through the mediation of spatial attention (Maunsell 2004). Recently, Chelazzi and colleagues (2014) found that reward-location coupling produces a long-lasting increase in the probability of detecting a target at that particular location, that they interpreted as evidence that reward signals can alter spatial attention (priority) maps (Chelazzi et al. 2013). Since it has been shown that attended objects can be perceived larger (Anton-Erxleben et al. 2007), our results in the size domain agree with the idea that more attentional ressources are allocated to the most rewarding location. However, such explanation does not fit with the fact that objects are not perceived brighter, while spatial attentions has been shown to increase the apparent contrast (Carrasco et al. 2004) and luminance (Tse 2005) of attended objects.

Assuming that the perceived size of visual objects is linked to the extent of activation they trigger in early visual cortex (Murray et al. 2006; Schwarzkopf and Rees 2013), an alternative explanation posits that coupling a reward to a particular location induces a cortical over-representation of that particular location. Such cortical remodeling could be mediated by dopaminergic neurons of the ventral tegmental area (VTA) that have already been shown to promote cortical remodeling in the auditory cortex (Bao et al. 2001) and to influence activity in early visual cortex (Serences 2008; Arsenault et al. 2013).

Whatever the underlying mechanisms, our results reveal that the influence of reward cannot be generalized to all dimensions of visual perception. This result echoes recent findings that visual motion does not affect all dimensions of auditory perception (Maniglia et al. 2017). Evidencing the limits of contextual influences on perception

represents an important step toward understanding the origins and functions of such phenomenom (Firestone and Scholls, 2016).

Ecologically, luminance strongly depends on external factors (time of the day, weather, etc) and it is not clear that a perceptual accentuation may have any functional utility. By contrast, perceiving behaviorally important objects as larger than they really are may ease their detection (Bruner 1957) and, additionally, may help making their rewarding status more appealing (Balcetis 2010).

REFERENCES

Anton-Erxleben K, Henrich C, Treue S. 2007. Attention changes perceived size of moving visual patterns. J Vis. 7:5.

Arsenault JT, Nelissen K, Jarraya B, Vanduffel W. 2013. Dopaminergic reward signals selectively decrease fMRI activity in primate visual cortex. Neuron. 77:1174–1186.

Balcetis E, Dunning D. 2006. See what you want to see: motivational influences on visual perception. J Personal Soc.

Balcetis E, Dunning D. 2010. Wishful seeing: more desired objects are seen as closer. Psychol Sci. 21:147–152.

Balcetis E, Lassiter GD. 2010. Social psychology of visual perception. Psychology Press.

Bao S, Chan VT, Merzenich MM. 2001. Cortical remodelling induced by activity of ventral tegmental dopamine neurons. Nature. 412:79–83.

Bogacz R, Brown E, Moehlis J, Holmes P, Cohen JD. 2006. The physics of optimal decision making: A formal analysis of models of performance in two-alternative forced-choice tasks. Psychol Rev. 113:700–765.

Bruner JS. 1957. On perceptual readiness. Psychol Rev. 64:123–152.

Bruner JS, Goodman CC. 1947. Value and need as organizing factors in perception. J Abnorm Psychol. 42:33–44.

Carrasco M, Ling S, Read S. 2004. Attention alters appearance. Nat Neurosci. 7:308–313.

Chelazzi L, E to inova J, Calletti R, Lo Gerfo E, Sani I, Della Libera C, Santandrea E. 2014. Altering Spatial Priority Maps via Reward-Based Learning. J Neurosci. 34:8594–8604.

Chelazzi L, Perlato A, Santandrea E, Della Libera C. 2013. Rewards teach visual selective attention. Vision Res. 85:58–72.

Den Daas C, Häfner M, de Wit J. 2013. Sizing opportunity biases in estimates of goal-relevant objects depend on goal congruence. Soc Psychol.

Firestone C, Scholl B. 2016. Cognition does not affect perception: Evaluating the evidence for “top-down” effects. Behav Brain Sci.

Macmillan N, Creelman C. 2004. Detection theory: A user’s guide.

Maniglia M, Ward J, Grassi M. 2017. Sounds Are Perceived as Louder When Accompanied by Visual Movement. Multisens Res. 30:159–177.

Maunsell JHR. 2004. Neuronal representations of cognitive state: reward or attention? Trends Cogn Sci. 8:261–265.

Murray SO, Boyaci H, Kersten D. 2006. The representation of perceived angular size in human primary visual cortex. Nat Neurosci. 9:429–434.

Schwarzkopf DS, Rees G. 2013. Subjective Size Perception Depends on Central Visual Cortical Magnification in Human V1. PLoS One. 8:e60550.

Serences JT. 2008. Value-Based Modulations in Human Visual Cortex. Neuron. 60:1169–1181.

Tse PU. 2005. Voluntary attention modulates the brightness of overlapping transparent surfaces. Vision Res. 45:1095–1098.

van Koningsbruggen GM, Stroebe W, Aarts H. 2011. Through the eyes of dieters: Biased size perception of food following tempting food primes. J Exp Soc Psychol. 47:293–299.

Veltkamp M, Aarts H, Custers R. 2008. Perception in the Service of Goal Pursuit: Motivation to Attain Goals Enhances the Perceived Size of Goal-Instrumental Objects. Soc Cogn. 26:720–736.

Wichmann FA, Hill NJ. 2001. The psychometric function: I. Fitting, sampling, and goodness of fit. Percept Psychophys. 63:1293–1313.

J. Annex 2

Please cite this article in press as: Arsenault et al., Role of the Primate Ventral Tegmental Area in Reinforcement and Motivation, Current Biology (2014), http://dx.doi.org/10.1016/j.cub.2014.04.044

Current Biology *24*, 1–7, June 16, 2014 ©2014 Elsevier Ltd All rights reserved http://dx.doi.org/10.1016/j.cub.2014.04.044

Report

Role of the Primate Ventral Tegmental Area in Reinforcement and Motivation

John T. Arsenault,[1,2] Samy Rima,[1] Heiko Stemmann,[1] and Wim Vanduffel[1,2,3,*]

[1]Laboratory for Neuro- and Psychophysiology, KU Leuven, 3000 Leuven, Belgium

[2]Athinoula A. Martinos Center for Biomedical Imaging, MGH, Charlestown, MA 02129, USA

[3]Department of Radiology, Harvard Medical School, Boston, MA 02115, USA

Summary

Monkey electrophysiology [1, 2] suggests that the activity of the ventral tegmental area (VTA) helps regulate reinforcement learning and motivated behavior, in part by broadcasting prediction error signals throughout the reward system. However, electrophysiological studies do not allow causal inferences regarding the activity of VTA neurons with respect to these processes because they require artificial manipulation of neuronal firing. Rodent studies fulfilled this requirement by demonstrating that electrical and optogenetic VTA stimulation can induce learning and modulate downstream structures [3–7]. Still, the primate dopamine system has diverged significantly from that of rodents, exhibiting greatly expanded and uniquely distributed cortical and subcortical innervation patterns [8]. Here, we bridge the gap between rodent perturbation studies and monkey electrophysiology using chronic electrical microstimulation of macaque VTA (VTA-EM). VTA-EM was found to reinforce cue selection in an operant task and to motivate future cue selection using a Pavlovian paradigm. Moreover, by combining VTA-EM with concurrent fMRI, we demonstrated that VTA-EM increased fMRI activity throughout most of the dopaminergic reward system. These results establish a causative role for primate VTA in regulating stimulus-specific reinforcement and motivation as well as in modulating activity throughout the reward system.

Results

VTA-EM Reinforces Operant Behavior

Experiment 1

The firing pattern of ventral tegmental area (VTA) neurons is consistent with their putative function in reinforcement learning and motivational behavior [1, 2, 9]. Establishing a causal role for the primate VTA in such processes, however, has been hampered by a lack of targeted focal perturbation studies. We therefore developed an MRI-guided method to perform chronic electrical microstimulation of VTA (VTA-EM) in nonhuman primates (see Supplemental Experimental Procedures available online). We used perioperative high-resolution imaging (Figure 1A; Movie S1) to direct the insertion of a guide tube and a microwire electrode array [10] and to confirm the final positioning of the electrodes (Figure 1B). After electrode implantation, we tested whether VTA-EM played a causal role in positive reinforcement by using an operant conditioning paradigm. All procedures were approved by the KU Leuven Committee on Animal Care and are in accordance with NIH and European guidelines for the care and use of laboratory animals.

Monkeys first performed a baseline cue preference test measuring their preferences between two simultaneously presented visual cues in a free-choice task. In each session, a new set of cues was used. Individual trials began with a randomized wait period (1,000–1,500 ms) during which the monkey was required to fixate on a centrally positioned white square. After this, the white square was removed, and two visual cues appeared simultaneously on the left and on the right side of the screen (Figure 2A). Monkeys were allowed to freely select one of the two cues by saccading to their choice. To motivate cue selection, we rewarded 50% of all saccades with juice (0.07 ml). Critically, juice reward probabilities were equalized across cue positions (left or right) and cue identity (cue A or cue B) and, hence, were completely independent of the monkey's choice (see Supplemental Experimental Procedures).

For consistency across sessions, the preferred and nonpreferred cues during the baseline test were deemed cue A and B, respectively. After the baseline preference test was completed, we began a cue B-*VTA-EM* block in which 50% of all cue B selections were followed by VTA-EM. VTA-EM consisted of a 200 ms train of bipolar stimulation pulses (200 Hz; 650 μA–1 mA; two VTA electrodes; electrical microstimulation [EM] parameters, except the current, were identical for experiments 1–3). Importantly, to determine whether VTA-EM reinforced preceding actions, we performed VTA-EM 32–48 ms after cue selection (Figure 2B). Juice rewards were given in 50% of the trials but were entirely independent of VTA-EM, cue identity, and cue position. After the cue B-*VTA-EM* block, we began pairing VTA-EM with cue A selections (by using the paradigm explained above) and stopped pairing VTA-EM with cue B selections (cue A-*VTA-EM* block).

To quantify the monkey's cue selection behavior, we calculated a cue preference index: ([cue B selections − cue A selections]/[cue B selections + cue A selections]). This index ranges from 1 to −1, indicating a total preference for cue B or A, respectively. Cue preference indices taken from example sessions of monkey 1 (M1) and M3 (Figures 2C and 2D) provide clear evidence that the subject's preference for the cue associated with VTA-EM increased during the cue-*VTA-EM* blocks. Furthermore, these data indicate that the shift in cue preference was largest during the later stages of an EM block, as expected after repeated reinforcement. To quantify these effects, we split the data into the first and second half of each block (baseline, cue A- and cue B-*VTA-EM*) and calculated the mean cue preference during each half block. Because the effect of VTA-EM on cue preference was most evident during the second half of EM blocks (i.e., after the value of both cues could be sampled repeatedly), the mean cue preference during the second half of each block was compared across sessions. The mean cue preference of both M1 and M3 (Figures S1A and S1C) showed a main effect of block (Friedman test, $p < 0.05$). Comparison of the mean cue preference during the second half of blocks from M1 and M3

*Correspondence: wim@nmr.mgh.harvard.edu

Please cite this article in press as: Arsenault et al., Role of the Primate Ventral Tegmental Area in Reinforcement and Motivation, Current Biology (2014), http://dx.doi.org/10.1016/j.cub.2014.04.044

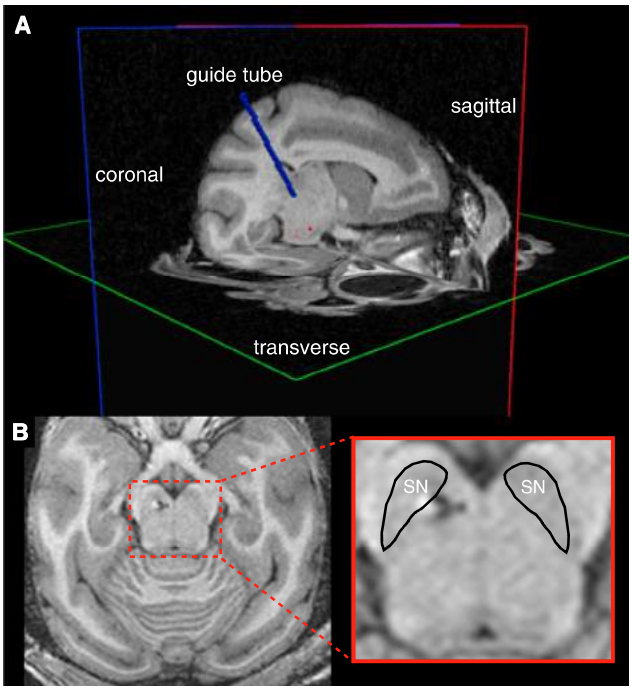

Figure 1. MRI-Guided Guide Tube and Electrode Implantation

(A) Triplanar cross-section of T1-weighted anatomical image acquired during guide tube insertion. Hypointensity induced by guide tube (see Movie S1) was used to estimate guide tube trajectory and position during surgery (blue cylinder). Estimated VTA target projected from the trajectory of the guide tube (red sphere).

(B) Postoperative T1-weighted anatomical image used to confirm the final electrode position. This transverse slice was the most ventral to exhibit hypointensity from the electrode. The inset displays an expanded view of the midbrain and electrode with the substantia nigra [SN] outlined.

See also Movie S1.

demonstrates the consistency of the VTA-EM effect across sessions (Figures 2E and 2F). Next, we hypothesized that the preference for the VTA-EM-associated cue should increase as a function of time within an EM block because positive feedback should occur between VTA-EM reinforcement and increased cue selection. Therefore, we calculated the correlation between elapsed time within a cue-VTA-EM block and preference for the cue associated with VTA-EM. Both M1 (mean r = 0.55, SEM r = 0.15, p = 0.03) and M3 (mean r = 0.47, SEM r = 0.06, p = 6.59×10^{-6}) exhibited a significant positive correlation (sign-rank test, $p < 0.05$) across blocks, confirming the hypothesis that cue preference increases as a function of time (Figures S1B and S1D).

In an effort to better understand the effect of juice and VTA-EM reinforcement on trial-by-trial cue selection behavior, we utilized Kalman filter learning models (http://www.cs.bris.ac.uk/home/rafal/rltoolbox/; see Supplemental Experimental Procedures) [11, 12]. For each monkey, two separate learning models were generated. One model used juice administration as the reward input, whereas the other model used VTA-EM. The other parameters of the model were assumed to be free. These free parameters were then fit to each subject's trial-by-trial cue selection behavior in order to maximize the likelihood of explaining the animal's observed behavior (Table S1). We found that the models utilizing VTA-EM as the reward input provided a better fit for the cue selection behavior (see Akaike information criterion [AIC] calculation in Supplemental Experimental Procedures) of both M1 ($\Delta AIC = 9.6$, $AIC_{weight} = 121.5$) and M3 ($\Delta AIC = 152.6$, $AIC_{weight} = 1.37 \times 10^{33}$). Thus, VTA-EM reinforcement explains trial-by-trial cue selection behavior better than juice administration, despite the same frequency of juice and VTA-EM events following the VTA-EM-associated cue. The better fit of VTA-EM reinforcement likely results from transition periods when the relative frequency of reinforcement events are exactly balanced between cues for juice, but not VTA-EM, predicting the subsequent shift in cue preference. We next examined the SD of the diffusion (σ_d) parameter to infer learning rates because larger σ_d values lead to higher learning rates. Juice models for M1 and M3 were found to display higher σ_d values. This indicates that cue selection was more sensitive to juice administration in recent trials, whereas reinforcement from VTA-EM events was integrated over longer periods of time. Next, the exploration (i.e., inverse temperature) parameter was compared between the two reinforcers because higher values indicate less-noisy selections (i.e., more-frequent selection of the high-value cue as calculated by the model). The larger exploration parameter of the VTA-EM models for both M1 and M3 therefore indicated that cue selection behavior was less noisy when VTA-EM reinforcement was modeled. Thus, the Kalman filter learning models confirmed in both animals that VTA-EM reinforcement better accounted for trial-by-trial cue selection behavior while indicating that VTA-EM reinforcement was integrated over longer time periods and was used to exploit the high-value cue more often, relative to equiprobable juice reinforcement.

Pavlovian Cue-VTA-EM Associations Motivate Future Cue Selection

Experiment 2

We developed a paradigm to assess whether Pavlovian cue-*VTA-EM* associations would motivate cue selection during a subsequent instrumental task. Importantly, within this paradigm there was no direct relationship between actions and VTA-EM during the association block or between the cue and VTA-EM during the instrumental block. Therefore, this paradigm offers insight into the motivational function of VTA-EM because it assesses whether a cue acquires incentive motivation during a Pavlovian association [13, 14]. This paradigm began with a 400-trial baseline cue preference test identical to the baseline test performed in experiment 1 in the absence of VTA-EM (Figure 3A). After this test, the subject was exposed to a 20 min Pavlovian cue-*VTA-EM* association block. Within this block, the subject performed a passive fixation task to obtain a juice reward (0.03 ml) every 800–1,200 ms while every 3,500–6,000 ms, one of the two visual cues was randomly presented. VTA-EM occurred 400 ms into every 500 ms presentation of the initially nonpreferred cue B. During this block, cue A was presented as often as cue B but never coupled with VTA-EM. After this Pavlovian association block, an identical 400-trial cue preference test was performed. If animal performance permitted, we performed another 20 min Pavlovian association block in which the VTA-EM-coupled cue was switched to cue A. This was followed by another 400-trial cue preference test block.

Cue preference indices from example sessions in M2 (Figure 3B) and M3 (Figure 3C) demonstrate an increased preference for cue B following the cue B-VTA-EM Pavlovian association block. After the subsequent cue A-VTA-EM association block, there was another shift in cue preference toward the cue previously associated with VTA-EM. To quantify the effect

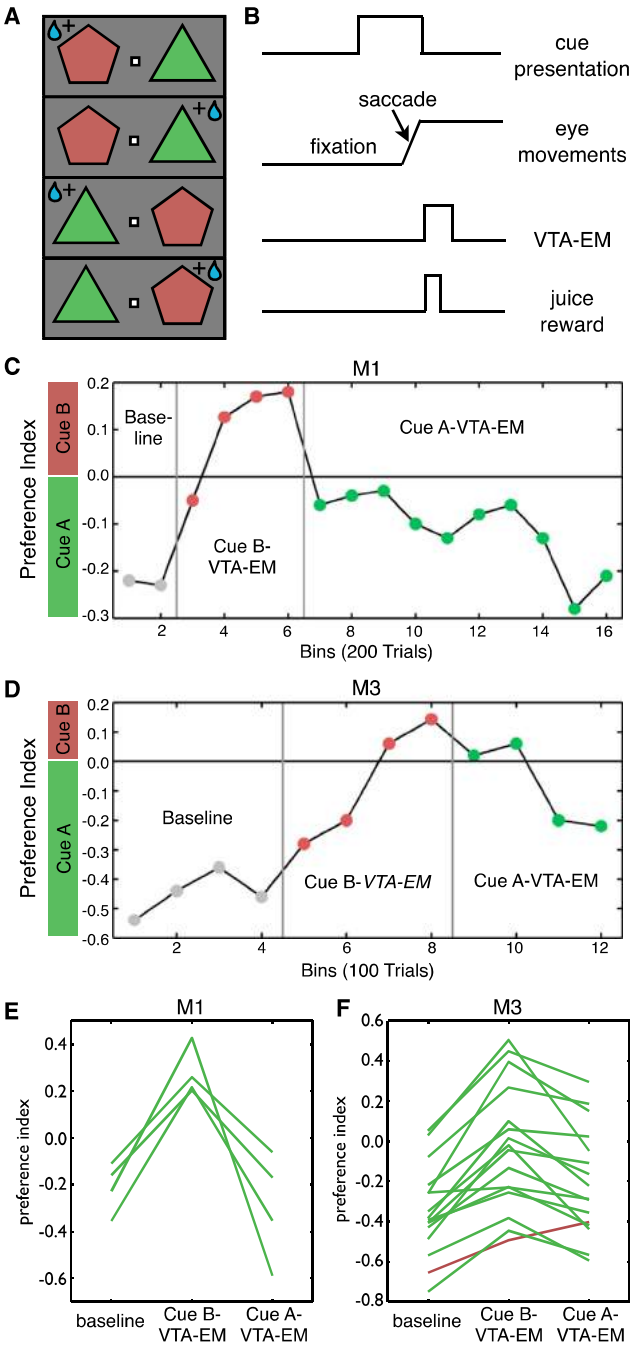

Figure 2. VTA-EM Reinforces Cue Selection in Experiment 1

(A) Four pseudorandomized, equiprobable trial types used in the free-choice visual cue preference test. New pairs of cues were used in each session. Juice reward probability was equalized across cue position and cue identity.

(B) Timing schematic of cue presentation, eye movements, juice reward (100 ms, 50% of trials), and VTA-EM (200 ms, 50% of selections of VTA-associated cue during cue-*VTA-EM* blocks). Juice and VTA-EM occurred 32–48 ms after cue selection.

(C and D) Cue preference index ([cue B selections – cue A selections])/(cue B selections + cue A selections]) during a single-example session of the operant task for subjects M1 (C) and M3 (D). Cue preference index was calculated in bins of 100 and 200 trials for M1 and M3, respectively. Color of data points denotes the cue selection followed by VTA-EM on 50% of the trials (gray: no *VTA-EM*; red: cue B-*VTA-EM*; green: cue A-*VTA-EM*). VTA-EM consisted of a 200 ms train of bipolar stimulation pulses (200 Hz; 650 μA [M1], 1 mA [M3]; two VTA electrodes stimulated simultaneously).

of cue-*VTA-EM* associations on cue preference, the mean cue preference before an association block was compared to the mean cue preference after an association block. For consistency across these pairs of cue preference test blocks, the cue associated with VTA-EM during the intervening association block was designated cue B. We found that both M2 and M3 (Figures S2A and S2B) exhibited a significantly increased preference for cue B after cue B-VTA-EM (sign-rank test, $p < 0.05$). Examination of the mean cue preference between the two preference tests demonstrates the consistency of the VTA-EM effect in experiment 2 for M2 and M3 (Figures 3D and 3E). This cue-specific effect is comparable to specific Pavlovian instrumental transfer (PIT) [15–17] because both paradigms demonstrate that incentive motivation acquired through Pavlovian association can be selectively transferred to an instrumental task. Importantly, to encourage responses, from which cue-selective effects could be monitored, the postassociation instrumental task was performed with 50% juice reward probability and was not under extinction as is characteristic for traditional PIT paradigms. Thus, our paradigm was not well suited to examine the general form of PIT during which general increases in vigor are displayed [15–17]. Nonetheless, because subjects could respond immediately after visual cue presentation, we examined changes in reaction times (RT) as an indicator of vigor. No significant change in the RT (sign-rank test, $p > 0.25$) for preference tests performed before and after Pavlovian association blocks was found for both M2 ($n = 6$ pairs of blocks, $p = 1.00$) and M3 ($n = 28$ pairs of blocks, $p = 0.265$). In general, experiment 2 demonstrated that cue-VTA-EM associations allowed a cue to gain incentive motivation leading to its increased selection during a subsequent operant task.

VTA-EM Increases fMRI Activity in the Dopaminergic Reward Network

The dopaminergic reward network consists of structures that receive dense dopaminergic innervation and respond to reward-related tasks. Comparison of a meta-analysis of 142 human fMRI studies of reward processing [18] and primate dopamine receptor innervation [19, 20] reveals the nucleus accumbens (NA), caudate, putamen, thalamus, orbitofrontal cortex (OFC), anterior insula, anterior cingulate cortex (ACC), and prefrontal cortex (PFC) as major nodes in this network. In addition, the hippocampus and the amygdala also exhibit reward responses and strong dopaminergic connections [20]. Human fMRI studies have found that nodes within the dopaminergic reward network, such as the ventral striatum and OFC, exhibit modulations in functional activity that correlate with similar reward prediction error signals as coded by the phasic activity of dopamine neurons [21, 22]. This correlative evidence suggests that reward activity within these regions may be driven, in part, by phasic VTA responses. Nonetheless, the distributed network of structures modulated by phasic changes in VTA activity has not been causally investigated in primates. To do so, we utilized combined VTA-EM fMRI [23].

During the scanning procedure, juice rewards (0.03 ml) were administered every 800–1,200 ms to maintain fixation

(E and F) Mean cue preference indices during the second half of each block type for each full session performed by M1 (E) and M3 (F). Green lines denote a session with a consistent trend for increased preference for the cue reinforced with VTA-EM, whereas red lines represent the opposite trend.

See also Figure S1 and Table S1.

Please cite this article in press as: Arsenault et al., Role of the Primate Ventral Tegmental Area in Reinforcement and Motivation, Current Biology (2014), http://dx.doi.org/10.1016/j.cub.2014.04.044

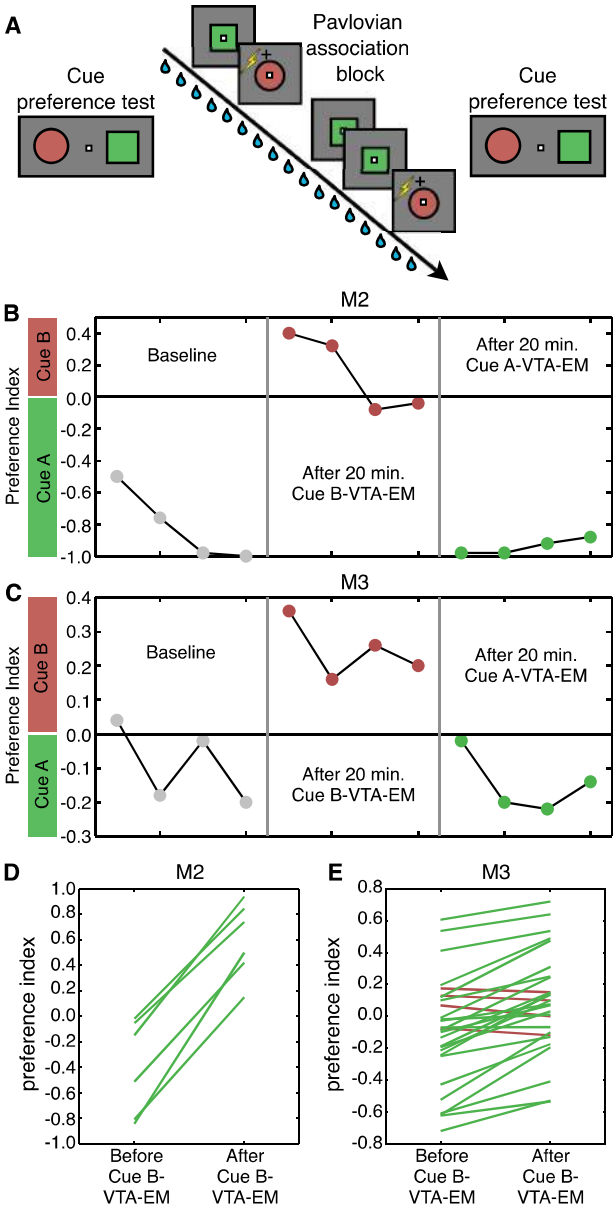

Figure 3. Pavlovian Cue-VTA-EM Association Motivates Future Cue Selection in Experiment 2

(A–C) Paradigm consisted of a 20 min Pavlovian cue-*VTA-EM* association block surrounded by two cue preference test blocks (no VTA-EM) (A). During the Pavlovian association block, the monkey performed a passive fixation task (0.03 ml of juice every 800–1,200 ms) while only one of the two visual cues (500 ms presentation) shown every 3,500–6,000 ms was temporally associated with VTA-EM (400 ms into cue presentation; bipolar; 200 ms; 200 Hz; 1 mA; two VTA electrodes stimulated simultaneously). The cue preference index from cue preference tests was calculated in bins of 100 trials from single-example sessions performed by M2 (B) and M3 (C). Color of data points denotes the preceding Pavlovian association block (gray: no VTA-EM; red: cue B-VTA-EM; green: cue A-VTA-EM).

(D and E) Mean cue preference index values for each pair of blocks performed by M2 (D) and M3 (E). Green lines denote pairs of cue preference test blocks with a trend for an increased preference of the cue associated with VTA-EM during the intervening Pavlovian association block, whereas red lines represent the opposite trend.

See also Figure S2.

behavior, whereas VTA-EM and control trials (no VTA-EM), used to assess the brain-wide functional effects of VTA-EM, occurred every 3,900–6,400 ms. To generate a representative map of the activations elicited by VTA-EM, fMRI data sets from each subject were first coregistered to the 112 RM-SL space [24]. A whole-brain, voxel-by-voxel general linear model analysis was then performed (see Supplemental Experimental Procedures). The resultant statistical image (VTA-EM − no VTA-EM, false discovery rate (FDR) corrected, $p = 0.001$, cluster size: 10 voxels) reveals a broad network of activated structures (Figure 4). To quantify the regions activated by VTA-EM, we determined the volume of overlap between a large group of anatomical regions of interest (ROIs) and activated voxels (Table S2A). Activations were found within many of the nodes of the dopaminergic reward network discussed above and were predominantly found ipsilateral to the site of VTA-EM. Interestingly, current levels used to robustly activate the dopaminergic reward network ($\leq$392 μA) were much weaker than those needed to reinforce behavior (>650 μA).

To more directly assess the correspondence between the regions activated by VTA-EM and those activated by a natural reinforcer, we compared VTA-EM-driven activity to fMRI activity generated by unexpected juice reward (see Supplemental Experimental Procedures). Because M1 and M2 were not available for further experiments, we made comparisons with a separate group of animals (see experiment 2 in [24]) Juice-driven activity was thresholded at the same level as VTA-EM in Figure 4 (juice − fixation, FDR corrected, $p = 0.001$, cluster size: 10 voxels), and a conjunction analysis was performed (Figure S3; see Supplemental Experimental Procedures). All anatomical ROIs displaying direct voxel-to-voxel colocalization of VTA-EM- and juice-driven activity are reported in Table S2B (highlighted in red). Several ROIs also displayed activations in response to both unexpected juice and VTA-EM but within nonoverlapping voxels (Tables S2A and S2C, highlighted in green). Despite this lack of an exact spatial correspondence at voxel level, this analysis demonstrates that the activation of these anatomical structures was common to both natural (unexpected juice) and artificial (VTA-EM) reinforcement. The majority of regions activated by both VTA-EM and juice (45B [PFC], areas 12 and 13 [OFC], area 24 [ACC], anterior intraparietal [AIP] area, caudate, gustatory, insula putamen, precentral opercular [PrCO], and ventral lateral nucleus [VL, thalamus]) were regions found in a meta-analysis of human reward studies [18] or were regions found to respond to primary reinforcers [25, 26]. This correspondence confirms that VTA-EM activates most of the structures typically activated by natural reinforcers. The other regions displaying juice and VTA-EM activations were mainly somatosensory and motor and/or premotor regions (areas 1 and 2, area 3a and 3b, frontal area 1 [F], F3, F5a, F5c, rostral inferior parietal lobule [PF], and secondary somatosensory cortex [SII]). Although activation of these structures in the juice experiment could result from the motor component of juice consumption, there were no differences in the juice administered temporally surrounding VTA-EM and the no VTA-EM events (see Supplemental Experimental Procedures). Interestingly, these regions receive dense dopaminergic innervation and are affected by dopaminergic modulation [27, 28]. Lastly, regions driven by juice, but not VTA-EM, were predominantly found within higher-order visual areas (dorsal visual area [V4D], inferior lateral intraparietal [LIPi], fundus of superior temporal [FST], lower superior temporal

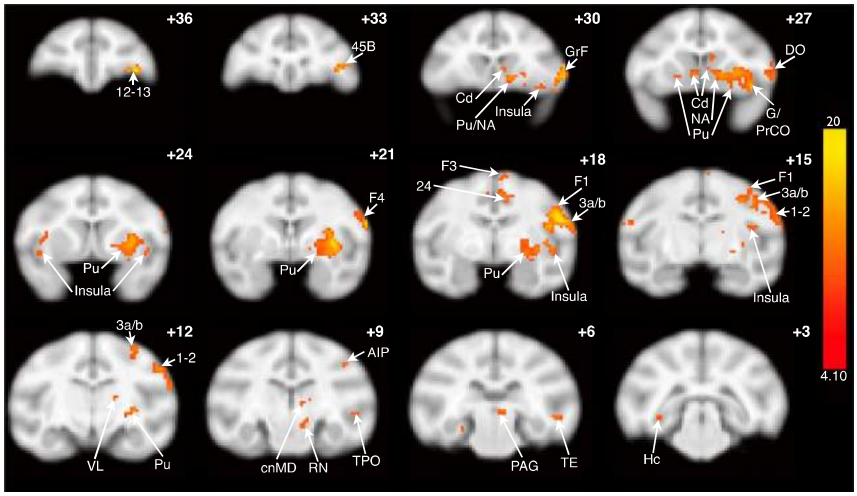

Figure 4. fMRI Activations Induced by VTA-EM in Experiment 3

Group analysis T score maps overlaid on coronal slices of the 112 RM-SL T1/T2* anatomical volume (n = 35 runs, M1 = 12 runs, M2 = 5 runs, M3 = 18 runs, fixed effect analysis, VTA-EM – no VTA-EM, FDR corrected, p = 0.001, cluster size: 10 voxels). VTA-EM consisted of a 200 ms train of bipolar stimulation pulses (200 Hz; 200 ms; 100 μA–392 μA; two VTA electrodes stimulated simultaneously).

The following abbreviations were used: AIP, anterior intraparietal; cnMD, centromedian nucleus; Cd, caudate; DO, dorsal opercular; G, gustatory; GrF, granular frontal; Hc, hippocampus; NA, nucleus accumbens; PAG, periaqueductal gray; Pu, putamen; PrCo, precentral opercular; RN, red nucleus; TPO, temporal parietal occipital; VL, ventral lateral nucleus.

See also Figure S3 and Table S2.

[LST], dorsal medial superior temporal [MSTd], middle temporal [MT], posterior inferior temporal cortex [TEO], anterior temporal cortex [TE], visual area 6 [V6], V6A, middle part of superior temporal polysensory [STPm]) (Table S2C). Activation of these regions in response to reward has been observed in previous monkey and human fMRI studies [29, 30]. This suggests that with the stimulation parameters utilized in this study, VTA-EM has little effect on higher-order visual regions. Lastly, the voxel-by-voxel analyses revealed that NA, a key node in the dopaminergic reinforcement network, was activated by VTA-EM, but not juice. In contrast, an ROI analysis of the anatomically defined NA revealed stronger activations by juice (n = 40 runs) than by VTA-EM (n = 35 runs) in left NA (VTA-EM mean percent signal change [PSC] = 0.09, juice mean PSC = 0.19, rank-sum test, p = 0.03) and right NA (VTA-EM mean PSC = 0.14, juice mean PSC = 0.24, rank-sum test, p = 0.007). This analysis suggests that juice reward increases fMRI activity more broadly throughout NA, whereas VTA-EM induced stronger yet more focal activations within NA. Despite the differences seen between activation maps generated by VTA-EM and unexpected juice reward, both reinforcers recruit a largely overlapping set of structures, many of them reward-processing structures with dense dopamine innervation.

Discussion

We have demonstrated that monkey VTA can be accurately and precisely targeted for chronic EM by using perioperative MRI guidance. VTA-EM was capable of selectively reinforcing and motivating behavior during operant and Pavlovian conditioning paradigms. This was demonstrated by an increased selection of a particular visual cue following the reinforcement of its selection with VTA-EM (experiment 1) or its previous Pavlovian coupling with VTA-EM (experiment 2). Therefore, this work establishes a causal role for primate VTA activity in the selective assignment of motivational value to visual cues, thus proving fundamental aspects of the hypothesized functional role of phasic neuronal VTA activity in primate behavior [1, 2, 13, 31]. Finally, by combining fMRI with simultaneous VTA-EM, we demonstrated that artificially increased VTA activity increased fMRI activity throughout most nodes of the dopaminergic reward network.

Comparison with VTA-EM and Optogenetic Stimulation in Rodents

Many rodent studies have demonstrated that VTA-EM [4, 7, 32], unaccompanied by other reinforcers, can reinforce operant behavior. In contrast, we monitored the behavioral effects of VTA-EM during tasks that were also reinforced with equiprobable juice reward. Juice rewards were employed because pilot experiments (M1, n = 10 sessions; M2 and M3, n = 1 session) demonstrated that VTA-EM alone, at least with the parameters utilized here, was not sufficient to maintain operant behavior. Consequently, balanced juice rewards were needed to maintain task performance, whereas unbalanced VTA-EM was used to affect cue preference. Therefore, although the VTA-EM-dependent effects on cue selection confirm VTA-EM's reinforcing properties, comparison with rodent results suggests that VTA-EM in rodents is a stronger reinforcer than VTA-EM in primates. Interestingly, operant reinforcement through optogenetic stimulation (OS) of dopamine neurons in rodents can also require the concurrent use of a primary reinforcer [3], but see [7, 32]. Because the majority of dopamine neurons phasically respond to unexpected reward [33], the typical motivational signal conveyed by the VTA to downstream structures likely involves VTA-wide activity. Therefore, a plausible interpretation of these results is that some OS paradigms in rodents (due to the smaller volume of tissue affected by OS [34]) and our EM paradigm in monkeys (due to the larger volume of VTA in primates) excite a smaller proportion of the total population of VTA neurons compared to rodent VTA-EM. Excitation of this smaller population may result in a weaker motivational signal and reduced behavioral effects. This is corroborated by our comparison of VTA-EM- and juice-induced fMRI activity within NA, which suggests that, in primates, natural reinforcers (juice) more broadly increase activity throughout reward structures. This may also explain why lower currents in the fMRI experiment were sufficient to drive the dopaminergic reward network, but higher currents were needed to reinforce behavior. In addition, an important caveat is that unlike the cell-type-specific OS now becoming common in rodent studies, VTA-EM likely stimulates dopaminergic (~65% of the population), GABAergic (~30%), and glutamatergic (~5%) cell types with little to no selectivity. Interestingly, OS of GABAergic VTA to NA projections has been shown to enhance stimulus-outcome associations [35]. Therefore, the

behavioral effect of VTA-EM's indiscriminate activation of VTA is likely a complex interaction of these different subpopulations and their targets. Despite this limitation, VTA-EM is an important first step in the causal understanding of VTA activity on motivation, reinforcement, and plasticity within the primate.

Comparison with Reinforcing Stimulation in Monkey

The primate exhibits greater dopamine innervation than the rodent. This expansion is evident in both densely (e.g., motor and premotor areas) and sparsely (i.e., parietal and temporal areas) innervated regions [8]. Furthermore, the laminar distribution of dopaminergic receptors differs between species, with layer 1 receiving the highest receptor density in primates while rodents display a more varied laminar distribution that is sparse in upper layers [8, 36]. These structural differences justify the importance of the primate model because they likely affect function. Nonetheless, the few studies assessing the reinforcing properties of EM in primate VTA or within a close proximity of VTA were large-scale mapping studies [37–39]. In these experiments, numerous locations were stimulated to determine reinforcing sites. The exact location of the EM sites was then determined using post hoc, ex vivo histology. Consequently, the behavioral experiments performed in these studies were conducted without precise knowledge of electrode positioning prohibiting a precisely targeted study of VTA function.

In addition, previous studies attempting to investigate the reinforcing effects of EM in VTA and neighboring structures have used a simple lever-pressing task. Although these studies demonstrated that EM reinforces operant behavior, they did not demonstrate the specificity of this reinforcement. For example, an important factor that governs Pavlovian and operant reinforcement is the temporal contiguity of the cue or the behavior and the reinforcement [40]. Because only one response was used in these earlier mapping studies, such studies cannot distinguish whether VTA-EM causes an aspecific increase in motivated behavior or whether it elicits effects that are specific to a particular cue or an action temporally associated with VTA-EM. In contrast, the changes in cue selection that we observed were dependent on temporal contiguity because increased cue selection was shown only for the cue whose presentation (Pavlovian) or selection (operant) was temporally coupled with VTA-EM. The specificity of this effect confirms that VTA-EM reinforcement selectively attributes motivational value to the cue temporally associated with VTA-EM. Moreover, the Pavlovian experiment demonstrates that VTA-EM can assign incentive motivation in a cue-selective way in the absence of any direct association with operant behavior.

In addition to VTA, EM has been shown to reinforce behavior at several other sites in the primate brain. These regions include NA, striatum, amygdala, OFC, lateral hypothalamus, mediodorsal nucleus, and locus coeruleus [38, 39, 41–43]. Interestingly, the majority of these sites contain a high density of dopamine receptors, and many of these same regions showed increased fMRI activity in response to VTA-EM and unexpected juice reward (see Figure 4 and Table S2). Moreover, it has been shown that systemic dopamine receptor blockade significantly reduced EM reinforcement within OFC, hypothalamus, and locus coeruleus [44]. Taken together, these findings suggest that these interconnected nodes of the dopaminergic reward network play important roles in reinforcement.

The absence over the last 40 years of any studies of primate VTA function causally linking activity with behavior and the complete absence of any previous work focusing specifically on VTA-EM highlight the difficulties of chronically targeting this small, but profoundly important, structure in primates. With the use of perioperative MRI-guided electrode implantation, we have circumvented these obstacles, allowing precise, chronic targeting of VTA. Furthermore, we have demonstrated the critical role of VTA in the selective reinforcement and motivation of visual cue selection. Finally, we combined fMRI with VTA-EM to demonstrate that VTA activity drives many of the nodes in the dopaminergic reward system. This work paves the way for future investigations of the relationship of increased VTA activity to reinforcement, motivation, learning, and plasticity throughout the primate brain.

Experimental Procedures

Please see Supplemental Experimental Procedures for a full description of the experimental design, methodology, and analysis.

Supplemental Information

Supplemental Information includes Supplemental Experimental Procedures, three figures, two tables, and one movie and can be found with this article online at http://dx.doi.org/10.1016/j.cub.2014.04.044.

Acknowledgments

We thank C. Klink, C. Fransen, C. Van Eupen, and A. Coeman for animal training and care; W. Depuydt, G. Meulemans, P. Kayenbergh, M. De Paep, S. Verstraeten, and I. Puttemans for technical assistance; and P. Balan and S. Raiguel for their valuable insights and comments on the manuscript. This work received support from Interuniversity Attraction Pole 7/21, Odysseus G.0007.12, Programme Financing PFV/10/008, Geconcerteerde Onderzoeks Actie 10/19, Impulsfinanciering Zware Apparatuur and Hercules funding of the KU Leuven, and Fonds Wetenschappelijk Onderzoek-Vlaanderen G090714N, G0888.13, G062208.10, G083111.10, G0719.12, and K7148.11. J.T.A. is a postdoctoral fellow of FWO-Vlaanderen. The Martinos Center for Biomedical Imaging is supported by National Center for Research Resources grant P41RR14075.

Received: June 25, 2013
Revised: March 27, 2014
Accepted: April 22, 2014
Published: May 29, 2014

References

1. Bromberg-Martin, E.S., Matsumoto, M., and Hikosaka, O. (2010). Dopamine in motivational control: rewarding, aversive, and alerting. Neuron *68*, 815–834.
2. Schultz, W., Dayan, P., and Montague, P.R. (1997). A neural substrate of prediction and reward. Science *275*, 1593–1599.
3. Adamantidis, A.R., Tsai, H.C., Boutrel, B., Zhang, F., Stuber, G.D., Budygin, E.A., Touriño, C., Bonci, A., Deisseroth, K., and de Lecea, L. (2011). Optogenetic interrogation of dopaminergic modulation of the multiple phases of reward-seeking behavior. J. Neurosci. *31*, 10829–10835.
4. Fibiger, H.C., LePiane, F.G., Jakubovic, A., and Phillips, A.G. (1987). The role of dopamine in intracranial self-stimulation of the ventral tegmental area. J. Neurosci. *7*, 3888–3896.
5. Tsai, H.C., Zhang, F., Adamantidis, A., Stuber, G.D., Bonci, A., de Lecea, L., and Deisseroth, K. (2009). Phasic firing in dopaminergic neurons is sufficient for behavioral conditioning. Science *324*, 1080–1084.
6. Esposito, R.U., Porrino, L.J., Seeger, T.F., Crane, A.M., Everist, H.D., and Pert, A. (1984). Changes in local cerebral glucose utilization during rewarding brain stimulation. Proc. Natl. Acad. Sci. USA *81*, 635–639.
7. Steinberg, E.E., Keiflin, R., Boivin, J.R., Witten, I.B., Deisseroth, K., and Janak, P.H. (2013). A causal link between prediction errors, dopamine neurons and learning. Nat. Neurosci. *16*, 966–973.

Please cite this article in press as: Arsenault et al., Role of the Primate Ventral Tegmental Area in Reinforcement and Motivation, Current Biology (2014), http://dx.doi.org/10.1016/j.cub.2014.04.044

8. Berger, B., Gaspar, P., and Verney, C. (1991). Dopaminergic innervation of the cerebral cortex: unexpected differences between rodents and primates. Trends Neurosci. *14*, 21–27.
9. Roelfsema, P.R., van Ooyen, A., and Watanabe, T. (2010). Perceptual learning rules based on reinforcers and attention. Trends Cogn. Sci. *14*, 64–71.
10. Bondar, I.V., Leopold, D.A., Richmond, B.J., Victor, J.D., and Logothetis, N.K. (2009). Long-term stability of visual pattern selective responses of monkey temporal lobe neurons. PLoS ONE *4*, e8222.
11. Dayan, P., and Abbott, L.F. (2001). Theoretical Neuroscience: Computational and Mathematical Modeling of Neural Systems (Cambridge: MIT Press).
12. Daw, N.D., O'Doherty, J.P., Dayan, P., Seymour, B., and Dolan, R.J. (2006). Cortical substrates for exploratory decisions in humans. Nature *441*, 876–879.
13. Wassum, K.M., Ostlund, S.B., Loewinger, G.C., and Maidment, N.T. (2013). Phasic mesolimbic dopamine release tracks reward seeking during expression of pavlovian-to-instrumental transfer. Biol. Psychiatry *73*, 747–755.
14. Flagel, S.B., Clark, J.J., Robinson, T.E., Mayo, L., Czuj, A., Willuhn, I., Akers, C.A., Clinton, S.M., Phillips, P.E., and Akil, H. (2011). A selective role for dopamine in stimulus-reward learning. Nature *469*, 53–57.
15. Corbit, L.H., Janak, P.H., and Balleine, B.W. (2007). General and outcome-specific forms of Pavlovian-instrumental transfer: the effect of shifts in motivational state and inactivation of the ventral tegmental area. Eur. J. Neurosci. *26*, 3141–3149.
16. Corbit, L.H., and Balleine, B.W. (2011). The general and outcome-specific forms of Pavlovian-instrumental transfer are differentially mediated by the nucleus accumbens core and shell. J. Neurosci. *31*, 11786–11794.
17. Talmi, D., Seymour, B., Dayan, P., and Dolan, R.J. (2008). Human pavlovian-instrumental transfer. J. Neurosci. *28*, 360–368.
18. Liu, X., Hairston, J., Schrier, M., and Fan, J. (2011). Common and distinct networks underlying reward valence and processing stages: a meta-analysis of functional neuroimaging studies. Neurosci. Biobehav. Rev. *35*, 1219–1236.
19. Lidow, M.S. (1995). D1- and D2 dopaminergic receptors in the developing cerebral cortex of macaque monkey: a film autoradiographic study. Neuroscience *65*, 439–452.
20. Oades, R.D., and Halliday, G.M. (1987). Ventral tegmental (A10) system: neurobiology. 1. Anatomy and connectivity. Brain Res. *434*, 117–165.
21. Schonberg, T., O'Doherty, J.P., Joel, D., Inzelberg, R., Segev, Y., and Daw, N.D. (2010). Selective impairment of prediction error signaling in human dorsolateral but not ventral striatum in Parkinson's disease patients: evidence from a model-based fMRI study. Neuroimage *49*, 772–781.
22. O'Doherty, J.P., Dayan, P., Friston, K., Critchley, H., and Dolan, R.J. (2003). Temporal difference models and reward-related learning in the human brain. Neuron *38*, 329–337.
23. Ekstrom, L.B., Roelfsema, P.R., Arsenault, J.T., Bonmassar, G., and Vanduffel, W. (2008). Bottom-up dependent gating of frontal signals in early visual cortex. Science *321*, 414–417.
24. McLaren, D.G., Kosmatka, K.J., Oakes, T.R., Kroenke, C.D., Kohama, S.G., Matochik, J.A., Ingram, D.K., and Johnson, S.C. (2009). A population-average MRI-based atlas collection of the rhesus macaque. Neuroimage *45*, 52–59.
25. Scott, T.R., Yaxley, S., Sienkiewicz, Z.J., and Rolls, E.T. (1986). Gustatory responses in the frontal opercular cortex of the alert cynomolgus monkey. J. Neurophysiol. *56*, 876–890.
26. Rolls, E.T., Scott, T.R., Sienkiewicz, Z.J., and Yaxley, S. (1988). The responsiveness of neurones in the frontal opercular gustatory cortex of the macaque monkey is independent of hunger. J. Physiol. *397*, 1–12.
27. Hosp, J.A., Pekanovic, A., Rioult-Pedotti, M.S., and Luft, A.R. (2011). Dopaminergic projections from midbrain to primary motor cortex mediate motor skill learning. J. Neurosci. *31*, 2481–2487.
28. Pleger, B., Ruff, C.C., Blankenburg, F., Klöppel, S., Driver, J., and Dolan, R.J. (2009). Influence of dopaminergically mediated reward on somatosensory decision-making. PLoS Biol. *7*, e1000164.
29. Arsenault, J.T., Nelissen, K., Jarraya, B., and Vanduffel, W. (2013). Dopaminergic reward signals selectively decrease fMRI activity in primate visual cortex. Neuron *77*, 1174–1186.
30. Weil, R.S., Furl, N., Ruff, C.C., Symmonds, M., Flandin, G., Dolan, R.J., Driver, J., and Rees, G. (2010). Rewarding feedback after correct visual discriminations has both general and specific influences on visual cortex. J. Neurophysiol. *104*, 1746–1757.
31. Salamone, J.D., and Correa, M. (2012). The mysterious motivational functions of mesolimbic dopamine. Neuron *76*, 470–485.
32. Witten, I.B., Steinberg, E.E., Lee, S.Y., Davidson, T.J., Zalocusky, K.A., Brodsky, M., Yizhar, O., Cho, S.L., Gong, S., Ramakrishnan, C., et al. (2011). Recombinase-driver rat lines: tools, techniques, and optogenetic application to dopamine-mediated reinforcement. Neuron *72*, 721–733.
33. Mirenowicz, J., and Schultz, W. (1996). Preferential activation of midbrain dopamine neurons by appetitive rather than aversive stimuli. Nature *379*, 449–451.
34. Diester, I., Kaufman, M.T., Mogri, M., Pashaie, R., Goo, W., Yizhar, O., Ramakrishnan, C., Deisseroth, K., and Shenoy, K.V. (2011). An optogenetic toolbox designed for primates. Nat. Neurosci. *14*, 387–397.
35. Brown, M.T., Tan, K.R., O'Connor, E.C., Nikonenko, I., Muller, D., and Lüscher, C. (2012). Ventral tegmental area GABA projections pause accumbal cholinergic interneurons to enhance associative learning. Nature *492*, 452–456.
36. Lidow, M.S., Goldman-Rakic, P.S., Gallager, D.W., and Rakic, P. (1991). Distribution of dopaminergic receptors in the primate cerebral cortex: quantitative autoradiographic analysis using [3H]raclopride, [3H]spiperone and [3H]SCH23390. Neuroscience *40*, 657–671.
37. Plotnik, R., Mir, D., and Delgado, J.M.R. (1972). Map of reinforcing sites in the rhesus monkey brain. Int. J. Psychobiol. *2*, 1–21.
38. Briese, E., and Olds, J. (1964). Reinforcing Brain Stimulation and Memory in Monkeys. Exp. Neurol. *10*, 493–508.
39. Routtenberg, A., Gardner, E.L., and Huang, Y.H. (1971). Self-stimulation pathways in the monkey, Macaca mulatta. Exp. Neurol. *33*, 213–224.
40. Schultz, W. (2006). Behavioral theories and the neurophysiology of reward. Annu. Rev. Psychol. *57*, 87–115.
41. Rolls, E.T., Burton, M.J., and Mora, F. (1980). Neurophysiological analysis of brain-stimulation reward in the monkey. Brain Res. *194*, 339–357.
42. Mora, F., Avrith, D.B., and Rolls, E.T. (1980). An electrophysiological and behavioural study of self-stimulation in the orbitofrontal cortex of the rhesus monkey. Brain Res. Bull. *5*, 111–115.
43. Bichot, N.P., Heard, M.T., and Desimone, R. (2011). Stimulation of the nucleus accumbens as behavioral reward in awake behaving monkeys. J. Neurosci. Methods *199*, 265–272.
44. Mora, F., Rolls, E.T., Burton, M.J., Shaw, G.S., and Shaw, G.S. (1976). Effects of dopamine-receptor blockade on self-stimulation in the monkey. Pharmacol. Biochem. Behav. *4*, 211–216.